Carbon Nitride as a Ligand: Synthesis, Characterisation and Application

Ben Arthur Coulson

Doctor of Philosophy

University of York

Chemistry

September 2018

Abstract

Carbon nitride's properties can be tuned through the coordination of metal atoms, which can lead to enhanced catalytic activity. However, to date, there are few reported examples of inner-sphere coordination of metal complex fragments to carbon nitride. Therefore, the effects of coordination of metal complex fragments to carbon nitride haves been investigated.

Reaction of the rhenium carbonyl complex, $[\mathrm{ReCl(CO)_5}]$ with the surface of urea-derived carbon nitride (UCN) results in $[\mathrm{ReCl(CO)_3(UCN)}]$, with a rhenium concentration of 0.39 mmol g^{-1}. The synthesis of the manganese analogue resulted in manganese oxidation leading to [Mn(UCN)] ([Mn] = 0.24 mmol g^{-1}). Infrared spectroscopy, along with crystal structures of molecular analogues, $[\mathrm{MCl(CO)_3(DMNA\text{-}\kappa^2}\mathit{N, N'})]$ (M = Re, Mn) was used to gain insight into the coordination of metals complex fragments to carbon nitride.

Two morphologies of carbon nitride, unstructured urea-derived carbon nitride (UCN) and porous cyanamide derived carbon nitride (CCN), were then decorated with $[\mathrm{Ru(bpy)_2}]^{2+}$ fragments. The carbon nitride structure affected metal loading, as $[\mathrm{Ru(bpy)_2(UCN)](PF_6)_2}$ ([Ru] = 0.016 mmol g^{-1}) showed lower metal loading compared to $[\mathrm{Ru(bpy)_2(CCN)](PF_6)_2}$ ([Ru] = 0.076 mmol g^{-1}). $[\mathrm{Ru(bpy)_2(DMNA\text{-}\kappa_2}\mathit{N, N'})](\mathrm{PF_6})_2$ was synthesised as a molecular analogue to gain insight into the coordination mode. The photocatalytic activities of $[\mathrm{Ru(bpy)_2(UCN)](PF_6)_2}$ and $[\mathrm{Ru(bpy)_2(UCN)](PF_6)_2}$ were completely inhibited compared to the undecorated materials. EPR and photoluminescence suggested the presence of rapid, efficient quenching of excited states in ruthenium decorated carbon nitride.

$[\mathrm{IrCl_2Cp^*(UCN)}]$ ([Ir] = 0.069 mmol g^{-1}) was synthesised to design a novel, recyclable hydrogenation catalyst. Direct hydrogenation reactions were carried out using hexane as a solvent, and despite low activity, $[\mathrm{IrCl_2Cp^*(UCN)}]$ showed good selectivity toward terminal alkenes and over 80% of catalytic activity was retained after 5 catalytic runs.

Direct coordination of metal complex fragments to carbon nitride is shown to be a viable route to tuning the properties of carbon nitride and developing recyclable novel catalysts.

Table of Contents

Table of Figures

Table of Tables

Table of Schemes

Acknowledgements

I would like to start by thanking my supervisors, Richard Douthwaite and Anne Duhme-Klair, for their academic support and advice throughout this project. I have learnt much from both of you which I will carry with me through the rest of my career.

I would also like to expressly thank all those who have provided help with the various instruments and techniques throughout this work, including Robert Michell, Emma Dux, Graeme McAllister, Karl Heaton, Pedro Aguiar, Heather Fish, Joyashish Debgupta, Rachel Bean, Sam Hart, Amanda Dixon, Daniel Raines, and Will Swansborough-Aston. Special thanks to those outside of York including Mark Isaacs, Michael Thompson and Amin Osatiashtiani.

I also want to acknowledge and thank past and present members of the RED and AKDK research groups, especially Daniel Raines, Christopher Unsworth, Natalie Pridmore, Danielle Jowett, Robert Mitchell, Thomas Sanderson, Aurelien Ducrot, Will Swansborough-Aston, Ellis Wilde and Joyashish Debgupta for their help, support, and general advice. Other members of the department, especially Luisa Ciano, David Pugh, Martin Steward, Lucy Milner, Emma Thimbleby, Nina Leeb, Phil Groves, Rachel Steen, Lewis Hall, Claire Fowler and Liz Wheeldon all deserve a special mention for their various roles in helping me partially retain my sanity.

Outside of Chemistry, I also want to deeply thank Frances Long, Conor Mullaney, Monty Grue, Luna Fowler, and Matthew Thorley for the emotional support that we all need so much more than we admit. I also want to express my deep appreciation and love of my family back home. There are too many of you to name, but the support of my parents, sisters and niblings means more to me than I can say.

I love you all, and you made me who I am.

Declaration

The research presented in this thesis was carried out at the University of York between October 2014 and September 2018. This work is, to the best of my knowledge, original and my own, except for the following:

TEM and H_2 GC calibration was performed by Dr Robert Mitchell (JEOL Nanocentre)

Elemental Analyses (CHN, Cl) were performed by Dr Graeme McAllister

ICP-MS metal analysis was carried out by Dr. Emma Dux and Michael Thompson

^{2}H NMR spectroscopy was carried out by Heather Fish

Mass spectroscopy was carried out by Mr Karl Heaton

Synthesis and single crystal growth of [IrClCp*(DMNA)](PF_6) was carried out by Dr Daniel Raines

XPS measurements and fitting was performed by Dr Mark Isaacs at Aston University

Single Crystal X-ray Crystallography performed by Rachel Bean and Sam Hart

EPR spectroscopy was carried out by Dr. Joyashish Debgupta

Acid site analysis was carried out by Amin Osatiashtiani (from the European Bioenergy Research institute at Aston University, UK)

SEM images collected by Will Swansborough-Aston (PhD Student)

This thesis has not been submitted for any other degree at this or any other University.

1 Introduction

1.1 Heterogeneous Catalysis and Carbon Nitride

A catalyst reduces the activation energy of a chemical process without modifying the overall energy change of the reaction without itself being consumed, resulting in an increased rate and reduced overall energetic cost of the reaction.[1] The design and implementation of novel catalytic processes can have world changing results. Perhaps the most impactful example of a catalytic process is the Haber-Bosch process of ammonia production, the process which accounts for nearly 50% of all nitrogen found in human tissues.[2-4] Photocatalysts are a class of catalysts which are capable of absorbing light energy to generate excited states which can go on to perform reduction or oxidation processes.

All catalysts can be classified as either homogeneous or heterogeneous in nature, dependant on the respective phases of the catalyst and reactants. Homogeneous catalysts, such as metal complexes, are often possible to characterise by e.g. IR or NMR spectroscopy *in situ*, allowing for easier investigation and understanding of mechanism and reactivity. In contrast, the active sites of heterogeneous catalysts can be difficult to characterise directly and their activity more challenging to understand. However, heterogeneous catalysts by their nature are easier to separate from reaction systems and allow more efficient processing, such as incorporation into flow systems and catalyst recycling.[5]

Carbon nitride is a material of great interest in heterogeneous catalyst research due to its excellent thermal and chemical stability, photocatalytic properties and the development of several cheap, scalable syntheses making the material highly accessible.[6-14] Tuning of the properties of carbon nitride by controlling synthesis conditions, post-modification of the material, or doping with metal atoms represents a large area of research in the field of catalyst development.

1.2 The Structure and Properties of Carbon Nitride Materials

1.2.1 The Structure of Carbon Nitride

Carbon nitride was first described by Liebig in 1834 as one of the products of the combustion of mercury thiocyanate, the so-called ‘Pharaoh’s Serpent’ reaction. Observing a yellow, insoluble solid with a measured atomic composition of C_3N_4, Liebig named the compound ‘melon’.[15] It was observed later on that ‘melon’ prepared by different methods had varying elemental compositions, which was postulated as a result of varying degrees of polymerisation of dicyanamide, making carbon nitride among the earliest discovered polymers.[16]

More recently, carbon nitride has been rediscovered as a family of polymeric compounds with differing carbon, nitrogen and hydrogen compositions depending on the conditions of synthesis and precursors.[8] The most thermodynamically stable structure of carbon nitride was calculated by density functional theory (DFT) methods by Kroke *et al.* to comprise a polymer based on tri-s-triazine (heptazine) units.[17] Kroke *et al.* proposed that the heptazine units polymerise to form ‘two-dimensional’ sheets which stack analogously to the structure of graphite (Figure 1.1). The resulting phase of carbon nitride is often referred to as ‘graphitic’ carbon nitride.

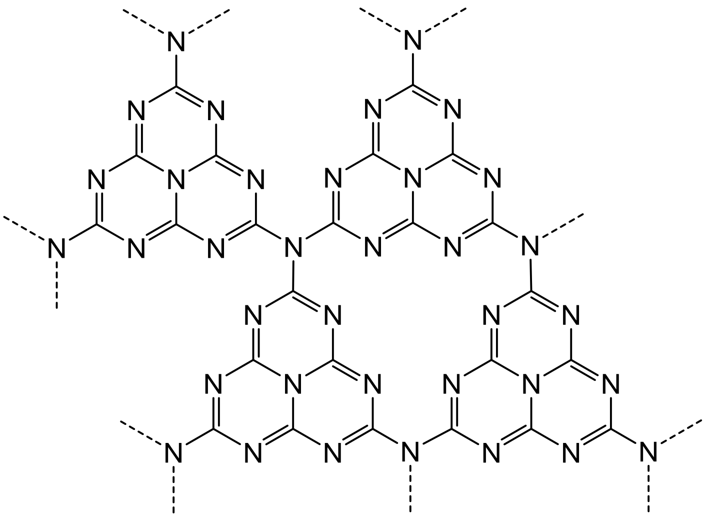

Figure 1.1: The structure of carbon nitride proposed by Kroke. et al.[17]

It should be stated that other phases of carbon nitride are known, namely cubic carbon nitride and hexagonal beta carbon nitride.[18-20] However, the majority of investigation to date has been performed on the graphitic phase due to the simpler synthesis, higher stability and consequent greater accessibility of this phase. In this work, the term ‘carbon nitride’ will refer exclusively to the graphic phase.

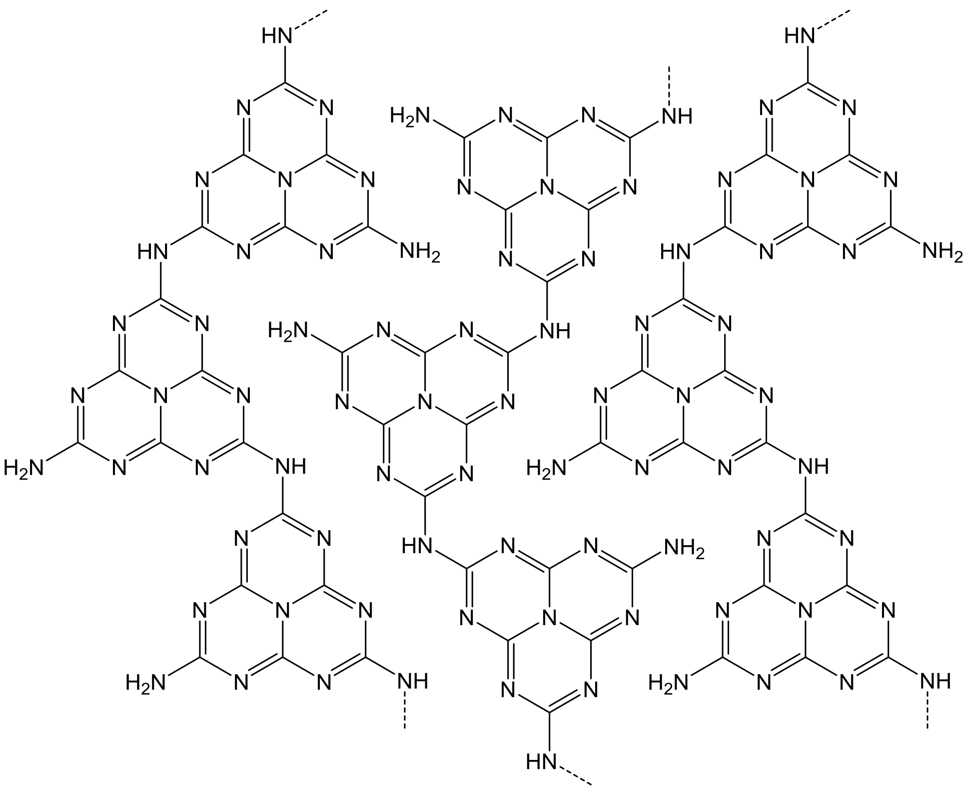

Figure 1.2: The structure of one layer of bulk graphitic carbon nitride

The chemical structure of graphitic carbon nitride has been thoroughly investigated in recent years by complementary techniques including solid-state nuclear magnetic resonance spectroscopy, Fourier-transform infrared spectroscopy, and x-ray diffractometry.[7] ^{13}C and ^{15}N solid-state NMR experiments support the molecular structure proposed by Kroke *et al.* as shown in Figure 1.1, namely, that carbon nitride is a polymer of heptazine units.[21] However, the overall bulk structure of the carbon nitride is currently understood to compose of 1-dimensional zig-zagging strands which hydrogen-bond together to form buckled sheets (Figure 1.2). These sheets then stack analogously to graphite.[7] The surface of carbon nitride can be described as having ‘face sites’ along the plane of the heptazine chains, and imine-rich ‘edge sites’ perpendicular to the plane of the sheets.[22, 23] Understanding the structure of carbon nitride is key to understanding the photophysics and photochemistry of the material.

1.2.2 Photophysical Properties of Carbon Nitride

Among the attractive properties of carbon nitride are its strong optical absorption and fluorescent properties, with delocalised electron-hole pairs formed rapidly after photon absorption.[24]

Although the structure is a polymer of a highly conjugated monomer, the electronic structure of the material is suggested to more closely resemble a metal oxide rather than a conjugated polymer. Luminescence studies coupled with time-dependant density functional theory (TD-DFT) measurements have suggested that excited electrons are not mobile along the polymer chains due to poor electron conjugation along the strands. Instead, electron mobility is achieved through π-stacking interactions between chains.[12, 24] This electron behaviour is in contrast to the 'classical' semiconductor model, where photoexcited electrons are relatively freely mobile within the material in all dimensions. Graphitic carbon nitride is often considered as a 'quasi-monomer' – that is, an array of physically interlinked individual photoactive molecules, rather than a true semiconductor.[12] Regardless, the energetic difference between the highest occupied and lowest unoccupied orbital in the ground state of carbon nitride is frequently referred to as a band gap. The band-gap of carbon nitride is highly dependent on the morphology, and therefore synthesis conditions.

1.2.3 Mechanism of Carbon Nitride formation by Thermal Condensation

The simplest method of carbon nitride synthesis involves the condensation of carbon and nitrogen rich precursors, such as melamine or cyanamide, at high temperatures.[25, 26] The mechanism of carbon nitride formation under these conditions has been shown to proceed via the pathway shown in Scheme 1.1.[27] Under high temperature conditions (above 340°C) low molecular weight, nitrogen rich compounds including cyanamide polymerise to form melamine.[28] Above 400°C, further condensation to melam, melem and eventually melon is observed, concomitant with the release of gaseous ammonia.[29, 30]

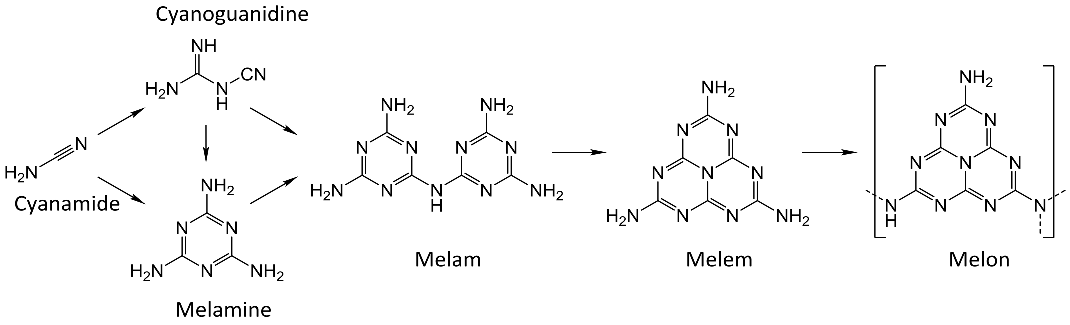

Scheme 1.1: Mechanism of carbon nitride formation via thermal condensation of nitrogen-rich precursors[27]

The final thermodynamic product of pyrolysis of nitrogen-rich organic precursors, therefore, is always a polymer of heptazine. However, by controlling the conditions of synthesis, elemental composition (i.e. C:H:N ratio), crystallinity and optical properties can all be tuned.

1.2.4 The effect of synthesis conditions on properties of carbon nitride

The synthesis of bulk carbon nitride can be achieved by the pyrolysis of different precursors. Table 1.1 shows selected literature data demonstrating the variety of methods of obtaining bulk carbon nitride, and the resulting materials band gaps and surface areas.

The same molecular structure is observed for carbon nitride acquired by all methods, as a polymer formed of heptazine rings. The observed band gap for carbon nitride, however, varies between syntheses, as does the surface area of the resulting material. For instance, using thiourea as a precursor, a higher synthesis temperature results in a change in the band gap.[31] It is proposed that the band gap decreases at higher temperatures as a result of a change in the crystallinity of the resulting carbon nitride.[8, 32] Higher temperatures result in more crystalline carbon nitride as a result of ammonia loss. However, the planar spacing cannot decrease due to the large number of non-bonding electron pairs localised on the nitrogen atoms. The heptazine-containing sheets therefore are proposed exhibit buckling predictably within the unit cell of carbon nitride when synthesised at higher temperatures.[33] This buckling strongly effects the lower-energy n-π* electronic transition, increasing the absorption coefficient at wavelengths around 465 nm.[32] This causes the apparent decrease in the band gap of the material as synthesis temperature is increased up to 600°C. At temperatures above 600°C, the thermal decomposition of carbon nitride becomes significant.[34, 35] Thermal decomposition then results in smaller particles of carbon nitride as reflected by a higher surface area. The smaller particle size increases the observed band gap as lower energy transitions become less efficient due to their arising from interactions between sheets.

Table 1.1: Demonstrating the effect of precursor on the synthesised carbon nitride

Precursor	Synthesis Temperature, Time, Atmosphere	Band Gap / eV	Surface Area / $m^2 g^{-1}$	Ref.
Cyanamide	550°C, 4h, air	2.70	10	[9]
Melamine	500°C, 2h, air	2.80	8	[36]
	580°C, 2h, air	2.75		
Dicyandiamide	550°C, 2h, air	2.75	10	[31]
Thiourea	450°C, 2h, air	2.71	11	[31]
	550°C, 2h, air	2.58	18	
	650°C, 2h, air	2.76	52	
Urea	550°C, 2h, air	2.78	31	[37]
Gyanidine	550°C, 2h, N_2	2.74	8	[38]
Thiocyanate	700°C, 2h, N_2	2.89	42	

In 2011 the synthesis of carbon nitride from urea in the absence of any additives was first published.[39] In line with previous work, Chen *et al.* demonstrated that when heated to 400°C, urea thermally condenses to form planar, graphitic carbon nitride. At higher temperatures, XRD data combined with optical spectroscopy suggested that the degree of crystallinity (i.e. order within the planes) increased with higher annealing temperatures, concomitant with the observation of a red shift of the visible light absorbance edge (although the actual band gap was not calculated for each synthesis temperature). Urea has since become a high-profile precursor for carbon nitride due to the negligible cost of the precursor and facile synthesis method of carbon nitride.[11, 13] In addition to the property differences resulting from the synthesis conditions, the properties of carbon nitride can also be controlled via physical post-modification.

1.2.5 Physical Post-modification of Carbon Nitride

The photochemical properties of carbon nitride have a strong dependence on the material structure. Subjecting bulk carbon nitride to ultrasonic exfoliation or oxidative etching has been shown to separate out the layers of heptazine sheets by breaking down the hydrogen-bonding networks between the layers.[40-42] The resulting carbon nitride 'nanosheets' have a higher band gap (2.97 eV) and a greatly enhanced surface area compared to bulk carbon nitride (306 m^2 g^{-1} compared to 10m^2 g^{-1}).[43] This supports the established understanding of low-energy transitions occurring between condensed sheets contributing to lower band gap carbon nitrides.[12] Carbon nitride nanosheets have found use as photocatalysts for hydrogen evolution and as fluorescent sensors for metal ions.[40, 42-45]

The properties of carbon nitride have been shown to be highly tuneable and controllable using only physical techniques. Understanding the relationship between structure and properties is key to developing novel carbon nitride catalysts. In addition to physical control over the material morphology, doping carbon nitride with metal species is a promising methodology to adding new properties to carbon nitride, such as novel catalytic sites and application, and enhanced light-absorption far beyond what is achievable by simply tuning morphology.

1.3 Modification of Carbon Nitride with Transition Metals

1.3.1 The effect of metal doping on carbon nitride

Incorporating iron into carbon nitride sheets was published by Antonietti *et al.* in 2009 via adding iron (III) chloride to the dicyandiamide precursor prior to thermal condensation.[46] It was proposed that the iron was localised to 'nitrogen pots' in the condensed sheets of carbon nitride (Figure 1.3). The incorporation of both Fe and Zn was initially examined, with loadings of 1-20% by mass, and in all cases a shrinking of the band gap was observed.

A similar work has been published showing that copper doping of carbon nitride improves the photocatalytic activity of the material. Incorporation of 5% copper caused a red-shift in the visible light absorbance edge of the material concomitant with a twofold increase in dye degradation activity compared to the undoped carbon nitride.[47] A similar work showed that copper-doped carbon nitride was a competent electrocatalyst for the hydrogen evolving reaction (HER).[48] The iron-doped carbon nitride was inactive as an electrocatalyst for HER, despite the similarity in the effects on the carbon nitride band gap of copper and iron doping. Therefore, although the photophysical properties of the carbon nitride are affected similarly by metal doping, the catalytic properties can be dependent on the metal species selected.

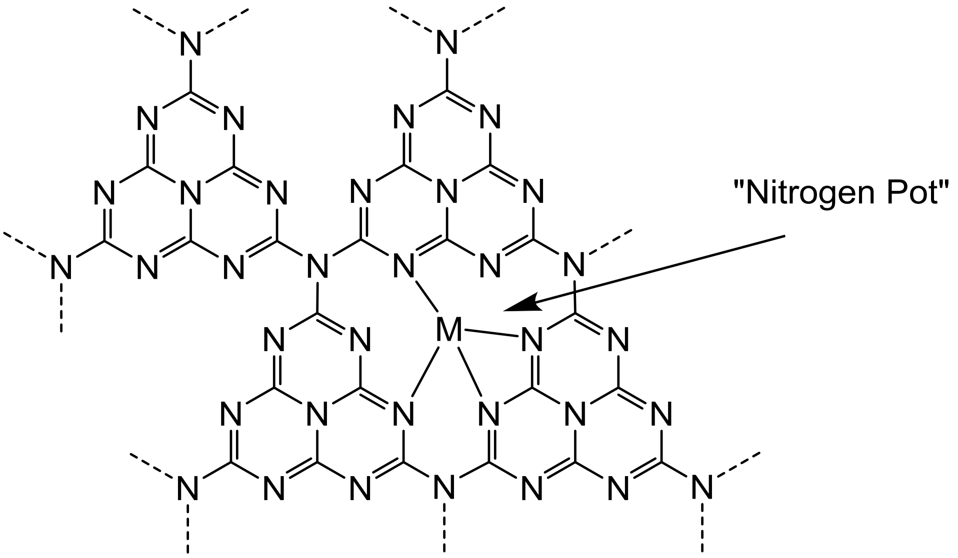

Figure 1.3: The 'nitrogen pot' environment within sheets of condensed carbon nitride as a site for metal coordination

Initially, the shift in band gap was suggested to involve low-energy d-electrons, however, the band gap of carbon nitride is also seen to be reduced when doped with Zr^{4+}, a formally d^0 metal.[49] Perhaps more interestingly, alkali metal doping is seen to have a similar band-gap shrinking effect.[50, 51] Potassium doping is seen to have the same effect as transition metal doping, with 9% potassium loading decreasing the band gap from 2.7 eV to 2.42 eV, and tuning the level of potassium was seen to tune the band gap positions.[52, 53] The valence band, measured by X-ray absorption, is seen to be reduced in energy as the potassium loading increases.[54] Therefore, because the band gap is decreasing, the energy level of the conduction band is reduced even more than the energy level of the valence band due to metal doping.

It is therefore observed that metal-doping of carbon nitride can be used in two ways to affect the photocatalytic activity of carbon nitride. In the bulk of the material, incorporated metal ions coordinate to multiple heptazine moieties, altering the bulk structure and resulting in a smaller band gap and decreased photoluminescence, often attributed to enhanced charge mobility within the material. Although the different metal dopants have different magnitude of band gap shrinking at different loading, this band gap shrinking phenomenon appears to be general.[47, 51, 52, 55]

The second principal effect that metal doping carbon nitride can have is the inclusion of metal-based catalytic sites which allow access to catalysis not possible with the undoped material. This appears to be specific to the metal ion chosen, with difference catalysis observed for different metal dopants. [47, 55, 56] These catalytic sites are likely to be relevant on the surface of the material. The coordination environment of the metal will strongly control the reactivity of the overall materials, but the investigation of single atom centres of carbon nitride is very challenging for several reasons. Among these are the high similarity of nitrogen and carbon atoms via extended X-ray absorption fine structure (EXAFS), the relatively low concentration of metal in the materials, and the relatively disordered surface of the carbon nitride. Therefore, indirect methods, such as DFT, are used to gain insight into metal coordination environment.[57]

1.3.2 The Coordination Sphere of Metal Atoms in Metal-doped Carbon Nitride

Cobalt (from $CoCl_3$) has been incorporated into the structure of carbon nitride by mixing dicyandiamide with a cobalt chloride prior to thermal condensation to carbon nitride.[58, 59]. The resulting Co-g-C_3N_4 material showed a high activity when used as a water oxidation catalyst, which the authors attributed to the cobalt atoms serving as catalytic sites. DFT analysis of the material suggested a coordination mode as shown in Figure 1.4, which, though supported by EXAFS data, shows a coordinatively unsaturated cobalt atom which is likely to be unstable experimentally. Similar modifications of carbon nitride including the incorporation of copper and nickel atoms have also been shown.[60, 61] These systems are not well characterised as metal complexes and it is likely that the coordination sphere of the metals is not well defined.

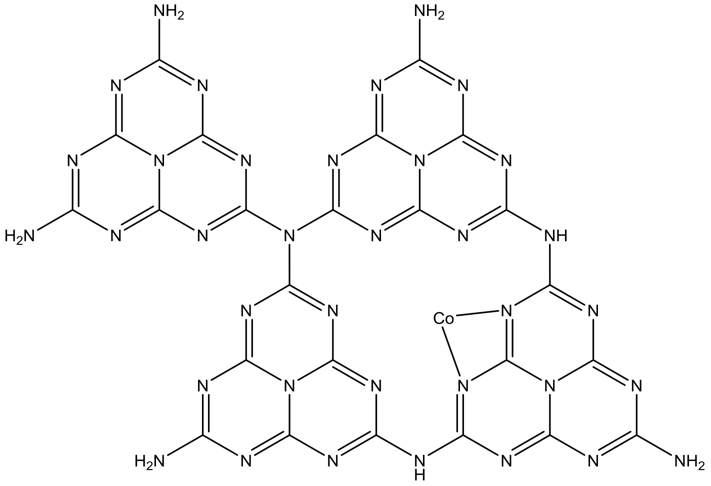

Figure 1.4: Coordination of cobalt to carbon nitride as calculated by DFT studies[62]

A related catalyst was synthesised via atomic-layer deposition of cobalt onto an existing carbon nitride surface in the design of a hydrogen evolution calalyst.[63] In this case, X-ray absorption near-edge structure (XANES) studies showed that the simulated spectra of a four-coordinate cobalt species matched experimental data (Figure 1.5). Here, the bidentate coordination of the heptazine rings to the metal centre is also predicted, but a more complete view is taken with other nitrogen atoms within the 'nitrogen pot' involved in coordination. The average bond length, as calculated from EXAFS measurements, was 2.01 Å, close to what has been measured from crystal structures of cobalt-naphthyridine complexes (2.10 - 2.31 Å).[63, 64] Although the environment around the cobalt atom was still poorly defined, the cobalt site at the surface was shown to act as a supported single atom co-catalyst on carbon nitride.

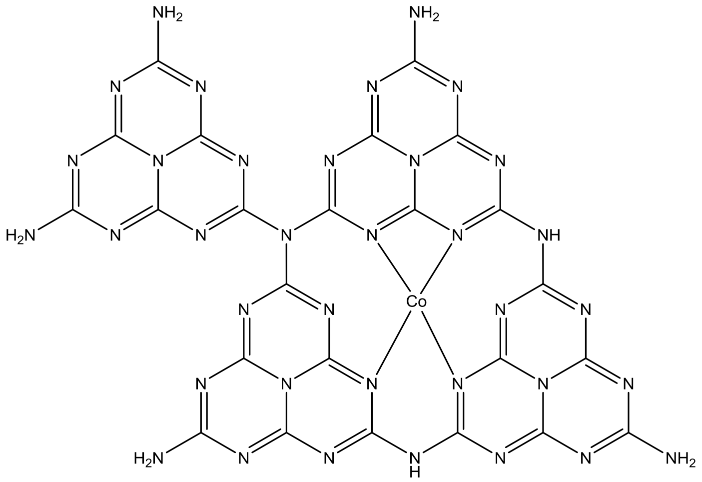

Figure 1.5: Tetradentate coordination of cobalt to carbon nitride as measured by XANES[63]

The previous examples are both based on the assumption that the metal coordinates inside the 'nitrogen pot' in between three connected heptazine rings. A DFT study on single atom Pd, Pt and Au coordination to the surface of carbon nitride was performed where more mobility was given to the heptazine units, and the lowest energy coordination is shown in Figure 1.6.[65] In this example, the metal ion coordinates readily to one heptazine molecule in a bidentate fashion, however a second heptazine unit is proposed to coordinate perpendicular to the plane of the former interaction. This indicates that the bidentate coordination to the imine 'naphthyridine-like' environment on carbon nitride is the strongest available mode, but that other coordination modes are accessible on the surface of carbon nitride. However, the coordination mode presented in Figure 1.6 seems unlikely to be experimentally available not only because of the instability due to coordinative saturation at the metal site (as mentioned previously), but also due to the assumption of an octahedral metal site geometry. The geometry of transition metal complexes, especially those in higher groups (including Pd, Pt and Au) can change based on the oxidation state of the metal.[66] The oxidation state of the metal atom in the case of these single-atom decorated materials is not known, and so it is challenging to comment on the validity of the coordination geometry shown in Figure 1.6.

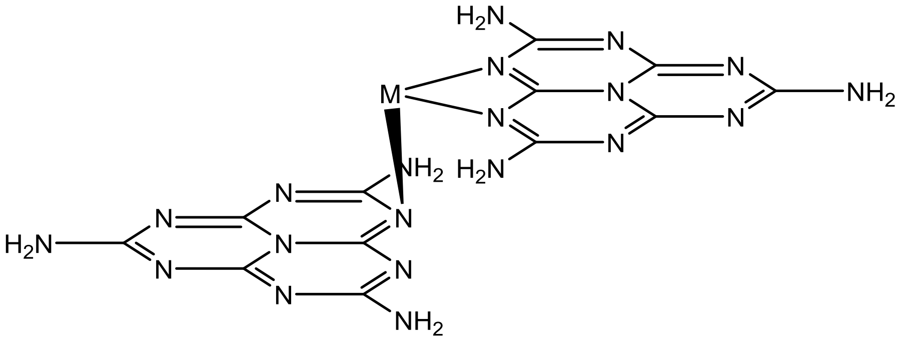

Figure 1.6: Coordination of single atoms of Pd, Pt and Au to carbon nitride

In practice, doping the surface of carbon nitride with single-atom species is highly challenging, as precipitation of the metal salt as impurities (i.e. via an oxide, or nanoparticles) can easily occur.[67] Single-atom doping has been achieved, however, with single atoms of platinum (loading 0.16% by mass) which have been shown to act as effective co-catalysts on the surface of carbon nitride. EXAFS measurements supported the single-atom nature of the platinum on the surface.[68] The performance of these single-atom species is even higher than previous nanoparticle-based platinum cocatalysts.[69]

1.3.3 Application of Carbon Nitride as a Support for Single Atom Catalysts

Single atom-heterogeneous catalysts (SACs), whereby a catalytically active single metal atom is dispersed on the surface of a supporting substrate to improve catalytic properties, are a rapidly expanding field in heterogeneous chemistry.[70-73] Although carbon nitride has been shown to function as a metal free photocatalyst for several reactions, including the reduction of protons to hydrogen, Friedel-Krafts acylations, and alcohol oxidation, it does not appear to possess any ‘dark’ catalytic properties.[6, 74, 75] Therefore, it is a good candidate as a substrate for single-atom catalysis for dark reactions, as catalysis can be ascribed purely to the single atom catalyst – although the surface amine moieties may be available as acid or base sites during catalysis.[76]

A series of hydrogenation catalysts have been produced by incorporating single atoms of gold, iridium, palladium, silver or platinum into carbon nitride.[76] Two methods were investigated – the first was a copolymerisation method, whereby the metal was combined with the carbon nitride precursor prior to thermal condensation. The second method investigated involved combining pre-synthesised carbon nitride with a metal salt, then reducing (using $NaBH_4$) the metal salt to result in stable single-atom metal catalysts. Characterisation by electron microscopy showed that although post-modification allowed for greater control of metal loading, metal clusters and nanoparticles are much more frequently observed compared to copolymerisation.

Carbon nitride has been successfully decorated with single atoms of palladium via a microwave-irradiation-assisted deposition, confirmed by aberration-corrected scanning transmission electron microscopy (AC-STEM) and EXAFS.[77] The resulting material was shown to act as an excellent catalyst for Suzuki cross-coupling reactions, demonstrating how the ligand properties of carbon nitride can be exploited to result in active catalytic systems for high-profile chemistry.

1.4 Decoration of Carbon Nitride with Transition Metal Complexes

1.4.1 Coordination through the outer sphere

Doping of carbon nitride with single metal atom species has been shown to impart catalytic activity to carbon nitride with high selectivity and activity, however, the characterisation of the dopant environment remains a challenge. Inorganic complexes are much easier to characterise (e.g. via NMR, infrared spectroscopy) compared to single-atom species and therefore are much easier to study and improve. In addition, metal complexes are generally more stable than single metal atoms, and are more resistant to degradation during material preparation, e.g. by oxide formation.

The combination of metal complexes with semiconductor materials has been well explored, for instance in the design of dye-sensitized solar cells.[78-81] The most common approach is to modify the 'outer sphere' of metal complexes with hydrogen-bonding groups such as carboxylic or phosphonic acids, which ensure good contact between the semiconductor and the metal complex.[82] The grafted metal complexes alter the surface properties of the resulting hybrid material compared to the undecorated material, and, in contrast to single-atom doping, are much easier to characterise.

Reisner *et al.* have published several works based on a DuBois-type nickel-based catalyst (NiP) shown to be competent in both electrochemical and photocatalytic water splitting (Scheme 1.2).[83] NiP was combined with carbon nitride via an interaction with phosphonic acid groups on the outer sphere of the metal complex. [84] Whilst initial reactions used EDTA (ethylene-diamine tetraacetic acid) as a sacrificial electron donor, later it was shown that the oxidation of 4-methoxybenzyl alcohol could also complete an electron transfer pathway to generate hydrogen photocatalytically.[85] This system has also been used to pair the oxidation of oxidation of lignocellulose with hydrogen evolution.[86] This demonstrated that the intrinsic catalytic properties of carbon nitride were accessible when utilising decorated systems.

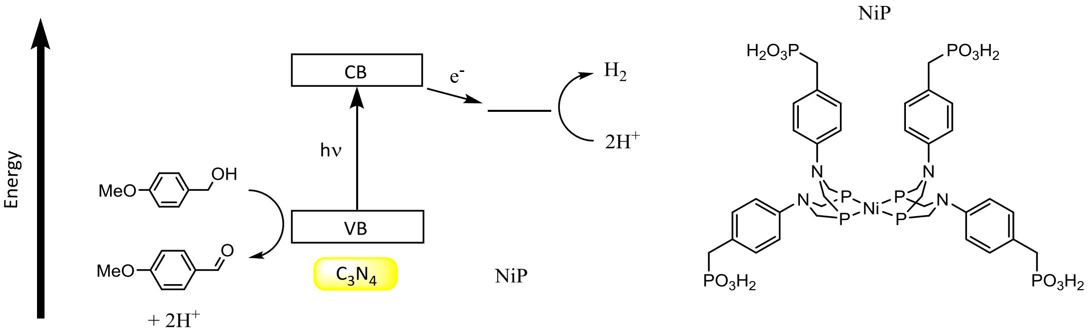

Scheme 1.2: Combination of a Ni DuBois-type catalyst with carbon nitride for hydrogen evolution catalyst, reproduced with permission from ref. 82

Maeda *et al.* have decorated carbon nitride with a ruthenium carbonyl complex to alter the photocatalytic properties of the material.[87] Whilst the undecorated carbon nitride was reported to be inactive for carbon dioxide reduction, the resulting material showed carbon dioxide reduction with selectivity (80%) toward formic acid when irradiated in the presence of an electron donor (triethanolamine) and carbon dioxide.[88] It was proposed that photoexcited electrons within the carbon nitride were transferred to the surface-bound ruthenium complex to drive catalysis. The activity of the material was found to be enhanced even further by the addition of Ag, which is speculated to promote the reaction by improving electron transfer to the surface of the material.[89]

This hybrid system was further developed by incorporating a dye between the carbon nitride and the catalytic site (Scheme 1.3).[90] This improved the carbon dioxide activity of the system by a factor of 30, and increased the selectivity to 99%. The incorporation of the ruthenium dye is suggested to enhance activity by a combination of enhancing the visible light absorptive properties of the material and improving control over electron pathway.[45, 91, 92] A similar system to that shown in Scheme 1.3 has also been reported, with the ruthenium carbonyl catalytic site replaced with an analogous rhenium carbonyl.[93] This suggests that this approach is flexible, and the various components can be interchanged to improve activity and selectivity.

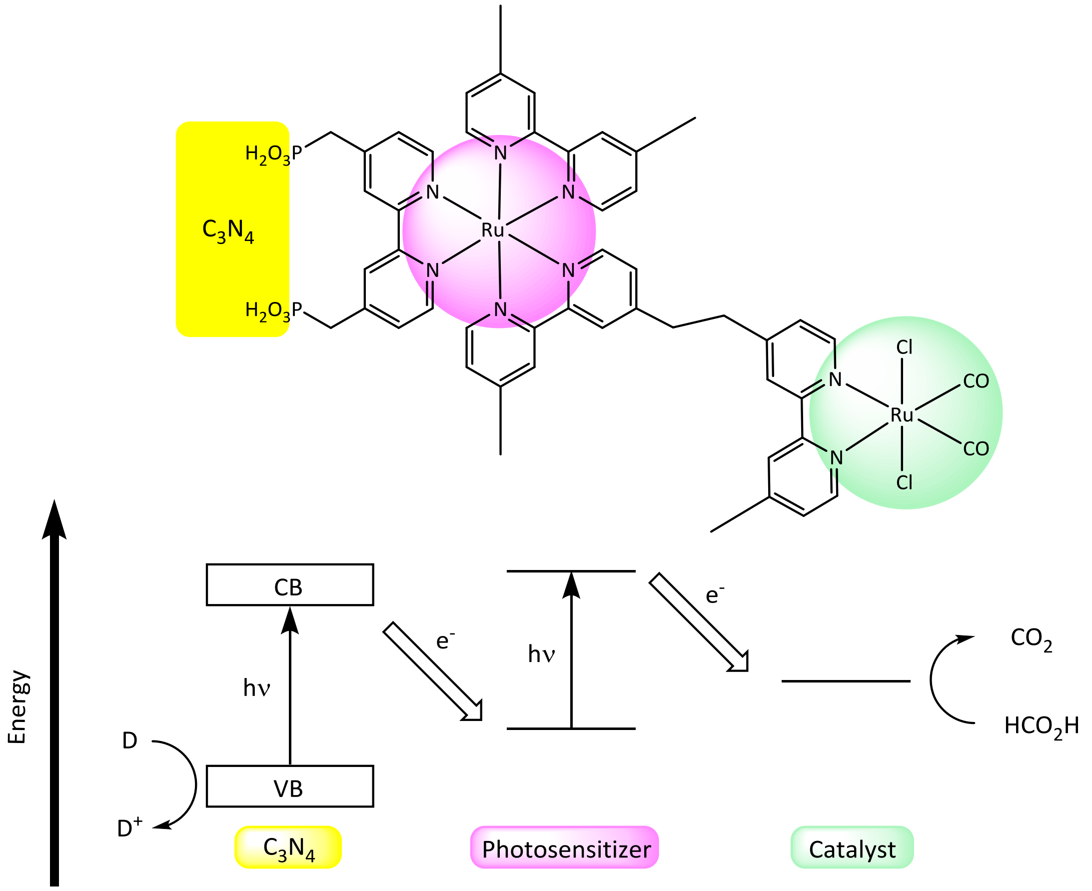

Scheme 1.3: Carbon nitride decorated with a bimetallic RuRu' catalyst shows high selectivity for carbon dioxide reduction, reproduced with permission from ref. 86

1.5 Coordination of metal complexes to carbon nitride through the inner sphere

It has been shown that directly coordinating ‘naked’ metal atoms to carbon nitride is an effective technique to alter the properties of carbon nitride, either to alter band gap and charge recombination or to confer catalytic properties to the material. It has also been shown that combining inorganic molecular species with carbon nitride via outer-sphere coordination can effectively alter the catalytic properties of the carbon nitride.

Relatively unexplored, in contrast, is the combination of approaches – that is, to introduce a coordinatively unsaturated metal complex fragment to carbon nitride to exploit its coordination chemistry. The ancillary ligands around the metal centre therefore simultaneously can act as reporters to aid characterisation (i.e. by NMR, IR spectroscopy) and can be altered to tune the material properties.

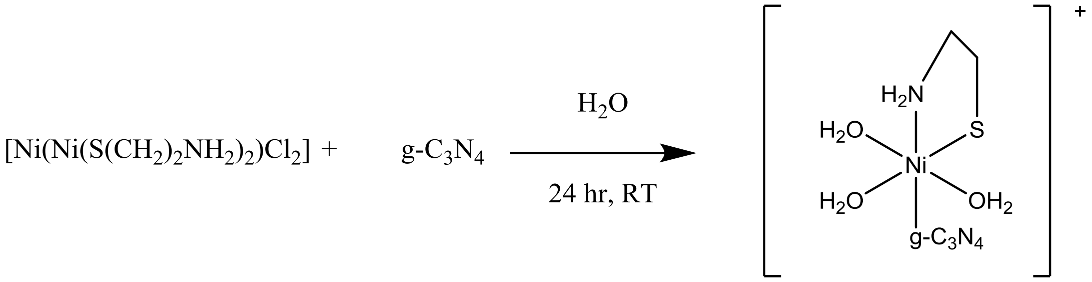

Scheme 1.4: Direct coordination of a nickel catalyst to carbon nitride via the inner sphere of the metal

An example of decorating carbon nitride via post-modification and coordination to the inner sphere of the metal is shown in Scheme 1.4.[94] Based on hydrogenase enzymes, nickel treatment of carbon nitride was proposed to result in the 6 coordinate species shown in Scheme 1.4, which conferred improved light-mediate hydrogen evolution activity to the carbon nitride. The nickel site was proposed to act as a catalytic site, and the structure was suggested as a result of x-ray photoelectron spectroscopy (XPS) measurements.[95]

Another attempt to utilise the coordination chemistry of carbon nitride with a metal complex fragment involved the grafting of a heteroleptic iridium dye via a simple evaporation method.[96] The increased visible light absorption due to the iridium complex enhances the overall activity of the catalyst, however the characterisation of the metal complex environment was not thoroughly investigated, and there is little evidence that direct coordination between the iridium and carbon nitride is occurring. However, these initial studies have shown that coordination through the inner sphere could be a promising method to modify the catalytic and photophysical properties of carbon nitride.

1.6 Conclusions

Carbon nitride is a promising material in the field of heterogeneous catalysis due to high stability, ease of access and favourable intrinsic properties. Photophysical and catalytic properties have been shown to be tuneable by doping with single metal atoms or decoration by metal complexes.

However, very little work exists investigating inner sphere coordination of a metal complex fragment (with ancillary ligands) directly to the surface carbon nitride. In those cases where is has been examined, although enhancement of the catalytic properties of the resulting composite material are observed, the characterisation of the material is usually achieved through bulk techniques, such as diffuse reflectance, powder X-ray diffractometry, and electrochemical measurements. The environment at the metal centre has not been thoroughly investigated in the previous works.

1.7 Aims

The principal aim of this work is to investigate the coordination of metal complex fragments to the surface of carbon nitride. Established work demonstrates metal ions can coordinate in a bidentate fashion to the heptazine monomers of carbon nitride. Metal complex fragments will be chosen to react with carbon nitride in order to attempt to probe the coordination environment available on the surface of carbon nitride, enhance the intrinsic photochemical properties of carbon nitride, and impart dark catalytic activity to carbon nitride.

The metal centres on decorated carbon nitrides will be investigated by spectroscopic methods, and a molecular analogue to bulk carbon nitride will be selected so that metal complexes which emulate the coordination to carbon nitride can be synthesised and fully characterised. A comparison between the spectroscopy of the metal-complex fragment decorated carbon nitride and an inorganic complex will allow for deeper insight into the interaction between the surface of carbon nitride and metal centres.

2 Synthesis and Characterisation of Metal Carbonyl Decorated Carbon Nitride

2.1 Introduction

In the field of artificial photosynthesis, Group 7 metal carbonyl complexes of the type *fac*-[MX(CO)$_3$(L)(L')] (where M = Mn, Re; X = Cl, Br; and L and L' represent a bidentate diimine ligand) have attracted a lot of attention since [ReCl(CO)$_3$(bpy)] (bpy = 2, 2'-bipyridine) was shown to act as a catalyst in the photoreduction of CO$_2$.[97-100] In addition, the distinct vibrational frequencies of the carbonyl ligands make them excellent 'reporter' ligands for identifying catalytically-relevant carbonyl species using infrared and Raman spectroscopy.[101-103]

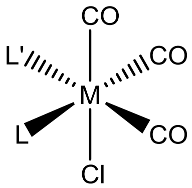

Figure 2.1: General geometry of fac-[MX(CO)$_3$(L)(L')]

Initial photochemical experiments on [ReCl(CO)$_3$(bpy)] revealed that photoexcitation produced a relatively-long lived (25-50 ns) excited state with triplet character.[104-106] This excited state was rapidly reductively quenched using an electron donor (such triethanolamine or triethylamine) to result in reduced [ReCl(CO)$_3$(bpy)]$^-$, with the electron primary localised on the 2, 2'bipyridine ligand.[103, 104, 107] The chloride ligand then dissociates, and derivatives of the resulting 5-coordinate species, [Re(bpy)(CO)$_3$]$^-$, are of the most active homogeneous catalysts for selective carbon dioxide reduction to carbon monoxide in acetonitrile or DMF known.[108] The reaction can be also performed electrochemically, with no need for photoexcitation, and proceeds via electron transfer from an electrode to a π* orbital on the diimine ligand.[109]

The high selectivity of the catalyst is proposed to arise from a HOMO with mixed metal-ligand character favouring CO$_2$ (π+σ) coordination rather than H$^+$ (σ only).[110] Several variations on the catalyst exist, with many studies performed to investigate the effects of changing the diimine ligand species.[111] Larger, bulkier ligands generally result in more stable, active catalysts, as the steric influence of the ligand prevents the formation of dimers which are catalytically inactive.[100]

Although initial reports claimed that $[Mn(bpy)(CO)_3]^-$ did not react with carbon dioxide in the same manner as $[Re(bpy)(CO)_3]^-$, it was found that the addition of Brønsted acids activated the catalysis.[112-114] Although addition of acids to rhenium catalysts also improves the turnover, the presence of acid is not in this case essential to see catalytic turnover.[110] Employing manganese as opposed to rhenium is attractive not only due to the higher abundance (Mn is ca. 1.3 million times more abundant on Earth compared to Re), but also due to the lower overpotential required using Mn systems as electrocatalysts.[100, 115-117]

Although homogeneous catalysts in general are easier to modify and analyse, heterogeneous catalysts benefit from easier product separation and catalyst recycling. Hybrid catalysts, consisting of ‘molecular-type’ catalytic sites on an insoluble support, present opportunities to combine the advantages of both molecular and bulk solid catalytic systems. In addition, utilising photoactive supports including carbon nitride have been shown to improve the activity of carbon dioxide reduction catalysts by promoting the photoreduction of the diimine ligand.[45, 92, 118]

Early work in combining metal carbonyl chemistry with heterogeneous catalyst advantages was performed by directly reacting metal carbonyl precursors with metal oxides, including MgO, Al_2O_3 and SiO_2.[119-121] The relatively disordered nature of the surface of metal oxide caused the resulting hybrid system to contain multiple rhenium carbonyl species as identified by infrared spectroscopy. Grafting a pre-synthesised rhenium tricarbonyl complex onto the surface of graphite resulted in more uniformity of the resulting catalyst, but required a more complex chemical preparation pathway.[122]

Less work has been published studying the incorporation of manganese carbonyl species into hybrid catalytic species. Although manganese carbonyls can be directly reacted with inert supports such as MgO to decorate the latter with metal carbon fragments, as with rhenium carbonyls, several manganese carbonyl species result from the reaction.[123] The few reports of manganese carbonyl systems being incorporated into photoactive supports shows a rapid release of carbon monoxide after irradiation with visible light as the carbonyl ligands are lost.[124, 125]

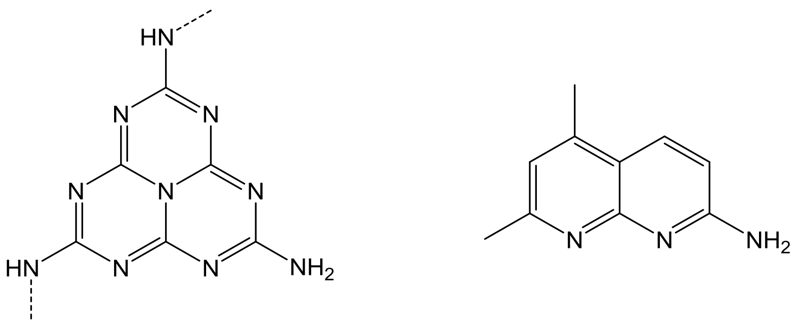

Heptazine (Carbon Nitride)   5,7-dimethyl-[1,8]-naphthyridine-2-amine (DMNA)

Figure 2.2 The monomeric unit of carbon nitride compared to 5, 7-dimethyl-[1,8]-naphthyridin-2-amine (DMNA)

In contrast to the relatively disordered metal oxide surfaces, carbon nitride, a polymeric semiconductor, has a well-defined repeating unit, heptazine (Figure 2.2). Heptazine ligands have structural similarities to diimine ligands such as naphthyridine and bipyridine, and so carbon nitride may present many coordination sites with the same environment for metal species. The direct reaction of carbon nitride with metal carbonyl precursors has not yet been investigated, and therefore represents a novel research direction in the development of hybrid catalytic systems.

2.1.1 Objectives

Metal carbonyl species with diimine ligands are a well-understood class of inorganic complexes due to the ease with which infrared spectroscopy can be applied to investigate the geometry and electronics of the system.[104, 107, 114] The structure of carbon nitride is a repeating unit of heptazine, which has a strong chemical resemblance to naphthyridine ligands, a class of diimine bidentate ligand.[21, 126] Despite the large quantity of literature covering both metal carbonyl species and carbon nitride, no investigation has to date been published where a metal carbonyl system has been grafted directly to carbon nitride through the metal centre.

It is suggested that treatment of carbon nitride with metal carbonyl precursors will result in materials with metal complex fragments coordinating to the diimine units in the heptazine on the edge-sites of the carbon nitride. To aid the characterisation of the material, a molecular analogue will be synthesised and fully characterised. 5, 7-dimethyl-[1,8]-naphthyridin-2-amine (DMNA) is a commercially available compound which presents a similar coordination environment to the heptazine unit, with two imine and a primary amine coordination site available.[127, 128] Metal complexes incorporating DMNA as a ligand will be characterised by methods including X-ray crystallography and infrared spectroscopy. Insight into the metal environment on carbon nitride will be gained by comparing the infrared spectroscopy of the molecular system with that of the material.

The metal-decorated carbon nitride will then be characterised fully to investigate the effect of the material properties of the carbon nitride, especially the photophysical properties. The stability of any metal-carbon nitride interaction will then be assessed before catalysis can be considered.

2.2 Synthesis and Characterisation of Carbon Nitride

2.2.1 Synthesis of UCN and CCN

Two different morphologies of carbon nitride were synthesised as potential substrates for metal complex fragments. Urea-derived carbon nitride (UCN) was synthesised via a simple thermal condensation of urea performed by heating to 550°C for 3 hours in a ceramic crucible with a lid (Scheme 2.1).

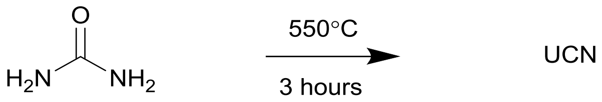

Scheme 2.1: Synthesis of UCN via thermal condensation of urea

In addition to UCN, a templated, mesoporous cyanamide-derived carbon nitride (CCN) was synthesised (Scheme 2.2).[129] An aqueous, acidic solution of cyanamide and tetraethylorthosilicate (TEOS) was co-precipitated by evaporation. The resulting co-precipitate of TEOS and cyanamide was then heated to 80°C to polymerise the TEOS to silica prior to thermal condensation of the trapped cyanamide to CCN. The silica template was then etched with ammonium bifluoride.

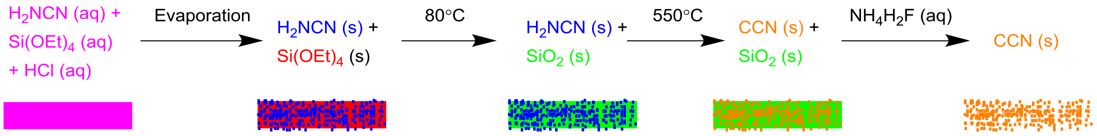

Scheme 2.2: Synthesis of CCN, showing how a porous structure is obtained in the resulting material

After synthesis, ‘raw’ CCN and UCN were both washed thoroughly with water and ethanol and stirred in a solution of ammonia in ethanol (2 mol dm^{-3}) for three hours before isolation by filtration and washing with ethanol again (see section 2.3). UCN and CCN were characterised and compared using elemental analysis, infrared and diffuse reflectance spectroscopy, and powder X-ray diffraction (PXRD).

2.2.2 Elemental Analysis (CHN) of UCN and CCN

Table 2.1 shows the result of CHN analysis of samples of UCN and CCN. Both have an empirical formula close to the thermodynamic minimum of C_3N_4, however both samples contain significant quantities of hydrogen. The hydrogen in carbon nitride samples is usually localised on the primary amines which connect heptazine units. The higher hydrogen content of CCN suggests a higher density of 'edge-sites' compared to UCN, which have a density on the surface compared to the bulk for connectivity reasons.[130, 131] The increased hydrogen content in CCN may also be a result of increased water adsorbed to these edge-sites on the material surface.

There is a significant portion of mass in CCN and UCN which does not arise from carbon, hydrogen, or nitrogen. As no crystalline impurities are indicated in the powder X-ray diffraction (see paragraph 2.2.5) it is likely that the rest of the elemental composition of the material arises from oxygen from water or surface carbonyl functionalities.

Table 2.1: Elemental composition of UCN and CCN

Material	% Mass				Empirical Formula
	C	H	N	Rest	
UCN	33.74	1.72	59.57	4.97	$C_3H_{1.9}N_{4.5}$
CCN	32.61	2.35	57.38	7.66	$C_3H_3N_{4.4}$

2.2.3 Infrared Spectroscopy of UCN and CCN

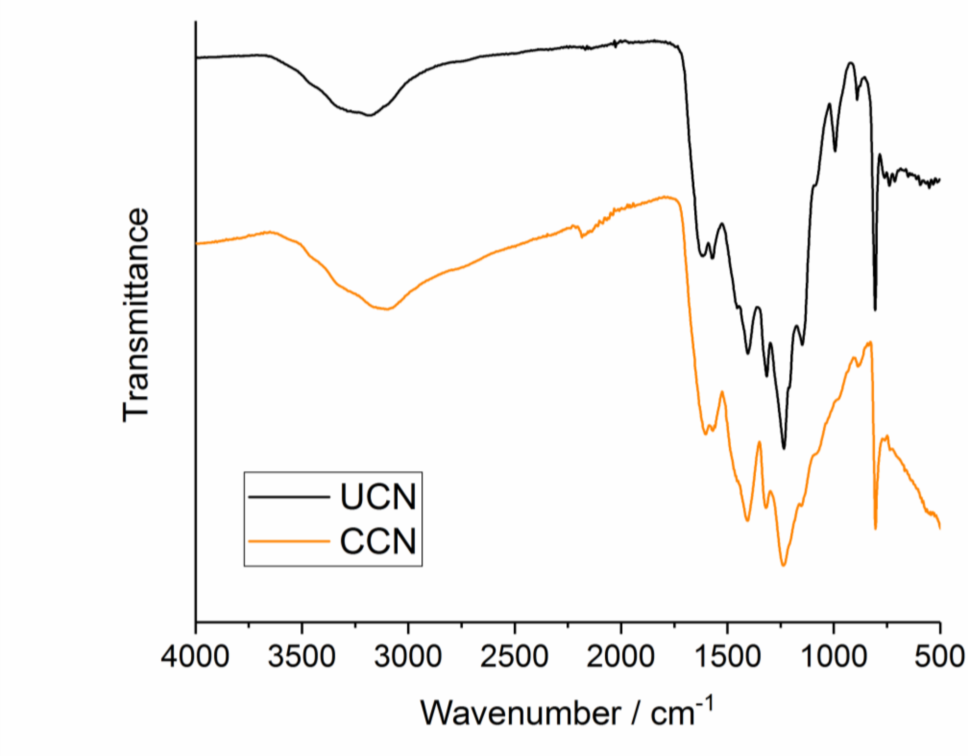

Figure 2.3: ATR Infrared spectra of UCN and CCN

The ATR-IR spectra of UCN and CCN are shown in Figure 2.3 and show several strong features. The band at 3000-3400 cm^{-1} corresponds to amine vibrations, whilst the many bands between 1000-1600 cm^{-1} correspond to C=N multiple bond vibrations. The sharp band at 800 cm^{-1} corresponds to the characteristic 'breathing' mode of the heptazine heterocycle.[130, 132] The infrared spectra of UCN and CCN are very similar and are consistent with both materials being polymers based on the heptazine unit.

2.2.4 Diffuse Reflectance Spectroscopy (DRS) of UCN and CCN

UCN and CCN are coloured powders, with UCN having a pale-yellow colour and CCN having a strong orange colour. To measure this more directly, diffuse reflectance spectroscopy of UCN and CCN was performed as shown in Figure 2.4. Low reflectance measurements in DRS spectra are attributed to absorption by the material. Whilst CCN shows broad absorption (i.e. low reflectance) across the visible light range, UCN only shows a sharp absorption at wavelengths below 420 nm. The reflectance above 100% at 450 nm observed for UCN is due to the luminescence of the material.

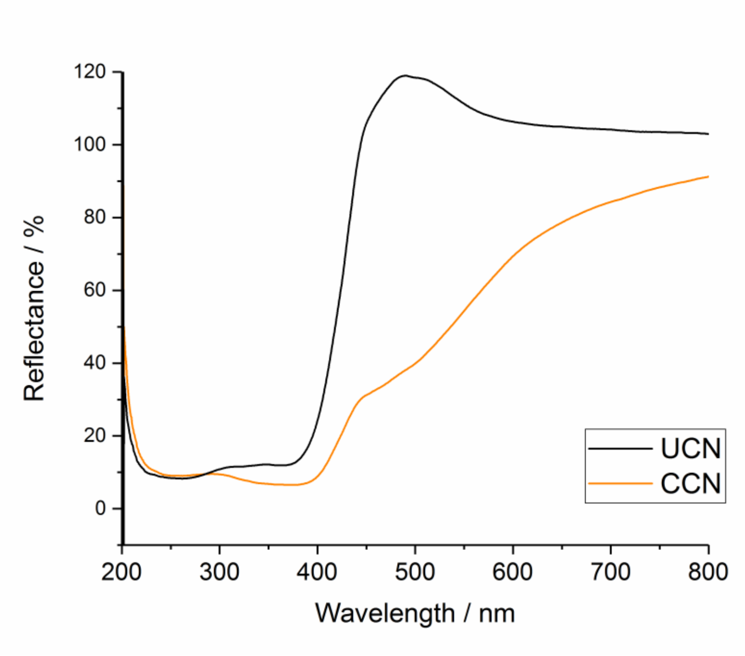

Figure 2.4: Diffuse Reflectance Spectra of UCN and CCN

The differences between the DRS reflect the morphology differences between the two materials. Carbon nitride can be described photophysically as an optical quasi-monomer, with poor exciton mobility along chains compared to relatively high exciton mobility between chains. [12, 24] Increased π-stacking with other chains within the material increases the absorption coefficient of the lower energy n-π* transition, which is located at around 465 nm.[32] Therefore, the increased absorption of visible light by CCN compared to UCN is indicative of a more condensed bulk material in the case of CCN. [12, 32]

2.2.5 Powder X-ray Diffraction of UCN and CCN

Figure 2.5 shows the PXRD diffractograms of UCN compared to CCN and a calculated diffractogram obtained from the ICSD.[133] The calculated diffractogram is based on the unit cell of carbon nitride and assumes a crystalline material. As-synthesised carbon nitride, however, is highly amorphous, causing significant broadening of the expected peaks in experimental spectra.[8, 75, 133-135] The five sharp peaks observed in both samples arise from the aluminium holder used during data collection and are marked with an asterisk (*). Both materials show a broad reflection at 27.4°,which corresponds to the interplanar distance between the sheets of carbon nitride.[136] The interlayer spacing is the same in UCN and CCN. The feature at 13.2° is proposed to arise from the spacing between the 'gaps' between heptazine moieties within the planes.[8, 137] The slightly increased sharpness of the peak at 13.2° in CCN compared to UCN is consistent with CCN being the more condensed, crystalline material, as supported by the DRS.

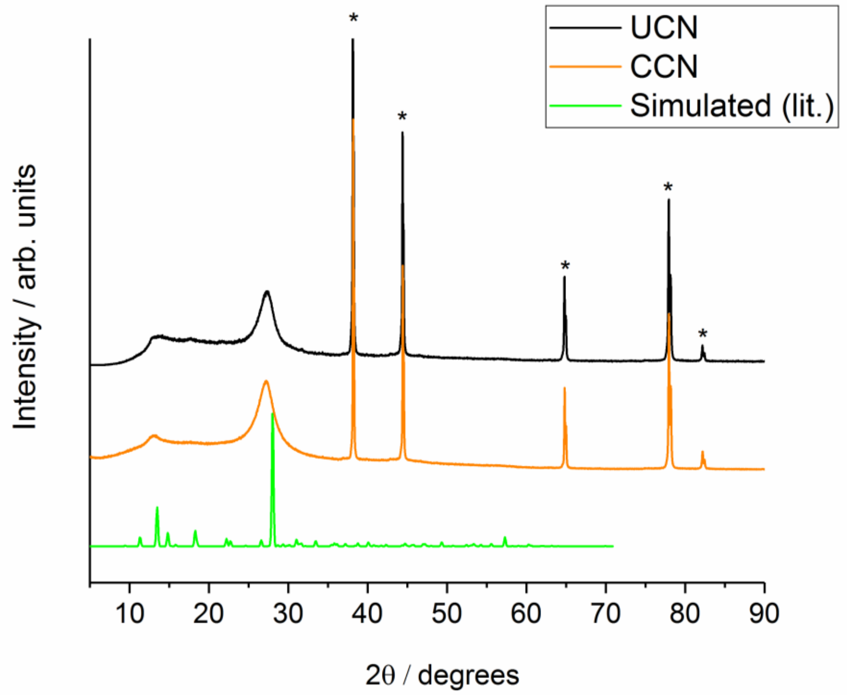

Figure 2.5:Powder X-ray diffractograms of UCN and CCN compared to a calculated diffractogram. Peaks marked with asterisk (*) arise from aluminium sample holder

2.2.6 Brunauer-Emmett-Teller (BET) Analysis of UCN and CCN

BET analysis (Figure 2.6) was performed to measure and compare the surface areas of UCN and CCN. The obtained values from the BET analysis, listed in Table 2.2, are very similar for each material, however the reliability of BET analysis for porous films is heavily debated.[138, 139] However, whereas UCN shows an isotherm typical of an unstructured powder (type III), the isotherm collected from CCN shows a hysteresis typical of a porous material (type V), suggesting structural differences between UCN and CCN.

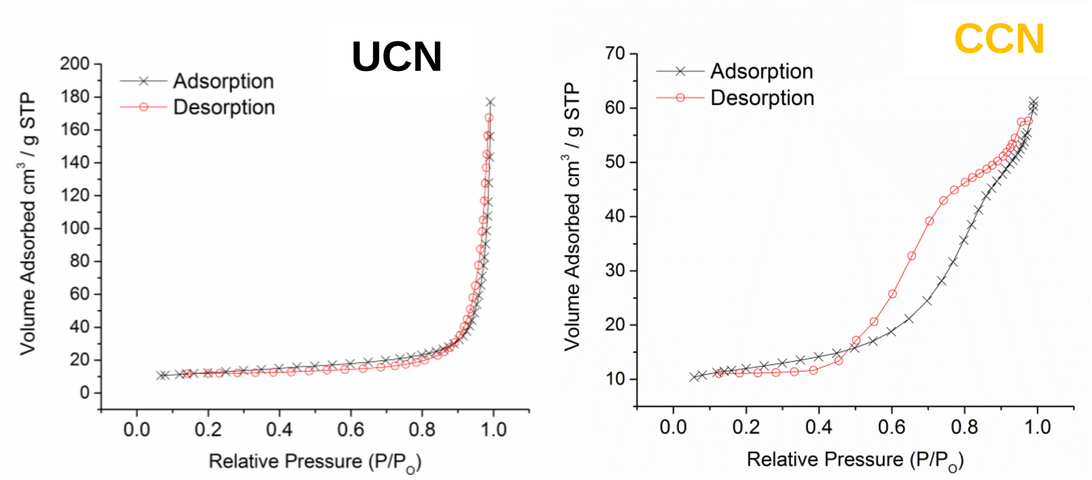

Figure 2.6: N_2 adsorption isotherms of UCN and CCN

The obtained BET surface area of CCN is approximately half of what was reported in the literature, likely a result of the lack of control in the templating method.[129] However, the shape of the desorption isotherm is a good indicator of a more porous structure in CCN as opposed to UCN, as it demonstrates adsorbent retention on the surface of CCN.

Table 2.2: Brunauer-Emmett-Teller (BET) surface area values of UCN and CCN calculated from nitrogen adsorption isotherm

Sample	BET Surface Area /m^2 g^{-1}
UCN	42.4 ± 0.4
CCN	40.5 ± 0.7

2.2.7 Comparison of UCN and CCN

Compared to UCN, CCN is a more structured material with increased porosity and a higher concentration of edge-sites as suggested by CHN and BET analysis. In addition, the bulk material (i.e. the walls of the pores) of CCN is more condensed as indicated by PXRD and DRS studies.

The molecular structure of the two materials is almost identical, with both UCN and CCN showing infrared spectroscopy consistent with a polymer based on heptazine units. Considering the overall target of investigating coordination to the heptazine unit, and the much quicker, more accessible and more scalable synthesis of UCN, UCN will be the primary material investigated for metal coordination in this chapter.

2.3 Effect of Base-treatment on UCN

Initial experiments involving heating solutions of metal complex fragments with carbon nitride (Scheme 2.3, see section 2.4.1) did not result in any change in the spectroscopy of the materials. It was proposed that the surface of 'as prepared' carbon nitride was contaminated by positively charged species including protons which inhibited coordination. Treatment of UCN with basic solutions by stirring for three hours was performed to deprotonate the carbon nitride surface.

2.3.1 Zeta-potential measurements of UCN

Zeta-potential measurements were performed on aqueous dispersions of carbon nitride to measure the average surface change of particles of UCN before and after base treatment. The surface of raw UCN has a negative overall charge as consistent with the literature.[140] The lack of metal coordination was suggested to be caused by 'blocking' of the coordination sites by acidic impurities. Treatment with base lowered the zeta potential and the resulting material showed positive results when decorated with metal complex fragments. Although treating UCN with aqueous hydroxide was shown to produce a material with a highly negatively charged surface, this is a result of UCN decomposition via amine substitution by hydroxide.[141] To minimise changes to the structure of the carbon nitride, ammonia in ethanol was used to pre-treat the UCN prior to metal coordination throughout this thesis.

Table 2.3: Zeta potential measurements of base treated UCN

Material	Zeta Potential
UCN (Raw)	-28.7 ± 0.8
UCN (NaOH treated)	-58.1 ± 0.8
UCN ($NH_3 \cdot$EtOH treated)	-33.3 ± 0.5

2.3.2 Effect of Base Species on the Catalytic Activity of UCN

In addition to zeta-potential, the photocatalytic hydrogen evolution activity of UCN after various base treatments was measured and is shown in Figure 2.7. UCN was stirred in a solution of one of three bases for three hours prior to isolation and drying. Bases used were NaOH (aqueous, 2 mol dm^{-3}), NH_4OH (aq, 2 mol dm^{-3}) and NH_3 (ethanolic, 2 mol dm^{-3}). The materials were then decorated with 1-3 nm platinum nanoparticles following a literature procedure prior to evaluating for photocatalytic hydrogen evolution by GC.[9] No hydrogen evolution is observed in the absence of platinum or sacrificial electron donor.

It can be clearly seen that UCN cannot perform photocatalytic after treating with NaOH, likely due to the substitution of primary amine surface groups for alcohol functional groups.[141] This effect is also likely to cause the eventual loss of activity seen when UCN is treated with aqueous ammonia, however, adsorbed ammonium provides a proton source for hydrogen evolution which is consumed after approximately 8 hours. In contrast, treating UCN with a base which does not contain hydroxide species does not remove the hydrogen evolution activity of the material.

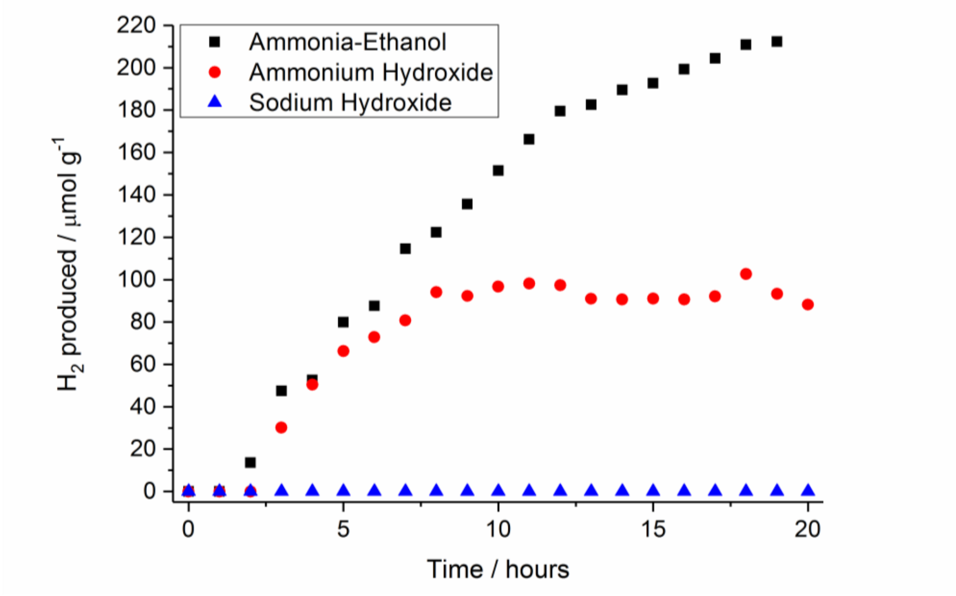

Figure 2.7: Effect of base treatment on photocatalytic hydrogen evolution activity of platinised UCN. Samples of UCN are treated with base for three hours at room temperature, then isolated and dried. UCN is then decorated with platinum nanoparticles (1-3 nm) by combining with 2% weight H_2PtCl_6 and photolyzing with 300 W Xe lamp in 10% vol. aqueous triethanolamine. Photocatalysis then performed on 30 mg catalyst, in 10% vol. aqueous triethanolamine (sacrificial electron donor) with λ > 420 nm.

Following the zeta-potential measurements and catalytic results, ethanolic ammonia was selected as the base used to treat carbon nitride prior to metal decoration. Ethanolic ammonia does not appear to significantly change the chemical composition of the carbon nitride.

2.3.3 Acid Site Analysis

In an attempt to compare the surface properties of to the raw and base-treated UCN, acid site analysis was carried out by Amin Osatiashtiani at Aston University. A standard method of acid site analysis can be performed by saturating a sample with n-propylamine and performing thermal gravimetric analysis (TGA) and analysing the decomposition product, propylene, by mass spectrometry.[142] The intensity of the mass signal at m/z = 41 as a function of decomposition temperature is collected and is shown in Figure 2.8.

The broad peak centred around 530°C corresponds to the temperature at which propylamine decomposes to propylene, whilst the peak around 700°C corresponds to decomposition of the carbon nitride itself, and is likely to arise from loss of other species, e.g. $[HNC\equiv N]^+$ ions, during decomposition.[29, 143] Analysis of the region at 530°C allows quantification of the number of acid sites in the samples, which is shown in Table 2.4, along with example materials with which to draw comparison.

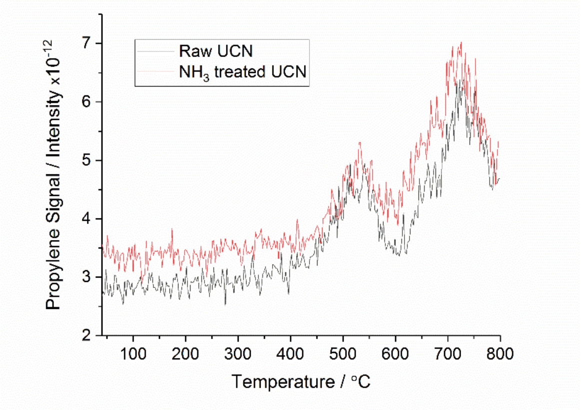

Figure 2.8: Change in intensity of signal at m/z = 41 as a function of decomposition temperature of samples of carbon nitride saturated with n-propylamine

The data listed in Table 2.4 suggests that more propylamine is released during thermal decomposition for the base-treated carbon nitride, which could be interpreted as the material becoming more acidic after treatment with ammonia, which is unexpected. However, one of the assumptions of the technique is that the material is not redox active, whereas carbon nitride is well known to show both oxidative and reductive chemistry.[10, 75, 85, 142, 144, 145] This methodology is not reported previously for carbon nitride. This measurement therefore does not give a measure of the basicity of the surface for carbon nitride, however does show a difference in the surface of UCN after base treatment, although the values are unlikely to be meaningful.[44, 146, 147] However, this technique does not appear to provide valid, useful results when used with carbon nitride.

Table 2.4: Acid site measurements of samples of carbon nitride

Sample	Acid loading / mmol g^{-1}	Desorption Temperature / °C
Raw UCN	0.05	530
NH_3 treated UCN	0.25	530
SiO_2	0.04	500
ZrO_2	0.13	400, 500
$PrSO_3H$ / SiO_2	1.5	370

2.4 Decoration of UCN with Metal Carbonyl Fragments

The principal aim of this chapter is to investigate whether carbon nitride can be utilised as ligand within a surface-bound metal complex. As the only significant different between UCN and CCN is the overall material structure, rather than its monomeric composition, and due to the considerably simpler, more scalable synthesis of UCN, UCN was selected for work within the rest of this chapter.

2.4.1 Synthesis of [Mn(UCN)] and [ReCl(CO)$_3$(UCN)]

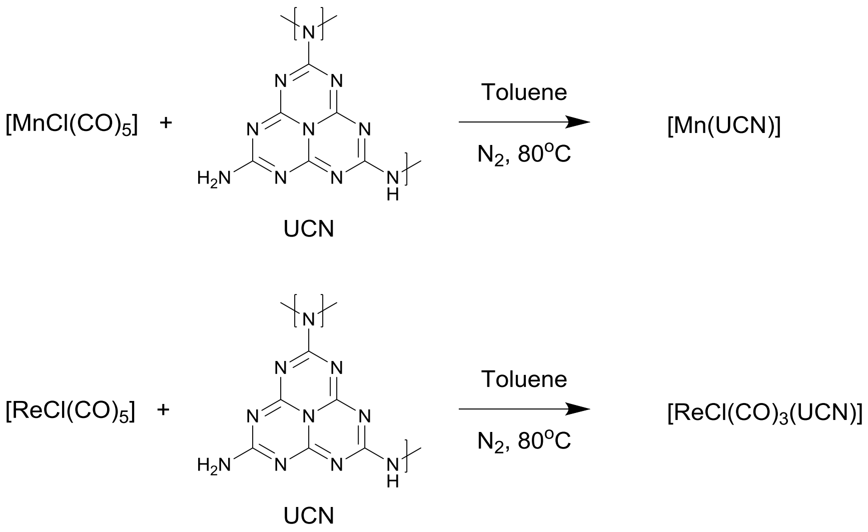

Scheme 2.3: Synthesis of metal carbonyl decorated UCN

[ReCl(CO)$_3$(UCN)]and [Mn(UCN)] were synthesised analogously, according to Scheme 2.3, by heating base-treated and dried UCN at reflux in a toluene solution of [MCl(CO)$_5$] under nitrogen. Overall, the data collected suggests that [ReCl(CO)$_5$] coordinates to UCN, resulting in [ReCl(CO)$_3$(UCN)]. In contrast, the reaction between [MnCl(CO)$_5$] and UCN appears to result in full decomposition of the manganese species, and atomic surface doping of UCN by manganese occurs to result in [Mn(UCN)].

The ICP-MS and PXRD of the samples will be presented first, demonstrating even distribution of metal decoration across the material surface. The molecular analogues of the materials, [ReCl(CO)$_3$(DMNA)] and [MnCl(CO)$_3$(DMNA)] will then be presented and the coordination environment of the metal to the DMNA briefly discussed. Direct comparison of the infrared spectroscopy of the materials to the molecular analogues will then be performed to gain insight as to the coordination of the metal complex fragments to the UCN.

2.4.2 Quantification of metal content in [Mn(UCN)] and [ReCl(CO)$_3$(UCN)] by ICP-MS

Inductively coupled plasma mass spectrometry (ICP-MS) was carried out on samples of [Mn(UCN)] and [ReCl(CO)$_3$(UCN)] to determine the metal loading, as shown in Table 2.5. The molar loading is of the same order of magnitude for both [Mn(UCN)] and [ReCl(CO)$_3$(UCN)], although Re has almost twice the loading compared to Mn. Chlorine analysis was also performed, which shows a Re: Cl ratio of 1: 0.85 close to the expected 1: 1 in [ReCl(CO)$_3$(UCN)]. In contrast, in [Mn(UCN)] the Mn: Cl ratio of 1: 3.5 suggests that the [MnCl(CO)$_3$] unit is not conserved in [Mn(UCN)].

Table 2.5: Metal and chlorine loading in [Mn(UCN)] and [ReCl(CO)$_3$(UCN)] per gram of UCN

Sample	Metal Loading / mg g^{-1}	Metal Loading / mmol g^{-1}	Cl content / mg g^{-1}	Cl content / mmol g^{-1}
[Mn(UCN)]	13.3	0.242	29.9	0.843
[ReCl(CO)$_3$(UCN)]	73.5	0.395	11.7	0.329

2.4.3 Powder X-ray Diffraction of [Mn(UCN)] and [ReCl(CO)$_3$(UCN)]

The overall morphology of the composite materials was measured by performing powder X-ray diffraction (XRD) on [Mn(UCN)] and [ReCl(CO)$_3$(UCN)] (Figure 2.9). The sharp peaks seen in all patterns at 2θ = 38.2, 44.5, 64.8, 78.0 and 82.2° arise from the aluminium holder used during data collection. [Mn(UCN)] and [ReCl(CO)$_3$(UCN)] show the same broad peak at 2θ = 27.4° (d=0.325 nm) as was observed in UCN, corresponding to the interlayer stacking of the aromatic heptazine units.[36, 74] The interlayer stacking distance is the same in [Mn(UCN)], [ReCl(CO)$_3$(UCN)] and UCN, suggesting no intercolation of the metal fragments between the planes is occurring. The lack of additional signals in the XRD patterns of [Mn(UCN)] and [ReCl(CO)$_3$(UCN)] suggests there are no significant crystalline impurities.

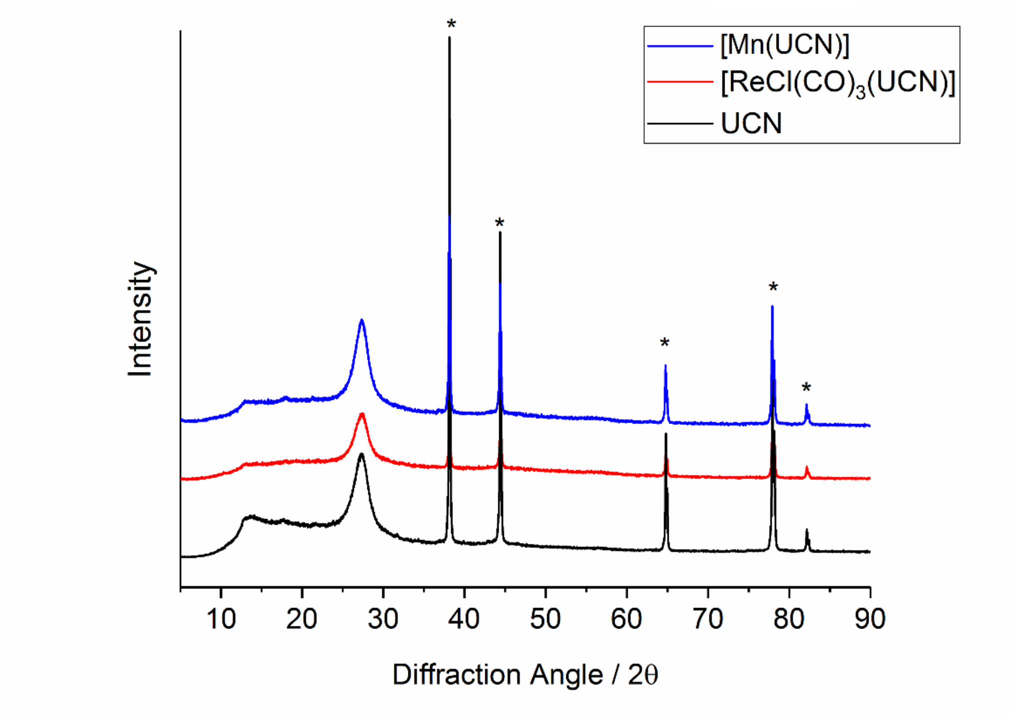

Figure 2.9: XRD patterns of UCN, [ReCl(CO)$_3$(UCN)] and [Mn(UCN)]. Resonances marked with an asterisk (*) arise from the aluminium sample holder.

2.5 Synthesis and Characterisation of [MCl(CO)$_3$(DMNA-κ^2*N,N′*)]

Carbon nitride is generally insoluble and amorphous, making direct investigation of the metal-carbon nitride interaction challenging. In order to try to understand the coordination between metals and carbon nitride, a commercially available molecular ligand, 5,7-dimethyl-[1,8]-naphthyridine-2-amine (DMNA), was selected to act as a molecular analogue to the heptazine motif present in UCN with both naphthyridine and primary amine functionality theoretically available for metal coordination.

In all previously published metal complexes containing DMNA, the coordination is between the naphthyridine nitrogen environments, with the primary amine uninvolved. Of the ten structures published in the CSD, six show coordination of DMNA to metal centres in a bidentate mode.[64] Of the remaining structures, two complexes show coordination to metal centres in a monodentate mode and two exhibit a bridging coordination mode between two metal centres.[64] Therefore, whilst bidentate coordination is the most common mode, other coordination modes are possible.

The complexes [ReCl(CO_3)(DMNA)] and [MnCl(CO_3)(DMNA)] were synthesised according to Scheme 2.4 and fully characterised by NMR, LIFDI-MS and CHN. X-ray crystallography and infrared spectroscopy was performed to characterise the coordination mode between the metal atoms and the DMNA, and in turn gain insight into the coordination mode between metal atoms and UCN.

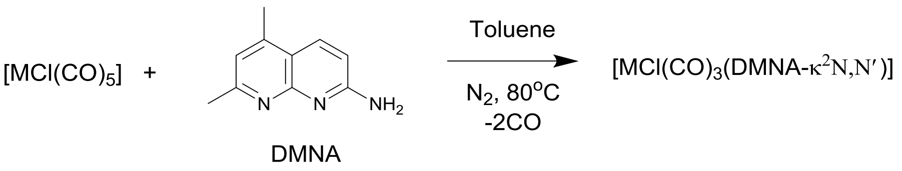

Scheme 2.4: Synthesis of [MCl(CO)$_3$(DMNA- κ^2N, N')] (M = Mn, Re)

2.5.1 X-ray Crystal Structure of [MCl(CO)$_3$(DMNA-κ^2*N, N'*)] (M = Re, Mn)

X-ray quality single crystals of [MCl(CO)$_3$ (DMNA)] were obtained by vapour diffusion of diethyl ether into a saturated solution of the complex in acetone. The X-ray crystal structures of [MCl(CO)$_3$(DMNA)] are shown in Figure 2.10. Both compounds form monoclinic crystal systems, but have different space groups, with [MnCl(CO)$_3$(DMNA)] being $P2_1/n$ and [ReCl(CO)$_3$(DMNA)] being C2/c. No unusual data refinement was carried out. Selected bond lengths and angles are listed in Table 2.6.

The coordination mode of the DMNA ligand to both manganese and rhenium is bidentate with both diimine nitrogen atoms coordinating to the metal, and the proximal primary amine group being uninvolved in metal coordination.

Selected interatomic distances and angles are shown in Table 2.6. As expected, the metal-nitrogen distances observed in [MnCl(CO)$_3$(DMNA)] (2.078(1) Å and 2.087(1) Å) are shorter compared to [ReCl(CO)$_3$(DMNA)] (2.212(2) Å and 2.218(2) Å). Both molecules show asymmetric coordination to the asymmetric bidentate ligand with M-N1 is the shorter metal-nitrogen bond, though the effect is less significant in [ReCl(CO)$_3$(DMNA)]. The C-O bond distances observed for the carbonyl ligands are not significantly different between the two molecules (Table 2.8).

The coordination environment around the metal centres can also be assessed by looking at the angles between the ligands. The ideal octahedral centre would have interligand angles of 90°. The environments in both complexes deviate from this ideal, as seen in the N2-M-Cl1 angle of 85.27(3)° in [MnCl(CO)$_3$(DMNA)] and 81.71(6)° in [ReCl(CO)$_3$(DMNA)].

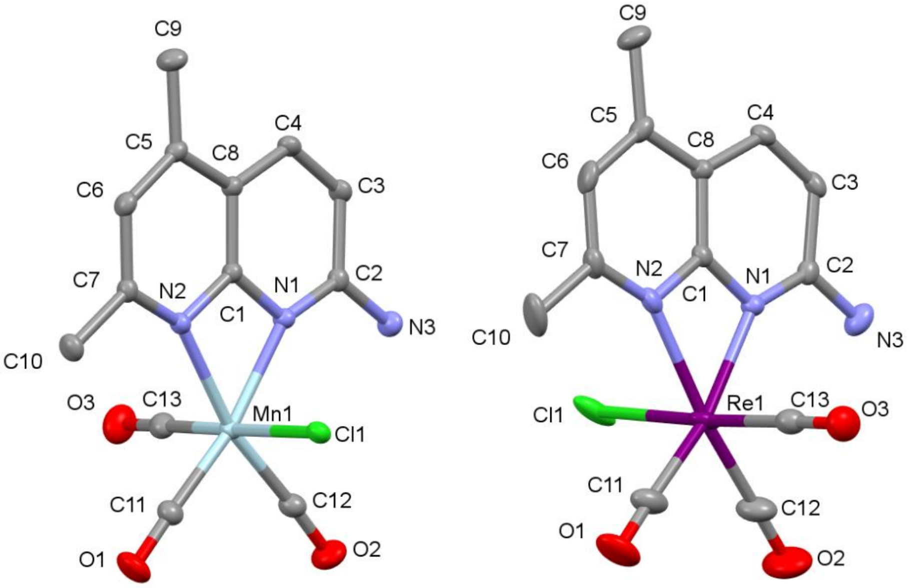

Figure 2.10: X-Ray crystal structure of [MnCl(CO)$_3$(DMNA-κ^{2}N, N')] and ReCl(CO)$_3$(DMNA-κ^{2}N, N')] with probability ellipsoids shown at the 50% level and hydrogens omitted for clarity

Table 2.6: Selected bond distances in [MnCl(CO)$_3$(DMNA-κ^{2}N, N')] and [ReCl(CO)$_3$(DMNA-κ^{2}N, N')]

Bond Distance / Å	[MnCl(CO)$_3$(DMNA- κ^2*N, N'*)]	[ReCl(CO)$_3$(DMNA-κ^2*N, N'*)]
M-N1	2.078(1)	2.212(2)
M-N2	2.087(1)	2.218(2)
M-C11	1.087(1)	1.912(4)
C11-O1	1.140(2)	1.149(4)
M-C12	1.808(2)	1.896(4)
C12-O2	1.142(2)	1.141(4)
M-C13	1.796(2)	1.899(3)
C13-O3	1.141(2)	1.150(4)
M-Cl1	2.4058(6)	2.4935(9)
Bond Angle / °		
N1-M-N2	64.05(5)	60.41(8)
C11-M-C12	88.60(7)	86.4(2)
C12-M-C13	89.48(7)	88.6(1)
C13-M-C11	90.14(7)	88.4(1)
N1-M-C13	90.54(6)	90.9(1)
N1-M-Cl1	89.44(3)	85.89(6)
N2-M-C13	93.23(6)	96.3(1)
N2-M-Cl1	85.27(3)	81.71(6)

The ligand 'bite angle' between the two coordinating nitrogen atoms and the metal centre is seen to be smaller in [ReCl(CO)$_3$(DMNA)], a result of the larger size of the rhenium atom and longer metal-nitrogen bonds.

The DMNA ligand itself distorts upon metal coordination in both [MnCl(CO)$_3$(DMNA)] and [ReCl(CO)$_3$(DMNA)], with a contraction of C1-C8 and a significant reduction of the N1-N2 distance and N1-C1-N2 angle (Table 2.7).[148] The N1-C2-N3 angle also slightly increases as well as the C2-N3 bond shortening after metal coordination, suggesting more electron-donation of the nitrogen lone pair into the aromatic system (i.e. increased sp^2 nature of the lone pair).

Table 2.7: Bond distance and angles in DMNA showing distortion upon coordination in [MCl(CO)3(DMNA-κ^{2}N, N')]

Bond Distance / Å	DMNA[148]	[MnCl(CO)$_3$(DMNA)].	[ReCl(CO)$_3$(DMNA)]
C1-C8	1.424(3)	1.393(2)	1.395(3)
N1-N2	2.304(3)	2.209(2)	2.229(3)
N3-C2	1.353(5)	1.347(2)	1.341(4)
Bond Angle / °			
N1-C1-N2	115.6(2)	109.0(1)	110.1(2)
N1-C2-N3	118.7(3)	119.3(1)	120.1(2)

This slight DMNA ligand distortion is seen in both [ReCl(CO)$_3$(DMNA)] and [MnCl(CO)$_3$(DMNA)], suggesting that structurally there is no significant difference in how energetically favourable the coordination is between the two metal complexes.

2.6 Comparison of [MCl(CO)$_3$(DMNA-κ^2*N, N'*)] to [Mn(UCN)] and [ReCl(CO)$_3$(UCN)]

2.6.1 Infrared Spectroscopy of [MCl(CO)$_3$(DMNA-κ^2*N, N'*)]

Measuring carbonyl ligand vibrational frequencies using infrared spectroscopy is a valuable tool in appraising the electron density on a metal and geometry around a metal in inorganic complexes. Infrared spectra of [MnCl(CO)$_3$(DMNA)] and [ReCl(CO)$_3$(DMNA)] were taken and the vibrations observed in the carbonyl region are summarised in Table 2.8.

Table 2.8: Carbonyl stretching frequencies (v(CO)/cm^{-1}) in DCM for MnCl(CO)$_3$(DMNA)] and [ReCl(CO)$_3$(DMNA)] showing comparison to the corresponding 2,2'-bipyridine complexes

Compound		v$_{CO}$ / cm^{-1}	
[MnCl(CO)$_3$(DMNA)]	2035	1935	1916
[MnCl(CO)$_3$(bpy)][149]	2025	1936	1913
[ReCl(CO)$_3$(DMNA)]	2025	1916	1899
[ReCl(CO)$_3$(bpy)][101]	2024	1921	1899

The number of carbonyl bands observed in the infrared spectrum of a metal complex immediately gives information about the number of carbonyl environments and the expected geometry. Facial metal tricarbonyl species such as [MCl(CO)$_3$(DMNA)] typically show three distinct vibrational bands in the carbonyl region of the infrared spectrum. [128, 150] Of the three bands, the band at highest energy is assigned as the totally symmetric in-phase A'(1) vibration. The remaining vibrational modes are the equatorially asymmetric A'' and totally symmetric out-of-phase A'(2) modes.[102, 151]

Metal carbonyl bonding can be understood as a combination of two principle interactions - donation from the carbonyl σ-orbital into an empty metal d-orbital, and 'back donation' from a filled metal d-orbital into the carbonyl π* orbitals. The more electron-rich a metal centre, and the better orbital overlap between molecular orbitals, the more back donation, which in turn results in a weaker carbonyl bond and lower vibrational frequency. This is the reason that manganese tricarbonyl systems usually show higher v(CO) compared to their rhenium counterparts.[100, 116, 117, 152]

2, 2'-bipyridine is a thoroughly investigated ligand both in metal carbonyl chemistry and in wider coordination chemistry applications when compared to the relatively small amount of research performed on naphthyridine complexes.[108, 150, 153-160] The number, intensity and values of carbonyl vibrational frequencies for [MCl(CO)$_3$(DMNA)] are comparable to those seen in [MCl(CO)$_3$(bpy)] (bpy = 2,2'-bipyridine), which suggests the electronic properties and coordination observed in DMNA are not significantly different to that of bpy.[101, 149]

2.6.2 Infrared Spectroscopy of [Mn(UCN)] and [ReCl(CO)$_3$(UCN)]

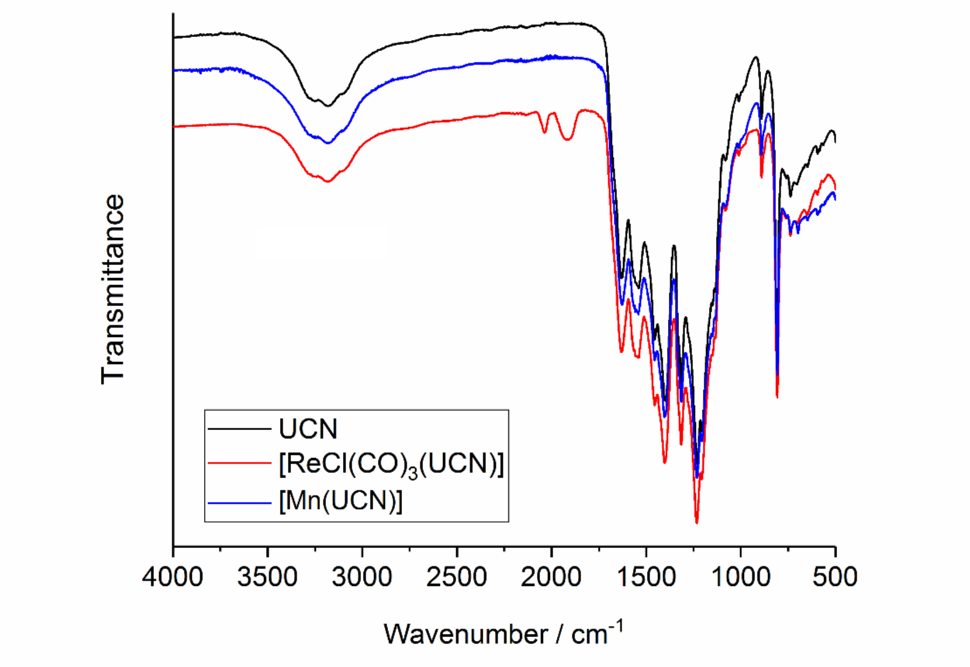

Figure 2.11: IR spectra of UCN, [Mn(UCN)] and [ReCl(CO)$_3$(UCN)]

Infrared spectroscopy is the simplest method by which to observed and characterise metal carbonyl species. The infrared spectra of UCN and [ReCl(CO)$_3$(UCN)] are shown in Figure 2.11. The ATR-IR spectrum of [Mn(UCN)] and [ReCl(CO)$_3$(UCN)] show that the structure of the carbon nitride has not been changed through the reaction, as the principle vibrational bands observed for UCN are observed in the decorated material. [ReCl(CO)$_3$(UCN)] also shows strong vibrational bands in the carbonyl region, with a broad band centred at 1916 cm^{-1} and a sharper band centred at 2034^{-1}. [Mn(UCN)] does not show these additional carbonyl-region vibrations. However, X-ray crystallography of [MnCl(CO)$_3$(DMNA)] suggests that coordination between manganese and naphthyridine, and by extension heptazine, is favourable, and ICP-MS shows a significant loading of manganese in [Mn(UCN)].

As manganese carbonyls are less electrochemically stable to redox chemistry in comparison to rhenium carbonyls, it seems likely that a reaction is occurring between manganese carbonyl species and UCN resulting in ligand loss (i.e. carbonyl release), which has been observed in other solid-state supported manganese systems.[124] Ligand loss is likely not observed in the case of [ReCl(CO)$_3$(UCN)] due to the higher oxidation potential (and lower reduction potential) of rhenium carbonyls compared to manganese carbonyls.[100, 116, 117, 152] The general label of "[Mn(UCN)]" is used to reflect that although presence of Mn is shown by ICP-MS, the environment around the manganese in this material is not known.

It is unclear whether ligand loss occurs before or after coordination of manganese to carbon nitride, and investigating the precise mechanism is nontrivial due to the insoluble nature of the carbon nitride. However, it is apparent that carbon nitride is capable of reacting with redox-active metals rather than being limited to coordination chemistry. The observation of this redox behaviour of carbon nitride should be considered in other applications of carbon nitride as a ligand. The remainder of this chapter will focus on the more stable [ReCl(CO)$_3$(UCN)].

2.6.3 Diffuse Reflectance Infrared Fourier Transform Spectroscopy (DRIFTS) of [ReCl(CO)$_3$(UCN)] and UCN

Diffuse Reflectance Infrared Fourier Transform Spectroscopy (DRIFTS) is an infrared technique with a higher surface sensitivity when compared to ATR-IR. DRIFTS was performed on UCN and [ReCl(CO)$_3$(UCN)] and is shown in Figure 2.12. In addition to the infrared vibrations observed in ATR-IR, DRIFTS of UCN shows weaker bands around 2200 cm^{-1} corresponding to cyano-group vibrations.[161] The ratio of metal-carbonyl vibrational band intensity to band intensity inherent to carbon nitride is higher when observed via DRIFTS compared to ATR. This suggests that species giving rise to the vibrational bands is concentrated on the surface rather than distributed through the bulk of the material.

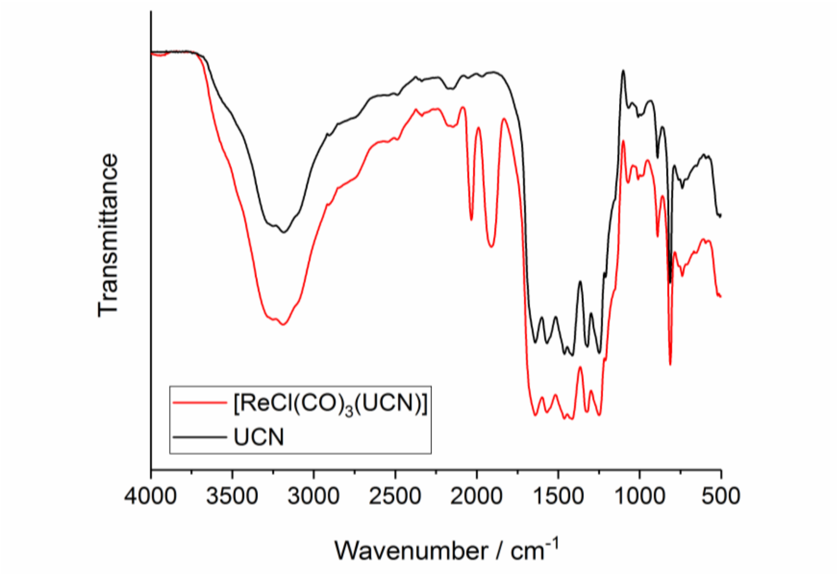

Figure 2.12: DRIFTS spectra of UCN and [ReCl(CO)$_3$(UCN)]

2.6.4 Comparison of [ReCl(CO)$_3$(DMNA-κ^2*N, N'*)] to [ReCl(CO)$_3$(UCN)]

The carbonyl region of the infrared spectrum of [ReCl(CO)$_3$(UCN)] is compared to [ReCl(CO)$_3$(DMNA)] and [ReCl(CO)$_5$] in Figure 2.13 and summarised in Table 2.9. The carbonyl vibrational band structure of [ReCl(CO)$_3$(DMNA)] in a solution of DCM shows 3 bands, as expected for octahedral rhenium tricarbonyl species with a facial carbonyl arrangement.[128, 150] However, due to the insolubility of [ReCl(CO)$_3$(DMNA)], the ATR-IR of [ReCl(CO)$_3$(DMNA)] is also performed. In the solid state, the vibrational bands broaden, causing an overlap of the peaks observed at 1899 and 1916 cm^{-1} in the solution spectrum of [ReCl(CO)$_3$(DMNA)].

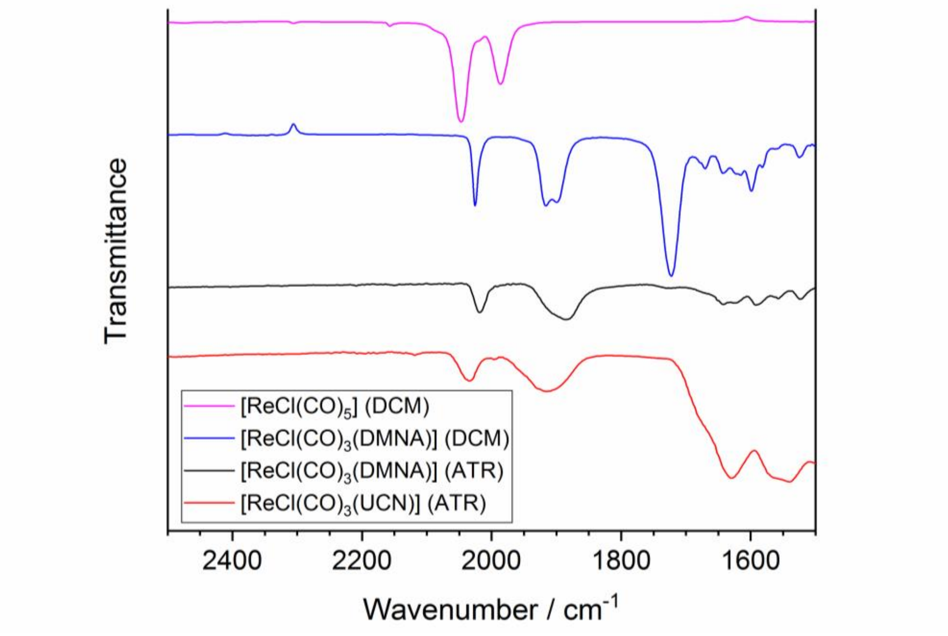

Figure 2.13: Infrared spectra of [ReCl(CO)$_3$(UCN)] and related compounds

Table 2.9: Infrared spectroscopy of [ReCl(CO)$_3$(UCN)] and related compounds

Compound (IR condition)	ν_{CO} / cm^{-1}
[ReCl(CO)$_5$] (DCM)	1986, 2047
[ReCl(CO)$_3$(DMNA)] (DCM)	1899, 1916, 2025
[ReCl(CO)$_3$(DMNA)] (ATR)	1886 (br), 2018
[ReCl(CO)$_3$(UCN)] (ATR)	1916 (br), 2034

The structure of the vibrational bands observed in [ReCl(CO)$_3$(UCN)] are different from those observed in [ReCl(CO)$_5$], indicating a chemical reaction has occurred between carbon nitride and the precursor rather than simply physisorption of the metal carbonyl to the surface. The bands seen in the carbonyl region of [ReCl(CO)$_3$(UCN)] are very similar to those observed for [ReCl(CO)$_3$(DMNA)]. The shift of ν_{CO} to higher frequency in [ReCl(CO)$_3$(UCN)] compared to [ReCl(CO)$_3$Cl(DMNA)] suggests that UCN is a less electron-donating ligand when compared to DMNA.

2.6.5 Solid-State ^{13}C CP-MAS NMR Spectroscopy

Solid state NMR spectroscopy (^{13}C CP-MAS) was performed with the goal of aiding the characterisation of the carbonyl environments in [ReCl(CO)$_3$(UCN)]. The ^{13}C CP-MAS spectra of [ReCl(CO)$_3$(UCN)] and UCN are shown in Figure 2.14.

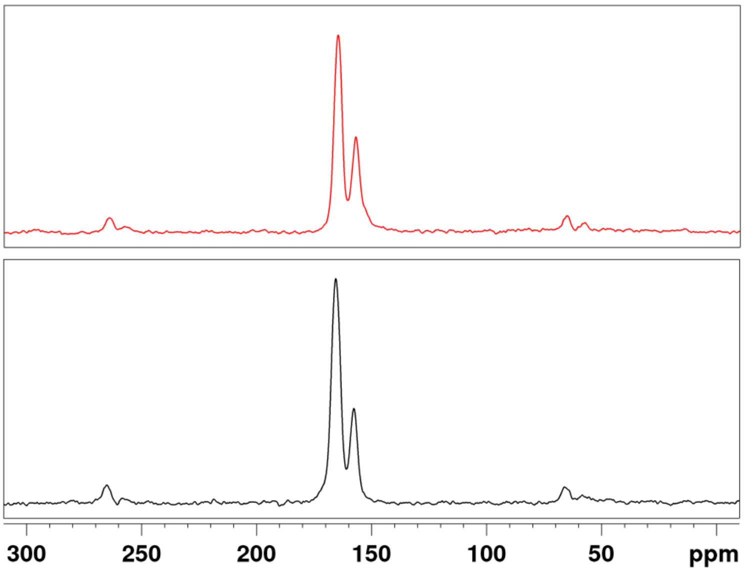

Figure 2.14: The ^{13}C CP-MAS NMR spectrum (10 kHz spin rate) of [ReCl(CO)$_3$(UCN)] (top) and UCN (bottom)

The two signals arising observed in UCN at 157.8 ppm and 165.7 ppm correspond to the CN_3 and N_2CNH_x environments respectively.[162] The other bands observed either side of the main peaks are spinning-side bands and are separated by the spin rate (10 kHz). No additional ^{13}C CP-MAS signals are observed in [ReCl(CO)$_3$(UCN)] arising from the carbonyl groups. Although this may simply arise due to a poorly defined metal site, it is also likely a result of a combination of the relatively low carbonyl concentration and quadrupolar broadening due to a rhenium-carbon interaction.[163, 164] This quadrupolar interaction between rhenium and carbon is responsible for the broadening seen in the ^{13}C NMR carbonyl signals in [ReCl(CO)$_3$(bpy)] in the region 220-180 ppm in Figure 2.15. In Figure 2.15, the sharp peaks between 120-160 ppm are due to the 2,2'-bipyridine ligand, and those between 0-40 and 240-280 are spinning side-bands of these peaks.

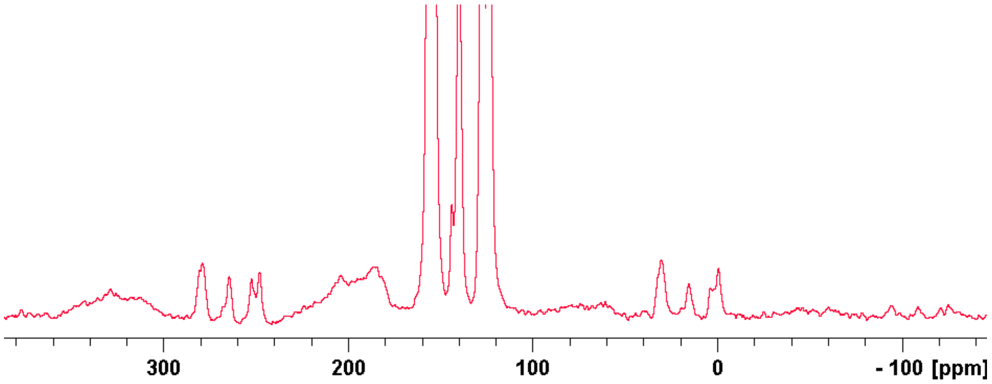

Figure 2.15: ^{13}C CP-MAS NMR spectrum (10 kHz spin rate) of [ReCl(CO)$_3$(bpy)]

2.6.6 X-ray Photoelectron Spectroscopy (XPS) of UCN and [ReCl(CO)$_3$(UCN)]

X-ray Photoelectron Spectroscopy (XPS) was performed on samples of [ReCl(CO)$_3$(UCN)] and UCN. A summary of the peaks, including full width half maxima of the fitted peaks, is shown in Table 2.10 and Table 2.11. The XPS spectra of the UCN are consistent with urea-derived amorphous carbon nitride.[165] The nitrogen 1s region is fitted to show similar signals for [ReCl(CO)$_3$(UCN)] and UCN in Figure 2.16. The strongest signal at 398.7 eV responds to the aromatic imine groups (CNC), with additional signals at 399.9 eV and 401 eV corresponding to the sp^3 nitrogen atom (NC_3) and the surface amine groups (CNH) respectively (Figure 2.17).

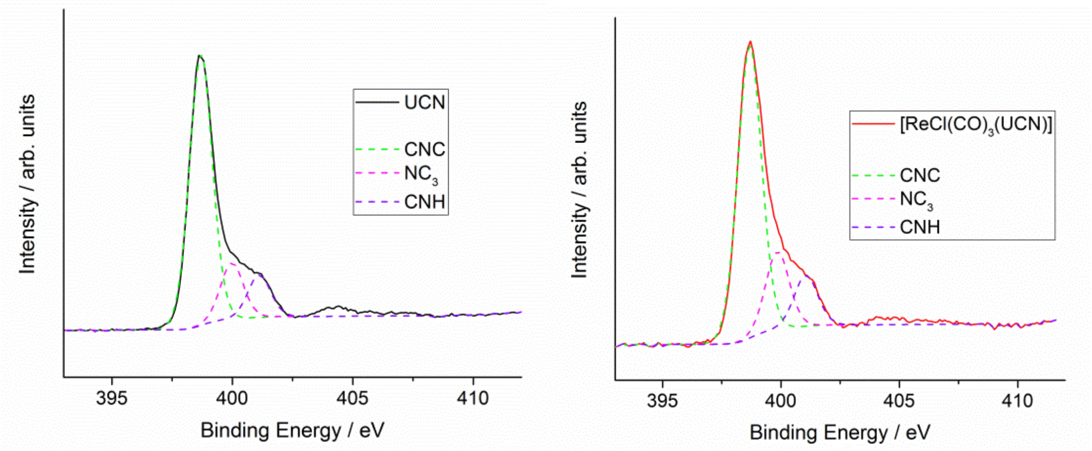

Figure 2.16: N 1s XPS Spectra of UCN and [ReCl(CO)$_3$(UCN)]

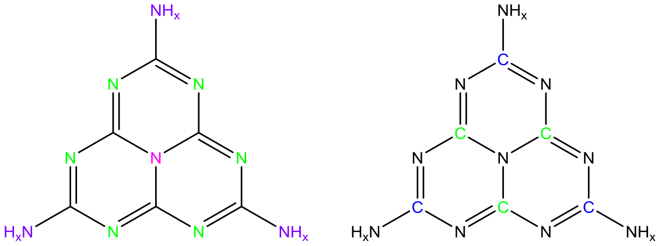

Figure 2.17: Structure of the monomer of UCN with nitrogen (left) and carbon (right) atoms colour-coded to XPS data

The C 1s region of the XPS spectra of [ReCl(CO)$_3$(UCN)] and UCN is shown in Figure 2.18. In UCN, two peaks are modelled to fit the signal. The signal at 284.8 eV is assigned to fit carbons adjacent to amines (C-N), while the signal at 288.6 eV is assigned to fit carbon environments adjacent to aromatic nitrogen atoms (C=N). A very weak peak at 286.1 eV is assigned to surface organic carbonyls (C=O) remaining from the urea precursor.

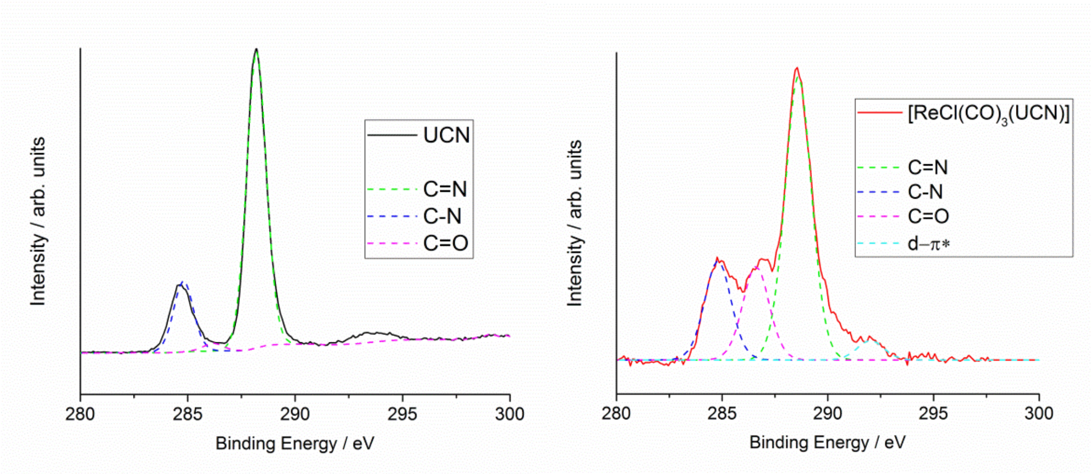

Figure 2.18: C 1s XPS Spectra ofUCN and [ReCl(CO)$_3$(UCN)]

Additional features are observed in the C 1s region of XPS spectrum of [ReCl(CO)$_3$(UCN)] compared to UCN. The new feature with the strongest peak, modelled at 286.6 eV, is fitted to arise from C=O environments in the carbonyl ligands.[166] A weaker signal fitted to 292 eV is also observed, which is suggested to arise from a shake-up transition.

It is proposed that the peak at 292 eV is observed due to the interaction of a photoelectron and a rhenium centre, causing excitation of an electron from the rhenium d-orbitals to a defined π* orbital on the coordinating heptazine. The photoelectron loses energy equal to the excitation energy of this state (3.4 eV, 364 nm, see Figure 2.26) and the detector registers this energy loss as an increase in the binding energy of the electron. This is referred to as a 'shake-up' peak. Section 2.8 discusses the photochemistry of [ReCl(CO)$_3$(UCN)] in more detail.

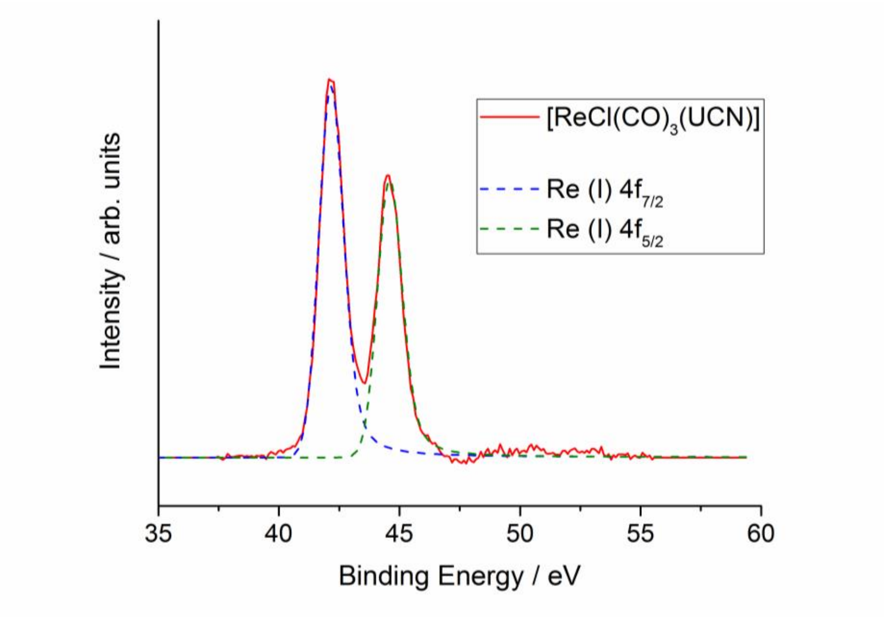

Figure 2.19: XPS spectra (Re 4f region) of a sample of [ReCl(CO)$_3$(UCN)] at two different sample collection times

The Re 4f region of the XPS spectrum of [ReCl(CO)$_3$(UCN)] is shown in Figure 2.19. The two peaks observed at 42.2 eV and 44.6 eV are fitted to the Re 4f$_{7/2}$ and Re 4f$_{5/2}$ signals respectively, and the sharpness of the peaks (fwhm = 1.25 eV) suggests a single rhenium environment. This is comparable to the shifts observed for a rhenium tricarbonyl phenanthroline species grafted onto graphene, which exhibited sharp peaks at 41.3 and 43.7 eV.[122] No metallic Re, which would be observed around 40.7 eV, was observed.[167] Rhenium oxides show broad peaks around the range of 42.1-46.4 eV, which would be inconsistent with the presence of carbonyl vibrations in the infrared spectrum and a single rhenium species.[168, 169] The Re peaks are therefore assigned as arising from a Re(I) carbonyl species.

Table 2.10: Summary of XPS fitted peaks observed in UCN

Sample	Region	Peak / eV	FWHM / eV	Assignment
UCN	N 1s	398.7	1.14	CNC
		400.0	1.29	NC_3
		401.1	1.46	CNH
	C 1s	288.2	1.11	C=N
		286.1	1.03	C=O
		284.8	1.07	C-NH

Table 2.11: Summary of XPS fitted peaks observed in [ReCl(CO)$_3$(UCN)]

Sample	Region	Peak / eV	FWHM / eV	Assignment
[ReCl(CO)$_3$(UCN)]	N 1s	398.7	1.20	CNC
		400.0	1.29	NC_3
		401.1	1.46	CNH
	C 1s	292.0	1.50	π-π*
		288.6	1.49	C=N
		286.6	1.50	C=O
		284.8	1.50	C-N
	Re 4f	44.6	1.25	Re (I) $4f_{7/2}$
		42.2	1.25	Re (I) $4f_{5/2}$

2.6.7 The Structure of [ReCl(CO)$_3$(UCN)]

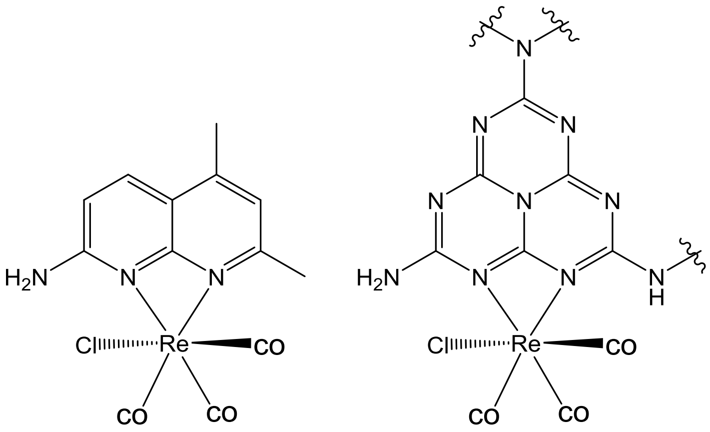

Figure 2.20: Coordination mode of Re to DMNA in [ReCl(CO)$_3$(DMNA- κ^{2}N, N')] and proposed coordination mode of Re to UCN in [ReCl(CO)$_3$(UCN)]

Due to the similarities in the structures of the infrared spectrum (Figure 2.13, Table 2.9) it is proposed that UCN and DMNA coordinate to Re analogously. Following the X-ray crystallography of the molecular analogues, it is proposed that the aromatic nitrogen environments in UCN coordinate in a bidentate mode to metal fragments as shown in Figure 2.20. This is consistent with all observations. The metal loading as measured by ICP-MS suggests that not all heptazine units are involved in coordination, and a higher concentration of metal carbonyl species exists on the surface as observed by DRIFTS. This supports the hypothesis that coordination is localised at the edge sites of the material, where the concentration of available diimine coordination environments is highest.[7]

2.7 Solution Stability of [ReCl(CO)$_3$(UCN)]

For the utility of carbon nitride as a ligand to be evaluated, the stability of the decorated material towards metal leaching was investigated. A simple leaching experiment was designed to show stability of [ReCl(CO)$_3$(UCN)] in solvent. Samples of [ReCl(CO)$_3$(UCN)] were stirred in different solvents for three hours, after which the [ReCl(CO)$_3$(UCN)] was isolated by filtration. Infrared spectroscopy was then performed on both the material and the filtrate.

2.7.1 ATR-IR of [ReCl(CO)$_3$(UCN)] after solvent soaking

The full ATR-IR spectrum of samples of [ReCl(CO)$_3$(UCN)] after soaking in different solvents is shown in Figure 2.21. Each spectrum was normalised to the vibrational peak arising from the UCN at 1250 cm^{-1}. The same data are expanded in Figure 2.22 on the carbonyl region.

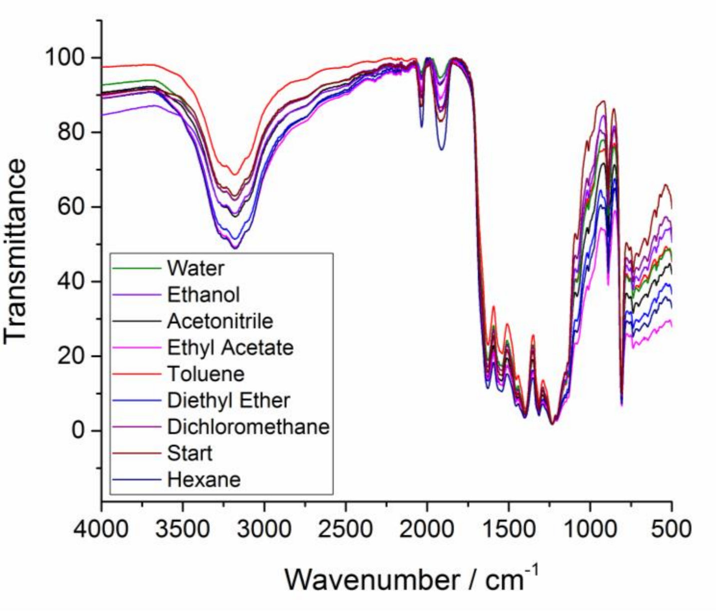

Figure 2.21: Infrared spectroscopy of [ReCl(CO)$_3$(UCN)] after soaking in different solvents

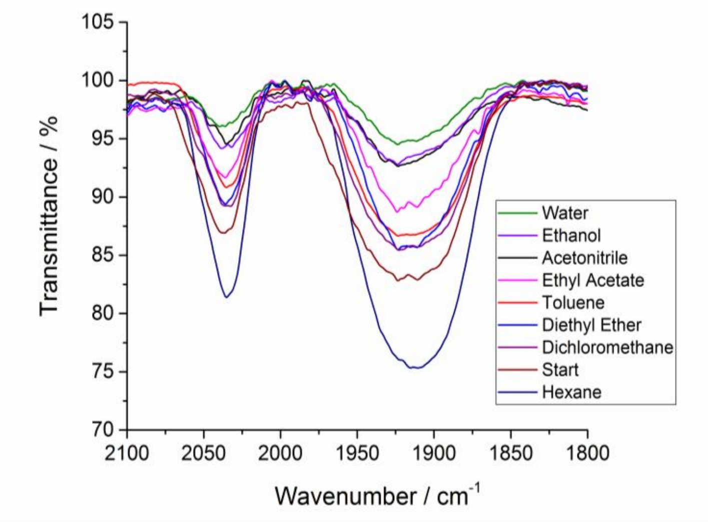

Figure 2.22: Expansion of carbonyl region of [ReCl(CO)$_3$(UCN)] after soaking in different solvents

Due to the high infrared activity of the UCN itself, quantification of the intensities of ν_{CO} vibrational bands is difficult. The ATR-IR spectra do, however, show a semi-quantitative measure of the stability of [ReCl(CO)$_3$(UCN)]. Soaking [ReCl(CO)$_3$(UCN)] in strongly coordinating solvents such as water, ethanol and acetonitrile results in a clear decrease in the intensity of the carbonyl vibrational bands. In contrast, soaking [ReCl(CO)$_3$(UCN)] in less strongly coordinating solvents such as hexane, toluene and dichloromethane, results in a smaller loss of carbonyl vibrational band intensity.

2.7.2 Solution IR of filtrate after [ReCl(CO)$_3$(UCN)] soaking

The solution infrared spectra obtained after [ReCl(CO)$_3$(UCN)] was soaked in different solvents are shown in Figure 2.23. Infrared vibrations in the carbonyl region are clearly observed in all cases, showing that rhenium-carbonyl solution species are present after soaking in even weakly-coordinating solvents. Other rhenium species (i.e. chlorides) may also be present in solution, but would not be observed as easily using infrared spectroscopy. In agreement with section, 2.7.1, more coordinating solvents result in stronger vibrational bands in the solution spectra, however, this is not quantitative as each vibrational signal will have a different absorption coefficient.

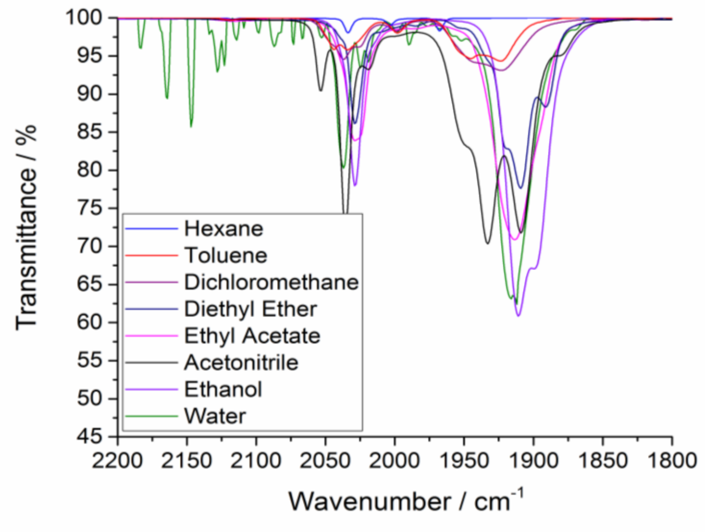

Figure 2.23: Solution infrared spectroscopy after solvent soaking of [ReCl(CO)$_3$(UCN)]

The data from Figure 2.23 is also shown in Figure 2.24, rescaled and stacked in order to more clearly show the vibrational band structure of the carbonyl region. It can be clearly seen that the vibrational band structure is dependent on the solvent, implying that the solvent is incorporated into the leached Re-containing species giving rise to the observed differences in the vibrational bands.

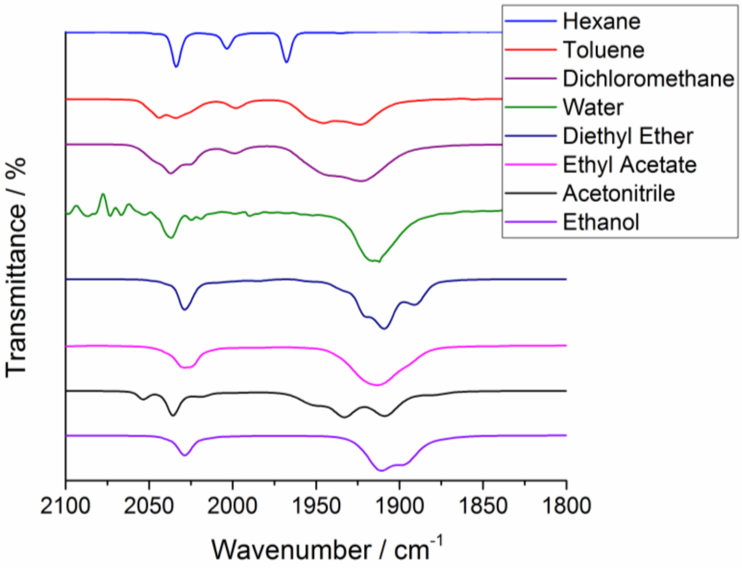

Figure 2.24: Solution infrared spectroscopy of after solvent soaking of [ReCl(CO)$_3$(UCN)]

It should be possible to identify the rhenium carbonyl 'leaching products' which give rise to the spectra observed in Figure 2.24 to gain insight into the mechanisms of decomposition. However, the signals observed in Figure 2.24 can be used to exclude the precursors, [Re$_2$(CO)$_{10}$] and [ReCl(CO)$_5$], as well as [Re(CO)$_5$]•, in all spectra. [170-173]

In acetonitrile, [ReCl(CO)$_3$(CH$_3$CN)$_2$] is not observed, but two signals at 2055 cm^{-1} and 1952 cm^{-1} may arise from [Re(CO)$_3$(CH$_3$CN)$_3$]$^+$.[173, 174] In toluene, the signals at 2028 cm^{-1}, 1948 cm^{-1} and 1935 cm^{-1} in the spectrum collected in toluene correspond to those observed for [(toluene·H)Re(CO)$_3$], although another unidentified species appears to be present.[174] In water, the peaks observed at 2037 cm^{-1} and 1916 cm^{-1} correspond to those of [Re(CO)$_3$(H$_2$O)$_3$]$^+$.[175]

Therefore, Figure 2.24 shows that when [ReCl(CO)$_3$(UCN)] is soaked in toluene, water or acetonitrile, the strong Re-C bonds persist, preserving the rhenium tricarbonyl moiety. The more labile Re-N and Re-Cl bonds allow solvent coordination and so leaching of rhenium into solution is observed. Figure 2.24 is therefore further evidence that rhenium-tricarbonyl fragments are present on the surface of UCN.

Carbon dioxide reduction is usually performed in acetonitrile due to the high solubility of CO$_2$ in this solvent. The strong leaching effect observed in most solvents, including acetonitrile, means that [ReCl(CO)$_3$(UCN)] is unsuitable for use as a heterogeneous carbon dioxide reduction catalyst. Due to the instability in appropriate solvents, the catalytic application of [ReCl(CO)$_3$(UCN)] was not investigated. However, the photochemistry of the decorated carbon nitride was briefly investigated.

2.8 Photophysical Behaviour of [ReCl(CO)$_3$(UCN)]

Following characterisation of the environment around the metal centre in [ReCl(CO)$_3$(UCN)], the photophysical properties of [ReCl(CO)$_3$(UCN)] were investigated in order to determine the effects, if any, on the properties of the bulk UCN after metal coordination. Diffuse reflectance spectroscopy, steady state luminescence and time-resolved luminescence were performed on UCN and [ReCl(CO)$_3$(UCN)].

2.8.1 Ground state optical spectroscopy of [ReCl(CO)$_3$(UCN)], UCN and [ReCl(CO)$_3$(DMNA)]

The diffuse reflectance spectra of UCN and [ReCl(CO)$_3$(UCN)] are overlaid on the absorption spectrum of a solution of [ReCl(CO)$_3$(DMNA)] in Figure 2.25. UCN shows a distinct absorbance at wavelengths below 450 nm, corresponding to the band gap of carbon nitride at 2.7 eV.[11] The band at 500 nm showing 120% reflection is a result of the strong fluorescence of the UCN during data collection (See section 2.8.2). In contrast to UCN, [ReCl(CO)$_3$(UCN)] shows absorption rather than emission between 420-520 nm. As absorption is not observed for wavelengths above 400 nm in [ReCl(CO)$_3$(DMNA)] or UCN, it is suggested that the absorption of light at λ > 420 nm by [ReCl(CO)$_3$(UCN)] is associated with electron transitions from filled rhenium d-orbitals positioned low in the band gap to the valence band of the carbon nitride – this can be considered a metal-to-ligand charge transfer (MLCT).

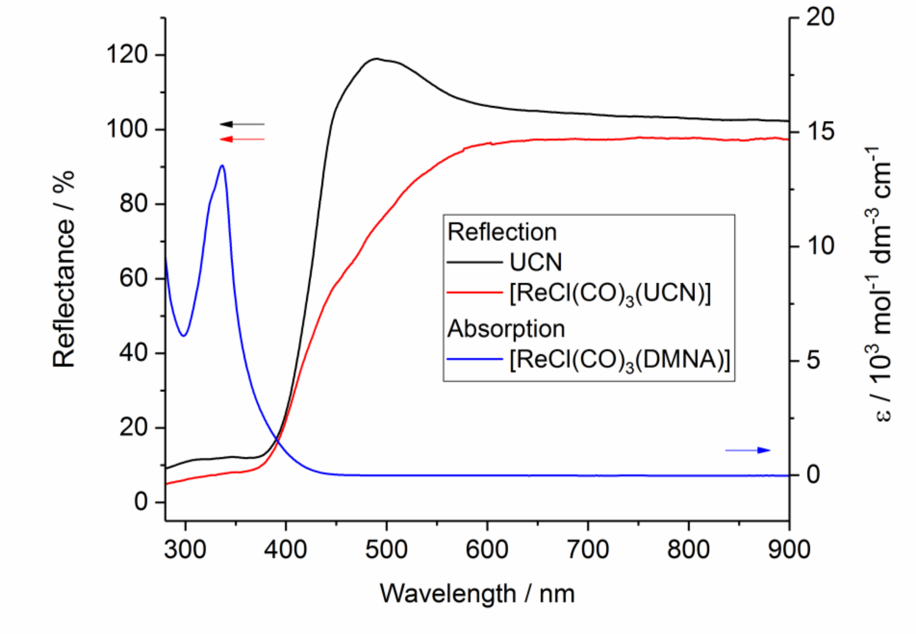

Figure 2.25: Diffuse reflectance spectra of UCN and [ReCl(CO)$_3$(UCN)] overlaid on absorption spectrum of [ReCl(CO)$_3$(DMNA)] (100 μmol dm^{-3} in DCM)

2.8.2 Steady-State Luminescence Behaviour of UCN, [ReCl(CO)$_3$(UCN)] and ReCl(CO)$_3$(DMNA)]

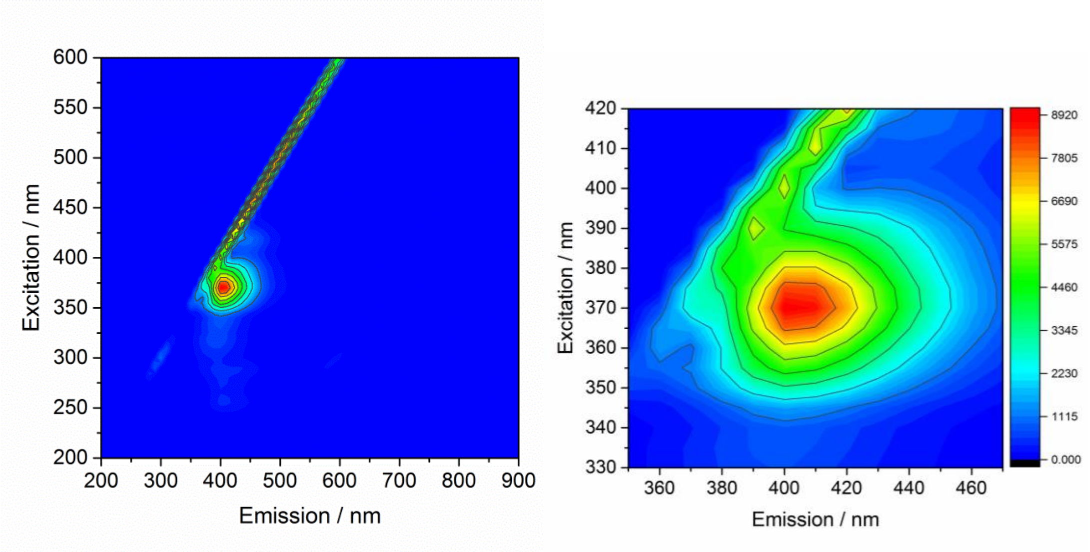

Figure 2.26: 3-dimensional excitation/emission spectrum of solution of [ReCl(CO)$_3$(DMNA)]

In order to gain the full understanding of the photochemical processes occurring within UCN and [ReCl(CO)$_3$(UCN)], 3-dimensional excitation/emission spectra were obtained of UCN, [ReCl(CO)$_3$(UCN)] and [ReCl(CO)$_3$(DMNA)]. 3-dimensional plots show how the emission spectrum of the materials varies as the excitation wavelength is changed, plotted as a contour map with the most intense signals coloured red and less intense signals coloured blue. [ReCl(CO)$_3$(DMNA)] shows a single emission band at λ_{ex} = 370, λ_{em} = 410 nm, emission arising from the radiative decay of the MLCT excited state between rhenium and the diimine ligand.[105]

3-dimensional excitation/emission spectra of UCN and [ReCl(CO)$_3$(UCN)] were also obtained and are shown in Figure 2.27 and Figure 2.28 respectively. Three intense lines are also seen across the spectra of solid state samples at emission wavelengths with integer multiples of the excitation wavelength as a result of diffraction of the incident light through the solid phase samples.The 3-dimensional spectrum of UCN shows two overlapping features: an emission band at λ_{ex} = 300, λ_{em} = 470; and another at λ_{ex} = 390, λ_{em} = 470. These same processes are also observed in [ReCl(CO)$_3$(UCN)], with no additional emission processes observed.

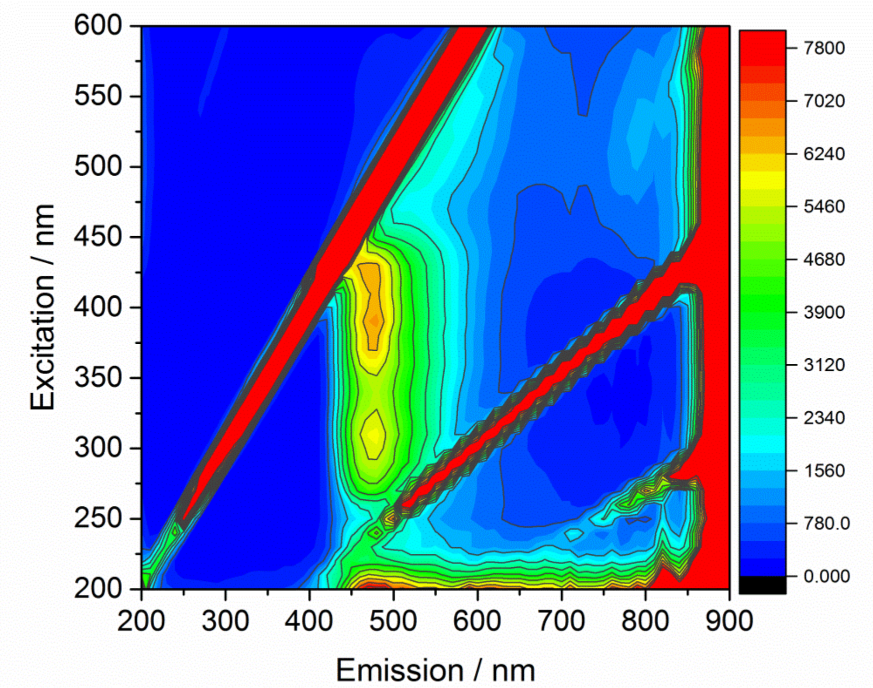

Figure 2.27: 3-dimensional excitation/emission spectrum of powder sample of UCN

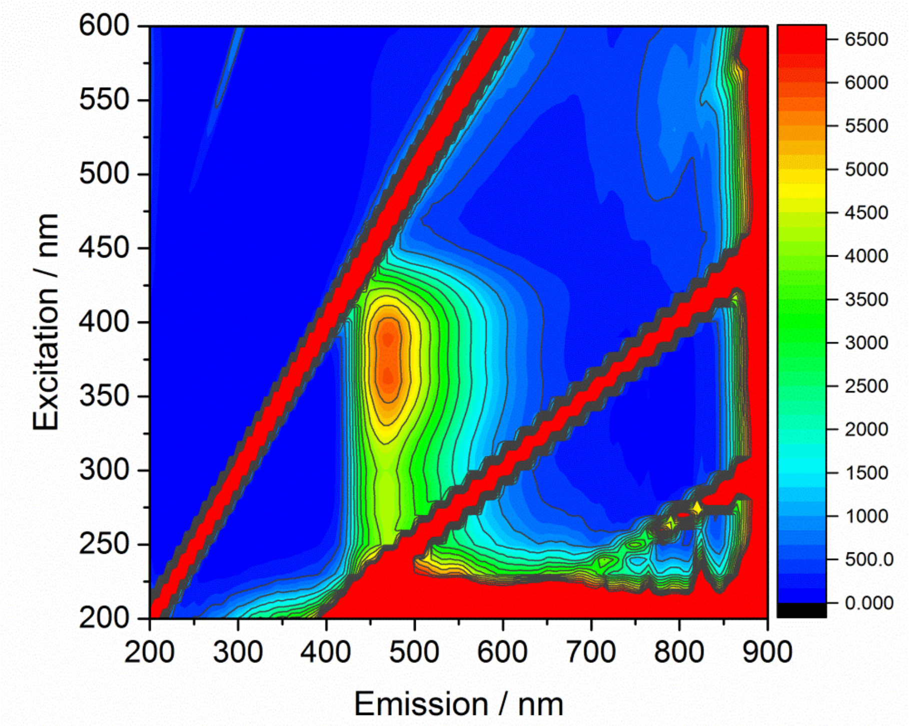

Figure 2.28: 3-dimensional excitation/emission spectrum of powder sample of [ReCl(CO)$_3$(UCN)]

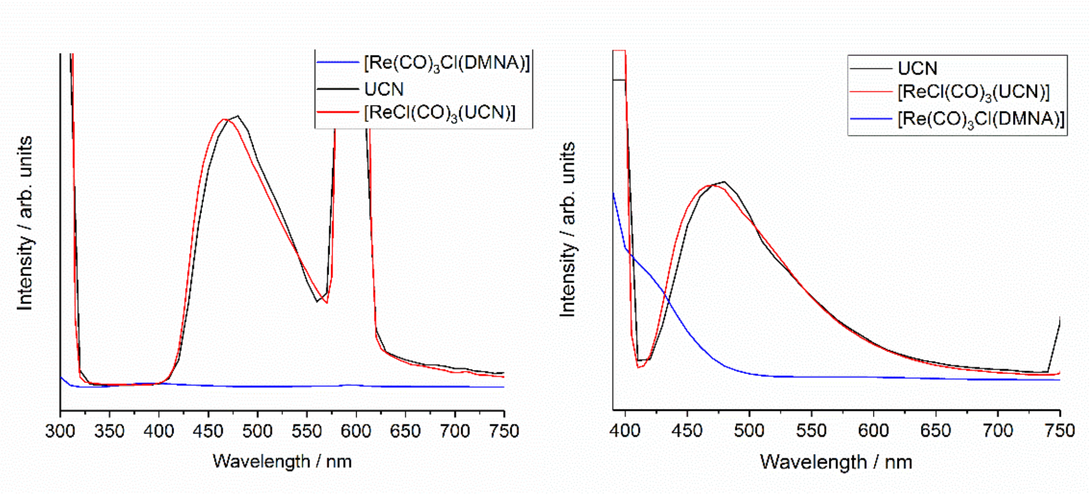

Figure 2.29: Emission spectra at λ_{ex} = 300 (left) and λ_{ex} = 390 (right) of UCN, [ReCl(CO)$_3$(UCN)] and [ReCl(CO)$_3$(DMNA)]

Data at λ_{ex} = 300 nm and 390 nm has been extracted from Figure 2.26, Figure 2.27 and Figure 2.28 and is shown in Figure 2.29 as 2-dimensional spectra for ease of comparison. It can be seen that [ReCl(CO)$_3$(UCN)] shows the same feature as UCN, however λ_{em} is blue-shifted by 10 nm (Figure 2.29). It is unclear whether this shift can be considered a shift in the band gap of the carbon nitride, or whether this shift is due to the introduction of a different emission process occurring in [ReCl(CO)$_3$(UCN)] which overlaps with the band gap of carbon nitride.

2.8.3 Time Resolved Luminescence Behaviour of [ReCl(CO)$_3$(UCN)]

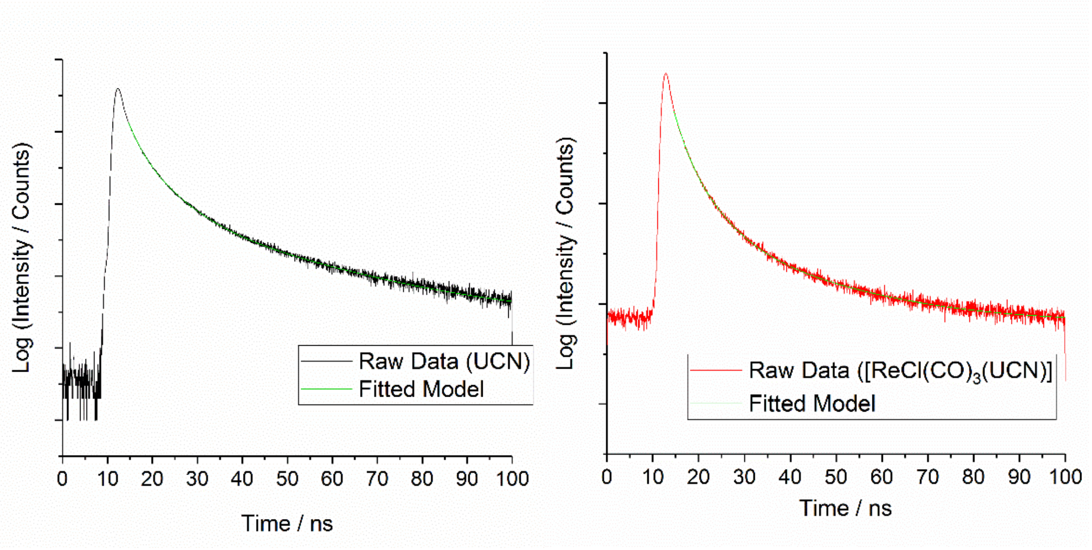

Figure 2.30: Time-resolved photoluminescence decay profiles obtained from toluene dispersions of UCN and [ReCl(CO)$_3$(UCN)] under nitrogen using λ_{ex} = 380 nm and λ_{em} = 440 nm

Time resolved photoluminescence (TRPL) measurements were taken for samples of UCN and [ReCl(CO)$_3$(UCN)] to determine the kinetics of the excited state or states obtained at λ_{ex} = 380 nm and λ_{em} = 440 nm. The raw decay curves, along with the fitted decay profiles, are shown in Figure 2.30. To reduce the strong reflectance effect observed in solid powder samples, dispersions in degassed toluene were used for the TRPL measurements. Toluene was chosen to minimise leaching of rhenium into solution as seen in section 2.7, however solution rhenium is likely to still be present and may affect measurements.

The raw decay profile is fitted to Equation 1, with the values obtained for lifetime component values and contribution shown in Table 2.12. For UCN, three components were used to bring the value of χ^2, the ‘goodness of fit’ factor closest to unity. The results indicate that the emission band observed from UCN arises due to three radiative processes. This assessment is strengthened by measuring the TRPL of UCN at two different emission wavelengths, 440 nm and 470 nm. Although the calculated values of the lifetime components don’t significantly vary with emission wavelength, the contribution of the longer lifetime component to the overall profile increases at the higher emission wavelength. This is concomitant with a decrease in the contribution of the shortest lifetime component at lower emission wavelengths.

$$\boldsymbol{R(t) = B_1 e^{\left(\frac{-t}{\tau_1}\right)} + B_2 e^{\left(\frac{-t}{\tau_2}\right)} + B_3 e^{\left(\frac{-t}{\tau_3}\right)}} \qquad \textit{Equation 1}$$

Table 2.12: Listed lifetime parameters (τ_X) and contribution to overall fit (B_X) obtained from fitting of TRPL experiments obtained from toluene dispersions of UCN and [ReCl(CO)$_3$(UCN)] using λ_{ex} = 380 nm

Material	λ_{em}	τ_1 / ns	B_1 / %	τ_2 / ns	B_2 / %	τ_3 / ns	B_3 / %	χ^2
UCN	440	2.1 ± 0.04	25	5.9 ± 0.12	47	22.7 ± 0.69	28	1.21
	470	2.2 ± 0.04	21	6.3 ± 0.16	43	24.6 ± 0.69	36	1.08
[ReCl(CO)$_3$(UCN)]	440	1.9 ± 0.05	24	5.1 ± 0.17	46	20.4 ± 0.77	30	1.11
	470	1.9 ± 0.06	18	5.2 ± 0.17	42	22.1 ± 0.63	40	1.13

The data shown for UCN in Table 2.12 are in agreement with literature data.[176] Previous work suggests that the three components arise from three difference classes of excitons: direct recombination at the site of excitation (τ_1); recombination after intraplanar exciton migration (τ_2); and recombination after interplanar exciton migration (τ_3).[176-178]

Of interest is how the data collected from [ReCl(CO)$_3$(UCN)] so closely matches the obtained data from UCN. This suggests that despite the change in the optical band gap, the radiative decay processes observed for each material are essentially unaffected by metal decoration. However, non-radiative decay processes are not measured by this technique, and the literature suggests that metal-carbon nitride interactions are generally non-radiative.[44, 179, 180]

2.8.4 Proposed Photophysical Processes Occuring in [ReCl(CO)$_3$(UCN)]

Figure 2.31 summarises a schematic of the proposed energy levels in [ReCl(CO)$_3$(UCN)], as well as the photochemical processes that may be occurring. This schematic is a hypothesis formed on the basis of observations listed in this chapter and further experimental evidence will be needed to confirm this interpretation.

Ordinary carbon nitride 'band gap' behaviour is observed in [ReCl(CO)$_3$(UCN)]. This gives rise to the absorption processes below 400 nm, and the luminescence behaviour of [ReCl(CO)$_3$(UCN)]. In addition, the DRS suggests that visible light absorption processes occur in [ReCl(CO)$_3$(UCN)] (Figure 2.25). If the orbital labelled 'd', corresponding to the HOMO in [ReCl(CO)$_3$(DMNA)] was positioned in energy between the valence band and the conduction band of the material, visible light would be absorbed (purple arrow) at a lower wavelength than the band gap as electrons are transferred from the d-orbitals on rhenium to the conduction band of the UCN. This would formally be a MLCT excited state, though in this case transition could also be described as a band-gap transition.

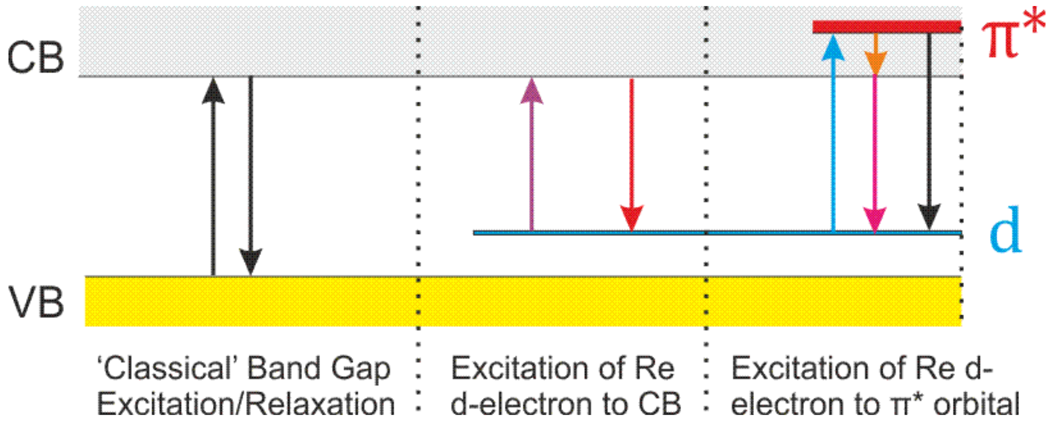

Figure 2.31 Simplified schematic of photophysical processes observed to occur within [ReCl(CO)$_3$(UCN)]

Figure 2.28 shows no signals in [ReCl(CO)$_3$(UCN)] corresponding to emission from the proposed MLCT state formed after excitation of an electron from a Re d-orbital to the conduction band (shown in red on Figure 2.31). The lack of observed emission may be a result of the localised, relatively dilute nature of the rhenium. A non-radiative relaxation pathway, such as Förster Resonance Energy Transfer (FRET), or vibrational relaxation, may also exist.[181] Ultrafast spectroscopy, such as that combining visible light pump-infrared probe techniques, could be performed to gain deeper insight into this process.

The XPS shake-up band observed in [ReCl(CO)$_3$(UCN)] (Figure 2.18) provides evidence of the existence of a state approximately 370 nm (3.35 eV) higher in energy than the ground state. This state is distinct and positioned within the conduction band and may be a π* state localised in space on the heptazine moiety coordinated to the rhenium (red, Figure 2.31). The transition occurring during the shake-up peak may be the [ReCl(CO)$_3$(UCN)] equivalent to the HOMO-LUMO (i.e. d-π*) transition in [ReCl(CO)$_3$(DMNA)].

The localised π* orbitals are not observed in absorption spectroscopy as the signal at 370 nm (shown in blue on Figure 2.31) would overlap with the absorption due to the band gap of the carbon nitride. It is also likely that an electron promoted to the π* orbital would quickly decay in energy within the conduction band continuum (orange arrow), and the resulting emission from the excited state would be identical to the MLCT state formed upon absorption at wavelengths above 400 nm. The excited π* state may also decay directly via charge transfer to the valence band, however this process would likely overlap with the 'band gap' emission also exhibited by [ReCl(CO)$_3$(UCN)].

The π* state is visible only in the XPS spectrum because of a specific interaction between the heavy rhenium atom and the high energy electron emitted in the XPS experiment. However, it is possible that ultrafast spectroscopic methods may also be able to discern this transition, and further experiments could confirm or deny the interpretation shown in Figure 2.31.

Figure 2.31 is consistent will all observations to date and provides insight into the interaction between carbon nitride and the metal fragment. Whilst the heptazine moieties comprising carbon nitride can individually act as ligands, the interaction between directly coordinated metal complex fragments and carbon nitride appear more complex compared to adsorbed metal complexes. XPS and optical spectroscopy hints that distinct orbitals are formed within the energy band structure of the carbon nitride as a result of metal coordination, and it is hypothesised that these orbitals are localised both on the metal atoms and the coordinating heptazine moieties.

2.9 Conclusions

Two materials, UCN and CCN, have been synthesised and compared. For the first time, UCN was decorated directly with a metal carbonyl fragment, characterised by various spectroscopic techniques and compared to a molecular analogue of the heptazine unit. Initial ICP-MS experiments showed loading of 0.395 mmol g^{-1} of rhenium and 0.242 mmol g^{-1} of manganese, although the manganese carbonyl species was seen to decompose on the surface of carbon nitride.

Although a simplistic model, DMNA was used to determine the most stable coordination mode likely to be observed on carbon nitride. A combination of crystal structures of molecular analogues with measurements by infrared spectroscopy provides evidence that the heptazine monomer within carbon nitride can act as a weak, 4-electron σ-donor ligand showing bidentate coordination to rhenium, comparable to bpy. The composite material is relatively stable in non-coordinating solvents but the metal-carbon nitride interaction breaks down in coordinating solvents over several hours. This leaching of metal into solution limits the application of $[ReCl(CO)_3(UCN)]$, because relevant catalysis of rhenium carbonyl complexes is generally performed in acetonitrile.

Preliminary photophysical experiments have shown tentative insight into the effects of the coordination on the bulk semiconductor, suggesting that low-lying d-orbitals within the band gap increase light absorption of the bulk material. This chapter provides a basis for the further exploration of utilising carbon nitride as a ligand, which will be covered in later chapters.

3 Ruthenium Decorated Carbon Nitride: Synthesis, Characterisation and Photophysics

3.1 Introduction

Carbon nitride is an established photocatalyst, but its band gap of 2.7 eV is too large to mediate visible light activated processes.[7, 10, 39, 126, 135] The band gap corresponds to an absorption wavelength of 400 nm, and though this can be tuned slightly by altering the structure of the material, the majority of photocatalytic activity is due to high-energy visible light.[12, 32] Combining molecular dyes capable of absorbing lower-energy visible light with carbon nitride has been shown to enhance the photoactivity of the composite material.[94, 182] However, the poor stability of organic dyes often leads to loss of this activity via dye decomposition during catalysis.[183]

Metal diimine complexes, especially the metal complex ion $[Ru(bpy)_3]^{2+}$ (bpy = 2,2'-bipyridine) have been long known for their photochemical properties.[184] Upon efficient absorption of a visible light photon, an electron is transferred from the ruthenium-based t_{2g} orbitals to the π^* orbitals localised on the bpy ligands.[185, 186] A triplet excited state, $[Ru(bpy)_3]^{2+*}$, is then formed with a lifetime on the hundreds of nanoseconds timescale.[153]

In the absence of quenching species, the excited state can decay radiatively, emitting a visible light photon. However, the excited state of $[Ru(bpy)_3]^{2+*}$ can also react with several species to quench the excited state either reductively or oxidatively.[184] The reduction and oxidation potentials under illumination have been exploited in several different applications, including sensors, luminescent devices and photocatalysis.[187-193]

Significant interest in the interaction between molecular dyes and semiconductors is applied to the field of dye-sensitized solar cells (DSSCs).[79] DSSCs commonly function by combining metal oxide semiconductors with derivatives of $[Ru(bpy)_2(L)_2]^{2+}$ functionalised with carboxylic acid or phosphonic acid groups.[158, 194] Adjustments to the ligand anchoring group can have effects on electron transfer rate and therefore material stability and activity.[195] This is because the excited state formed on the ruthenium tris-diimine moiety is transferred to the semiconductor via the ligand anchoring group in the outer sphere of the metal complex.

Figure 3.1 is an energy diagram constructed using the measured reduction potentials of the HOMO and LUMO of $[Ru(bpy)_3]^{2+}$ (1.29 and -1.33 V respectively) and the valence and conduction bands of carbon nitride (-1.15 and 1.55 V) in aqueous conditions at neutral pH.[196, 197] It can be anticipated that an electron in a Ru t_{2g} orbital could be excited by a photon of visible light into the π* orbital on the bpy ligands prior to transfer of this excited electron into the valence band of the carbon nitride. However, the direction of electron transfer will vary heavily on the relative energy levels of the π* orbital on the bpy ligands compared to the valence band of the carbon nitride, which in turn can be tuned by (among several other significant factors) altering the ligands coordinated to the ruthenium.[197]

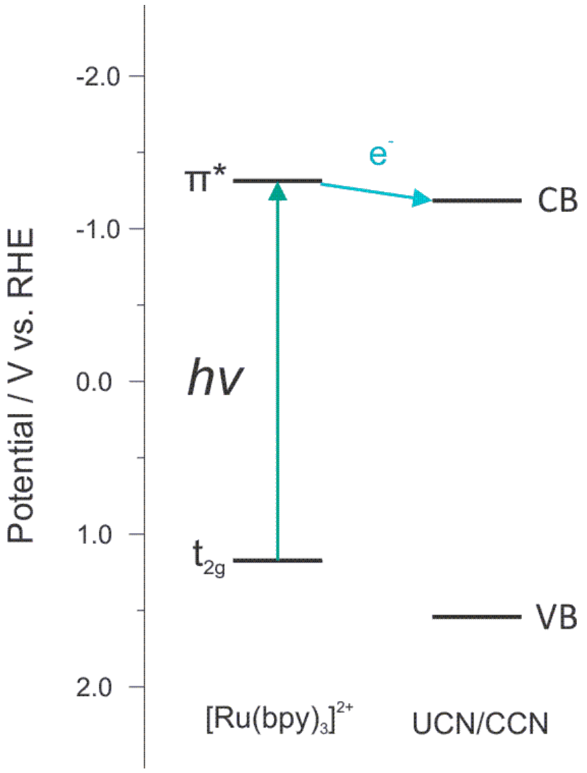

Figure 3.1: Measured reduction potentials of [Ru(bpy)$_3$]$^{2+}$ compared to measured band positions carbon nitride (UCN/CCN)

There are a small number of examples where carbon nitride has been modified by derivatives of [Ru(bpy)$_3$]$^{2+}$ in order to improve photocatalytic activity of the material.[45, 82, 92, 118] However, in these examples, the [Ru(bpy)$_3$]$^{2+}$ derivative is placed between a catalytic site and the carbon nitride, behaving as an electron mediator where the electron transfer from catalytic site to semiconductor can be accelerated upon visible light irradiation (see Chapter 1).[90] Electron transfer to the [Ru(bpy)$_3$]$^{2+}$ derivative improves the catalytic properties of the composite material by reducing recombination. In this case electron transfer occurs in the opposite direction to that shown in Figure 3.1, however it should be noted that this is caused by oxidation of the ruthenium dye component by a covalently attached catalytic centre during the reaction.

There is only one example at the time of writing, which was published during this work, which claims to have directly coordinated a metal complex to carbon nitride to improve the visible light photocatalysis.[96] Scheme 3.1 shows how a heteroleptic iridium complex (Ir-T) was grafted directly to the surface of mesoporous, surface hydroxide modified carbon nitride (npg-C_3N_4-OH). The resulting material, referred to as ‘npg-C_3N_4-Ir-T’ showed a marked decrease in band gap (2.40 eV for npg-C3N4-OH compared to 2.24 eV for npg-C_3N_4-Ir-T) and orders of magnitude of improvement in the rate of CO_2 reduction to methanol.

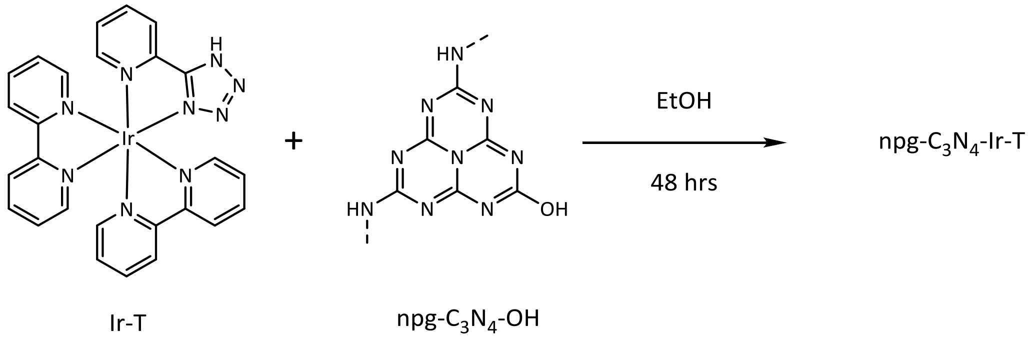

Scheme 3.1: Decoration of carbon nitride with a heteroleptic light-absorbing iridium complex

However, in the case of npg-C_3N_4-Ir-T, only ICP-MS, XPS, PXRD, TEM and EDX were reported for the composite material, making it difficult to know the exact species and environment of the iridium content.[96] Ideally, spectroscopy which can be targeted at characterising the metal environment (i.e. NMR, IR) would be performed in order to gain an understanding of both the carbon nitride-metal complex interaction, and the mechanism by which any change in the properties takes place.

3.1.1 Aims

Following the coordination between [ReCl(CO)$_3$] and carbon nitride analogous to a diimine, the coordination of [Ru(bpy)$_2$]$^{2+}$ moiety to carbon nitride was investigated to give a composite material comprising two photoactive units. Following the previous chapter, a molecular analogue of the composite, [Ru(bpy)$_2$(DMNA)](PF$_6$)$_2$, was also synthesised to aid characterisation.

Previous independent application of carbon nitride and [Ru(bpy)$_3$]$^{2+}$ to solar energy conversion and photocatalysis, and more recent examples of systems incorporating mixtures of carbon nitride and [Ru(bpy)$_3$]$^{2+}$ derivatives, provided motivation to explore direct coordination of ruthenium to carbon nitride and the photophysical processes of the resulting composite. It may be anticipated that direct coordination may increase the rate of electron transfer between carbon nitride and [Ru(bpy)$_2$]$^{2+}$ moieties, reducing the rate of recombination helping to drive complimentary photocatalytic processes occurring on carbon nitride of [Ru(bpy)$_2$]$^{2+}$.

3.2 Synthesis of UCN and CCN

UCN and CCN were synthesised and compared as previously described in Chapter 2. Although the synthesis of CCN is more time consuming, decorating both UCN and CCN with ruthenium is desirable when the higher photocatalytic activity of CCN is considered along with the aim of increasing the efficiency of photocatalysis. Decorating two different morphologies of carbon nitride would also provide insight as to how altering the macrostructure of the carbon nitride affects the metal-carbon nitride coordination and consequently the overall properties of the material.

3.3 Synthesis of $[Ru(bpy)_2(CCN)](PF_6)_2$ and $[Ru(bpy)_2(UCN)](PF_6)_2$

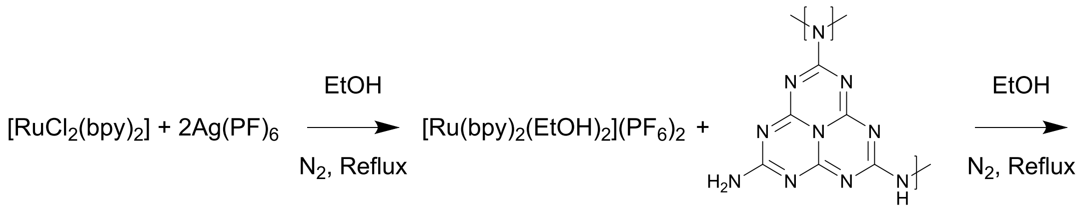

Scheme 3.2: Synthesis of $[Ru(bpy)_2(CCN)](PF_6)_2$/$[Ru(bpy)_2(UCN)](PF_6)_2$

Commercially available $[RuCl_2(bpy)_2]$ was used as the ruthenium precursor for the synthesis of ruthenium decorated carbon nitrides. Initial reactions were performed by heating a solution of $[RuCl_2(bpy)_2]$ with samples of carbon nitride at reflux. No significant change in the spectroscopy of the carbon nitrides was observed which was attributed to chloride ligands preventing ligand substitution.

Therefore, $[RuCl_2(bpy)_2]$ was first reacted with two equivalents of $Ag(PF_6)$ under nitrogen in order to remove the chloride ligands via precipitation of AgCl. To avoid complications with the separation of the AgCl precipitate from carbon nitrides, the red, ruthenium-containing solution was separated from the AgCl by filtration directly onto a sample of base-treated carbon nitride under an atmosphere of nitrogen (Scheme 3.2).

The reaction mixture was then heated to reflux under nitrogen and the progress of the reaction was monitored by measuring the visible-light absorption spectrum of an aliquot of filtered solution at selected time intervals. The absorption band with max. absorbance at 500 nm was monitored and plotted against time (Figure 3.2). The decrease in the intensity of this band was assumed to reflect the ruthenium coordination to carbon nitride. Whereas ruthenium coordination was seen to be approximately complete within 24 hours for UCN, coordination to CCN was seen to continue for a week before the reaction was stopped. The material was isolated by filtration and washed with excess water and ethanol to remove uncoordinated ruthenium species.

The difference in depletion of the ruthenium from solution is reflected in the final metal content of the two materials as determined by ICP-MS (Table 3.1), with a much higher loading observed for [Ru(bpy)$_2$(CCN)](PF$_6$)$_2$ compared to [Ru(bpy)$_2$(UCN)](PF$_6$)$_2$.

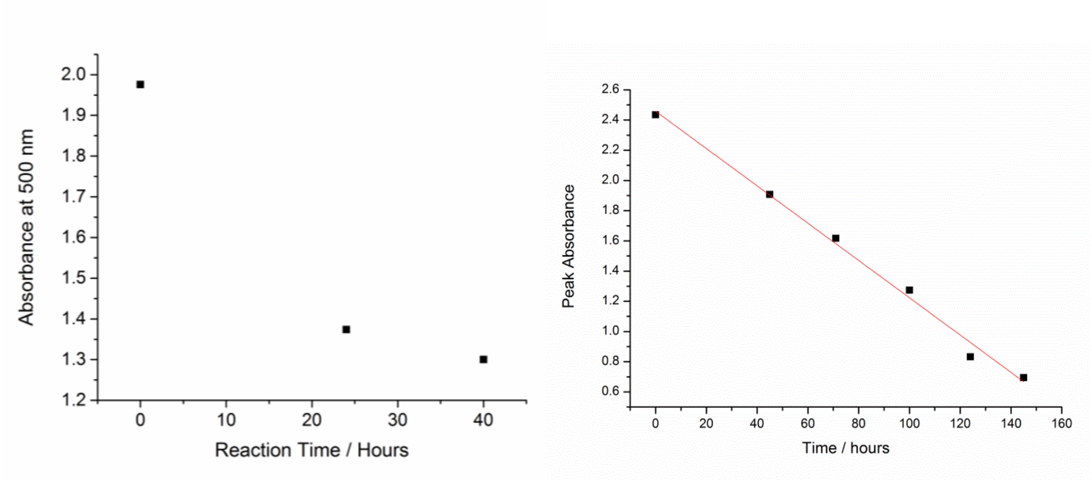

Figure 3.2: Change in solution absorbance at 500 nm of an ethanol solution of [Ru(bpy)$_2$]$^{2+}$ heated at reflux with UCN (left) and CCN (right)

3.4 Bulk Characterisation of Ruthenium-Decorated Carbon Nitrides

3.4.1 Elemental Analysis (ICP-MS)

The ruthenium loading of CCN and UCN was measured by inductively-coupled plasma mass spectrometry (ICP-MS) analysis after digestion of the samples in nitric acid (Table 3.1). In accordance with the results obtained by visible light absorption spectroscopy, the ruthenium content of [Ru(bpy)$_2$(**C**CN)](PF$_6$)$_2$ is approximately five times higher than that of [Ru(bpy)$_2$(UCN)](PF$_6$)$_2$. This increased loading of CCN implies that there are more edge-sites available compared to UCN, which is corroborated by the respective elemental composition of UCN and CCN (see Chapter 2).

Table 3.1: Ruthenium loading on $[Ru(bpy)_2(UCN)](PF_6)_2$ and $[Ru(bpy)_2(CCN)](PF_6)_2$ as measured by ICP-MS

Material	Ru Loading/ mg g^{-1}	Ru Loading/ mmol g^{-1}
$[Ru(bpy)_2(UCN)](PF_6)_2$	1.64	0.016
$[Ru(bpy)_2(CCN)](PF_6)_2$	7.77	0.076

3.4.2 Powder X-Ray Diffraction (PXRD)

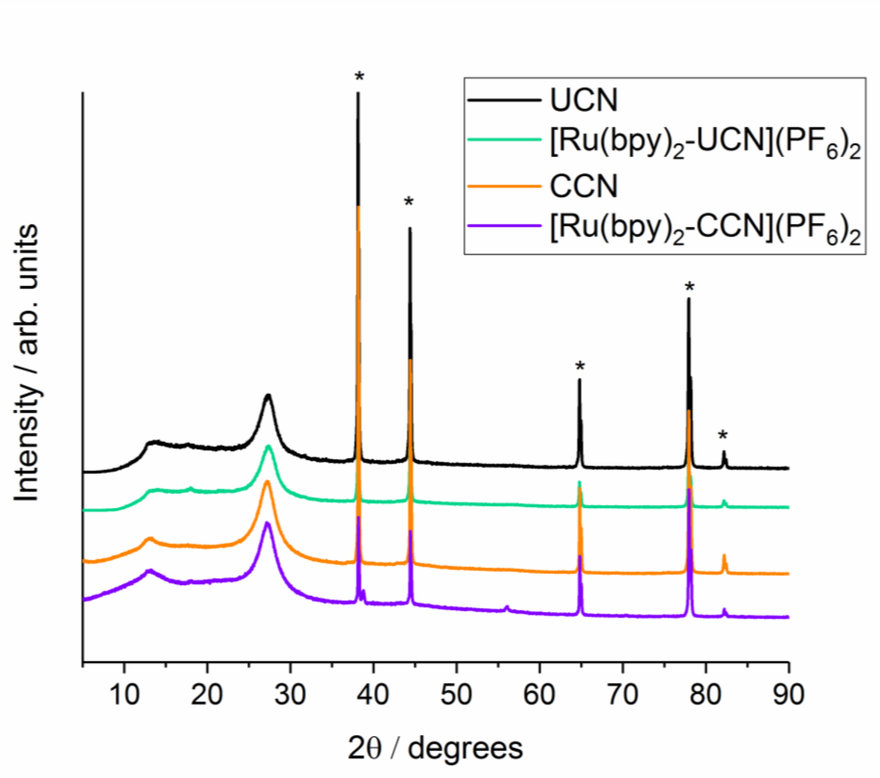

Figure 3.3: Powder X-Ray diffractograms of ruthenium-decorated carbon nitrides. Resonances marked with an asterisk (*) arise from the aluminium sample holder.

Figure 3.3 shows the PXRD diffractograms of decorated and undecorated carbon nitrides. The five sharp peaks observed in all samples arise from the aluminium holder used during data collection. The intensity of the broad feature at 13.2° is more distinct in CCN than in UCN, and is proposed to relate to an in-plane feature, likely the spacing between the 'gaps' between heptazine moieties.[8, 137] The increased sharpness of this peak in CCN is consistent with a more condensed, crystalline microstructure.

All four materials show a broad resonance at 27.4°, corresponding to the interplanar distance between the sheets of carbon nitride.[136] The consistency across decorated and undecorated samples in the interlayer spacing suggests that ruthenium is not intercalating between the carbon nitride layers. In addition, no significant resonances are observed that suggest other crystalline impurities.

3.4.3 Scanning Electron Microscopy (SEM)

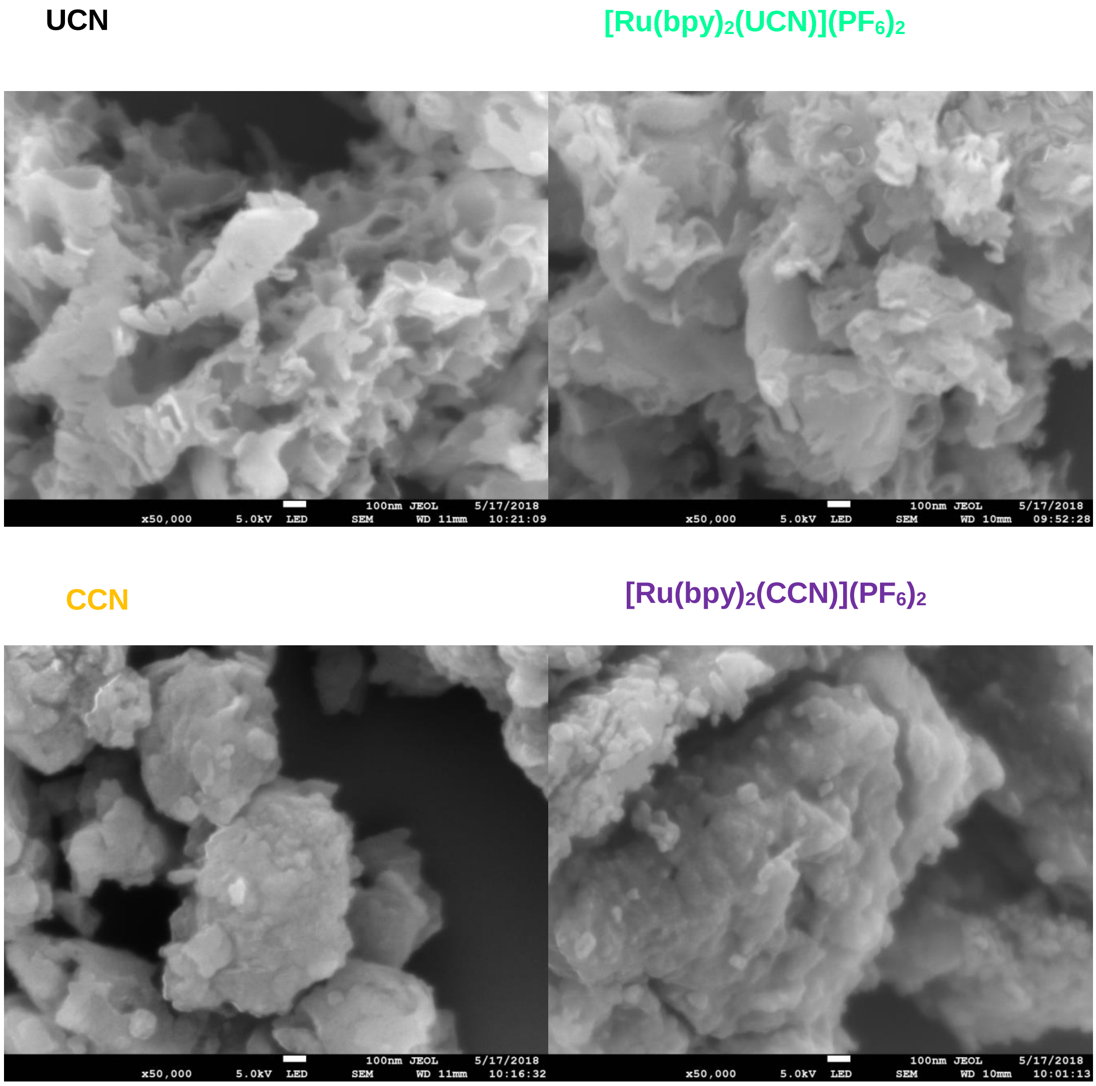
UCN

$[Ru(bpy)_2(UCN)](PF_6)_2$

CCN

$[Ru(bpy)_2(CCN)](PF_6)_2$

Figure 3.4: SEM images (x50000 magnification, scale bar = 100 nm) of UCN, CCN, $[Ru(bpy)_2(UCN)](PF_6)_2$ and $[Ru(bpy)_2(CCN)](PF_6)_2$

SEM was performed on all samples to gain insight into their morphology. Representative images (x50000 magnification) are shown in Figure 3.4. As discussed in Chapter 2, UCN has a highly amorphous morphology resulting from the uncontrolled synthetic method. In contrast, CCN appears more condensed, as reflected in both the DRS (Figure 3.6) and the PXRD data (Figure 3.3). Ruthenium treatment does not result in significant changes to the morphology of either material as visible by SEM, and no evidence of aggregates of ruthenium on the surface of UCN or CCN is observed.

3.4.4 Brunauer-Emmett-Teller (BET) Analysis

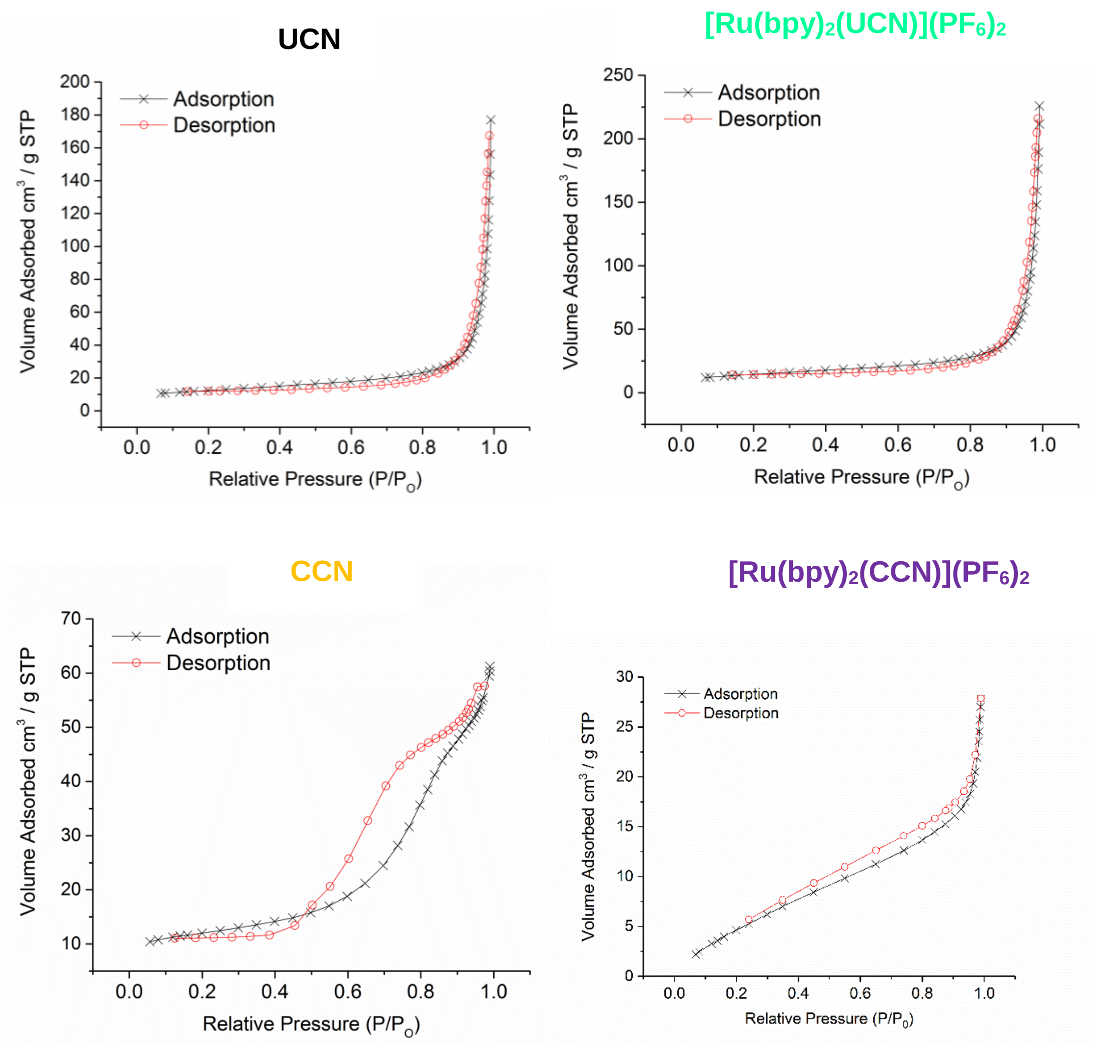

Figure 3.5: N_2 adsorption isotherms of UCN, CCN, $[Ru(bpy)_2(UCN)](PF_6)_2$ and $[Ru(bpy)_2(CCN)](PF_6)_2$

Nitrogen adsorption isotherms (Figure 2.6) were taken of each decorated and undecorated sample in order to measure their surface areas (listed in Table 2.2) according to Brunauer-Emmett-Teller (BET) theory. The surface area of the two undecorated samples of carbon nitride is similar, with both at around 40 m^2 g^{-1}. However, whilst the isotherm of UCN follows the expected shape for monolayer gas adsorption onto a non-porous solid, the Type V hysteresis observed during the desorption from CCN is indicative of gas retention by micropores within the material structure.

The surface area of $[Ru(bpy)_2(UCN)](PF_6)_2$ is higher than that of undecorated UCN, likely a result of the long period of time during which stirring the carbon nitride is subjected to stirring, leading to the grinding of the carbon nitride. In contrast, the $[Ru(bpy)_2(CCN)](PF_6)_2$ shows a decrease in the surface area compared to CCN. This is likely a result of the ruthenium moieties blocking the micropores, thereby decreasing the effective surface area.

Table 3.2: Brunauer-Emmett-Teller (BET) surface area values calculated from nitrogen isotherm (Figure 1.5

Sample	BET Surface Area /m^2 g^{-1}
UCN	42.4 ± 0.4
$[Ru(bpy)_2(UCN)](PF_6)_2$	50.5 ± 0.5
CCN	40.5 ± 0.7
$[Ru(bpy)_2(CCN)](PF_6)_2$	24.5 ± 0.2

3.4.5 Dynamic Light Scattering (DLS) and Zeta-Potential Measurements

Dynamic light scattering experiments were performed on undecorated and ruthenium-decorated samples of carbon nitrides. Average particle sizes were highly polydisperse in addition to being very large, making interpretation of each value in isolation difficult. However, there are two significant observations.

The first is the increased particle size observed for samples based on CCN. Correlating well with BET and SEM data, the CCN appears to form larger, more condensed particles in suspension. In addition, treating each sample with ruthenium results in a decrease of the average size, likely due to the extended period of ‘grinding’ the stirred suspension during metal decoration.

Table 3.3: Average particle diameter and particle surface charge

Sample	Average Diameter / nm	Zeta-Potential / mV
UCN	629.0 ± 14.7	-33.3 ± 0.5
$[Ru(bpy)_2(UCN)](PF_6)_2$	530.7 ± 6.13	25.1 ± 0.6
CCN	848.8 ± 96.1	-29.0 ± 1.4
$[Ru(bpy)_2(CCN)](PF_6)_2$	761 ± 21.7	12.2 ± 0.4

By performing DLS experiments on a suspension under the effects of an electric field, the zeta-potential, or electrokinetic potential, can be measured. The absolute values of the undecorated carbon nitride samples are as expected for samples of carbon nitride at pH = 7.[40, 198] Of more interest is the observation of a significantly more positive zeta potential after metal coordination, suggesting that a positively charged species (i.e. Ru^{2+}) has been grafted to the surface of the particle. The lower zeta potential of $[Ru(bpy)_2($**C**CN$)](PF_6)_2$ compared to $[Ru(bpy)_2(UCN)](PF_6)_2$ is again suggestive of ruthenium being incorporated into the pores of CCN, distributing the charge more evenly through each particle, and therefore being less localised to the surface.

3.4.6 Diffuse Reflectance Spectroscopy (DRS)

The DRS spectra of undecorated and ruthenium-decorated carbon nitrides are shown in Figure 3.6. A clear difference in the absorption profile of UCN and CCN is observed, as CCN is shown to absorb significantly more light at wavelengths above 400 nm. This is due to the more condensed nature of the CCN compared to the UCN resulting in lower-energy transitions between more condensed π-stacked heptazine moieties.[12, 32]

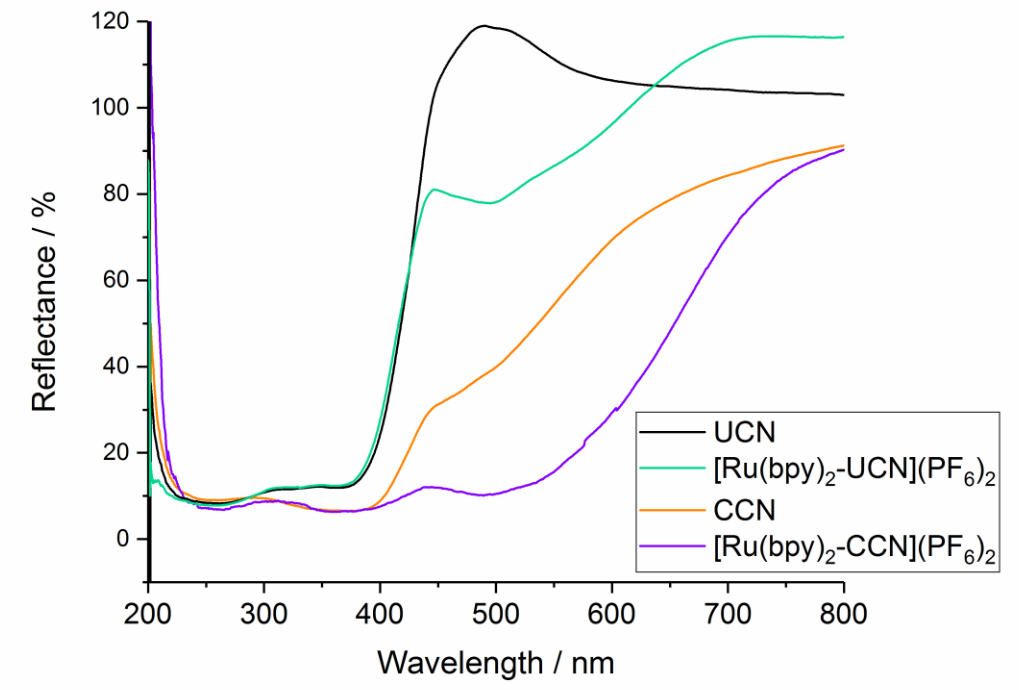

Figure 3.6 Diffuse reflectance spectroscopy of ruthenium decorated and undecorated carbon nitrides

After ruthenium decoration, both materials show a very clear colour change. UCN changes from yellow to pink, whilst CCN changes from orange to dark red. The latter is indicated by the DRS as the appearance of a strong, broad absorbance band centred at 500 nm. The broadness of this band extends almost across the entire visible range.

3.5 Local characterisation of ruthenium-decorated carbon nitride

In addition to the bulk properties of metal decorated carbon nitride, NMR and IR spectroscopic methods were used to attempt to gain insight into the coordination environment around the ruthenium centre in both $[Ru(bpy)_2(\mathbf{C}CN)](PF_6)_2$ and $[Ru(bpy)_2(UCN)](PF_6)_2$.

3.5.1 Infra-red spectroscopy of $[Ru(bpy)_2(UCN)](PF_6)_2$ and $[Ru(bpy)_2(CCN)](PF_6)_2$

Figure 3.7 shows the ATR-IR spectra of the undecorated and ruthenium-decorated carbon nitrides. The ATR-IR spectra of UCN and CCN show the same structure, with a sharp band corresponding to the heptazine 'breathing' mode and a broader region corresponding to several C=N bond vibrations.[199] A new band at 844 cm^{-1} , corresponding to the $(PF_6)^-$ anion, is seen in both the decorated materials.[200] In addition, in $[Ru(bpy)_2(\mathbf{C}CN)](PF_6)_2$, where the ruthenium loading is higher, a band at 752 cm^{-1} is observed, corresponding to a 2,2'-bipyridine twisting vibration mode.[201] No vibrational bands are observed at 844 cm^{-1} or 752 cm^{-1} in either of the undecorated materials.

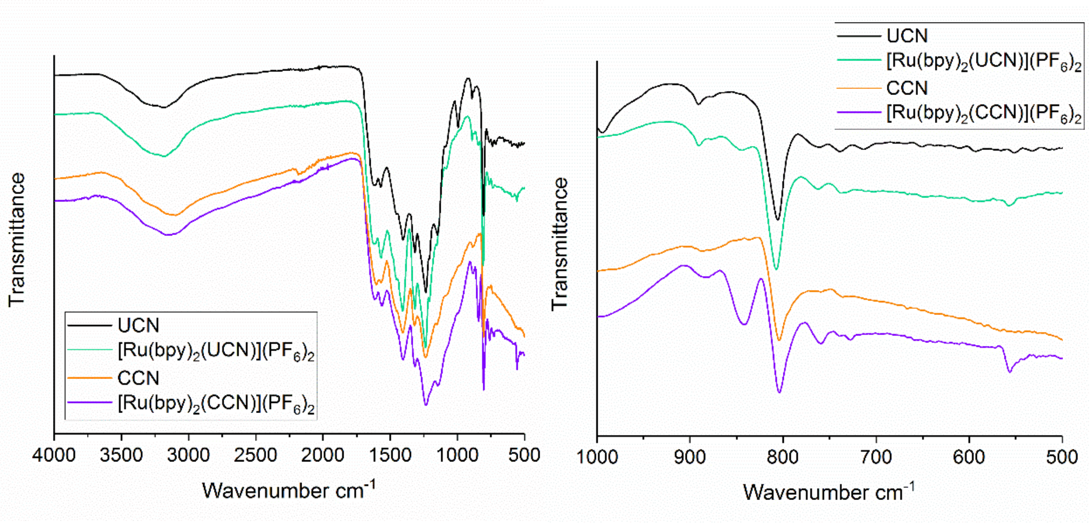

Figure 3.7 IR spectroscopy of ruthenium-decorated and undecorated carbon nitrides

3.5.2 Solid-State NMR Spectroscopy

Figure 3.8 shows the ^{13}C CP-MAS NMR spectra of the ruthenium-decorated and undecorated carbon nitrides. Both undecorated materials show resonances at 164.6 and 156.7 ppm, both indicative of the heptazine moiety of carbon nitride.[7] Although CCN and UCN show different morphology by SEM and XRD, the ATR-IR and CP-MAS NMR experiments suggest that the local structure within the sheets of carbon nitride is the same, with the changes in properties of the two materials arising from differences on a larger scale. This is expected from previous observations in the literature.[7, 8, 202] The weak peaks at around 60 and 260 ppm are spinning side-bands.

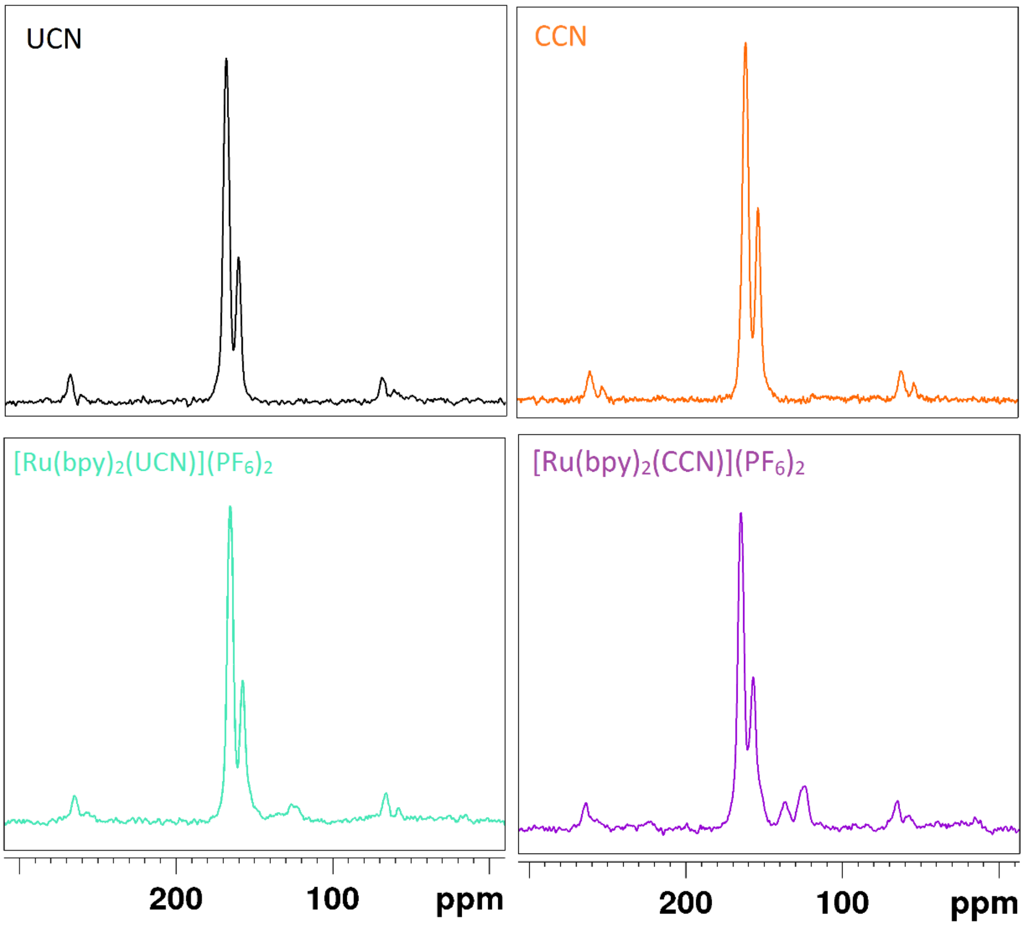

Figure 3.8: ^{13}C CP-MAS spectrum of ruthenium-decorated carbon nitrides (spin rate 10 kHz)

The solution ^{13}C NMR spectrum of $[Ru(bpy)_3]Cl_2$ shows resonances at 156.7, 123.6, 137.2, 126.7 and 151.1 ppm.[203] In addition to the resonances arising from carbon nitride, the ruthenium-decorated materials show resonances at 136.0 ppm and 123.6 ppm in the CP-MAS ^{13}C NMR spectrum. The solid-state nature of these experiments causes broadening which is observed, and the peak at 123.6 ppm has a high intensity likely due to the overlap of two ^{13}C NMR signals. The remaining two resonances expected from the 2,2'-bipyridine ligands are not seen as they overlap with the intense bands associated with the carbon nitride. As reflected in the ICP-MS results (Table 3.1) the bipyridine signals are significantly less intense in $[Ru(bpy)_2(UCN)](PF_6)_2$ compared to $[Ru(bpy)_2($**C**$CN)](PF_6)_2$.

3.5.3 X-ray Photoelectron Spectroscopy (XPS) of $[Ru(bpy)_2(UCN)](PF_6)_2$ and $[Ru(bpy)_2(CCN)](PF_6)_2$

The XPS spectra of $[Ru(bpy)_2(UCN)](PF_6)_2$ and $[Ru(bpy)_2(CCN)](PF_6)_2$ were measured and key regions are shown in Figure 3.9, Figure 3.10, and

Figure 3.11. The data is summarised in Table 3.4 and Table 3.5. The XPS data of UCN and CCN is also shown to demonstrate the differences not only between each ruthenium-decorated material, but also between the decorated and undecorated materials.

The Ru 3d-C 1s region of $[Ru(bpy)_2(UCN)](PF_6)_2$ compared to UCN is shown in Figure 3.9. The spectrum of $[Ru(bpy)_2(UCN)](PF_6)_2$ in this region is complicated by the overlap of the C 1s and Ru 3d regions. The Ru 3d bands are observed at 281.1 eV and 285.2 eV, consistent with a single molecular ruthenium-bipyridine species grafted onto a solid surface.[80, 193] The C 1s regions of both $[Ru(bpy)_2(UCN)](PF_6)_2$ and $[Ru(bpy)_2(CCN)](PF_6)_2$ are fitted with an additional feature centred at 286.1 eV, corresponding to the C=C environments in the bipyridine ligands.[193]

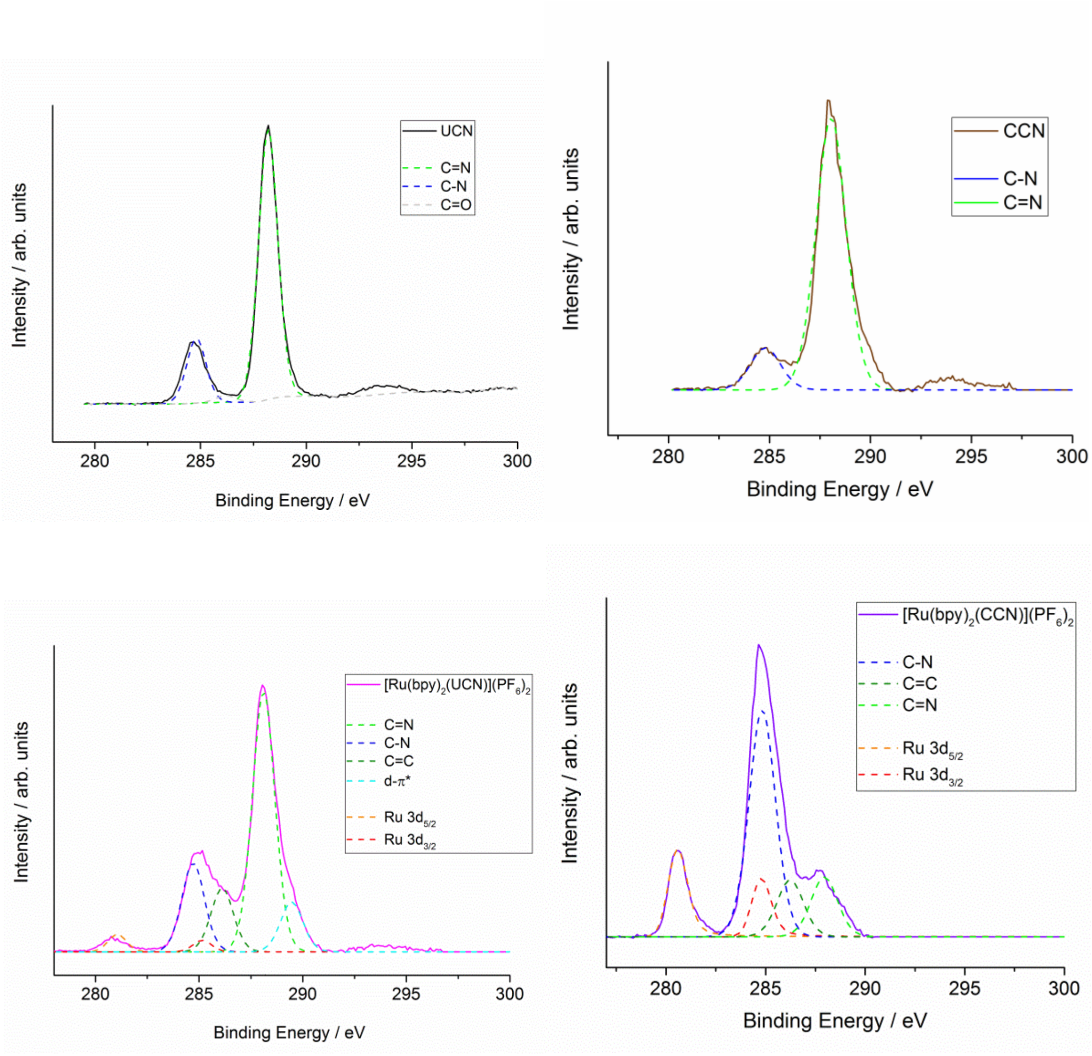

Figure 3.9: XPS spectra of UCN, CCN, [Ru(bpy)$_2$(UCN)](PF$_6$)$_2$ and [Ru(bpy)$_2$(CCN)](PF$_6$)$_2$ (Ru 3d-C 1s region)

The main C 1s peak, fitted at 288.1 eV, shows a shoulder fitted at 289.5 eV in [Ru(bpy)$_2$(UCN)](PF$_6$)$_2$ which is absent in UCN. It is suggested that this is a shake-up peak, comparable to that seen in Re-UCN. This shake-up peak may arise from energy transfer from a liberated photoelectron and a ruthenium atom, promoting an electron from ruthenium d-orbitals to some higher energy state. It is labelled as a d-π* transition.

The XPS of [Ru(bpy)$_2$(UCN)](PF$_6$)$_2$ shows several marked differences to [Ru(bpy)$_2$(CCN)](PF$_6$)$_2$. Corresponding to previous ICP-MS and ^{13}C CP-MAS NMR measurements, the intensity of the ruthenium signals as well as the C=C and C-N signals associated with the 2,2'bipyridine, is much higher in [Ru(bpy)$_2$(CCN)](PF$_6$)$_2$. The positions of the fitted peaks are not significantly shifted, indicating that the ruthenium environment is the same in each decorated material. The d-π* shake-up signal is not observed in $[Ru(bpy)_2(CCN)](PF_6)_2$, which may be the result of no transitions occurring. The d-π* state may be formed, however observation is more challenging due to the weaker relative intensity and the increased FWHM (broadening) of the C=N peak in $[Ru(bpy)_2(CCN)](PF_6)_2$,

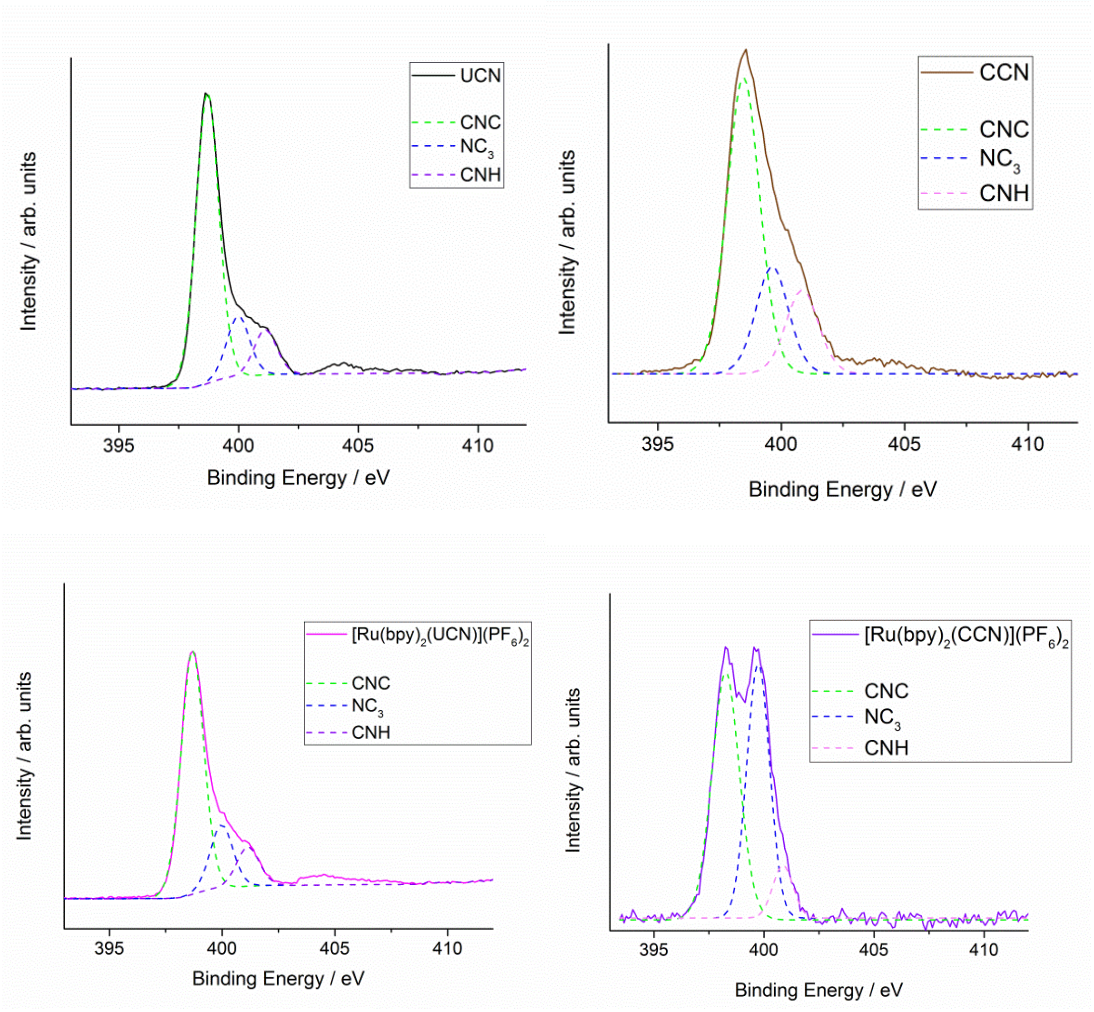

Figure 3.10: XPS spectra of $[Ru(bpy)_2(UCN)](PF_6)_2$ and $[Ru(bpy)_2(CCN)](PF_6)_2$ (N 1s region)

In contrast to the Ru 3d-C 1s region, the N 1s region (Figure 3.10) looks very similar between UCN and $[Ru(bpy)_2(UCN)](PF_6)_2$. However, the ratio between the peak heights in the N 1s spectrum vary, indicating a higher presence of imine-type nitrogen environments (associated with the 2-2'-bipyridine ligands) in $[Ru(bpy)_2(UCN)](PF_6)_2$. The difference between CCN and $[Ru(bpy)_2(CCN)](PF_6)_2$ is more considerable, again due to the increased concentration of 2,2'-bipyridine on the material surface.

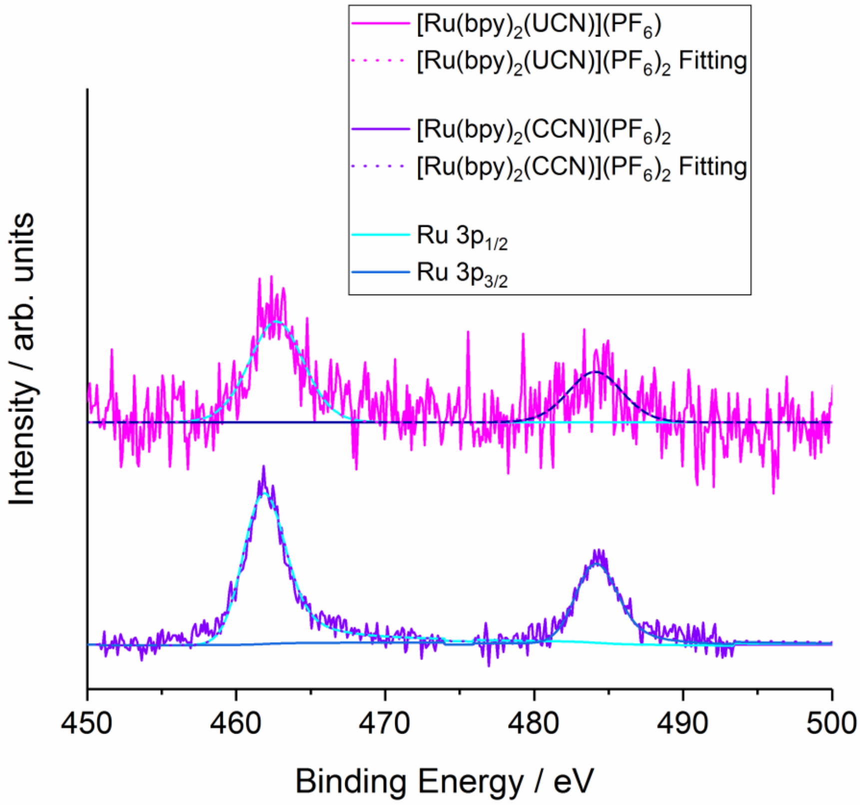

Figure 3.11: XPS spectrum of [Ru(bpy)$_2$(UCN)](PF$_6$)$_2$ (Ru 3p region)

Due to the overlap of the Ru 3d and C 1s regions, the Ru 3p region was also analysed in each material (Figure 3.11). Due to the low concentration of ruthenium coupled with the lower population of the Ru 3p region compared to the 3d, the resulting specta are of relatively signal-to-noise ratio. Two peaks are fitted for each material, at 462.7 and 484.1 eV for [Ru(bpy)$_2$(CCN)](PF$_6$)$_2$, and 462.0 and 484.2 eV for [Ru(bpy)$_2$(CCN)](PF$_6$)$_2$. These peaks corresponds to non-metallic ruthenium, but little confidence can be placed in this region of the spectrum due to the low signal-to-noise ratio and the high broadness of each peak.[204] The Ru 3d signals can be considered to be more reliable.

Table 3.4:Summary of XPS Data for UCN and CCN

Sample	UCN		CCN		Assignment
Region	Peak / eV	FWHM / eV	Peak / eV	FWHM / eV	
N 1s	398.7	1.14	398.5	1.57	CNC
	400.0	1.29	399.6	1.58	NC_3
	401.1	1.46	400.8	1.58	CNH
C 1s	288.2	1.11	288.0	1.79	C=N
	286.1	1.03	-	-	C=O
	284.8	1.07	284.8	1.79	C-NH

Table 3.5: Summary of XPS Data for $[Ru(bpy)_2(UCN)](PF_6)_2$ and $[Ru(bpy)_2(UCN)](PF_6)_2$

Sample	$[Ru(bpy)_2(UCN)](PF_6)_2$		$[Ru(bpy)_2(CCN)](PF_6)_2$		Assignment
Region	Peak / eV	FWHM	Peak / eV	FWHM	
N 1s	398.7	1.21	398.3	1.49	CNC
	400.0	1.30	399.7	1.23	NC_3
	401.1	1.46	400.9	1.08	CNH
C 1s	289.5	1.30	-	-	d-π*
	288.1	1.30	287.9	1.60	C=N
	286.1	1.30	286.2	1.60	C=C
	284.7	1.30	284.8	1.30	C-N
Ru 3d	281.1	1.06	280.6	1.19	Ru $3d_{5/2}$
	285.2	1.06	284.8	1.19	Ru $3d_{3/2}$
Ru 3p	462.7	4.36	462.0	3.65	Ru $3p_{1/2}$
	484.1	4.36	484.2	3.49	Ru $3p_{3/2}$

3.6 Synthesis and Structure of $[Ru(bpy)_2(DMNA\text{-}\kappa^2 N, N')](PF_6)_2$

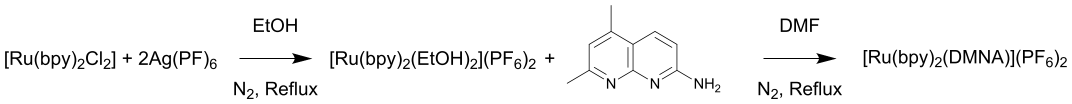

Scheme 3.3: Synthesis of $[Ru(bpy)_2(DMNA\text{-}\kappa^2N, N')](PF_6)_2$

In order to gain further insight into the coordination to carbon nitride, a molecular analogue, 5,7-dimethyl-1,8-naphthyridine-2-amine (DMNA) was used to simulate the coordination environment on carbon nitride whilst allowing for additional characterisation. $Ru(bpy)_2(DMNA)](PF_6)_2$ was synthesised analogously to ruthenium-decorated carbon nitrides (Scheme 3.3), fully characterised by NMR, MS and CHN analysis, and single crystals were grown by vapour diffusion of diethyl ether into a solution of the complex in acetone. The obtained single crystals are triclinic and the structure was solved in the P-1 space group with one complex in the asymmetric unit. No unusual data refinement was carried out.

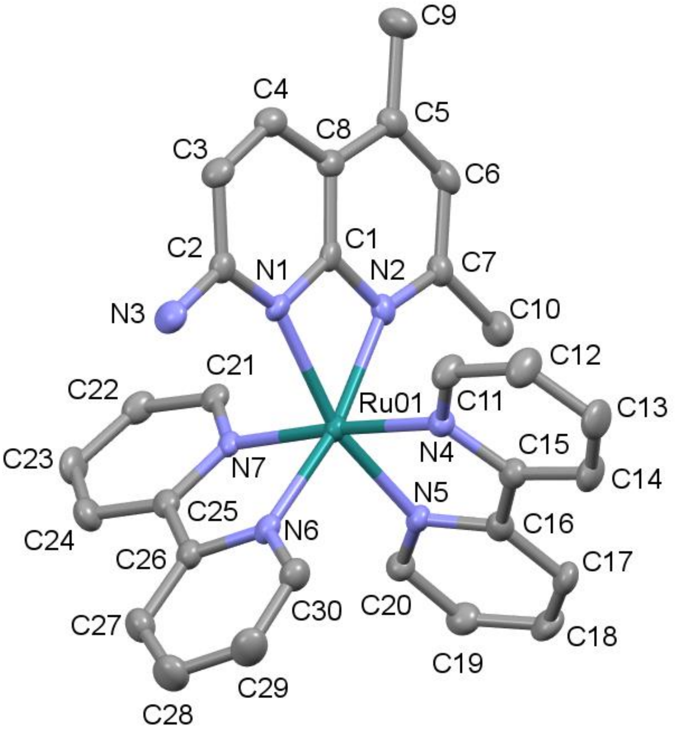

Figure 3.12: X-ray crystal structure of $[Ru(bpy)_2(DMNA\text{-}\kappa^2N, N')](PF_6)_2$ with hydrogens and counterions omitted for clarity, probability ellipsoids at the 50% level

The X-ray crystal structure (Figure 3.12) shows a bidentate (κ^2-N,N') coordination mode of the DMNA to the ruthenium centre. Bond lengths and angles are listed in Table 3.6, where they are compared to $[Ru(bpy)_3](PF_6)_2$ and $[Ru(tpy)_2](PF_6)_2$.[205, 206] The comparison is referenced in section 3.9, where luminescent properties of the compounds is discussed.

Table 3.6: Selected distances measured for $[Ru(bpy)_2(DMNA)](PF_6)_2$ compared to $[Ru(bpy)_3]^{2+}$ and $[Ru(tpy)_2]^{2+}$

$[Ru(bpy)_2(DMNA)]^{2+}$	Distance / Å	$[Ru(bpy)_3]^{2+}$	Distance / Å	$[Ru(tpy)_2]^{2+}$	Distance / Å
Ru-N1	2.134(2)	Ru-N1	2.08(1)	Ru-N1	2.082(6)
Ru-N2	2.109(3)	Ru-N2	2.09(1)	Ru-N2	1.949(7)
Ru-N4	2.046(3)	Ru-N3	2.08(1)	Ru-N3	2.047(6)
Ru-N5	2.033(2)	Ru-N4	2.10(1)	Ru-N4	2.052(7)
Ru-N6	2.051(3)	Ru-N5	2.09(1)	Ru-N5	1.955(7)
Ru-N7	2.043(3)	Ru-N6	2.07(1)	Ru-N6	2.063(7)

Table 3.7: Selected angles measured for $[Ru(bpy)_2(DMNA)](PF_6)_2$ compared to $[Ru(bpy)_3]^{2+}$ and $[Ru(tpy)_2]^{2+}$

$[Ru(bpy)_2(DMNA)]^{2+}$	Angle / °	$[Ru(bpy)_3]^{2+}$	Angle / °	$[Ru(tpy)_2]^{2+}$	Angle / °
N1-Ru-N2	63.1(1)	N1-Ru-N2	78.9(6)	N1-Ru-N2	77.6(3)
N4-Ru-N5	78.7(1)	N3-Ru-N4	79.8(5)	N2-Ru-N3	81.1(3)
N5-Ru-N7	79.1(1)	N5-Ru-N6	79.2(6)	N4-Ru-N5	80.6(3)
				N5-Ru-N6	78.4(3)
N1-Ru-N5	163.2(1)	N1-Ru-N4	171.0(6)	N1-Ru-N3	158.7(3)
N2-Ru-N6	168.6(1)	N2-Ru-N5	170.8(6)	N2-Ru-N5	177.9(3)
N4-Ru-N7	175.9(1)	N3-Ru-N6	169.8(6)	N4-Ru-N6	158.9(3)

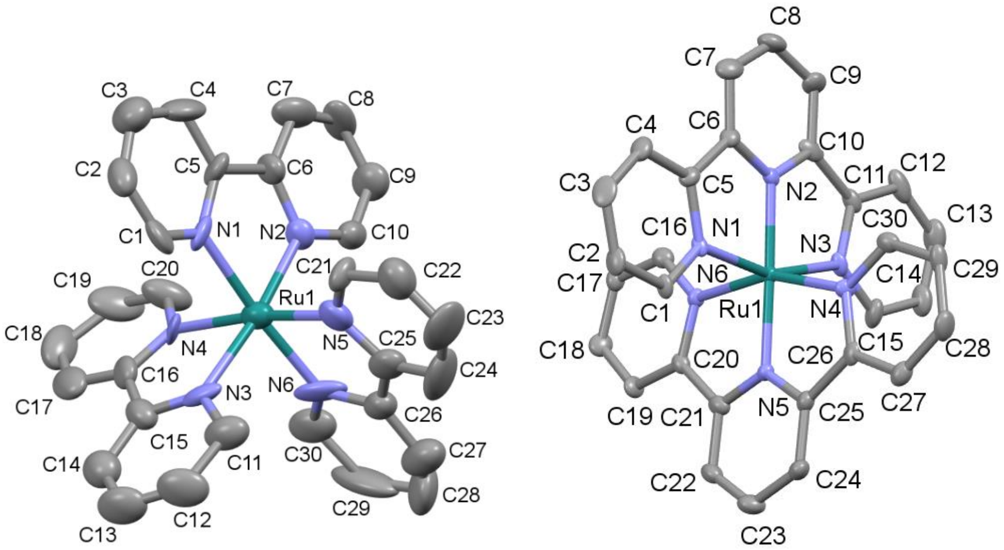

Figure 3.13: X-ray crystal structure of $[Ru(bpy)_3](PF_6)_2$ and $[Ru(tpy)_3](PF_6)_2$ with hydrogens and counterions omitted for clarity, probability ellipsoids at the 50% level[205, 206]

In $[Ru(bpy)_2(DMNA)]^{2+}$, the Ru-N bonds to the DMNA are longer than those to the bpy ligand (2.134(2) Å and 2.051(3) Å respectively), due to the strained coordination of the 1,8-naphthyridine moiety of the DMNA. The average Ru-N distance to bpy ligands in $[Ru(bpy)_2(DMNA)]^{2+}$ (2.043(3) Å) is shorter than that for $[Ru(bpy)_3]^{2+}$ (2.08(1) Å), likely in compensation for the longer bonds to DMNA.[206] The average Ru-N bond distance measured in $[Ru(tpy)_2]^{3+}$ is shorter yet (2.025(6) Å), due to the relative rigidity of the coordinated tpy unit.

The 'bite angle' of DMNA (63.1(1)°) is smaller than that of bpy (78.9(6)°). The bite angle of the bpy ligand is not seen to change significantly between metal complexes, and there is no significant difference between the bite angles of bpy (78.9(6)°) and tpy (80.6(3)°).

Ideally, each imine ligand would be positioned exactly 180° from the ligand trans to it. This is not seen in any of the three complexes, however the least deviation from this ideal geometry is seen in $[Ru(bpy)_3]^{2+}$, with an average trans-angle of 170.5(6)°. The closest trans-angle to 180° is observed for $[Ru(tpy)_2]^{2+}$, with N2-Ru-N5 at 177.9(3)°. However, the remaining four ligands are over 21° out of ideal alignment with the ligand *trans* to them, resulting in an average trans angle of 165.1(3)° for $[Ru(tpy)_3]^{2+}$. The distortion seen in $[Ru(bpy)_2(DMNA)]^{2+}$ is partway between the other two examples due to the asymmetry caused by the DMNA ligand, with an average trans angle of 169.2(1)°.

Table 3.8: Selected distances and angles in the DMNA ligand showing distortion upon ruthenium coordination

Bond Distance / Å	DMNA[148]	$[Ru(bpy)_2(DMNA)](PF_6)_2$
C1-C8	1.424(3)	1.389(5)
N1-N2	2.304(3)	2.220(4)
N3-C2	1.353(5)	1.342(5)
Bond Angle / °		
N1-C1-N2	115.6(2)	108.7(3)
N1-C2-N3	118.7(3)	118.7(3)

As in previous systems, significant distortion is observed in the DMNA ligand after ruthenium coordination (Table 3.8). The C1-C8 and N1-N2 distances are reduced in $[Ru(bpy)_2(DMNA)]^{2+}$ compared to the free ligand as the N1-C1-N2 angle is reduced. Although the C2-N3 distance is also reduced upon ruthenium coordination, unlike in the case of $[MCl(CO)_3(DMNA)]$, there is no observed change in N1-C2-N3 angle. As with previous systems, the primary amine group is involved with hydrogen bonding with solvent molecules of crystallisation (not shown).

3.6.1 Coordination Mode of $[Ru(bpy)_2]^{2+}$ to Carbon Nitride

The crystal structure of DMNA provides a model for coordination of $[Ru(bpy)_2]^{2+}$ to carbon nitride that contains pseudo-tri-s-triazine and amine metal coordination sites. Characterisation of $[Ru(bpy)_2(CCN)](PF_6)_2$ and $[Ru(bpy)_2(UCN)](PF_6)_2$ supports the presence of $[Ru(bpy)_2]^{2+}$ moieties. ^{13}C CP-MAS NMR and IR spectroscopy suggest the presence of bpy ligands, with the IR vibrational frequencies of the bpy consistent with bpy coordinated to a metal centre. The retention of the $(PF_6)^-$ ligand, as seen again by ATR-IR, suggests a charged species, supported by the zeta-potential measurements. PXRD and XPS data shows no evidence of other ruthenium species either intercalated or coordinated to the carbon nitride as single-molecule species or as crystalline impurities (i.e RuO_2).

Therefore, based on the available evidence, coordination of $[Ru(bpy)_2]^{2+}$ to carbon nitride is consistent with the motif shown in Figure 3.14. Following IUPAC convention, the materials can be referred to as $[Ru(bpy)_2(CCN\text{-}\kappa^2 N, N')](PF_6)_2$ and $[Ru(bpy)_2(UCN\text{-}\kappa^2 N, N')](PF_6)_2$.

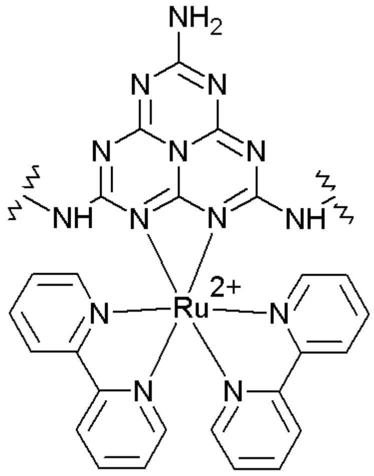

Figure 3.14: Proposed coordination mode of $[Ru(bpy)_2]^{2+}$ to carbon nitride

3.7 Photochemical Properties of $[Ru(bpy)_2(CCN)](PF_6)_2$ and $[Ru(bpy)_2(UCN)](PF_6)_2$

3.7.1 Photocatalytic Activity of Ruthenium Decorated Carbon Nitrides

The effects on the absorption spectrum of UCN and CCN after $[Ru(bpy)_2]^{2+}$ coordination was clear, with a new, strongly absorbing band centred at 500 nm (Figure 3.6). Increasing light absorption can result in an increase in the efficiency of photochemical reactions, including photocatalysis, and therefore photocatalytic hydrogen production was investigated which is a well-established application of carbon nitride materials.

Platinum nanoparticles have been shown to act as co-catalysts for several systems active for hydrogen evolution, including carbon nitride.[9, 207]Decorated and undecorated carbon nitrides were treated with 2% wt platinic acid in a 10% aqueous solution of triethanolamine (TEOA) under UV light to deposit 1-3 nm diameter platinum nanoparticles onto the surface of the materials, and then characterised by ICP-MS to measure Pt loading (Table 3.10).[9] The rates of hydrogen evolution are show in Figure 3.15 and summarised in Table 3.9. Controls were performed which showed no activity in the absence of either platinum or the sacrificial electron donor (triethanolamine).

Table 3.9: Hydrogen evolution rates from platinised ruthenium decorated and undecorated carbon nitrides

Material	Hydrogen Evolution Rate / μmol g^{-1} hr^{-1}
CCN-Pt	338
UCN-Pt	15.1
[Ru(bpy)$_2$(**C**CN)](PF$_6$)$_2$-Pt	0
[Ru(bpy)$_2$(UCN)](PF$_6$)$_2$-Pt	0

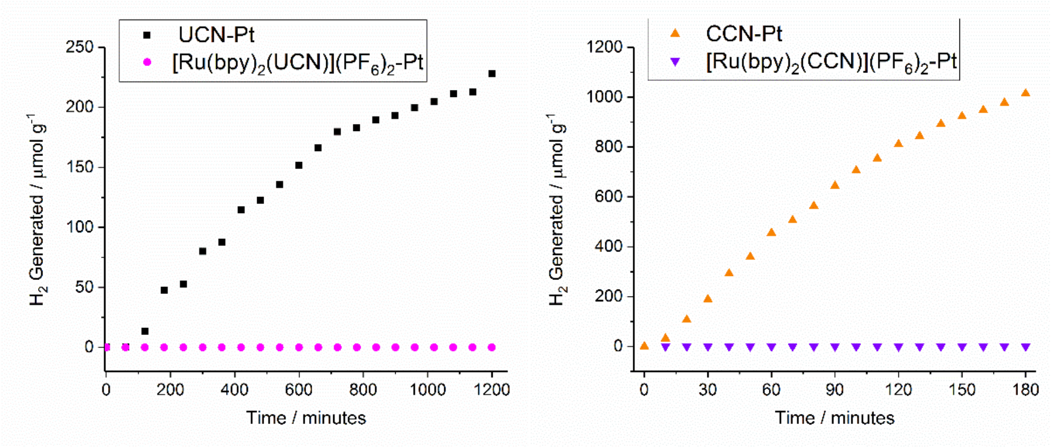

Figure 3.15: Photocatalytic (λ > 400 nm) hydrogen evolvution as monitored by GC over time when using Ru(bpy)$_2$(CCN)](PF$_6$)$_2$-Pt, CCN-Pt, UCN-Pt and [Ru(bpy)$_2$(UCN)](PF$_6$)$_2$ Samples are decorated with platinum nanoparticles (1-3 nm) by combining with 2% weight H_2PtCl_6 and photolyzing with 300 W Xe lamp in 10% vol. aqueous triethanolamine. After isolation of platinised materials via filtration and drying, photocatalysis then performed on 30 mg catalyst, in 10% vol. aqueous triethanolamine (sacrificial electron donor) with λ > 420 nm

UCN-Pt and CCN-Pt both demonstrate activity toward hydrogen evolution (Figure 3.15, Table 3.9), although at different rates (Table 3.9). The principal cause for this difference in activities of the platinised carbon nitride is in part due to the different light absorption properties of UCN and CCN. Variations in surface sites and defects is also likely to play a significant role but are more experimentally challenging to quantify.

The complete inactivity of the ruthenium decorated materials was unexpected and intriguing. ICP-MS results and TEM analysis (Table 3.10, Figure 3.16) have shown that platinum nanoparticles of the expected size are formed on the surface of the $[Ru(bpy)_2(CCN)](PF_6)_2$-Pt, indicating presence of co-catalyst on the surface of carbon nitride. The incident light filter was also changed from λ > 420 nm to λ > 470 nm to attempt to localise excited states on $[Ru(bpy)_2(CCN)](PF_6)_2$-Pt to the ruthenium moieties, however no catalysis was observed in this case either.

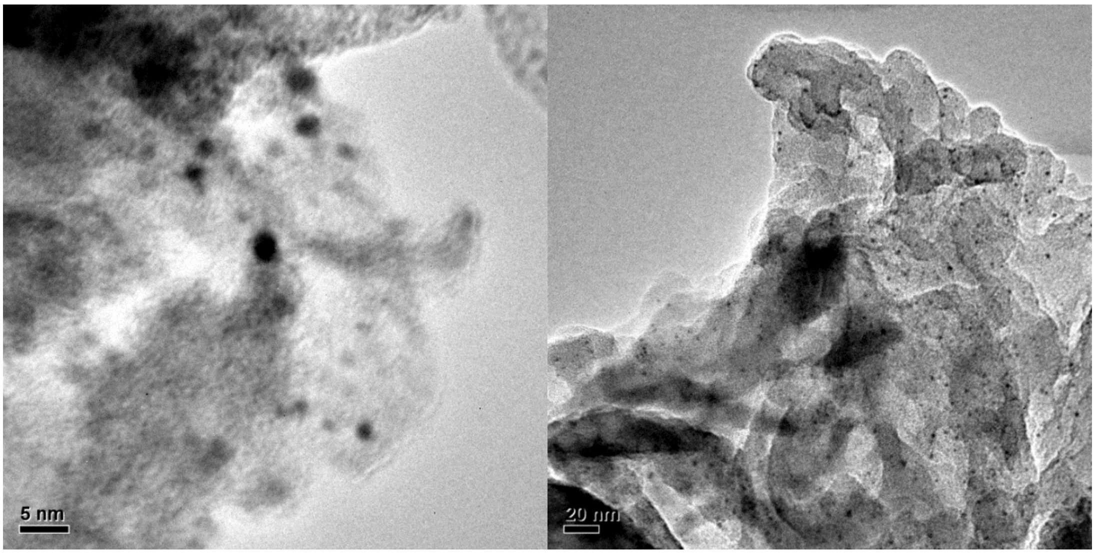

Figure 3.16: TEM images of $[Ru(bpy)_2(CCN)](PF_6)_2$-Pt showing the presence of Pt nanoparticles

Further controls were performed on CCN samples to investigate the reasons behind the lack of hydrogen evolution activity in ruthenium decorated carbon nitride. To emulate the thermophysical treatment subjected to a sample of $[Ru(bpy)_2(CCN)](PF_6)_2$ during synthesis, CCN was subjected to stirring under refluxing in ethanol for one week prior to platinization. No significant change in activity was observed in the resulting CCN-Pt, suggesting a physical change in the surface sites or bulk material is not the cause of the lack of activity.

Another explanation of the inactivity of $[Ru(bpy)_2(CCN)](PF_6)_2$ could be that the active sites for hydrogen evolution in CCN are all 'blocked' by the adsorption of ruthenium, preventing catalysis. Therefore, CCN-Pt was first synthesised and then decorated with ruthenium, resulting in Pt-CCN-Ru. In this case, the most active sites for hydrogen evolution are available for (and therefore accessible to) the platinum cocatalyst. However, $[Ru(bpy)_2(CCN\text{-}Pt)](PF_6)_2$ also demonstrated a lack of hydrogen evolution activity, suggesting that the physical changes to the material surface are not the cause of the lack of activity for the other ruthenium-decorated carbon nitrides.

Table 3.10: Metal loadings for decorated CCN samples as measured by ICP-MS, zeta-potential measurements

Material	Ru Loading / mg g^{-1}	Pt Loading / mg g^{-1}	HER / µmol g^{-1} hr^{-1}	Zeta-potential / mV
CCN-Pt	0	2.59	338	-46.4 ± 1.3
$[Ru(bpy)_2($**C**CN$)](PF_6)_2$-Pt	5.4	1.06	0	-44.5 ± 0.4
$[Ru(bpy)_2($**C**CN-Pt$)](PF_6)_2$	9.6	1.25	0	23.8 ± 0.6

Zeta-potential measurements were also carried out to investigate whether the change in the electrostatic change in the surface would provide an explanation for the lower activity (Table 3.10). In the active CCN-Pt, a low zeta potential of -46.4 mV is measured. This is expected as the addition of platinum nanoparticles generally causes a marked decrease in zeta-potential.[69] Although the zeta potential of $[Ru(bpy)_2($**C**CN$)](PF_6)_2$ is significantly higher than that of CCN, after platinization, the zeta potential of $[Ru(bpy)_2($**C**CN$)](PF_6)_2$-Pt is very similar to that of CCN-Pt. This makes an explanation of the lack of activity based on the different surface potentials difficult to rationalise.

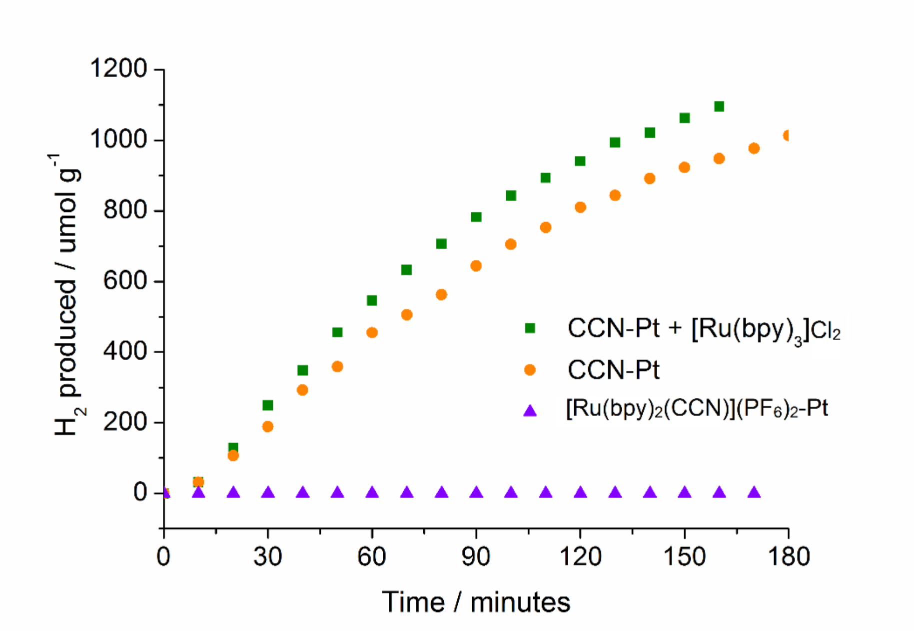

Figure 3.17: A comparison of the hydrogen evolution activity of CCN-Pt and $[Ru(bpy)_2(CCN)](PF_6)_2$-Pt to a sample of CCN-Pt with 0.5 mg [Ru(bpy)3]Cl_2 added in solution. Reaction conditions identical to those shown in Figure 3.15.

Figure 3.17 shows the importance of surface-bound ruthenium to the lack of hydrogen evolution activity. Although $[Ru(bpy)_2(CCN)](PF_6)_2$-Pt shows no hydrogen evolution activity, adding the same quantity of ruthenium in the form of $[Ru(bpy)_3]Cl_2$ to the photocatalytic reaction using CCN-Pt does not significantly affect the hydrogen evolution activity, suggesting that a close physical proximity of ruthenium and carbon nitride are required for the quenching to occur.

Having ruled out some of the simpler explanations for the catalytic inactivity of $[Ru(bpy)_2(UCN)](PF_6)_2$ and $[Ru(bpy)_2(\mathbf{C}CN)](PF_6)_2$, the effect on the photophysical properties of carbon nitride due to ruthenium decoration was investigated.

3.8 Excited State Characterisation of $[Ru(bpy)_2(CCN)](PF_6)_2$ and $[Ru(bpy)_2(UCN)](PF_6)_2$

3.8.1 3-Dimensional Steady State Luminescence of $[Ru(bpy)_2(CCN)](PF_6)_2$ and $[Ru(bpy)_2(UCN)](PF_6)_2$

3-Dimensional excitation-emission spectroscopy was performed on UCN, CCN, $[Ru(bpy)_2(UCN)](PF_6)_2$ and $[Ru(bpy)_2(CCN)](PF_6)_2$ (Figure 3.18). A full emission spectrum is collected at different excitation wavelengths to gain a full overview of the emission bands observed. Due to the solid-state nature of the samples, strong peaks are observed at $\lambda_{em} = \lambda_{ex}$ and $\lambda_{em} = 2\lambda_{ex}$ due to first and second order diffraction of the incident light. The fluorescent signals of UCN and CCN are very similar, with broad emission bands at around 470 nm after excitation between wavelengths of 300-400 nm as expected from the literature.[131]

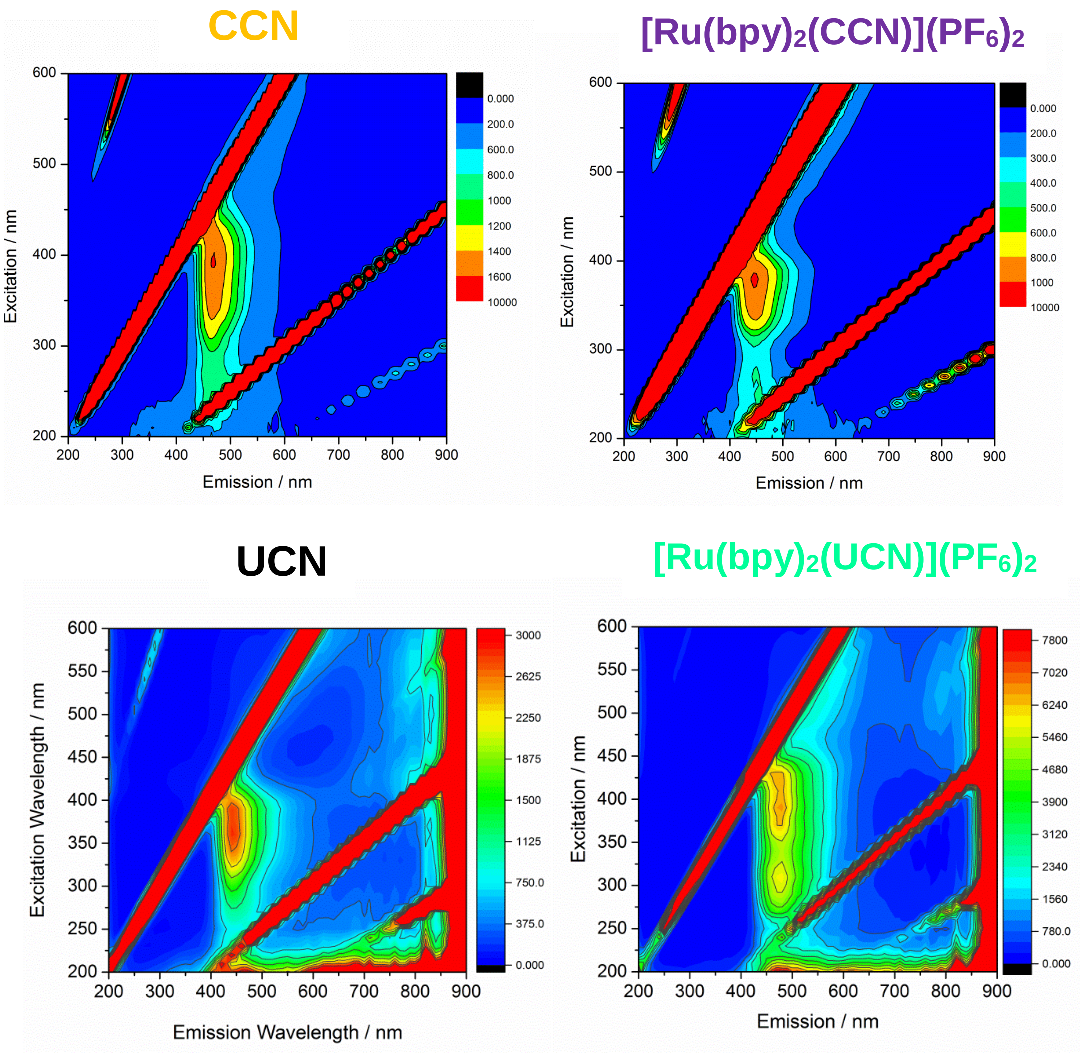

Figure 3.18 3D Excitation-emission spectroscopy of solid-state undecorated and ruthenium-decorated carbon nitrides

3.8.2 2-Dimensional Steady State Luminescence of [Ru(bpy)$_2$(CCN)](PF$_6$)$_2$ and [Ru(bpy)$_2$(UCN)](PF$_6$)$_2$

Although 3-dimensional emission spectra allow a wide view of the radiative processes occurring within a system, it is difficult to directly compare the ‘contour maps’ shown in Figure 3.18. to ease comparison between the systems, data at λex = 300 nm and λex = 390 nm is extracted from the 3D spectra and are shown in Figure 3.19 and Figure 3.20.

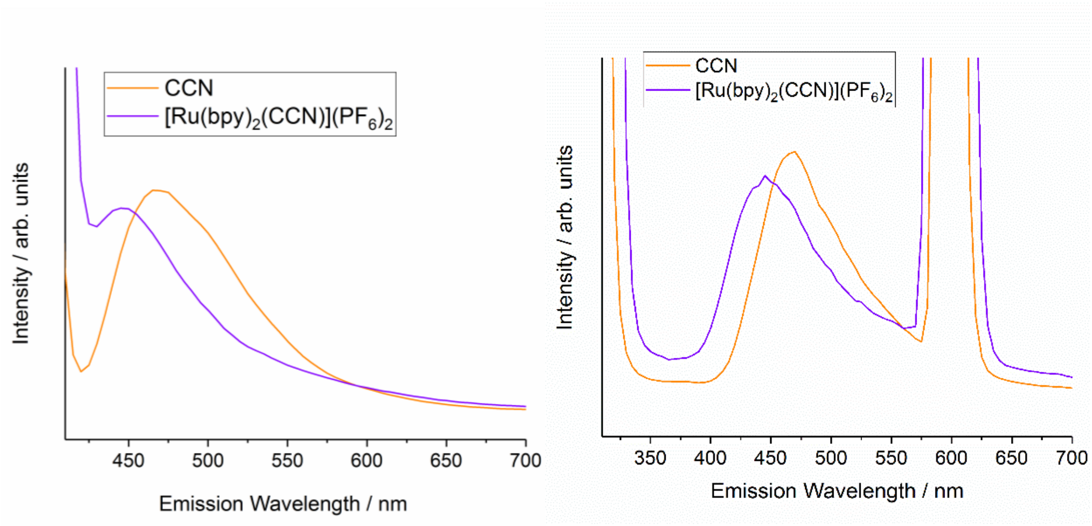

Figure 3.19: Emission spectra of CCN and [Ru(bpy)$_2$(CCN)](PF$_6$)$_2$ at λ_{em}=300 nm (left) and 390 nm (right)

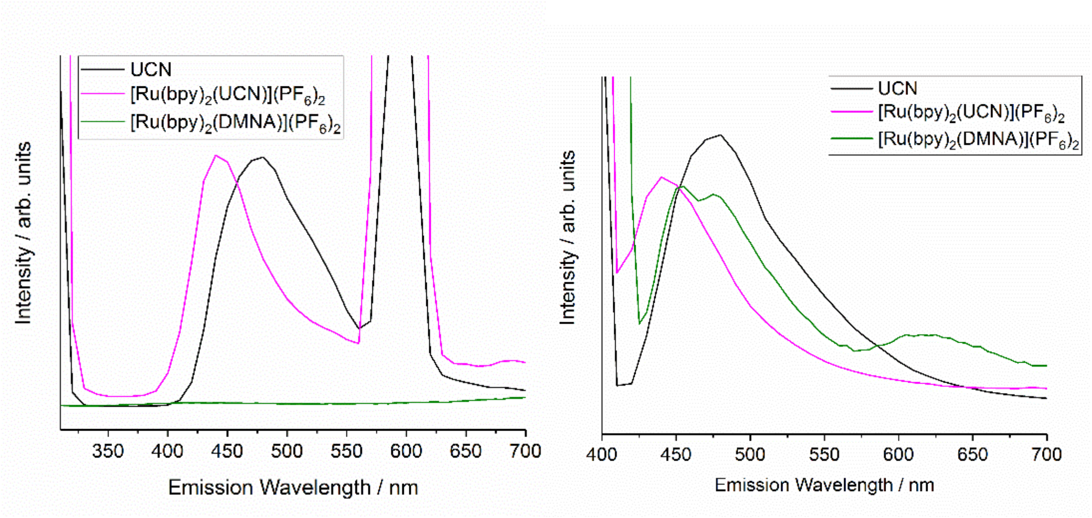

Figure 3.20: Emission spectra of UCN and [Ru(bpy)$_2$(UCN)](PF$_6$)$_2$ at λ_{em}=300 nm (left) and 390 nm (right)

After decoration with ruthenium, a change is observed in the position of the band associated with bulk carbon nitride. As is the case with rhenium decoration (see section 2.8), the emission wavelengths decrease by approximately 30 nm. (Figure 3.19 and Figure 3.20). This may be associated with the perturbation of the higher energy surface states on the carbon nitride upon ruthenium coordination.

Of particular interest in the emission spectroscopy of [Ru(bpy)$_2$(CCN)](PF$_6$)$_2$ or [Ru(bpy)$_2$(UCN)](PF$_6$)$_2$ is the lack of any emissive signal arising from the new light absorption band (centred at 500 nm, Figure 3.6). Ruthenium diimine species often give rise to strong emission from the decay of triplet metal-to-ligand charge transfer (MLCT) excited states at λ_{ex} = 450 nm λ_{em} = 500 nm.[153, 184] The lack of this emission is indicative either of no MLCT state forming in the first place, or of the quenching of the formed excited state. In order to gain more information, an investigation into the electronic properties of the molecular analogue, $[Ru(bpy)_2(DMNA)](PF_6)_2$, was carried out.

3.9 Characterisation of $[Ru(bpy)_2(DMNA\text{-}\kappa^2\textit{N, N'})](PF_6)_2$

3.9.1 Steady-state luminescence of $[Ru(bpy)_2(DMNA\text{-}\kappa^2\textit{N, N'})](PF_6)_2$

$[Ru(bpy)_3]^{2+}$ is ubiquitous in photochemistry as a highly luminescent complex with a lifetime on the microsecond timescale.[79, 154, 184, 208] In order to draw a comparison between $[Ru(bpy)_3]^{2+}$ and $[Ru(bpy)_2(DMNA)]^{2+}$, and hence gain insight into the photophysical properties and the reactivity (or lack thereof) of $[Ru(bpy)_2(\mathbf{C}CN)](PF_6)_2$ and $[Ru(bpy)_2(UCN)](PF_6)_2$, a photochemical and electrochemical analysis of $[Ru(bpy)_2(DMNA)]^{2+}$ was performed.

The 3-dimensional excitation-emission spectrum of $[Ru(bpy)_2(DMNA)](PF_6)_2$ was collected in a solution of acetonitrile and is shown in Figure 3.21 alongside its absorption spectrum. The two methods show good agreement, with three principle features.

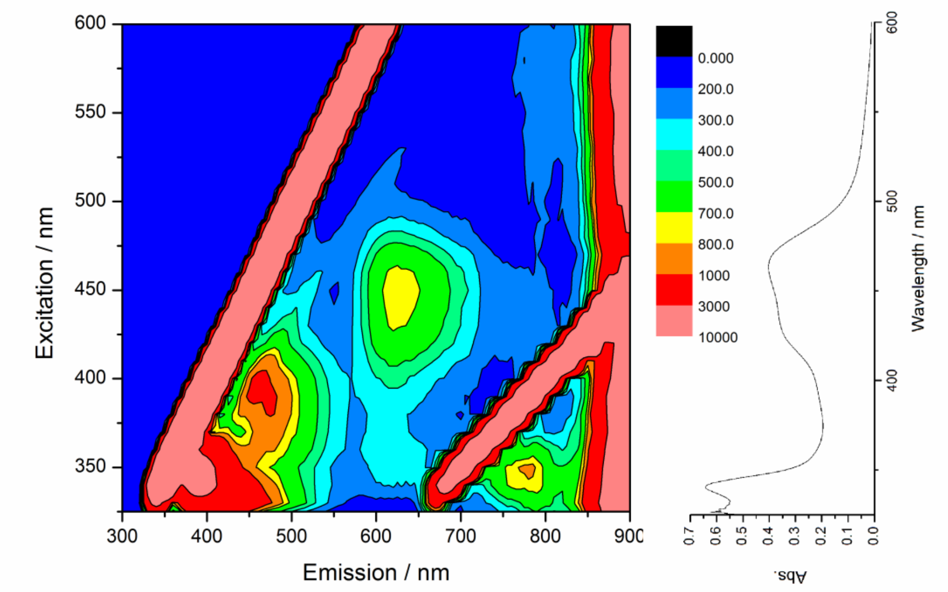

Figure 3.21: 3-Dimensional emission-excitation spectrum of a solution of $[Ru(bpy)_2(DMNA)](PF_6)_2$ in acetonitrile

The highest energy transition observed gives rise to an intense absorption around 340 nm, and excitation into this band leads to a strong emission at 400 nm, associated with π-π* transitions between ligand orbitals.[209] Excitation into two further absorption bands, centred around 400 nm and 450 nm, leads to emissions at 470 nm and 610 nm respectively, are associated with d-π* metal-to-ligand charge transfer (MLCT) bands.[184] Significant overlap is seen in the last two absorption bands.

It is generally seen that the MLCT region of the absorption band of ruthenium tris-triimine complexes shows multiple contributing peaks in heteroleptic systems.[192] It has been calculated that the lower-energy transition in heteroleptic systems is associated with the molecular orbital with the poorest mixing with the metal t_{2g} orbitals.[210] In the case of $[Ru(bpy)_2(DMNA)](PF_6)_2$ it is therefore proposed that the lowest energy MLCT transition is associated with an electron from ruthenium t_{2g} orbitals to π* molecular orbitals with high electron density on the DMNA ligand, as the longer ruthenium-nitrogen bonds to DMNA compared to bpy are likely to lead to poorer orbital overlap and less mixing. This is loosely correlated by the relative emission intensities of the two states in Figure 3.21, as the lowest energy MLCT transition has approximately half the intensity of the higher energy MLCT transition.

Emission spectra of $[Ru(bpy)_2(DMNA)](PF_6)_2$ are shown after excitation at 380 nm. Emission spectra from λ_{ex} = 380 nm in different solutions are shown in Figure 3.22. After excitation at 380 nm, a DCM solution of $[Ru(bpy)_2(DMNA)](PF_6)_2$ shows two emission bands at 415 and 460 nm. No significant change is seen in the relative intensities of the two emission bands as a function of concentration, suggesting these are due to two discrete states as seen in the three-dimensional spectrum.

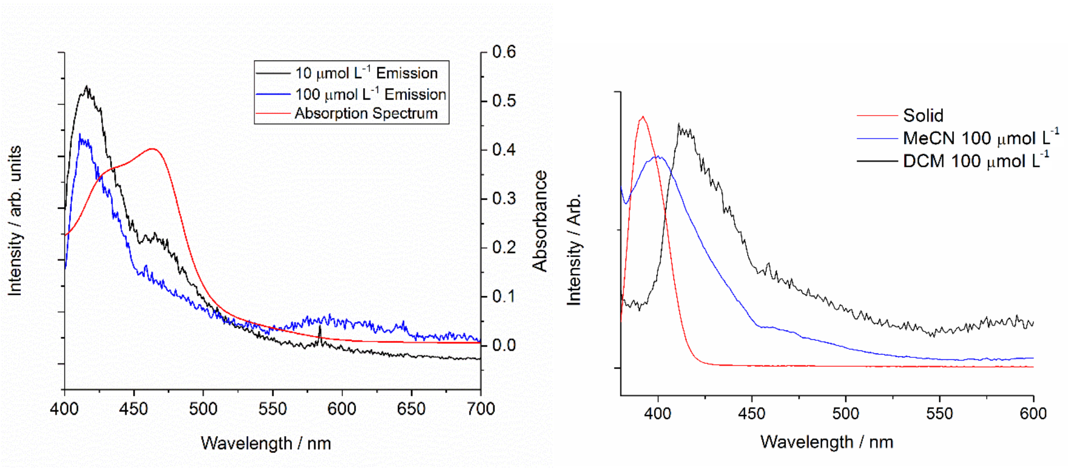

Figure 3.22: Emission spectrum after λ_{ex} = 380 nm for $[Ru(bpy)_2(DMNA)](PF_6)_2$ at different concentrations in DCM (left) and different solvents (right)

The emission band at 415 nm is assigned to a π-π* state associated with the ligand orbitals, and is shown to be solvent sensitive, blue-shifting in a hydrogen-bonding solvent (acetonitrile) or in the solid state compared to DCM (Figure 3.22). The band at 460 nm is considerably weaker in acetonitrile compared to DCM, and absent in the solid state. It is likely that the band at 460 nm is related to decay of a MLCT state, as shown in the three-dimensional spectrum. It should be noted that all spectra are taken in the absence of oxygen except in the case of solid-state samples due to experimental limitations. Therefore, oxygen may quench this emission in the solid-state case and explain the absence of the peak at 460 nm under these conditions.

3.9.2 Time-resolved luminescence of $[Ru(bpy)_2(DMNA)](PF_6)_2$

Time resolved emission spectroscopy of these peaks was carried out for both acetonitrile and DCM solutions. A good fitting of the overall emission decay profiles (Figure 3.23) was found using two components, which arise due to the formation of multiple excited states due to excitation at 380 nm; τ_1 corresponds to the decay of the π-π* excited state, and τ_2 corresponds to the decay of one of the MLCT charge-transfer states. The emission lifetimes of $[Ru(bpy)_2(DMNA)](PF_6)_2$ after excitation at 380 nm are shown in Table 3.11, and appear to be solvent independent.

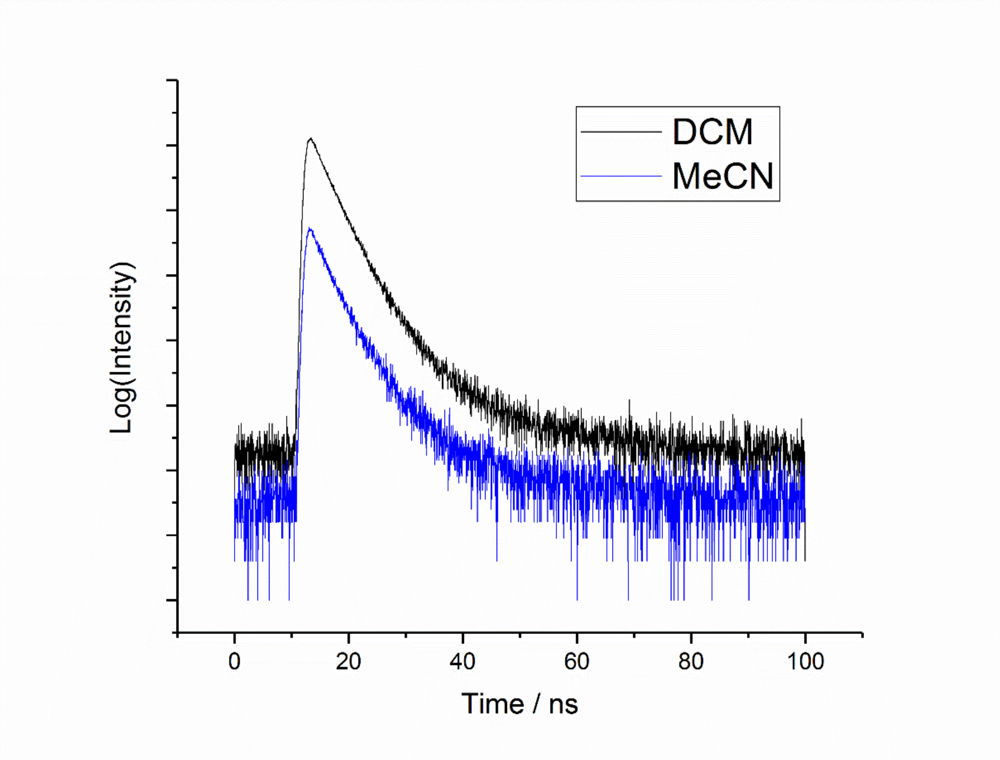

Figure 3.23: Emission decay profile over time of $[Ru(bpy)_2(DMNA)](PF_6)_2$ (10 umol L^{-1}) at λ_{ex} = 380 nm, λ_{em} = 510 nm in DCM and MeCN (offset).

Table 3.11: Values of lifetime components τ_1 and τ_2 in the emission of $[Ru(bpy)_2(DMNA)](PF_6)_2$ after excitation at 380 nm

Solvent	τ_1 / ns	τ_2 / ns
Acetonitrile	4.96 ± 0.26	15.3 ± 2.5
DCM	4.29 ± 0.06	15.8 ± 2.1

The contributions of both components measured at different wavelengths in acetonitrile and DCM solution is shown in Figure 3.24. It is seen that the longer component, τ_2, gives rise to the emission at longer wavelength, which is consistent with the assignment of the states the bands arise from.

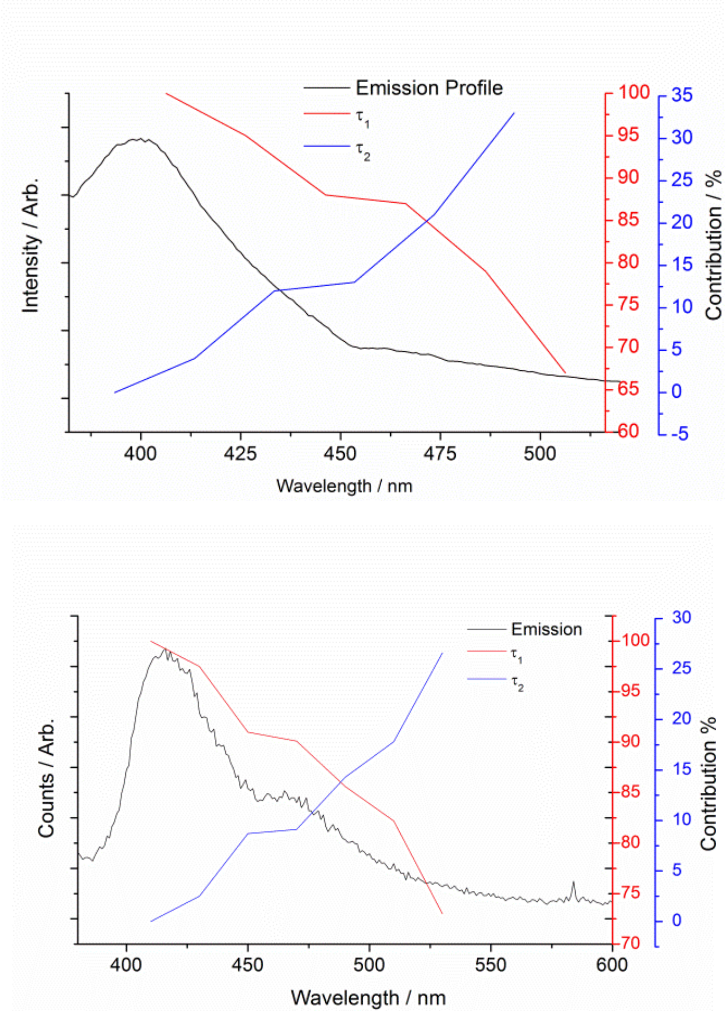

Figure 3.24: Change in contribution of lifetime components at different wavelength in 100µmol solutions of $[Ru(bpy)_2(DMNA)](PF_6)_2$ in acetonitrile (left) and DCM (right)

In addition to emission after excitation at 380 nm, $[Ru(bpy)_2(DMNA)](PF_6)_2$ also shows longer lived emission at 600 nm after excitation at 470 nm. The time-resolved decay curves (Figure 3.25, Table 3.12) show two components in the overall lifetime.

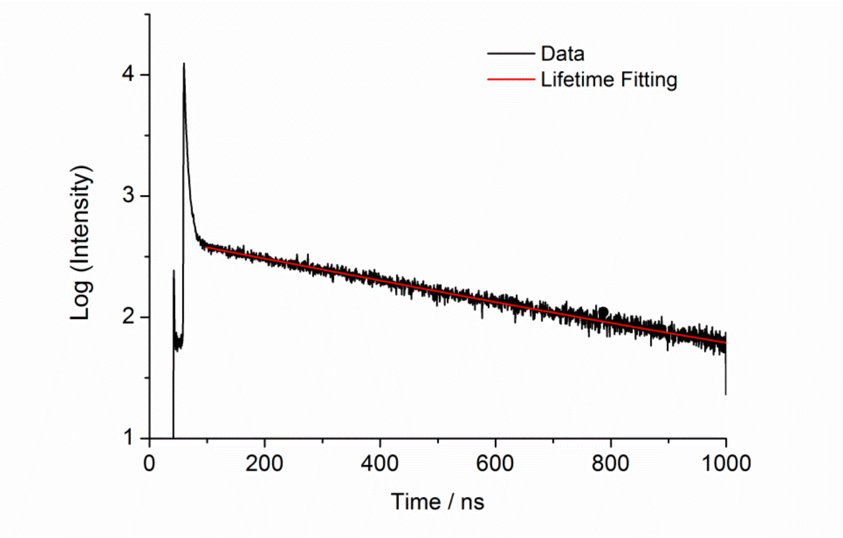

Figure 3.25: Example decay curve of [Ru(bpy)$_2$(DMNA)](PF$_6$)$_2$ of the excited state at λ_{ex} = 470 nm, λ_{em} = 600 nm

The longer component lifetime, τ_2, is of the same order of magnitude to the values previously measured for [Ru(bpy)$_3$]$^{2+}$ and is proposed to result from radiative decay of a long-lived ^{3}MLCT state.[153] Though the contribution of τ_1 is very small (Table 3.12) the calculated fitting with a single component is significantly worse (χ^2 = 2.98 for one component, χ^2 = 1.19 for two components). There is expected to be a large degree of uncertainty in the value of the contribution from each component due to the very significant difference in their magnitudes.

Table 3.12: Lifetime component summary for emission in [Ru(bpy)$_2$(DMNA)](PF$_6$)$_2$ at λ_{ex} = 470 nm, λ_{em} = 600 nm

		[Ru(bpy)$_2$(DMNA)]$^{2+}$			[Ru(bpy)$_3$]$^{2+}$
Solvent	τ_1 / ns	Contribution / %	τ_2 / ns	Contribution / %	τ_1 / ns
MeCN	5.9 ± 0.1	3	702 ± 26	97	855
DCM	5.0 ± 0.2	1	544 ± 9	99	488

The two components of the decay curve at λ_{ex} = 470 nm, λ_{em} = 600 nm are likely to arise from two different excited states with overlapping emission and absorption bands. In the excited state of [Ru(bpy)$_3$]$^{2+}$, ultrafast vibrational spectroscopy has provided evidence of localization of the excited electron to one of the ligands on the nanosecond time scale.[186, 211] It is therefore suggested that in [Ru(bpy)$_2$(DMNA)]$^{2+}$, following absorption at 470 nm, three excited states are formed.

One state involves localisation of the high energy electron on the DMNA ligand, while the other two degenerate states involve localisation on a 2,2'-bipyridine ligand. One of the states has a longer lifetime than the other, but further spectroscopy (involving ultrafast vibrational spectroscopy) is required to gain insight into how these features relate.

Although $[Ru(bpy)_2(DMNA)](PF_6)_2$ shows emission from a MLCT state, no analogous emission is observed on the ruthenium moieties coordinated to carbon nitride (Figure 3.18). In order to attempt to explain this phenomenon, a molecular orbital diagram of $[Ru(bpy)_3]^{2+}$ is shown in Figure 3.26.[154, 212]

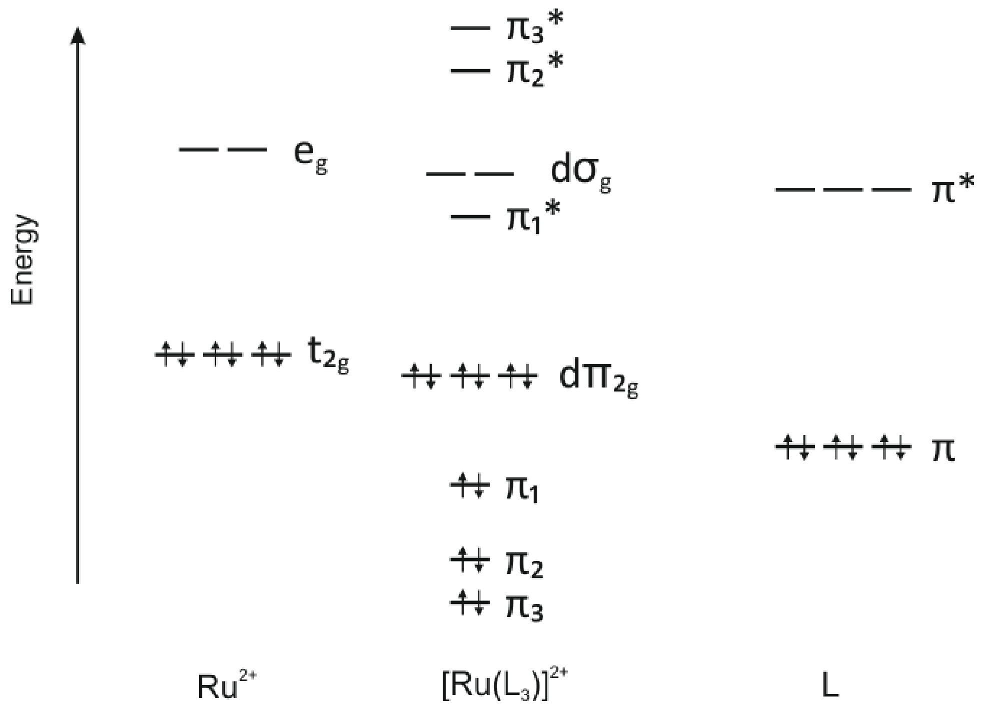

Figure 3.26: MO diagram showing π-interaction between the frontier orbitals of the Ru with the surrounding ligands (L = 2,2'-bipyridine). The d-orbitals on Ru are shown already affected by the σ-bonding between Ru and L.

In $[Ru(bpy)_3]^{2+}$, the ^{3}MLCT excited state has a long lifetime due to how ligand π* orbitals lie lower in energy than the $d\sigma_g$ orbitals, meaning that a metal-centred (MC) state is not an energetically favourable decay pathway.[185, 213, 214] However, in systems with weaker ligand field effects (such as in $[Ru(tpy)_2]^{2+}$, tpy = terpyridine) the $d\sigma_g$ orbitals can have energies closer to the ligand π* orbitals, meaning that a MC state is a viable intermediate in non-radiative decay.[213] As was shown in section 3.6, the crystal structure of $[Ru(bpy)_2(DMNA)]^{2+}$ shows deviation from the geometry seen in $[Ru(bpy)_3]^{2+}$, and comparison can be drawn to $[Ru(tpy)_2]^{2+}$.

In the previous chapter, where $[ReCl(CO)_3]$ fragments were coordinated to the surface of carbon nitride, infrared spectroscopy suggests that carbon nitride acts as a less electron-donating ligand when compared to DMNA. If this is because of decreased σ-overlap, carbon nitride can be classified as providing a weaker ligand field compared to DMNA. Therefore, whilst $[Ru(bpy)_2(DMNA)]^{2+}$ displays an electronic structure and luminescence comparable to $[Ru(bpy)_3]^{2+}$¸ the relative positions of the π* and $d\sigma_g$ orbitals in $[Ru(bpy)_2(UCN)](PF_6)_2$ may be more comparable to in $[Ru(tpy)_2]^{2+}$ in terms of the electronics of the metal. The state formed at 500 nm may therefore decay via a non-radiative ^{3}MC state and be of too short a lifetime to perform useful photochemistry.

It is also possible that no luminescence is seen in $[Ru(bpy)_2(UCN)](PF_6)_2$ because of immediate electron transfer of from an excited MLCT state to the conduction band of the carbon nitride. This electron-transfer emission quenching has been observed in dyes covalently grafted to carbon nanotubes, as well as having been observed in dye-sensitized solar-cells technology between ruthenium dyes and titania.[209, 215, 216] Further investigation was carried out to determine the mechanism of quenching of catalysis and luminescence in ruthenium-decorated carbon nitrides.

3.9.3 Electrochemistry of $[Ru(bpy)_2(DMNA)](PF_6)_2$

The electrochemistry of $[Ru(bpy)_2(DMNA)](PF_6)_2$ was investigated and compared to $[Ru(bpy)_3]Cl_2$. Dynamic electrochemical measurements allow the energetic levels of reduction and oxidation processes to be measured to enable comparison with the positions of the conduction and valence bands of carbon nitride to gain insight as to where the thermodynamic positions of redox processes in $[Ru(bpy)_2(CCN)](PF_6)_2$ and $[Ru(bpy)_2(UCN](PF_6)$ could be expected.

The cyclic voltammogram of $[Ru(bpy)_2(DMNA)](PF_6)_2$ (Figure 3.27) shows four processes, one metal-based ($E_{1/2}$ = 1.26 V) and three ligand based processes ($E_{1/2}$ = -1.26, -1.48 and -1.67 V). The scans in red and blue demonstrate that these processes can occur independently.

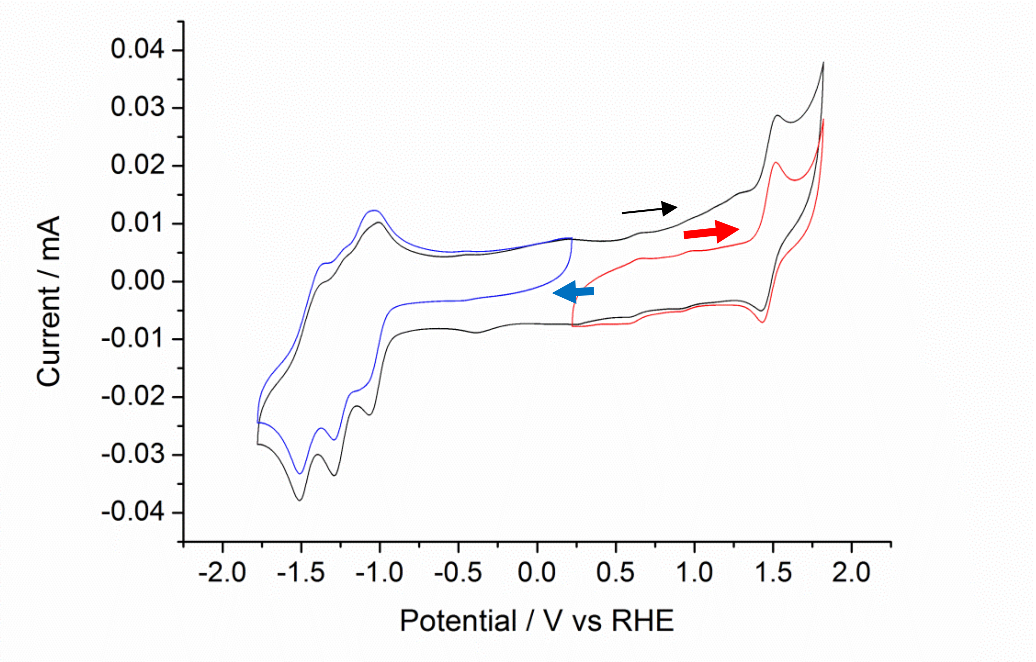

Figure 3.27: Cyclic Voltammogram of [Ru(bpy)$_2$(DMNA)](PF$_6$) (1 mmol dm^{-3}) in DMF with (NEt$_4$)(PF$_6$) (100 mmol dm^{-3}) as electrolyte. Ag/AgCl electrode used as reference, with carbon disk as working electrode and platinum wire as counter

As shown in Table 3.13, the potentials of these processes on [Ru(bpy)$_2$(DMNA)](PF$_6$)$_2$ are within 100 mV of the same processes on [Ru(bpy)$_3$]Cl$_2$ (collected under identical conditions), processes occurring at more reducing (i.e. lower) potentials in [Ru(bpy)$_2$(DMNA)](PF$_6$)$_2$. This corresponds to an increase in frontier energy levels in [Ru(bpy)$_2$(DMNA)](PF$_6$)$_2$, likely a result of the poorer orbital overlap between the ruthenium and DMNA molecular orbitals compared to 2,2'-bipyridine.[185]

Table 3.13: Electrochemistry of [Ru(bpy)$_2$(DMNA)](PF$_6$)$_2$ compared to [Ru(bpy)$_3$]Cl$_2$. All potentials in units of volts vs. SHE. Ru(bpy)$_2$(DMNA)](PF$_6$) (1 mmol dm^{-3}) in DMF with (NEt$_4$)(PF$_6$) (100 mmol dm^{-3}) as electrolyte. Ag/AgCl electrode used as reference, with carbon disk as working electrode and platinum wire as counter

Reduction Process	[Ru(bpy)$_3$]Cl$_2$			[Ru(bpy)$_2$(DMNA)](PF$_6$)$_2$		
	E_{pa} (Ox.)	E_{pc} (Red.)	$E_{1/2}$	E_{pa} (Ox.)	E_{pc} (Red.)	$E_{1/2}$
Ru^{2+}/Ru^{3+}	1.41	1.30	+1.36	1.31	1.21	+1.26
$(L_3)/(L_3)^-$	-1.16	-1.22	-1.19	-1.23	-1.28	-1.26
$(L_3)^-/(L_3)^{2-}$	-1.34	-1.40	-1.37	-1.44	-1.51	-1.48
$(L_3)^{2-}/(L_3)^{3-}$	-1.59	-1.67	-1.63	-1.61	-1.73	-1.67

The reduction/oxidation measurements for the processes listed in Table 3.13 are compared to the energy levels of the conduction band and valence band of carbon nitride in Figure 3.28.[196] Assuming that the redox potentials in ruthenium-decorated carbon nitrides occur at a similar electrochemical potential to the molecular analogue, Figure 3.28 suggests that, thermodynamically, electron transfer from the ligand π* orbitals in the ruthenium moiety to the conduction band in the carbon nitride may be possible. However, as the absorption spectra of $[Ru(bpy)_2(DMNA)](PF_6)_2$ and ruthenium-decorated carbon nitride show a different maximum peak absorption wavelength for the MLCT state (470 nm in the complex compared 500 nm on the material) the positions of the molecular orbitals in each case are unlikely to be in identical positions.

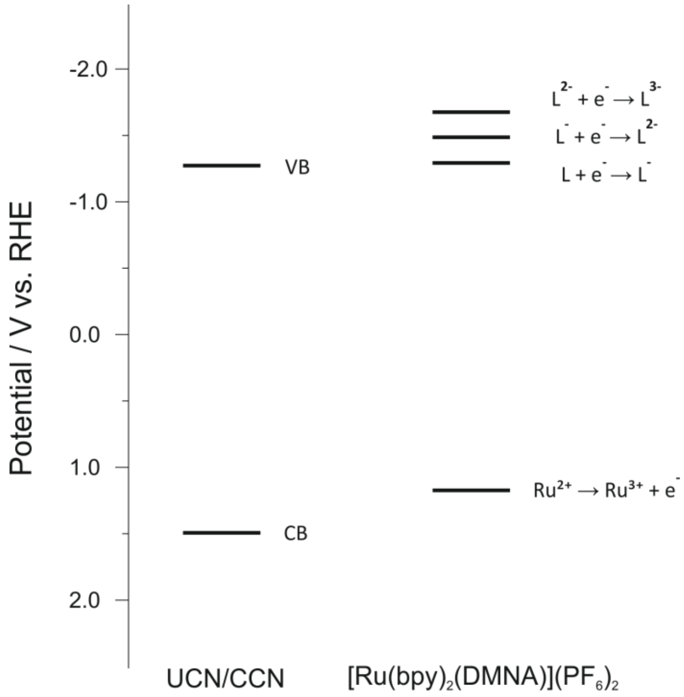

Figure 3.28: Energetic positions of the redox processes observed for $[Ru(bpy)_2(DMNA)](PF_6)_2$

3.10 The excited state of $[Ru(bpy)_2(UCN)](PF_6)_2$ compared to UCN

3.10.1 Time-resolved Luminescence of Ruthenium Decorated Carbon Nitride

To explore a photophysical explanation of the lack of lower-energy emission and photocatalytic activity, time-resolved luminescence studies on the decorated carbon nitride were carried out. For the experimental design, it was important that oxygen quenching of excited states be ruled out. Therefore, suspensions of UCN and $[Ru(bpy)_2(UCN)](PF_6)_2$ needed to be used rather than solid-state materials. To minimise ruthenium leaching (i.e. to ensure all photochemistry measured was due to the material rather than dissolved ruthenium species) the stability of $[Ru(bpy)_2(UCN)](PF_6)_2$ in different solvents was measured qualitatively.

Figure 3.29 shows the UV-visible light absorption spectra of various solvents after samples of $[Ru(bpy)_2(UCN)](PF_6)_2$ were stirred in them for 3 hours and solid removed via filtration. Comparable to the results seen in other coordinated metal systems, more coordinating solvents such as isopropanol and acetonitrile result in the emergence of significant absorption peaks corresponding to solution ruthenium species.

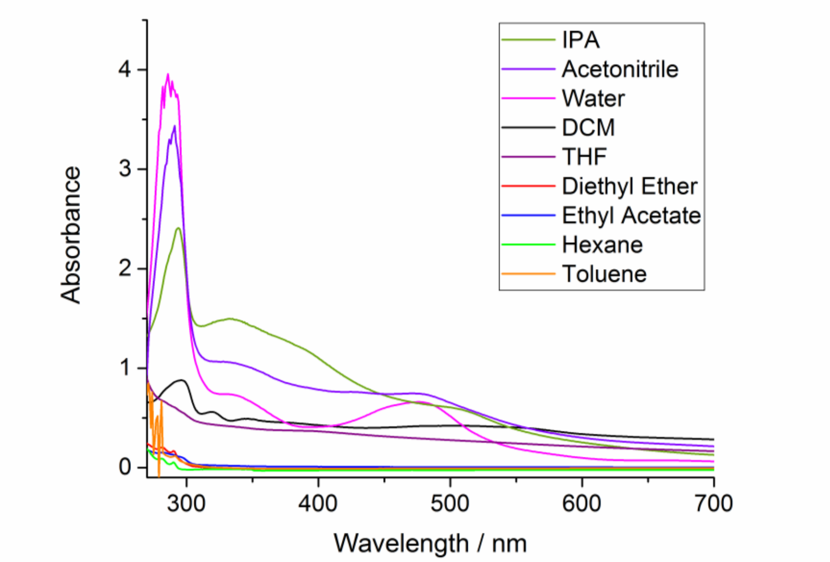

Figure 3.29: UV-visible light absorption spectra of different solvents after leaching of Ru from $[Ru(bpy)_2(UCN)](PF_6)_2$

Non-polar solvents, such as hexane and toluene, did not show any significant leaching of metal species into solution. As a result, toluene was chosen to act as the solvent for suspensions of $[Ru(bpy)_2(UCN)](PF_6)_2$ and UCN for time-resolved fluorescence analysis (Figure 3.30).

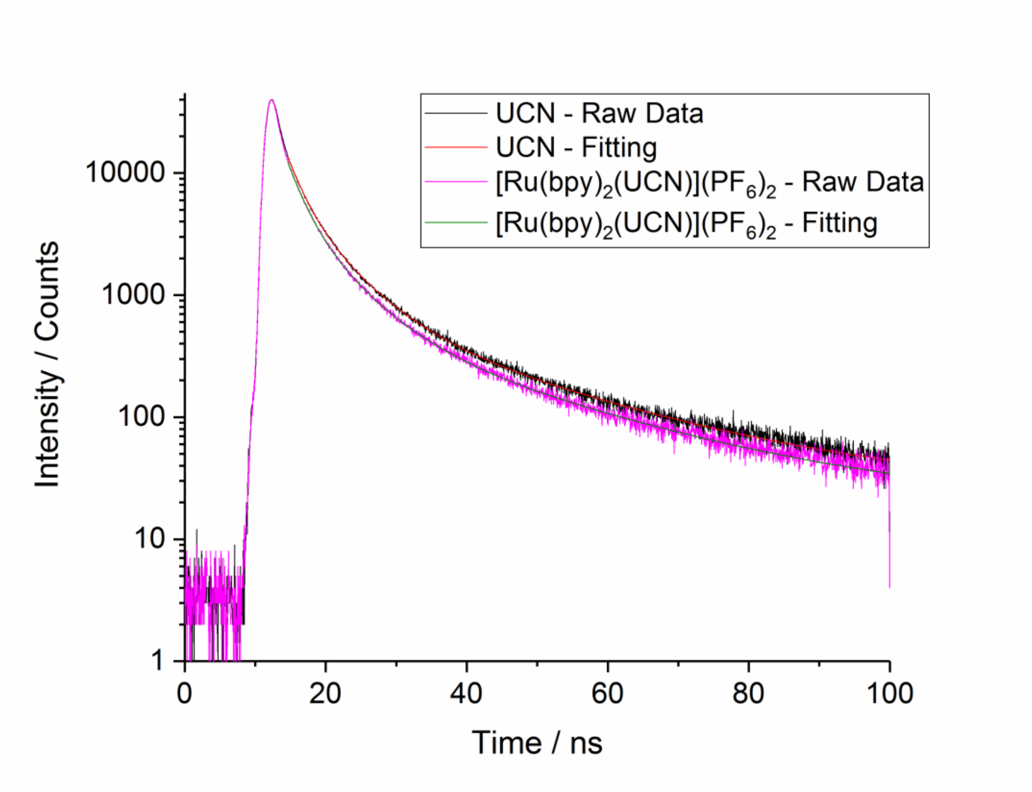

Figure 3.30: Time-resolved emission intensity of UCN and [Ru(bpy)$_2$(UCN)](PF$_6$)$_2$ in toluene dispersions under nitrogen atmosphere at λ_{ex} = 380 nm, λ_{em} = 440 nm

Figure 3.30 shows the time-resolved emission intensity of toluene dispersions of UCN and [Ru(bpy)$_2$(UCN)](PF$_6$)$_2$ at λ_{ex} = 380 nm and λ_{em} = 440 nm under nitrogen. A cut-off filter ($\lambda \geq 380$ nm) placed between the sample minimises signal due to scattering. The decay of the excited state of UCN follows an exponential curve, which has been fitted using a combination of three lifetime parameters, shown in Table 3.14. The values obtained are expected for bulk carbon nitride.[217, 218] The values of these parameters are within error of each other for both [Ru(bpy)$_2$(UCN)](PF$_6$)$_2$ and UCN, suggesting that the excited states as observed by emission spectroscopy are essentially of the same nature, arising from electronic transitions within the band gap of carbon nitride.

Table 3.14 Lifetime parameters for UCN and [Ru(bpy)$_2$(UCN)](PF$_6$)$_2$ at λ_{ex} = 380 nm, λ_{em} = 440 nm

Parameter	UCN (χ2 = 1.217)		[Ru(bpy)$_2$(UCN)](PF$_6$)$_2$ (χ2=1.183)	
	Lifetime / ns	Contribution / %	Lifetime / ns	Contribution / %
τ_1	2.07±0.04	25.4	2.05±0.04	28.0
τ_2	5.88±0.14	46.5	5.87±0.15	45.8
τ_3	22.67±0.69	28.0	22.71±0.76	26.2

3.10.2 Electron Paramagnetic Resonance (EPR) Spectroscopy

Whilst emission spectroscopy can inform about the energetics and lifetimes of excited states, very little information about the nature of the excited states can be gained from this technique. EPR spectroscopy, however, can provide information about the location, number, and mobility of electrons within semiconductor materials. In particular, EPR spectroscopy may provide evidence for the presence of paramagnetic Ru(I) or Ru(III) species which would arise from electron transfer processes between the ruthenium moieties and carbon nitride.

EPR spectroscopy of UCN and [Ru(bpy)$_2$(UCN)](PF$_6$)$_2$ was performed at 77K in both the light and dark to learn more about the nature of the excited state formed in each case (Figure 3.31). The EPR spectrum of UCN shows a single, distinct signal with g = 2.0025, compared to the slight difference in [Ru(bpy)$_2$(UCN)](PF$_6$)$_2$ where g = 2.0013. This matches previously observed EPR spectra of carbon nitride and corresponds with the signal expected from a carbon atom within the aromatic ring of the heptazine – likely arising from defects within the material.[219-221]

Upon illuminating the sample of UCN in the EPR cavity with a UV light, the overall integration of the EPR spectrum increases by almost a factor of four (Table 3.15), showing the excitation of electrons into the conduction band and the consequent increase in concentration of unpaired electrons.

In contrast to the undecorated material the [Ru(bpy)$_2$(UCN)](PF$_6$)$_2$ shows a very small increase in spin integration upon illumination with UV light, indicating a lower concentration of excited states under illumination compared to UCN. This suggests that excited states in [Ru(bpy)$_2$(UCN)](PF$_6$)$_2$ are quenched rapidly, decreasing their concentration compared to UCN.

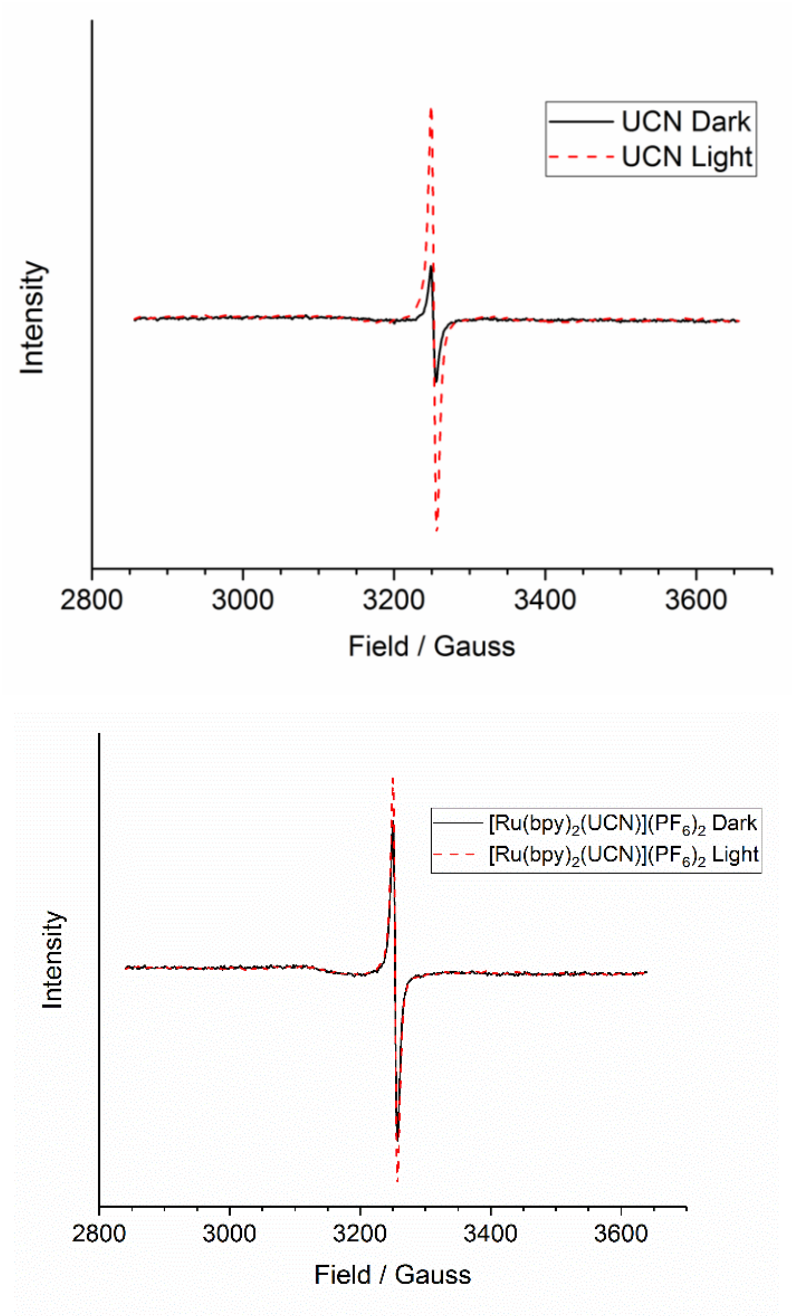

Figure 3.31: EPR spectra of UCN compared to [Ru(bpy)$_2$(UCN)](PF$_6$)$_2$ in both dark and light (100 W Xe lamp with broadband output)

Table 3.15: EPR parameters extracted from EPR spectroscopy of UCN and [Ru(bpy)$_2$(UCN)](PF$_6$)$_2$

Material	*g*	Spin integration light: Spin integration dark
UCN	2.0025 ± 0.0003	3.79
[Ru(bpy)$_2$(UCN)](PF$_6$)$_2$	2.0013 ± 0.0000	1.23

It is therefore likely that a quenching pathway exists between the metal and carbon nitride. Although EPR spectroscopy does not show evidence of a paramagnetic ruthenium species, the low concentration of the metal coupled with a short lifetime of the paramagnetic Ru species could explain the lack of this signal in the EPR spectrum. In addition, the broadening of Ru peaks can make them impossible to detect in the presence of high concentration spin systems, e.g. on titania.[222]

3.10.3 Quenching of Emission in Ruthenium-decorated Carbon Nitride

The quenching of carbon nitride excited states by interaction with solution species has been thoroughly studied. Despite numerous claims that the quenching of excited states in carbon nitride is caused exclusively by a single, specific species (including Hg^{2+}, Cu^{2+}, Ag^{2+}, Fe^{3+}, uric acid, propyl gallate, Cr (IV) and I^-) the volume of literature suggests that this is a general rather than a specific quenching mechanism.[44, 146, 147, 179, 180, 217, 223-227] In general, the proposed mechanism involves the excited state in carbon nitride decaying via non-radiative processes involving electron transfer to the solution species, however the mechanism has not been confirmed by experiment.

The results shown in this chapter suggest that the surface excited states of carbon nitride are quenched by coordinated ruthenium. This quenching manifests as a lack of activity in photochemical hydrogen evolution reactions, and the significant decrease in the number of free electrons observed by EPR under UV-illumination. It is possible that the mechanism of the quenching involves non-radiative transfer of an electron to a state in between the energy of the conduction and valence bands of carbon nitride, although further ultrafast spectroscopic methods coupled with DFT calculations would be required to confirm this as the mechanism and to gain insight as to the actual mechanism of this quenching process.

It is also possible that a non-radiative quenching mechanism, including Förster Resonance Energy Transfer (FRET) is occurring, whereby energy is transferred non-radiatively between $[Ru(bpy)_2]^{2+}$ moieties and heptazine quasi-monomers in carbon nitride.[12, 228, 229] To determine the exact method by which the quenching of the MLCT state formed in ruthenium-decorated carbon nitride occurs, further spectroscopy, including ultrafast transient absorption measurements, coupled with DFT analysis, could be performed.

3.11 Conclusion

Following results showing coordination of a rhenium moiety directly to the heptazine unit of carbon nitride, a ruthenium-containing complex fragment was coordinated to carbon nitride in the same manner. Spectroscopic measurements on the ground state of the materials support the hypothesis of bidentate (κ^2-*N,N'*) coordination of the carbon nitride to the ruthenium metal complex fragment. Two morphologies of carbon nitride, unstructured UCN and mesoporous CCN were decorated in ruthenium fragments. CCN had a higher concentration of edge-sites (i.e. free diimine-type coordination sites) compared to UCN as measured by elemental analysis and BET surface area. This correlated with CCN being able to support almost 5 times the amount of ruthenium as UCN as measured by ICP-MS.

Although the ruthenium fragments strongly improve the light absorbing properties of the decorated materials, this does not translate into either improved luminescence or improved photocatalytic activity. In contrast, no luminescence is seen to arise from the ruthenium-based absorption process, and photocatalytic hydrogen evolution activity is lost after ruthenium decoration. Time-resolved luminescence and EPR studies suggested that the coordinated ruthenium moieties allowed a highly efficient quenching of excited states formed near the surface to take place.

4 Synthesis and Characterisation of Iridium-Decorated Carbon Nitride in the Development of Novel Catalysts

4.1 Introduction

In previous chapters, the coordination chemistry of carbon nitride has been discussed, with initial efforts made to coordinate metal complex fragments to the surface of carbon nitride to augment the material properties. An unexplored application of direct coordination between carbon nitride and a metal complex is the use of carbon nitride as a coordinating support for molecular catalysts.

4.1.1 The Hydrogenation of Unsaturated Bonds

Hydrogenation reactions, whereby an unsaturated multiple bond is reduced by the addition of hydrogen, are of global importance both in research and industrial settings.[230-232] A wide variety of functional groups in different systems can be hydrogenated and as such a lot of research effort has been developing catalysts with favourable chemo-, regio- and stereo selectivity. Well known examples of transition-metal catalysts for hydrogenation include Wilkinson's catalyst, which is highly selective towards terminal alkenes, and the highly active Crabtree's catalyst (Figure 4.2).[233-236]

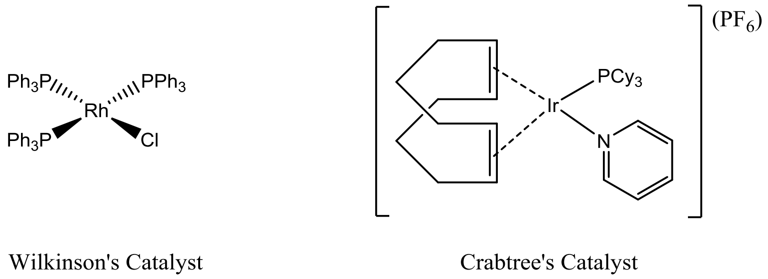

Figure 4.1: Wilkinson's catalyst and Crabtree's catalyst are key homogeneous catalysts for hydrogenation

In general, hydrogenation catalysts react with dihydrogen under elevated pressures to form reactive metal hydride species which go on to reduce saturated systems. The highly reactive nature of the metal hydride intermediate can limit their application (i.e. with poor solvent or functional group tolerance), and so iridium pentamethylcyclopentadienyl complexes, also referred to as iridium 'piano-stool' or 'half-sandwich' complex (Figure 4.2), were developed as catalysts with improved water and air stability.[237] Iridium piano-stool complexes are now established not only in direct hydrogenation, but also in the field of catalytic transfer hydrogenation (CTH).[238-243]

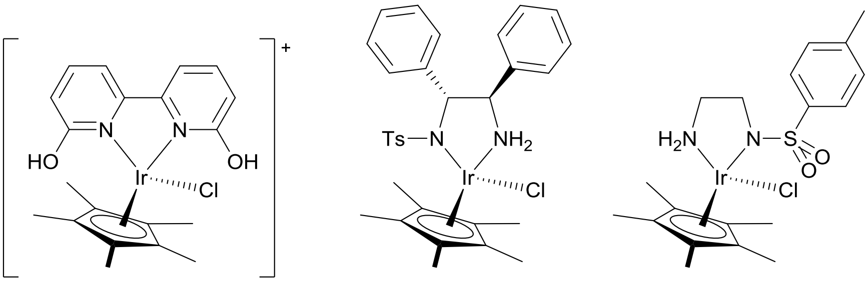

Figure 4.2: Examples of iridium 'piano stool' complexes competent in aqueous CTH reactions

In contrast to direct hydrogenation, in CTH a solution-phase hydride donor (such as an alcohol) is employed in combination with a proton donor, removing the hazards associated with high-pressure hydrogen. Iridium piano-stool catalysed CTH can even be performed in water (often using the formate anion as a hydride source), which is a positive step towards sustainable chemistry with low environmental impact.[237, 244-246]

4.1.2 Mechanism of Aqueous Catalytic Transfer Hydrogenation

The mechanism of aqueous catalytic transfer hydrogenation has been well investigated. Initial observations that hydrogenation was seen to proceed slower for more electron-rich carbonyl centres (i.e. substrates with electron donating groups) suggested the rate-determining step involves nucleophilic addition of a metal-hydride species to the electrophilic carbon centre.[240] The reaction was also shown to be highly pH-sensitive, favouring a neutral pH and with activity dropping significantly outside of the pH range 5-10.[238] A later work also showed that the acidity of the primary amine ligand moiety can affect the catalyst activity, with higher acidity of the amine relating to a faster reaction rate.[247]

Bearing the previous observations in mind, a mechanism (Scheme 4.1) was proposed.[238] Initial formate coordination is followed by elimination of carbon dioxide, forming the active metal-hydride species.[238, 248] At neutral pH (dependant on catalyst and solvent) the metal-hydride species transfers the hydride to the electrophilic carbon centre via nucleophilic addition. Protons are then transferred to the other unsaturated atom from water or another Bronsted acid. This step is where the enhancement from an acidic proximal primary amine arises, as a nearby amine can protonate the substrate more efficiently than the solvent.[247] This explains the strong pH dependence of the reaction. At high pH, metal-hydroxide species are formed which are catalytically inactive. At lower pH, formate anions protonate to formic acid, decreasing the reaction rate as the concentration of available hydride donor decreases. This explains the observation that relatively neutral pH ranges (5-10) present optimal conditions for the reaction.[238]

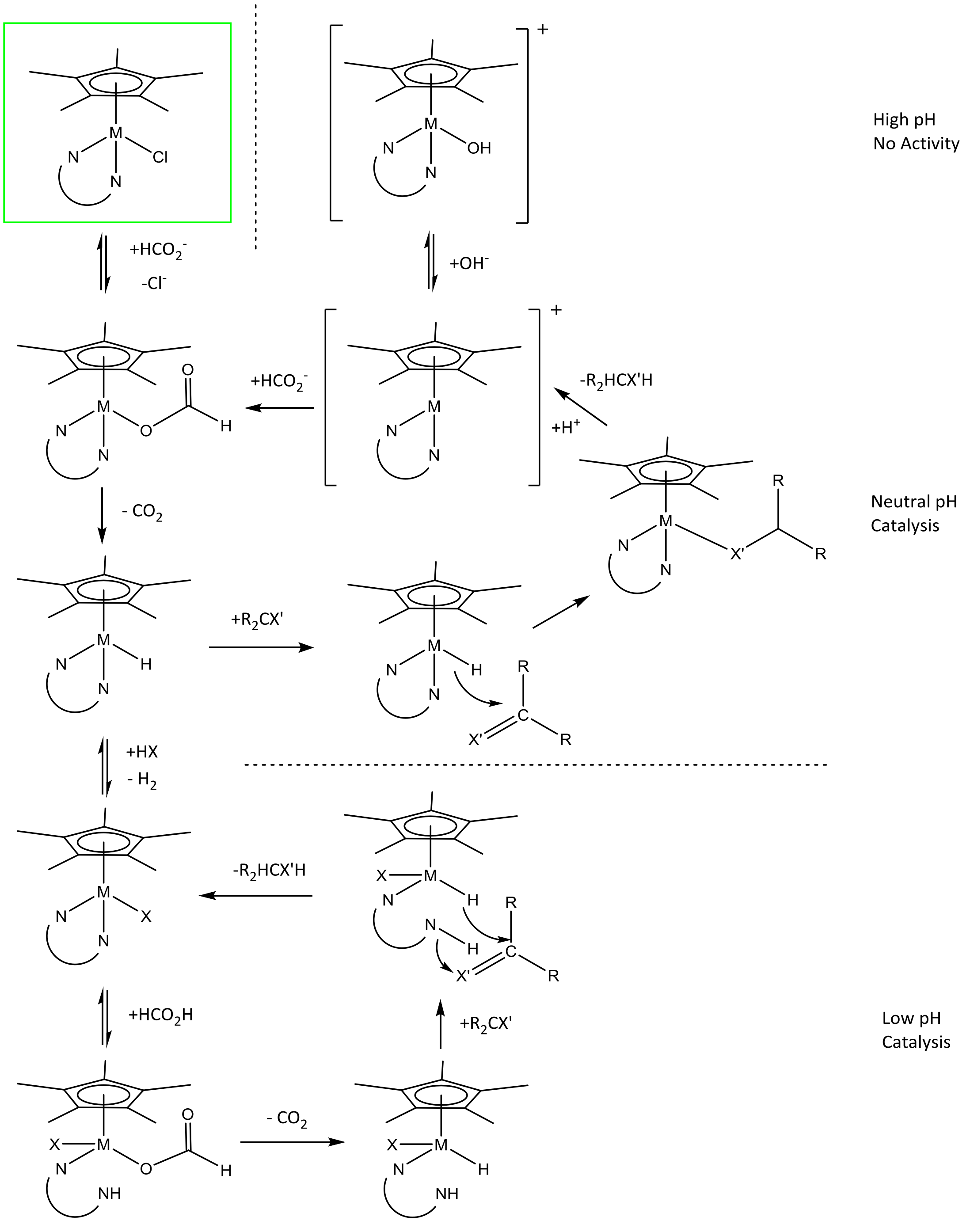

Scheme 4.1: Mechanism of Aqueous Catalytic Hydrogen Transfer (M = Ru, Ir, Rh; X = Cl^-, HCO_2^-; X' = O, NH)[238]

4.1.3 Combining Heterogeneous and Homogeneous Chemistry

The high cost of iridium presents an economic barrier to widespread application of CTH chemistry. Improving the recyclability of these catalysts is an active area of research, involving the anchoring of catalytic sites to heterogeneous substrates to ease catalyst separation, recovery, and reuse. Catalysts for CTH reactions have already been covalently grafted to several solid-state supports, including carbon nanotubes, polystyrene, silica and zirconium-based metal-organic frameworks.[249-253] Li et. al. grafted iridium piano-stool complexes onto the surface of magnetic Fe_3O_4 nanoparticles.[254] The magnetic nanoparticles allowed facile recycling of the catalyst for a reported ten cycles with minimal activity loss. Related rhodium-based CTH catalysts grafted to silica have also been shown to keep enantioselectivity after twelve cycles.[255]

Iridium piano-stool complexes are also of interest as molecular water oxidation catalysts.[256, 257] Silica co-polymerised with 2,2'-bipyridine moieties has been shown to coordinate to an iridium piano-stool complex fragment to result in a recyclable water oxidation catalyst.[258] In these hybrid systems, the activity of the homogeneous catalyst was retained, but the advantages of heterogeneous catalysis including recyclability, can also be utilised.

In the cases listed above, multistep syntheses are required to obtain the resulting catalyst, which are time- and resource-intensive. For instance, grafting molecular catalysts to silica involves the incorporation of silicon alkoxides into the structure of the pre-catalyst, complicating the synthesis of the catalyst. Incorporation of metal fragments into bipyridine-containing silica has a simpler methodology, but the initial synthesis of the silica involves the use of an expensive organosilicon compound.[259]

Direct coordination to carbon nitride represents a much more accessible supporting method, with a simple two-step procedure. Carbon nitride has a simple synthesis from urea, a cheap, green precursor.[11, 39] Coordination of iridium piano-stool complexes to carbon nitride has been attempted in previous works by simple heating of an iridium precursor at reflux with carbon nitride, but a low iridium content of the resulting material meant that no characterisation further than ICP-MS was reported. However, a heptazine-based framework was also synthesised, which was capable of supporting a higher loading of iridium and was used successfully as a recyclable catalyst.[260]

Structurally related to heptazine, naphthyridine (napy) ligands are capable of exhibiting multiple coordination modes to metal centres.[261] Iridium piano-stool complexes displaying the monodentate, bidentate and bridging coordination modes have all been synthesised previously.[262]

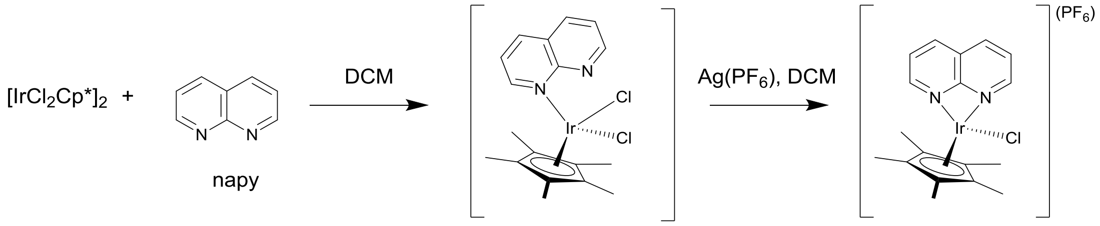

Scheme 4.2: Reaction between [IrCl$_2$Cp]$_2$ and 1,8-naphthyridine (napy) and effect of reacting with Ag(PF$_6$)*[262]

The reaction between 1,8-naphthyridine and [IrCl$_2$Cp*]$_2$ in DCM has been reported to result in the formation of [IrCl$_2$Cp*(napy)] with monodentate coordinating naphthyridine ligand (Scheme 4.2). Addition of one equivalent of Ag(PF$_6$) to [IrCl$_2$Cp*(napy)] removes one chloride ligand from the complex and drives bidentate coordination of the iridium to the 1,8-napthyridine.[262] This previous work demonstrates that iridium half-sandwich fragments readily coordinate to naphthyridine ligands, and therefore provides a good basis for investigating the interaction between iridium half-sandwich fragments and carbon nitride.

4.1.4 Objectives

Carbon nitride is a material which has been shown to coordinate to metal centres through the diimine functionality in the heptazine monomers, with the connecting amine groups largely uninvolved in coordination. Exploiting the coordination properties of carbon nitride with the aim to use the material as a solid support via direct coordination to a metal centre in catalyst design has not yet been reported. Iridium-piano stool moieties are active catalysts for both transfer and direct hydrogenation reactions, especially in complexes with bidentate nitrogen ligands and proximal proton donors and acceptors (i.e. amines).[247]

The iridium-piano stool fragment, [IrCp*Cl], is therefore a good candidate for a metal complex fragment to combine with carbon nitride, as the resulting material is likely to have catalytic activity for both transfer and direct hydrogenation. It is suggested that, as with previously observed naphthyridine complexes, there are multiple accessible coordination modes between carbon nitride and iridium piano-stool fragments. Determining the nature of the carbon nitride-iridium interaction will be undertaken with this established coordination chemistry in mind. Carbon nitride also contains a large number of amine sites which are proximal to the coordination sites, which may assist in hydrogenation reactions.

Carbon nitride will be decorated with iridium-piano stool moieties and characterised to investigate the interaction between the iridium and the carbon nitride. In addition, the resulting material will be evaluated as a catalyst in hydrogenation reactions with an aim to providing a novel approach to synthesising recyclable catalysts via coordination of a metal centre to carbon nitride.

4.2 Synthesis of $[IrCl_2Cp^*(UCN)]$ and $[IrClCp^*(UCN)](PF_6)$

$[IrCl_2Cp^*]_2$ was selected as an established and available iridium precursor. UCN, urea-derived carbon nitride, was selected as the carbon nitride source due its scalable, rapid synthesis. Following previous experimental conditions from chapters 2 and 3, UCN was decorated with an $IrCl_2Cp^*$ fragment by heating base-treated UCN at reflux in a solution of $[IrCl_2Cp^*]_2$ under nitrogen (Scheme 4.3). The decorated material, $[IrCl_2Cp^*(UCN)]$, was isolated after 24 hours by filtration. Excess, non-surface bound iridium was removed by washing with ethanol and water.

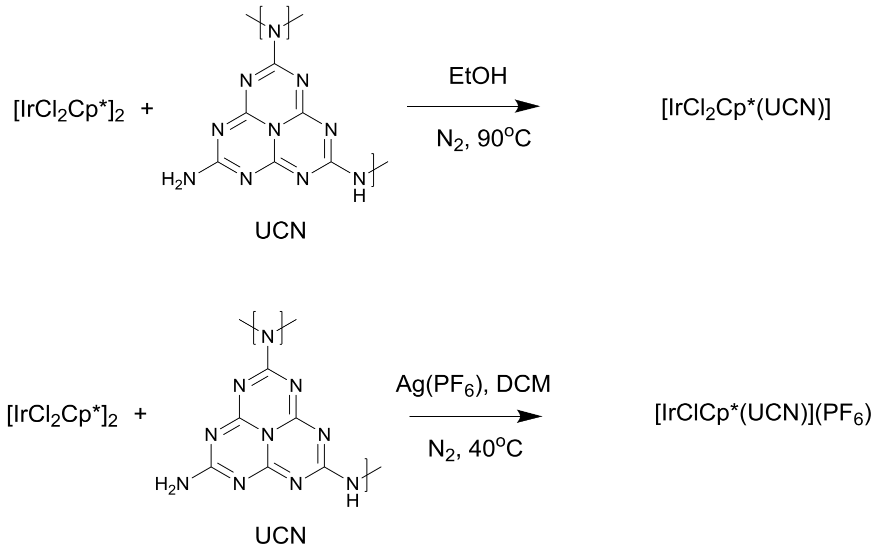

Scheme 4.3: Synthesis of $[IrCl_2Cp^*(UCN)]$ and $[IrClCp^*(UCN)](PF_6)$

To investigate the denticity of the coordination between iridium and carbon nitride further, carbon nitride was also decorated with iridium fragments after the removal of one equivalent of the chloride anion from the precursor (Scheme 4.3). Chloride removal by precipitation as AgCl was performed before coordination of iridium to carbon nitride to minimise impurities in the resulting material.

If the coordination between UCN and naphthyridine are comparable, chloride removal will drive coordination to be bidentate in the resulting $[IrClCp^*(UCN)](PF_6)$. With this in mind, comparing $[IrCl_2Cp^*(UCN)]$ and $[IrClCp^*(UCN)](PF_6)$ may provide further insight into the iridium environment in each material.

4.3 Characterisation of [IrCl$_2$Cp*(UCN)] and [IrClCp*(UCN)](PF$_6$)

4.3.1 Powder X-Ray Diffraction of [IrCl$_2$Cp*(UCN)] and [IrClCp*(UCN)](PF$_6$)

Initial characterisation of PXRD (Figure 4.3) was performed to whether the reaction of UCN with [IrCl$_2$Cp*]$_2$ caused structural changes to the UCN.

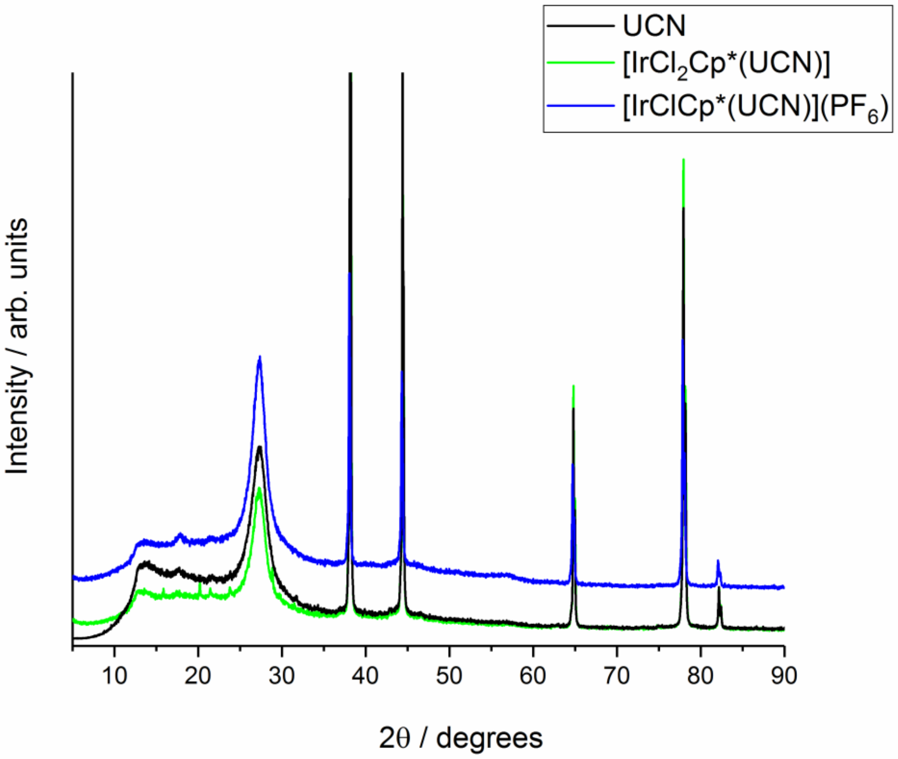

Figure 4.3: PXRD patterns of UCN, [IrCl$_2$Cp(UCN)], and [IrClCp*(UCN)](PF$_6$)*

PXRD patterns for [IrClCp*(UCN)](PF$_6$) compared to UCN and [IrCl$_2$Cp*(UCN)] are shown in Figure 4.3. As with previous metal systems, the peak at 27.4° in UCN is unshifted in both [IrCl$_2$Cp*(UCN)] and [IrClCp*(UCN)](PF$_6$), suggesting that the iridium is again not intercalating between the planes of the UCN and is instead primarily surface-bound.[7]

The absence of any significant crystalline impurities is consistent with the hypothesis of coordination of individual, molecular iridium complex fragments to the surface of carbon nitride.

4.3.2 Inductively Coupled Plasma Mass Spectroscopy (ICP-MS) and Elemental Analysis of [IrCl$_2$Cp*(UCN)] and [IrClCp*(UCN)](PF$_6$)

Having established a lack of crystalline impurities via PXRD, the elemental composition of the two composite materials was measured. Samples of UCN, and [IrCl$_2$Cp*(UCN)] and [IrClCp*(UCN)](PF$_6$) were analysed by ICP-MS to measure the content of iridium by mass. No significant quantity of iridium was measured in untreated UCN, but the iridium concentration of [IrCl$_2$Cp*(UCN)] was measured to be 13.4 ± 0.3 mg g^{-1}. A very similar loading was observed for [IrClCp*(UCN)](PF$_6$) (Table 4.1).

Table 4.1: Iridium content of UCN, [IrCl$_2$Cp(UCN)] and [IrClCp*(UCN)](PF$_6$)*

Sample	Iridium Content / mg g^{-1}	Iridium Content / mmol mg^{-1}
UCN	0	0
[IrCl$_2$Cp*(UCN)]	13.4 ± 0.3	69.8
[IrClCp*(UCN)](PF$_6$)	13.3	69.3

Samples of UCN, [IrCl$_2$Cp*(UCN)] and [IrClCp*(UCN)](PF$_6$) were also analysed for chlorine and fluorine content (summarised in Table 4.2). Base-treated, dry UCN contains approximately 0.5% by mass chlorine, possibly originating from an impurity in the urea precursor concentrated during the thermal condensation. The chlorine content of [IrCl$_2$Cp*(UCN)] and [IrClCp*(UCN)](PF$_6$) are corrected by subtracting the chlorine content measured in the undecorated carbon nitride. Significant variation is observed due to the low concentration of chlorine and fluorine approaching the instrument limitations.

The iridium loading of carbon nitride, as measured by ICP-MS, is of the same order of magnitude as observed in other metal-fragment decorated samples of carbon nitride.[260] Similarity in metal loading in [IrClCp*(UCN)](PF$_6$) and [IrCl$_2$Cp*(UCN)] suggests that the concentration of available sites for iridium-coordination on the UCN is similar for each reaction. This implies that the same type of site on the UCN is involved in coordination to the iridium in each material, which is suggested to be the edge-sites (i.e. diimine sites) of the carbon nitride.

Table 4.2: Chlorine and Fluorine analysis of UCN, [$IrCl_2Cp^*(UCN)$] and [$IrClCp^*(UCN)$](PF_6)

Sample	Cl Content / mmol mg^{-1}	Corrected Cl Content / mmol mg^{-1}	F Content / mmol mg^{-1}	Ir: Cl: F Ratio
UCN	138 ± 27	0	0	-
[$IrCl_2Cp^*(UCN)$]	265 ± 9	127 ± 28	0	1: 1.9: 0
[$IrClCp^*(UCN)$](PF_6)	212 ± 37	74 ± 45	368 ± 89	1: 1.1: 5.3

The ratios of Ir: Cl: F measured for each sample are within error of the molecular formula proposed in both [$IrCl_2Cp^*(UCN)$] and [$IrClCp^*(UCN)$](PF_6). [$IrCl_2Cp^*(UCN)$] displays two equivalents of chlorine per equivalent of iridium, whereas in [$IrClCp^*(UCN)$](PF_6), one of the equivalents of Cl is replaced with almost 6 equivalents of fluorine. This is consistent with the replacement of Cl by $(PF_6)^-$.

4.3.3 Surface Analysis by Zeta-Potential

Following elemental analysis of [$IrCl_2Cp^*(UCN)$] and [$IrClCp^*(UCN)$](PF_6), the surface of iridium-decorated carbon nitrides were analysed by zeta potential to measure the surface charge of particles. If the interaction between the iridium and carbon nitride was the same in both materials, the surface of each material would be expected to have the same zeta-potential.

Compared to UCN, both [$IrCl_2Cp^*(UCN)$] and [$IrClCp^*(UCN)$](PF_6) demonstrate a significantly higher particle surface charge (Table 4.3). This supports the hypothesis that the iridium is distributed at the surface of the carbon nitride. However, the values measured for [$IrCl_2Cp^*(UCN)$] and [$IrClCp^*(UCN)$](PF_6) are significantly different.

Table 4.3: Zeta-potential measurement of carbon nitrides

Sample	Surface Zeta Potential / mV
Raw UCN	-22.1 ± 0.3
NH_3-treated UCN	-28.7 ± 0.8
[$IrCl_2Cp^*(UCN)$]	27.7 ± 0.8
[$IrClCp^*(UCN)$](PF_6)	32.5 ± 0.3

It can be speculated that the difference in the zeta potential between [IrClCp*(UCN)](PF$_6$) and [IrCl$_2$Cp*(UCN)] could arise from different coordination equilibria positions occurring in the two materials. The less positive value for [IrCl$_2$Cp*(UCN)] could be interpreted as due to the coordination of an extra equivalent of chloride to the iridium reducing the bulk positive charge at the surface of carbon nitride and favouring monodentate coordination in favour of bidentate in [IrClCp*(UCN)](PF$_6$) – this is observed for the established naphthyridine complexes.[262] However, zeta-potential of colloids is a bulk measurement and is strongly affected by several factors, including particle size, shape, and conductivity.[140, 198]

4.3.4 Solid-State NMR Spectroscopy

Although the bulk composition and surface properties have been investigated, the interaction between the iridium and carbon nitride has not yet be established. To probe this interaction, ^{13}C CP-MAS NMR can be employed to specifically investigate the Cp* signal.

The solid-state ^{13}C CP-MAS NMR spectra of UCN, [IrCl$_2$Cp*(UCN)], [IrClCp*(UCN)](PF$_6$) and [IrCl$_2$Cp*]$_2$ are shown in Figure 4.4 and key signals are listed in Table 4.4. The peaks at 164.6 ppm and 156.7 ppm due to carbon nitride are also present in [IrCl$_2$Cp*(UCN)] and [IrClCp*(UCN)](PF$_6$) as expected.[7] The presence of the additional resonances at 88.2 ppm and 12.0 ppm for [IrCl$_2$Cp*(UCN)] and 89.3 ppm and 9.4 ppm for [IrClCp*(UCN)](PF$_6$) are indicative of Cp* moieties within the materials, and the chemical shifts of the Cp* groups are consistent with Cp*ligands coordinated to iridium (III) sites.[159 256, 258]

Table 4.4: ^{13}C CP-MAS NMR shifts of Cp ligands in Iridium-containing compounds and supported materials*

Samples	Cp* ^{13}C Shift Inner (**C**CH$_3$)$_5$ / ppm	Cp* ^{13}C Shift Inner (C**C**H$_3$)$_5$ / ppm
[IrCl$_2$Cp*]$_2$	87.1	11.1
[IrCl$_2$Cp*(UCN)]	88.2	12.0
[IrClCp*(UCN)](PF$_6$)	89.3	9.4

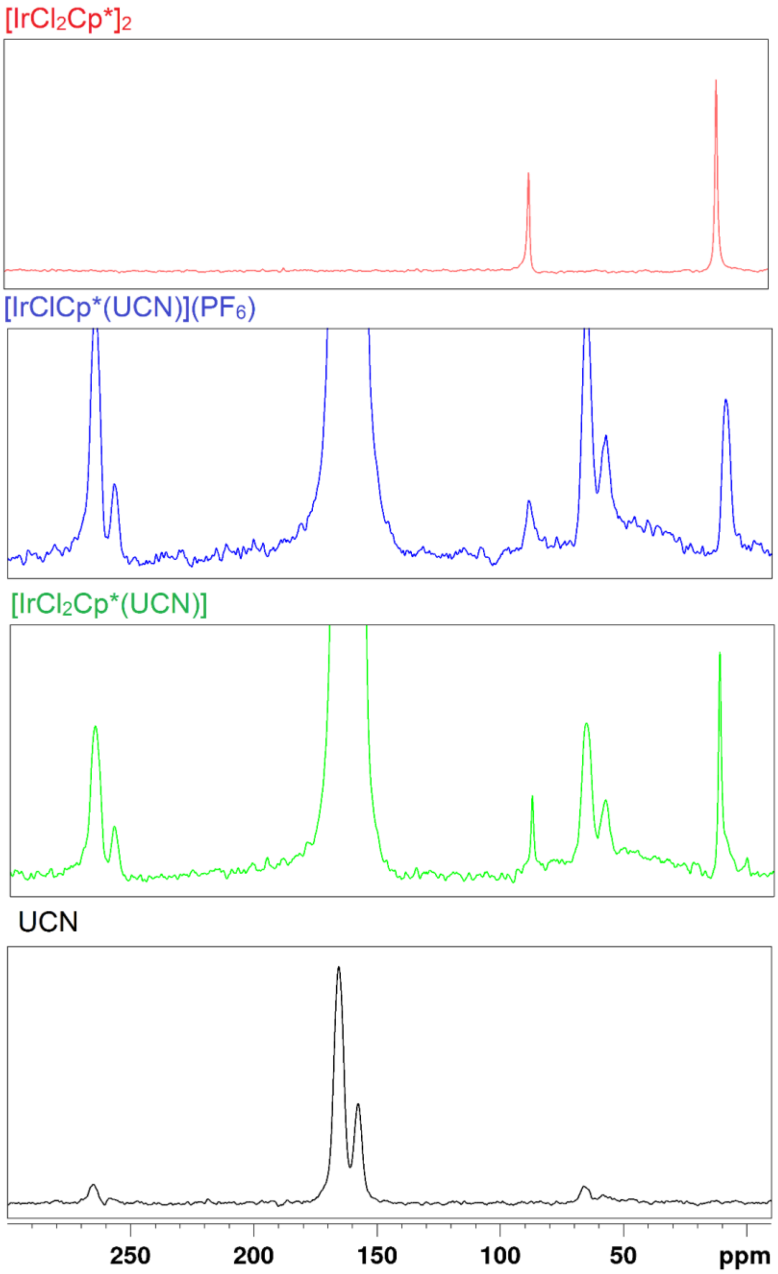

Figure 4.4: ^{13}C CP-MAS NMR Spectrum of (top to bottom) [IrCl$_2$Cp]$_2$, [IrCl$_2$Cp*(UCN)] and UCN. Adamantane (29.5 ppm) used as external reference.*

The solid-state ^{13}C CP-MAS NMR experiment therefore indicates that the [IrCl$_2$Cp*]$_2$ has coordinated to the carbon nitride and that the iridium-cyclopentadienyl interaction is conserved in the coordinated metal fragment in both iridium-decorated materials.

The spectra show a slight but significant difference between [IrClCp*(UCN)](PF$_6$) (89.3, 9.4 ppm) and [IrCl$_2$Cp*(UCN)] (88.2, 12.0 ppm) in the resonances associated with the Cp* ligand. The slightly higher chemical shift of the ^{13}C CP-Mas resonance for the internal carbon environment in the Cp* ligand observed for $[IrClCp^*(UCN)](PF_6)$ compared to $[IrCl_2Cp^*(UCN)]$ echoes the slightly higher ^1H resonance for the Cp* observed in $[IrClCp^*(napy\text{-}\kappa^2N,N')](PF_6)$ compared to $[IrCl_2Cp^*(napy\text{-}\kappa N)]$ (see section 4.4.3).

This is consistent with a hypothesis of a different mode of coordination between the heptazine and the iridium in the two iridium-decorated carbon nitrides. It is tentatively proposed that the coordination mode between the iridium fragment and the carbon nitride is monodentate in $[IrCl_2Cp^*(UCN\text{-}\kappa N)]$ and bidentate in $[IrClCp^*(UCN\text{-}\kappa^2N,N')](PF_6)$.

4.3.5 Infrared Spectroscopy

Infrared spectroscopy can also provide valuable insight into metal coordination. Figure 4.5 shows the infrared spectra of UCN, $[IrCl_2Cp^*(UCN)]$ and $[IrClCp^*(UCN)](PF_6)$. The ATR-IR spectrum of UCN has been discussed previously, and no significant differences from UCN are seen in either the ATR-IR of $[IrCl_2Cp^*(UCN)]$ or $[IrClCp^*(UCN)](PF_6)$.[7, 21] The low concentration of the iridium, coupled with the high infrared activity inherent to the UCN, means that no structural information about $[IrCl_2Cp^*(UCN)]$ or $[IrClCp^*(UCN)](PF_6)$ can be gained via infrared spectroscopy.

In the synthesis of $[IrClCp^*(UCN)](PF_6)$, one equivalent of chloride in the precursor, $[IrCl_2Cp^*]_2$, is proposed to be replaced with an equivalent of $(PF_6)^-$ anion. However, ATR-IR spectroscopy (Figure 4.6) does not clearly show the presence of the infrared mode corresponding to the $(PF_6)^-$ anion in $[IrClCp^*(UCN)](PF_6)$. This is likely a result of the low concentration of iridium, and subsequently PF_6^-, present in the material, as the presence of fluorine in $[IrClCp^*(UCN)](PF_6)$ has already been confirmed by elemental analysis.

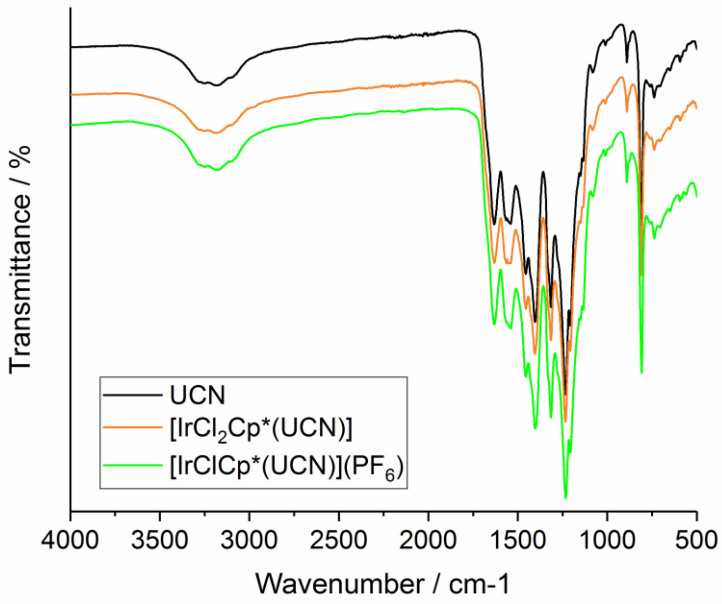

Figure 4.5: ATR-IR spectra comparing UCN to [$IrCl_2Cp^*(UCN)$] and IrClCp*(UCN)](PF_6)

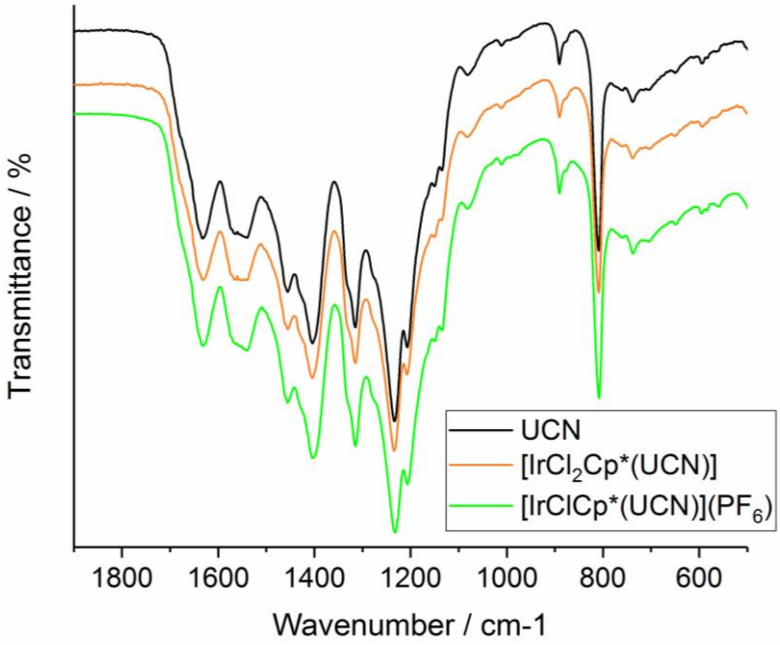

Figure 4.6: Expanded ATR-IR spectra of UCN to [$IrCl_2Cp^*(UCN)$] and [IrClCp*(UCN)](PF_6)

4.3.6 X-Ray Photoelectron Spectroscopy

XPS was performed on samples of [$IrCl_2Cp^*(UCN)$] and [$IrClCp^*(UCN)$](PF_6) to gain further structural and electronic information, summarised in Table 4.5. As expected, the N 1s regions (Figure 4.7) of the XPS spectra look very similar in UCN, [$IrCl_2Cp^*(UCN)$] and [$IrClCp^*(UCN)$](PF_6), with no additional nitrogen environments added upon iridium decoration.[19]

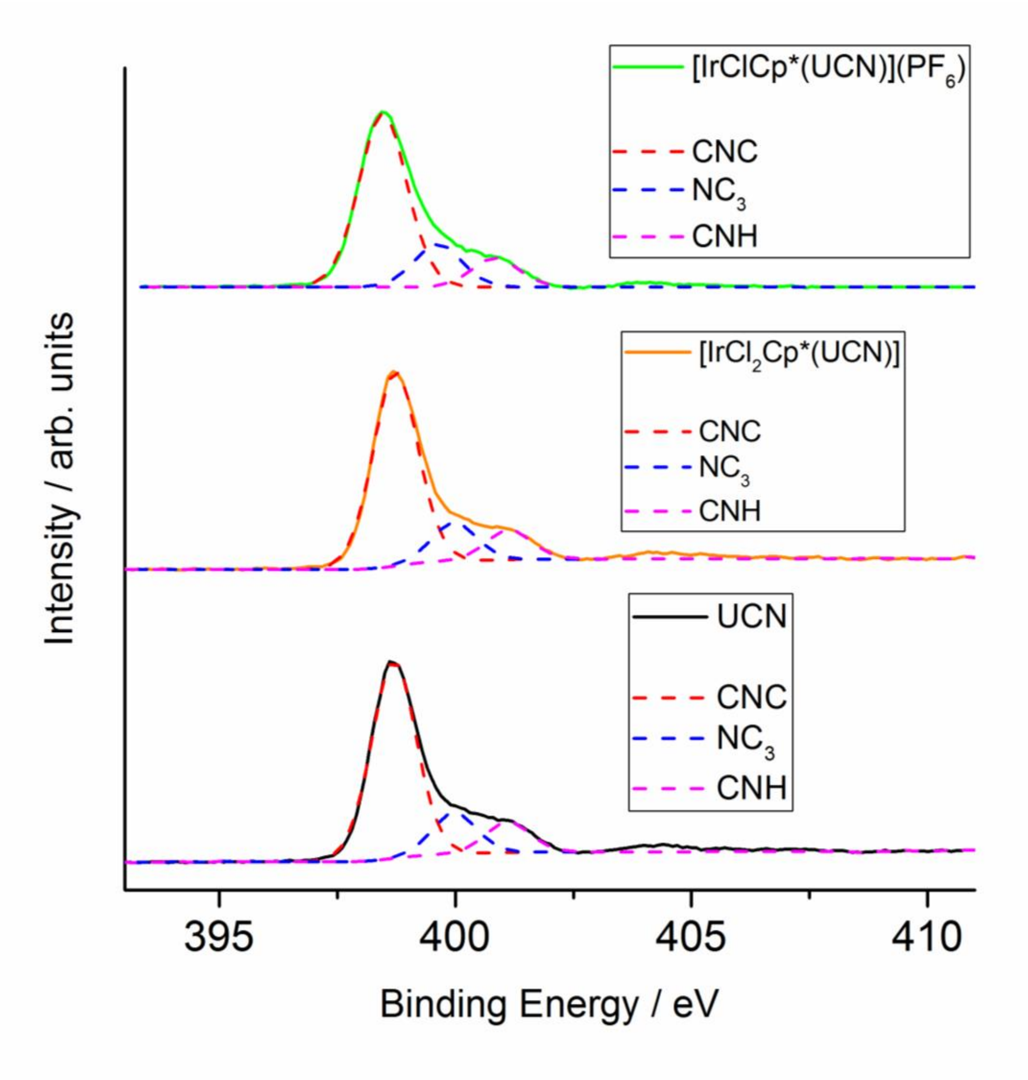

Figure 4.7: XPS (N 1s region) of (top to bottom) [$IrClCp^*(UCN)$](PF_6), [$IrCl_2Cp^*(UCN)$] and UCN

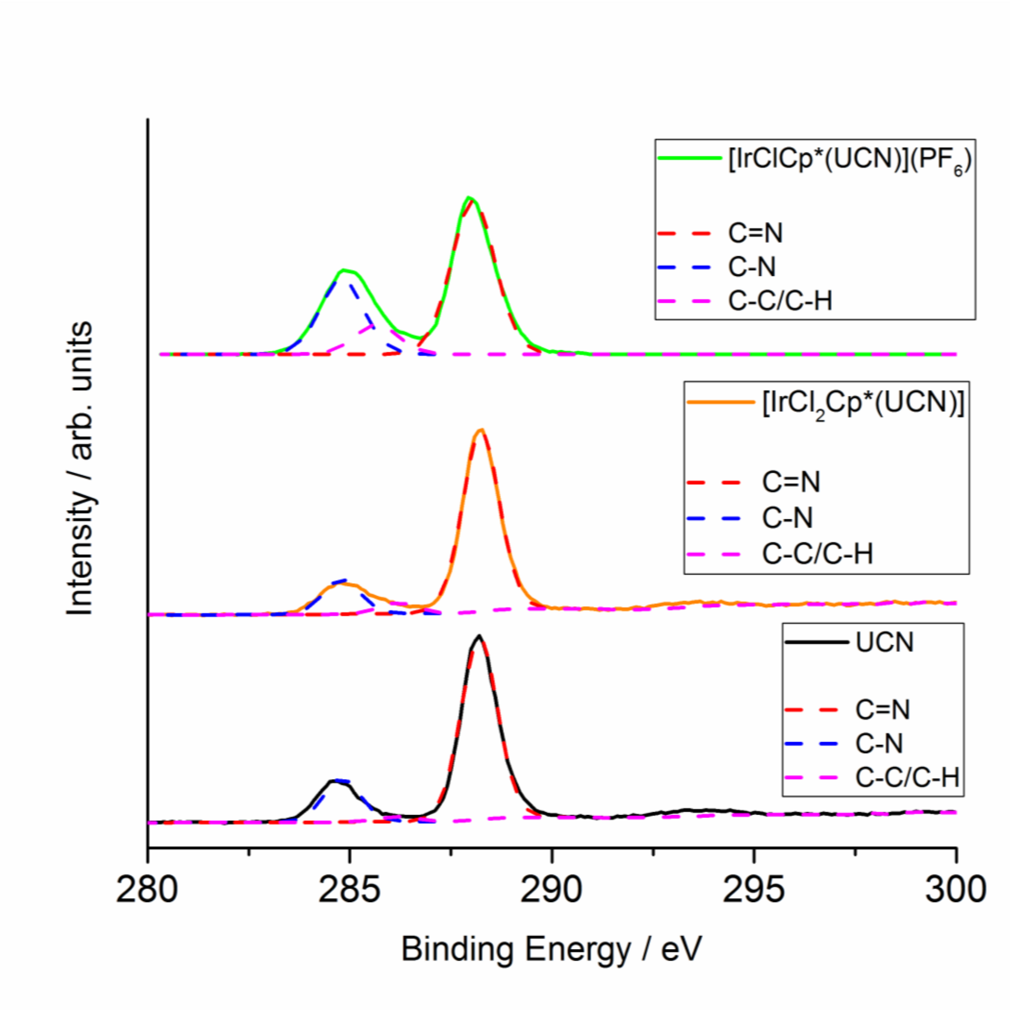

Figure 4.8: XPS (C 1s region) of (top to bottom) [IrClCp(UCN)](PF_6), [IrCl$_2$Cp*(UCN)] and UCN*

In contrast, the C 1s region (Figure 4.8) of [IrCl$_2$Cp*(UCN)] and [IrClCp*(UCN)](PF_6) show a different peak shape compared to UCN. This can be explained by the inclusion of a new peak (286.2 eV in [IrCl$_2$Cp*(UCN)], 285.7 eV in [IrClCp*(UCN)](PF_6)), consistent with the C-H/C=C environments in the Cp* rings. As XPS is surface-sensitive, the observation of Cp* supports the hypothesis of surface-localised metal-coordinated Cp* ligands. Unlike in the previous chapters, where shake-up peaks are observed for metal-decorated systems, no such features are observed in the spectrum of either [IrCl$_2$Cp*(UCN)] or [IrClCp*(UCN)](PF_6).

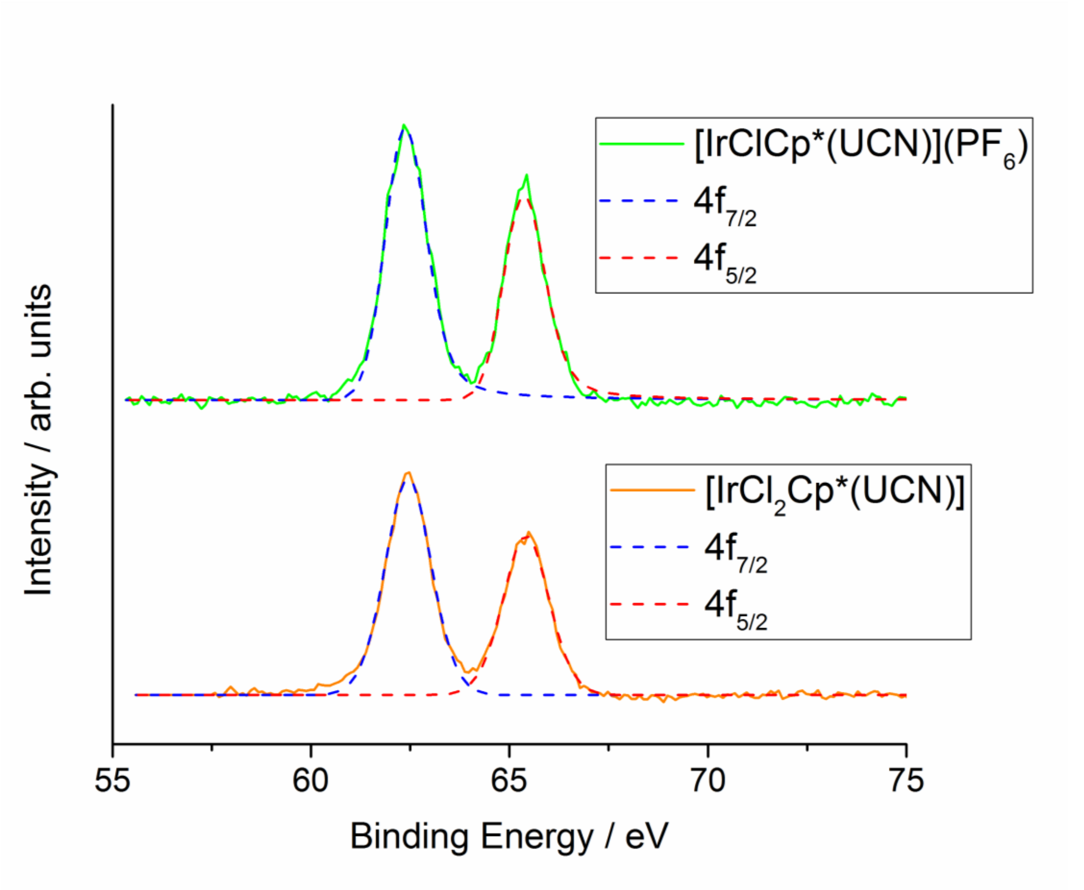

Figure 4.9: XPS (Ir 4f region) of [IrCl$_2$Cp(UCN)]*

The Iridium 4f region (Figure 4.9) shows peaks centred at 65.4 and 62.5 eV in both [IrCl$_2$Cp*(UCN)] and [IrClCp*(UCN)](PF$_6$), which is consistent with an iridium (III) Cp* complex immobilised onto the surface of the carbon nitride.[263] The XPS spectra (Ir 4f region) do not show any evidence of metallic iridium or of any iridium oxide species, suggesting that the molecular moiety is the only source of iridium present on [IrCl$_2$Cp*(UCN)] and [IrClCp*(UCN)](PF$_6$).[264] The narrow FWHM is also an indicator of a single iridium species in each case.

Although the XPS peaks in the Ir 4f region appear in the same place for each of the two materials, this does not directly indicate the same chemical environment at iridium in each material. ^{13}C CP-MAS, a more sensitive technique, shows that the magnetic environment in [IrCl$_2$Cp*(UCN)] and [IrClCp*(UCN)](PF$_6$) is very similar, but different (section 4.3.4). As XPS probes core electrons, which are highly shielded from the environment around the iridium atom, the similar environments can be expected to give signals in XPS which appear identical.

Table 4.5: Tabulated XPS peaks for UCN, [IrCl$_2$Cp(UCN)] and [IrClCp*(UCN)](PF$_6$)*

Sample	Region	Peak / eV	FWHM / eV	Assignment
UCN	N 1s	398.7	1.14	CNC
		400.0	1.29	NC_3
		401.1	1.46	CNH
	C 1s	288.2	1.11	C=N
		286.1	1.03	C=O
		284.8	1.07	C-NH

Sample	[IrClCp*(UCN)](PF$_6$)		[IrCl$_2$Cp*(UCN)]		
Region	Peak / eV	FWHM / eV	Peak / eV	FWHM / eV	Assignment
N 1s	398.5	1.21	398.7	1.15	CNC
	399.6	1.21	400.0	1.32	NC_3
	400.8	1.21	401.1	1.51	CNH
C 1s	288.1	1.30	288.3	1.15	CNC
	285.7	1.30	286.2	1.09	C-C/C-H
	284.8	1.30	284.8	1.12	C-NH
Ir 4f	65.4	1.27	65.4	1.38	$4f_{5/2}$
	62.4	1.27	62.5	1.37	$4f_{7/2}$

4.3.7 SEM of UCN and [$IrCl_2Cp^*(UCN)$]

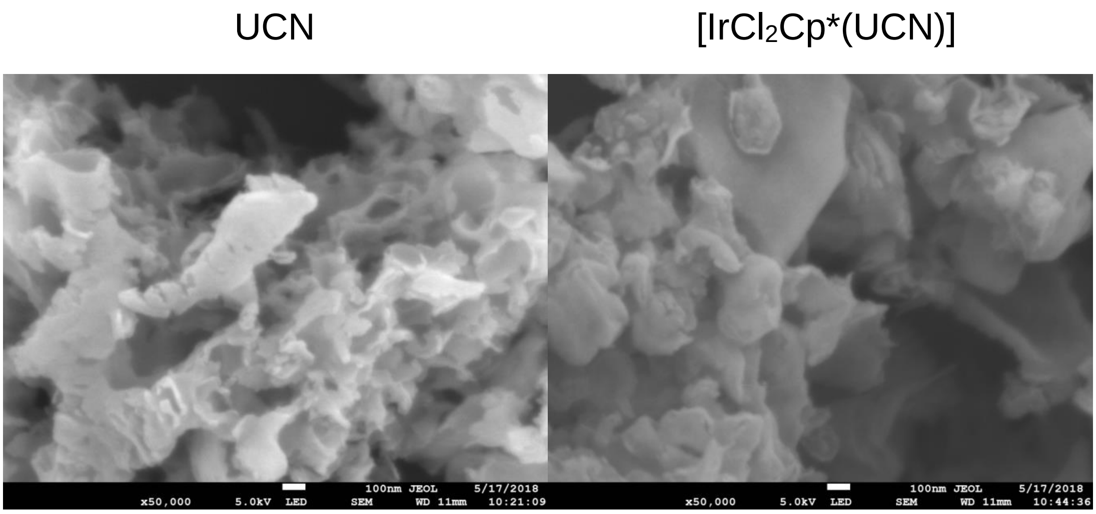

Figure 4.10: Representative SEM images (x50,000) of UCN and [$IrCl_2Cp^*(UCN)$]

Scanning electron microscopy (SEM) was performed to gain insight of the morphology of UCN and [$IrCl_2Cp^*(UCN)$] (Figure 4.10). As for previous metal-carbon nitride systems, the morphology of carbon nitride is not observed to change significantly after metal treatment and no impurities are observed.

4.3.8 Diffuse Reflectance

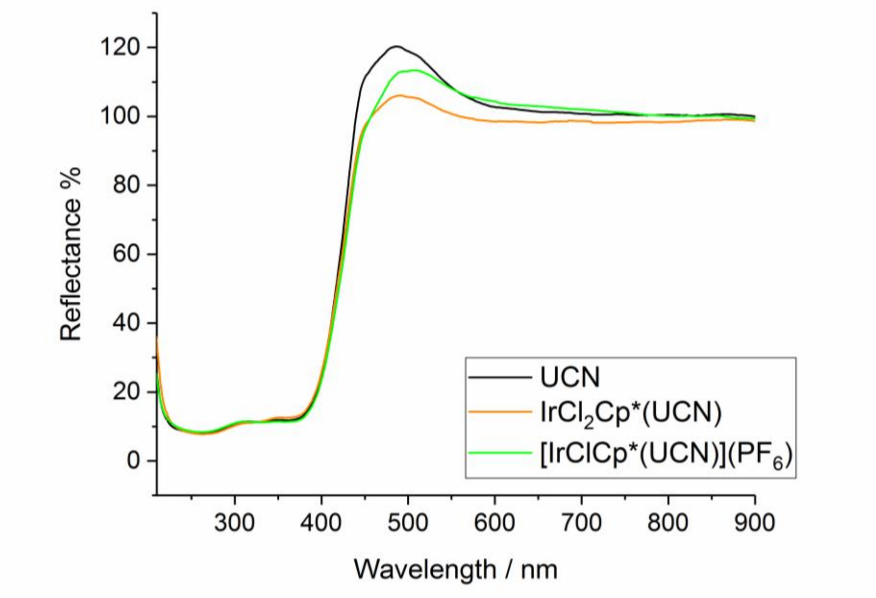

Figure 4.11: Diffuse reflectance spectroscopy of UCN, [$IrCl_2Cp^*(UCN)$] and [$IrClCp^*(UCN)$](PF_6)

The diffuse reflectance spectra of UCN as compared to [IrCl$_2$Cp*(UCN)] and [IrClCp*(UCN)](PF$_6$) is shown in Figure 4.11. The principal difference is the decrease in the reflection peak at 460 nm after iridium decoration. The reflection in this region is greater than 100% due to the strong luminescence of carbon nitride, and a decrease in this region may simply be caused by the quenching of UCN fluorescence.[44, 223, 265] It is also possible that absorption is occurring as low-lying d-electrons are promoted to the valence band of the carbon nitride, reducing the overall reflectance. The small differences in the reflectance spectra of [IrCl$_2$Cp*(UCN)] and [IrClCp*(UCN)](PF$_6$) may add support to the hypothesis of different ligand denticity in each material.

4.4 Synthesis and Characterisation of Molecular Analogues for [IrCl$_2$Cp*(UCN)] and [IrClCp*(UCN)](PF$_6$).

4.4.1 Synthesis of a molecular analogue to [IrCl$_2$Cp*(UCN)]

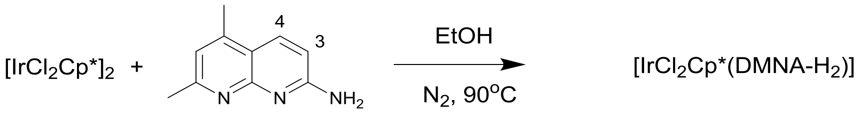

Scheme 4.4: Reaction between [IrCl$_2$Cp]$_2$ and DMNA in EtOH*

As with previous decorated carbon nitrides, synthesis of a molecular analogue using DMNA as ligand was attempted using the conditions used to synthesise [IrCl$_2$Cp*(UCN)]. In contrast to previous examples, which were simple ligand complexations which ran selectively, multiple products are observed in the reaction outlined in Scheme 4.4 – the isolated product is shown, and the ^{1}H NMR spectra is displayed in Figure 4.12.

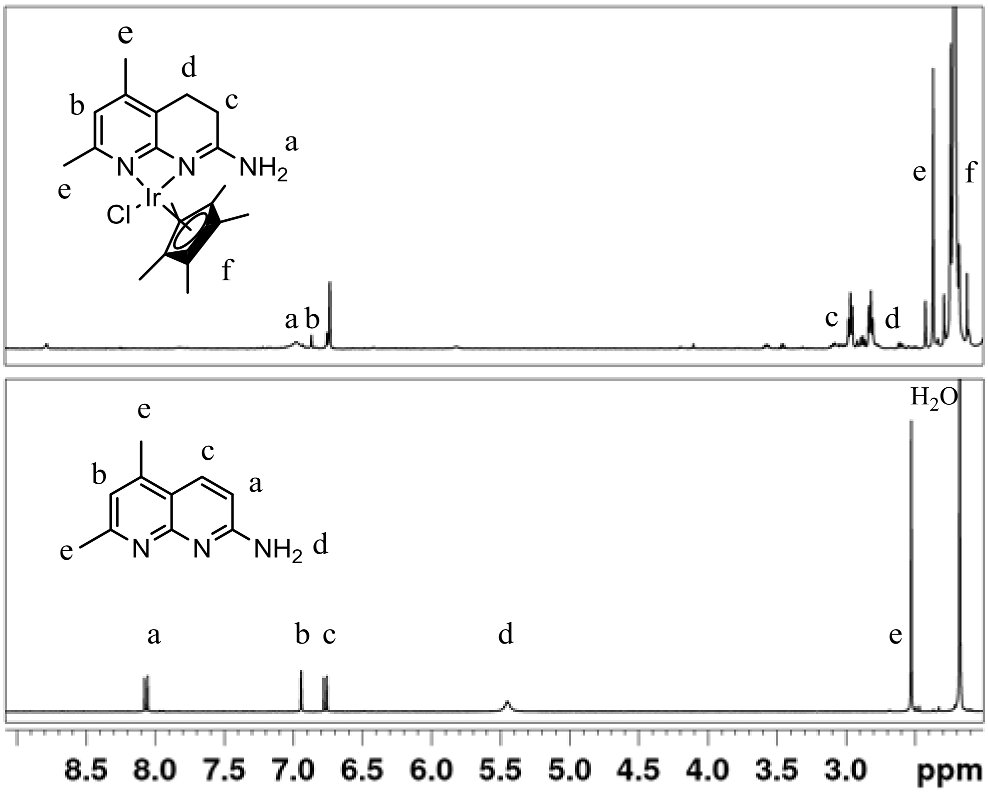

Figure 4.12: 1H NMR spectrum (d_3-MeCN) of [$IrCl_2Cp^*$(DMNA-H_2)] (top) and DMNA (bottom)

The doublet resonances at 8.07 and 6.77 ppm in the ^1H NMR spectrum of DMNA are gone in the product, which instead displays triplet resonances at 2.96 and 2.81 ppm integrating to 2 protons each. In addition, two additional peaks are seen in the ^{13}C NMR spectrum of the product at 17.8 and 21.2 ppm, which are shown to be CH_2 resonances in the DEPT-135 spectrum. The ^1H and ^{13}C NMR spectroscopy therefore suggests that the major product appears to result from hydrogenation at the 3 and 4 positions of the DMNA ligand. [157, 240] Liquid Injection Field Desorption Ionisation mass spectrometry (LIFDI-MS) indicates a molecular formula of [$IrCl_2Cp^*$(DMNA-H_2)], implying a monodentate coordination mode to the DMNA-H_2 ligand. This is consistent with the behaviour of these iridium complexes, but does not represent a true ‘molecular analogue’ for [$IrCl_2Cp^*$(UCN)], as no peaks due to hydrogenation are observed in [$IrCl_2Cp^*$(UCN)].[262]

4.4.2 Synthesis of a molecular analogue for [IrClCp*(UCN)](PF_6)

[IrClCp*(DMNA)](PF_6) was synthesised by Dr Daniel Raines analogously to [IrClCp*(UCN)](PF_6) to act as a molecular analogue to the material (Scheme 4.5). No hydrogenation is seen due to the lack of alcohol (i.e. lack of hydride donor) during the reaction. The molecular analogue, [IrClCp*(DMNA)](PF_6), shows lower chemical shift in the internal carbon atom in Cp* compared to [IrClCp*(UCN)](PF_6). This is consistent with previous data suggesting UCN is donates less electron density to coordinated metal centres compared to DMNA.

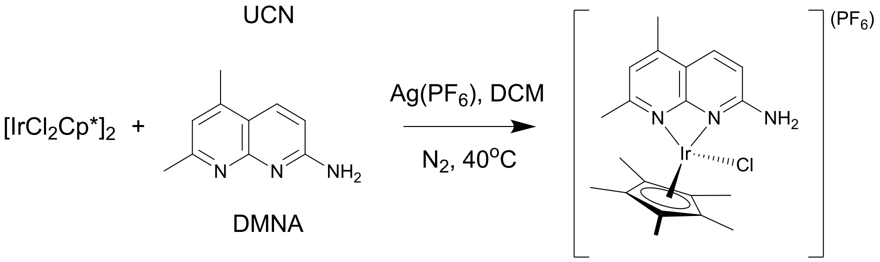

Scheme 4.5: Synthesis of IrClCp(DMNA)](PF_6)*

Table 4.6: Comparison of 13C CP-MAS NMR of [IrClCp(DMNA)](PF_6) to [IrClCp*(UCN)](PF_6)*

Samples	Cp* ^{13}C Shift Inner (**<u>C</u>**CH$_3$)$_5$ / ppm	Cp* ^{13}C Shift Inner (C**<u>C</u>**H$_3$)$_5$ / ppm
[IrClCp*(DMNA)](PF_6)	87.8	9.9
[IrClCp*(UCN)](PF_6)	89.3	9.4

4.4.3 Structure of [IrClCp*(DMNA-κ^2*N,N'*)](PF_6) compared to [IrCl$_2$Cp*(napy-κ*N*)] and [IrClCp*(napy-κ^2*N,N'*)](PF_6)

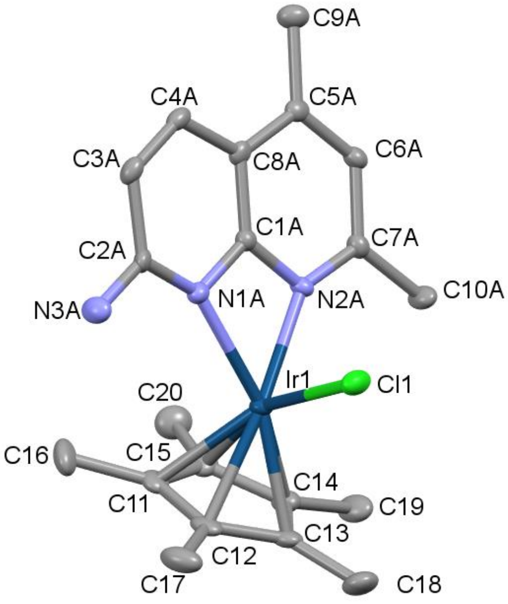

Figure 4.13: Crystal Structure of [IrClCp(DMNA)](PF_6) with hydrogen and counterions omitted for clarity. Probability ellipsoids at 50%.*

Single crystals of [IrClCp*(DMNA)](PF$_6$) were obtained by layering of diethyl ether over a solution of the complex in acetonitrile. The crystals are triclinic and belong to the P-1 space group. The crystal structure is shown in Figure 4.13. Significant disorder is seen as the two enantiomers of the [IrClCp*(DMNA)]$^+$ ion are interchangeable in the crystal structure – constraints to keep the two enantiomers within 5% of each other's geometry were used.

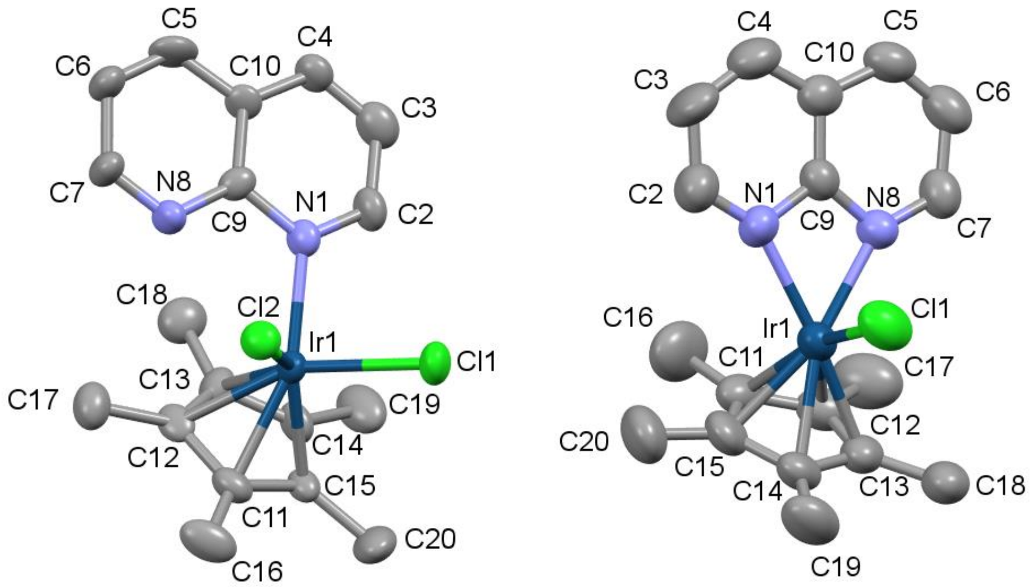

Figure 4.14: Crystal Structures of [IrCl$_2$Cp(napy)] and [IrClCp*(napy)](PF$_6$) with hydrogen and counterions omitted for clarity. Probability ellipsoids at 50%.*[262]

Selected bond lengths and angles in [IrClCp*(DMNA)](PF$_6$) are shown in Table 4.7, where they are compared to [IrCl$_2$Cp*(napy)] and [IrClCp*(napy)](PF$_6$) (Figure 4.14).[262] The Ir-N distances between iridium and DMNA (2.143(4) Å and 2.180(4) Å) are smaller than those observed for the napy ligand (2.157(6) Å and 2.272(7) Å). The monodentate-coordinated napy ligand has an even shorter Ir-N distance (2.15(1) Å), as it is not constrained in the same manner as when coordinated in a bidentate mode. All three complexes have pseudo-octahedral geometry, as indicated by the N-Ir-Cl angles being close to 90°. This is common for piano-stool complexes of this type.[266]

Despite these differences, the effect on the Ir-Cp* interaction seems minimal in each of the three cases. The Ir-Cl bonding appears to compensate for any changes in the coordination mode, as the average Ir-Cp* distance does not appear to be significantly affected by the napy coordination mode. This is reflected in the similarity of the Cp* ligand ^1H NMR resonances in [$IrCl_2Cp$*(napy)] (1.54 ppm) and [IrClCp*(napy)](PF_6) (1.55 ppm).[262] This indicates that in the case of naphthyridine complexes, only a small change in the ^{13}C NMR resonance of Cp* may be observed in different coordination modes. It is likely that any change in the coordination mode of iridium to carbon nitride will be even more difficult to observe directly due to the solid-state nature of the materials and low iridium concentration.

Table 4.7: Selected distances and angles in [IrClCp(DMNA)](PF_6), [IrClCp*(bpy)](ClO_4) and [IrClCp*(napy)](PF_6)*

Bond Distance / Å	[IrClCp*(DMNA)](PF_6)	[$IrCl_2Cp$*(κ^1-napy)][262]	[IrClCp*(κ^2-napy)](PF_6)[262]
Ir-N1	2.180(4)	2.15(1)	2.272(7)
Ir-N2	2.143(4)	3.21(1)	2.157(6)
Ir-Cl1	2.3902(9)	2.412(4)	2.381(2)
Ir-Cl2	-	2.405(4)	-
Ir-C11	2.141(4)	2.17(2)	2.129(9)
Ir-C12	2.136(4)	2.16(2)	2.124(9)
Ir-C13	2.155(4)	2.15(1)	2.145(9)
Ir-C14	2.163(4)	2.15(2)	2.181(7)
Ir-C15	2.137(4)	2.15(2)	2.139(8)
Mean Ir-Cp*	2.146	2.15	2.143
δ (^1H, Cp*) / ppm	1.80	1.54	1.55
Bond Angle			
N1-Ir-N2	60.9(1)	47.4(4)	60.5(2)
N1-Ir-Cl1	85.2(1)	84.9(3)	84.4(2)

As with previous metal-DMNA complexes, distortion is observed in the DMNA ligand after iridium coordination (Table 4.8). The C1-C8 distance contracts to reduce the N1-N2 distance and improve overlap between the nitrogen ligand and metal d-orbitals. A distortion similar to this is expected to occur on the UCN to accommodate the coordinated metal ions.

Table 4.8: Selected distances and angles in [IrClCp(DMNA)](PF_6) showing distortion in the DMNA ligand*

Bond Distance / Å	DMNA[148]	[IrClCp*(DMNA)](PF_6)
C1-C8	1.424(3)	1.386(5)
N1-N2	2.304(3)	2.190(5)
N3-C2	1.353(5)	1.335(5)
Bond Angle / °		
N1-C1-N2	115.6(2)	108.0(3)
N1-C2-N3	118.7(3)	120.8(4)

4.5 Aqueous Catalytic Transfer Hydrogenation Activity of [IrCl₂Cp*(UCN)]

4.5.1 Hydrogenation of Imines

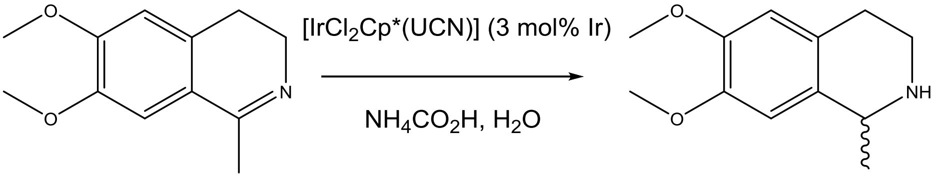

Scheme 4.6: Aqueous transfer hydrogenation from ammonium formate to 1-methyl-6,7-dimethoxy-3,4-dihydroisoquinoline

Iridium pentamethylcyclopentadienyl complexes are well established in the field of aqueous catalytic transfer hydrogenation (CTH).[157, 238, 254, 267, 268] An established method of evaluating catalysts for aqueous CTH was used to determine the activity of [$IrCl_2Cp^*(UCN)$] in comparison to [$IrCl_2Cp^*$]$_2$ (Scheme 4.6).[238, 240, 248] Reactions were performed at room temperature by adding an aqueous solution of 1-methyl-6,7-dimethoxy-3,4-dihydroisoquinoline to a suspension of [$IrCl_2Cp^*(UCN)$] (3 mol% iridium to substrate) in aqueous NH_4CO_2H (3 mol dm^{-3}). Aliquots were removed periodically from the reaction, the reaction halted by addition of a solution of glutathione, and then analysed by HPLC. Kinetic runs of the reactions were measured and are shown in Figure 4.15.

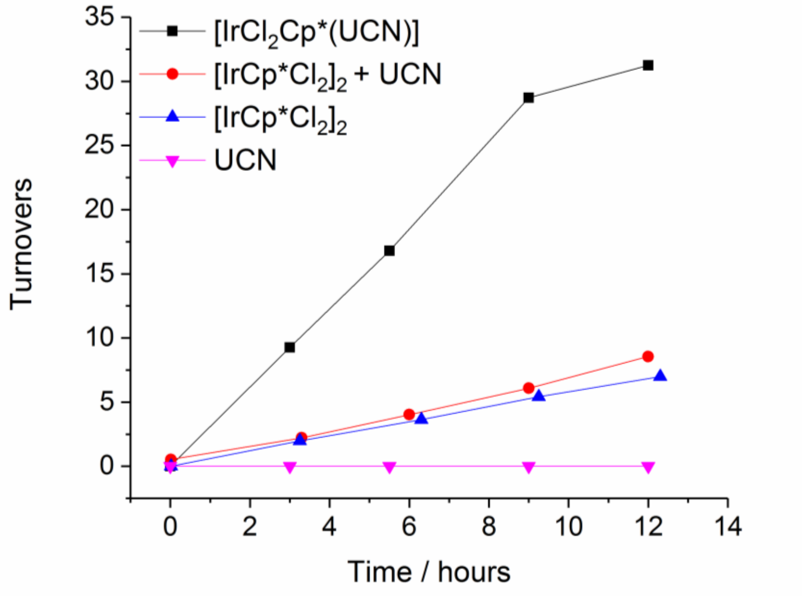

Figure 4.15: Reactivity of [$IrCl_2Cp^*(UCN)$] and [$IrCl_2Cp^*$]$_2$ towards transfer hydrogenation of 1-methyl-6,7-dimethoxy-3,4-dihydroisoquinoline in an aqueous solution of NH_4CO_2H (3 mol dm^{-3}) at 25°C

Conversion was calculated as a function of turnovers per atom of iridium. As Figure 4.15 shows, [$IrCl_2Cp$*(UCN)] is a significantly more active catalyst compared to the iridium precursor, [$IrCl_2Cp$*]$_2$. In addition, the undecorated UCN shows no activity, demonstrating the activity is limited to iridium sites on the carbon nitride, and addition of UCN to an aqueous solution of [$IrCl_2Cp$*]$_2$ does not result in higher activity. This shows that [$IrCl_2Cp$*(UCN)] can perform as a competent hydride transfer catalyst.

The TOF of aqueous CTH catalysis observed for [$IrCl_2Cp$*(UCN)] is very low at 3 h^{-1}, compared to numbers in excess of 200 h^{-1} measured for the best solid-supported iridium piano-stool catalysts .[238, 245] The reduction in rate is not likely to be a result of the heterogeneous nature of the catalyst, as high rates in excess of 50 h^{-1} are frequently seen for solid-supported catalysts.[254, 255] The coordination sites available in carbon nitride are different to those used in the top performing catalysts, so the lower activity seen for the material is can be explained by a less optimal coordination environment of the iridium. Whereas catalyst immobilisation methods such as supporting on magnetic nanoparticles are costly and time-consuming, carbon nitride provides a synthetically cheaper and simpler opportunity for catalyst heterogenization.

4.5.2 Substrate scope of aqueous transfer hydrogenation

[$IrCl_2Cp$*(UCN)] was also used to catalyse the hydrogenation of three other substrates (10 μL) in ammonium formate (1 mL, 3 mol dm^{-3} in D_2O) solution. The reactions were performed at 40°C and monitored by NMR. Conversions and turnovers were calculated and are shown in Table 4.9.

Table 4.9: Rates of aqueous transfer hydrogenation towards different substrates

Substrate	Conversion	Product	TON	TOF / h^{-1}
Allyl Alcohol	<1%	1-propanol	0	0
Acetophenone	50%	1-phenylethanol	48	4
Benzaldehyde	100%	Benzyl alcohol	117.6	≥9.8

[$IrCl_2Cp$*(UCN)] is shown to be an active catalyst for the aqueous catalytic transfer hydrogenation of C=O and C=N bonds. However, under aqueous conditions, no reduction of the C=C bond in allyl alcohol was observed. The selectivity against C=C bonds is observed for other heterogeneous systems, and is generally dependant on the solvent.[269] The selectivity is caused by multiple competing factors, including solubility of product and competing chemical interaction between solvent, catalyst, and substrate.[270]

4.5.3 Recycling of [IrCl$_2$Cp*(UCN)] in aqueous transfer hydrogenation

One suggested advantage of the UCN supported system is the heterogeneous nature of the catalyst, facilitating catalyst removal and recycling. A sample of [IrCl$_2$Cp*(UCN)] was used for a CTH reaction and then isolated by centrifugation and washing with water three times before adding to another, identical reaction. The kinetic data collected from the two reactions are shown in Figure 4.16. Two recycling processes were used, one involving drying by heating between each centrifugation and washing step and one only heating to dry the catalyst at the end of three centrifugation steps.

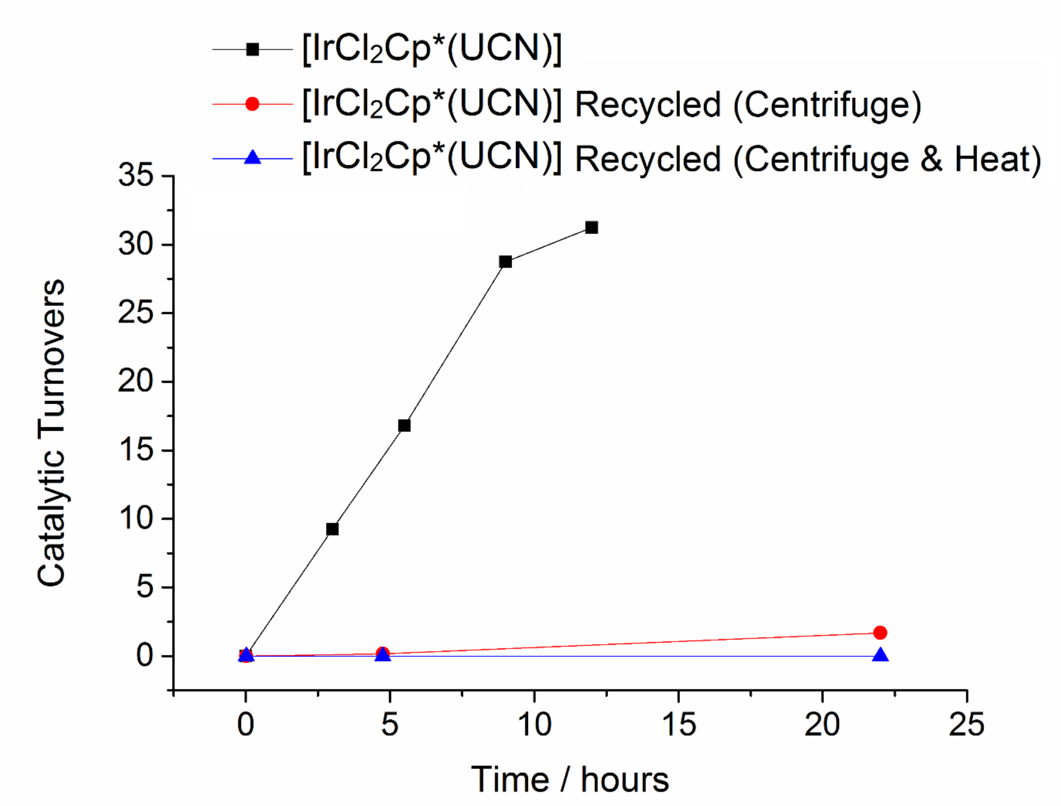

Figure 4.16: Recycling studies of [IrCl$_2$Cp(UCN)] in aqueous catalytic hydrogen transfer reactions*

Figure 4.16 shows that the activity of the catalyst is almost entirely lost in the recycling step, suggesting significant leaching of iridium species from the surface into solution or degradation of the active catalyst. It is likely, therefore, that a combination of solution and adsorbed iridium species contribute to the overall activity shown in aqueous catalytic transfer reactions. In order to show a recyclable heterogeneous catalyst, a reaction system must be selected with minimal iridium leaching.

4.5.4 Stability of iridium-decorated carbon nitride in different solvents

Figure 4.16 suggests that [$IrCl_2Cp^*(UCN)$] is not suitable for use as a recyclable catalyst in aqueous systems. To qualitatively assess the stability of [$IrCl_2Cp^*(UCN)$] in various solvents, a sample of [$IrCl_2Cp^*(UCN)$] was stirred in solvent for three hours. The UV-visible light absorption spectrum of each solvent after stirring with [$IrCl_2Cp^*(UCN)$] is shown in Figure 4.17.

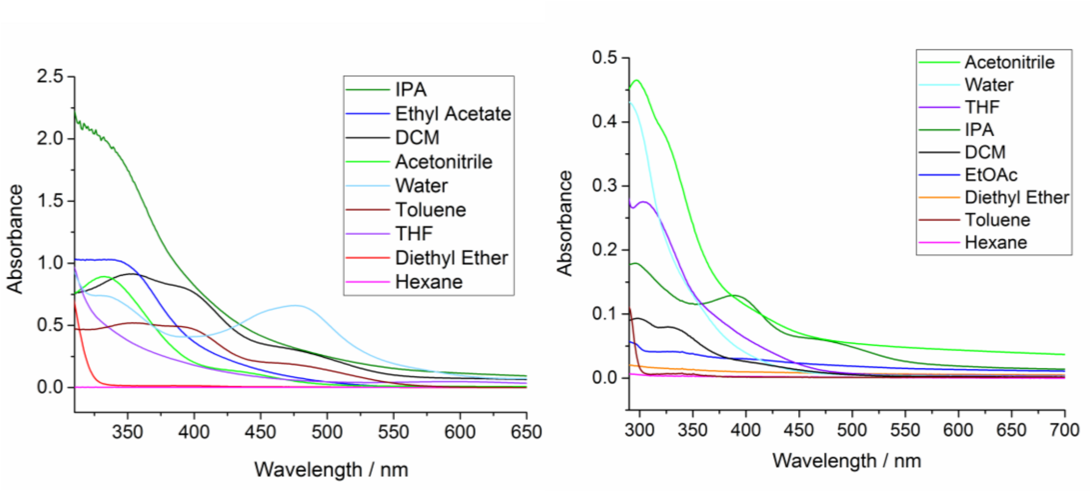

Figure 4.17: Leaching study of [$IrCl_2Cp^*(UCN)$] (left) compared to [$IrClCp^*(UCN)$](PF_6) (right)

Most solvents show the appearance of an absorption band, suggesting iridium leaching into solution from the [$IrCl_2Cp^*(UCN)$]. Each solution shows a different band structure, making quantification by this method difficult. However, a qualitative understanding of the stability of the material can be obtained. In general, more coordinating solvents give rise to stronger absorption bands, with water, acetonitrile and isopropyl alcohol showing the most intense bands. This indicates that leaching of iridium from [$IrCl_2Cp^*(UCN)$] into solution is higher in more coordinating solvents, explaining the poor recyclability of the catalyst under aqueous transfer hydrogenation conditions. In contrast, minimal leaching is seen to occur at a reduced rate in non-polar solvents, such as hexane. Further catalytic studies, therefore, would be carried out under conditions that minimised catalyst degradation.

The leaching of iridium from [IrClCp*(UCN)](PF_6) into solution was also assessed using the same simple UV-visible light absorption protocol as was performed on [$IrCl_2$Cp*(UCN)]. The spectra shown in Figure 4.17 show that despite essentially identical metal loading, the intensity of UV bands arising in solutions due to metal leaching as significantly weaker in [IrClCp*(UCN)](PF_6) compared to [$IrCl_2$Cp*(UCN)].

The leached species are different, and therefore the change in intensity and position of the UV bands is expected. However, the order of the intensities in different solvents is different between the decorated carbon nitrides. For example, leaching from [$IrCl_2$Cp*(UCN)] into toluene shows strong absorption bands comparable in intensity to those observed for THF or H_2O. In contrast, leaching from [IrClCp*(UCN)](PF_6) into toluene shows only a very weak UV band comparable to stability in hexane or diethyl ether.

The apparent differences in the solvent stability of [$IrCl_2$Cp*(UCN)] and [IrClCp*(UCN)](PF_6) could also be interpreted to support a different coordination environment between the iridium and the heptazine in each material.

4.6 Direct Hydrogenation by [$IrCl_2$Cp*(UCN)]

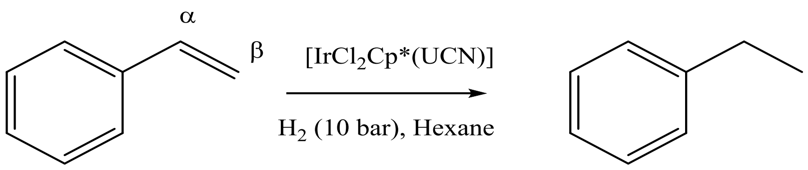

Scheme 4.7: Direct hydrogenation of styrene

The principle aim of this chapter is to investigate whether a decorated carbon nitride can provide a basis for the design of a recyclable, heterogeneous catalyst. Due to the relative stability of [$IrCl_2$Cp*(UCN)] in hexane, a reaction was sought which could be performed using hexane as a solvent.

Following an example of direct hydrogenation of unsaturated systems by an iridium complex in hexane, [$IrCl_2$Cp*(UCN)] was utilised as a heterogeneous catalyst for direct hydrogenation (Scheme 4.7).[271] Reactions were performed on small scale (1 mL solvent, with 100 equivalents of substrate) and analysed by GC after one hour to measure an initial turnover frequency (TOF / h^{-1}) per atom of iridium.

4.6.1 Effect of Pressure on the rate of hydrogenation

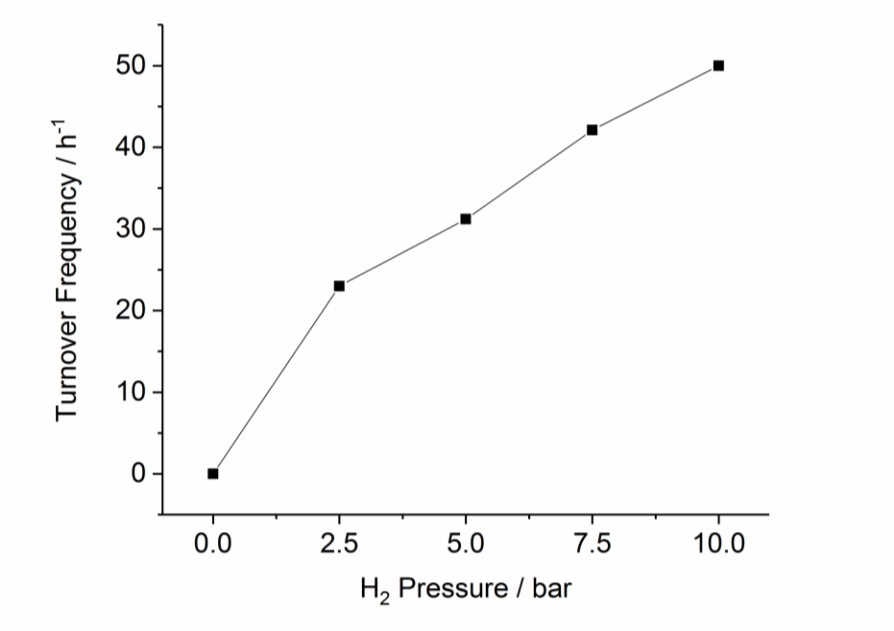

Figure 4.18: Effect of hydrogen pressure on TOF in the direct hydrogenation of styrene catalysed by [IrCl$_2$Cp(UCN)]*

To gain initial insight for suitable reaction conditions, direct hydrogenation of styrene was performed in hexane, and the effect on TOF of hydrogen pressure was investigated. The rate of hydrogenation is seen to be approximately first order with regard hydrogen pressure (Figure 4.18). Due to instrumental limitations, a pressure of 10 bar was selected for future experiments, but it is noted that higher turnover frequencies may be accessible with higher pressures. Due to the elevated pressures of flammable gas, unless otherwise stated, all reactions were performed at 25°C.

4.6.2 Direct Hydrogenation Activity of [IrClCp*(UCN)](PF$_6$) compared to [IrCl$_2$Cp*(UCN)]

Having established a general set of conditions for hydrogenation, the activities of UCN, [IrCl$_2$Cp*]$_2$, [IrCl$_2$Cp*(UCN)], [IrClCp*(UCN)](PF$_6$) and [IrClCp*(DMNA)](PF$_6$) were measured and compared. In addition to styrene as a substrate, α-methyl styrene and β-methyl styrene were investigated to initially see how using a more substituted alkene as a substrate affects the turnover frequency of the reaction. Initial turnover frequencies (measured after 1 hour) are summarised in Table 4.10.

Table 4.10: Comparison of activity of UCN, $[IrCl_2Cp^*(UCN)]$ and $[IrClCp^*(UCN)](PF_6)$ with molecular species

Catalyst	Substrate	Product	TOF / h^{-1}
UCN	Styrene	-	0
$[IrCp^*Cl_2]_2$	Styrene	Ethylbenzene	5
$[IrCp^*Cl(DMNA)](PF_6)$	Styrene	Ethylbenzene	0
$[IrCl_2Cp^*(UCN)]$	Styrene	Ethylbenzene	50
$[IrClCp^*(UCN)](PF_6)$	Styrene	Ethylbenzene	20
$[IrCp^*Cl_2]_2$	α-methyl styrene	Cumene	7
$[IrCp^*Cl(DMNA)](PF_6)$	α-methyl styrene	Cumene	0
$[IrCl_2Cp^*(UCN)]$	α-methyl styrene	Cumene	37
$[IrClCp^*(UCN)](PF_6)$	α-methyl styrene	Cumene	44
$[IrCp^*Cl_2]_2$	β-methyl styrene	n-Propylbenzene	6
$[IrCp^*Cl(DMNA)](PF_6)$	β-methyl styrene	n-Propylbenzene	0
$[IrCl_2Cp^*(UCN)]$	β-methyl styrene	n-Propylbenzene	6
$[IrClCp^*(UCN)](PF_6)$	β-methyl styrene	n-Propylbenzene	5

Control experiments utilising UCN as catalyst did not yield any hydrogenation product. These preliminary results show that, in hexane, $[IrClCp^*(DMNA)](PF_6)$ is not a competent hydrogenation catalyst. This is likely due to poor solubility in hexane. Although $[IrCl_2Cp^*(UCN)]$ and $[IrClCp^*(UCN)](PF_6)$ show comparable activity toward the hydrogenation of α-methyl styrene, the activity of $[IrClCp^*(UCN)](PF_6)$ towards unsubstituted styrene is considerably lower compared to $[IrCl_2Cp^*(UCN)]$.

This suggests that the iridium environment is different in each material and the two catalysts can exhibit different selectivity. Due to its higher hydrogenation activity, the remaining investigation into the direct hydrogenation is focussed on catalysis by $[IrCl_2Cp^*(UCN)]$.

4.6.3 Substrate Scope of Hydrogenation by $[IrCl_2Cp^*(UCN)]$

To determine the chemoselectivity of $[IrCl_2Cp^*(UCN)]$ as a direct hydrogenation catalyst, the hydrogenation of different unsaturated groups was performed (Table 4.11). A high selectivity is shown towards C=C double bonds, as

[$IrCl_2Cp^*(UCN)$] is shown not to be a competent catalyst for the hydrogenation of C=O or C=N groups in hexane. The stark difference in chemoselectivity between direct hydrogenation and aqueous catalytic transfer hydrogenation is likely a result of the different solvent system, as hydrogen bonding in water can stabilise reactive intermediates in aldehyde reduction much more effectively than in hexane.[269, 270]

The addition of C=O-containing compounds to a hydrogenation of styrene (such that the concentration of the styrene and additive is the same) is shown to dramatically reduce the rate of hydrogenation, implying that in hexane, C=O groups still interact with iridium centres, but the reaction cannot go to completion and some reaction sites are blocked for viable substrates.

Table 4.11:Chemoselectivity of [$IrCl_2Cp^*(UCN)$] catalysed hydrogenation

Substrate	Additive	Product (TOF / h^{-1})
Styrene	-	Ethylbenzene (50)
Acetophenone	-	- (0)
Benzaldehyde	-	- (0)
Benzonitrile	-	- (0)
Styrene	Acetophenone	Ethylbenzene (15)
Styrene	Benzaldehyde	Ethylbenzene (3)

The selectivity of [$IrCl_2Cp^*(UCN)$] was investigated further by subjecting various unsaturated carbon-carbon bonds to hydrogenation conditions. Table 4.12 shows the high selectivity of [$IrCl_2Cp^*(UCN)$] as a hydrogenation catalyst. Hydrogenation is highly selective toward primary alkenes, including 1-octene, styrene, and α-methyl styrene. No conversion of internal aliphatic alkenes is observed, with no activity seen towards hydrogenation of 2-octene or cyclohexene. Very limited conversion is observed for trans-β-methyl styrene.

Not only is [$IrCl_2Cp^*(UCN)$] not capable of hydrogenation of 3-methyl-1,3-pentadiene, but total inhibition of styrene hydrogenation is observed when 3-methyl-1,3-pentadiene is present in the reaction. The lack of activity suggests irreversible coordination of dienes to the iridium centres in [$IrCl_2Cp^*(UCN)$], deactivating the catalyst.

Table 4.12: Selectivity of [IrCl$_2$Cp(UCN)] in direct hydrogenation*

Substrate	Additive	Product (TOF / h^{-1})	Selectivity / %
Styrene	-	Ethylbenzene (50)	>99
Phenylacetylene	-	- (0)	-
Styrene	Phenylacetylene	- (0)	-
1-Octene	-	Octane (25)	>99
2-Octene	-	- (0)	-
1-Octyne	-	- (0)	-
Styrene	1-Octyne	- (0)	-
α-methyl styrene	-	Isopropyl benzene (37)	>99
Trans-β-methyl styrene	-	n-propyl benzene (>5)	>99
Cyclohexene	-	- (0)	-
3-methyl-1,3-pentadiene	-	- (0)	-
Styrene	3-methyl-1,3-pentadiene	- (0)	-

A lack of hydrogenation activity of [IrCl$_2$Cp*(UCN)] toward alkynes is also observed. In the case of both phenylacetylene and 1-octyne, no hydrogenation is observed, with alkene hydrogenation also completely inhibited by the presence of alkynes. This seems likely to be a result of irreversible coordination of the alkyne to the iridium site resulting in catalytically inactive species.[272]

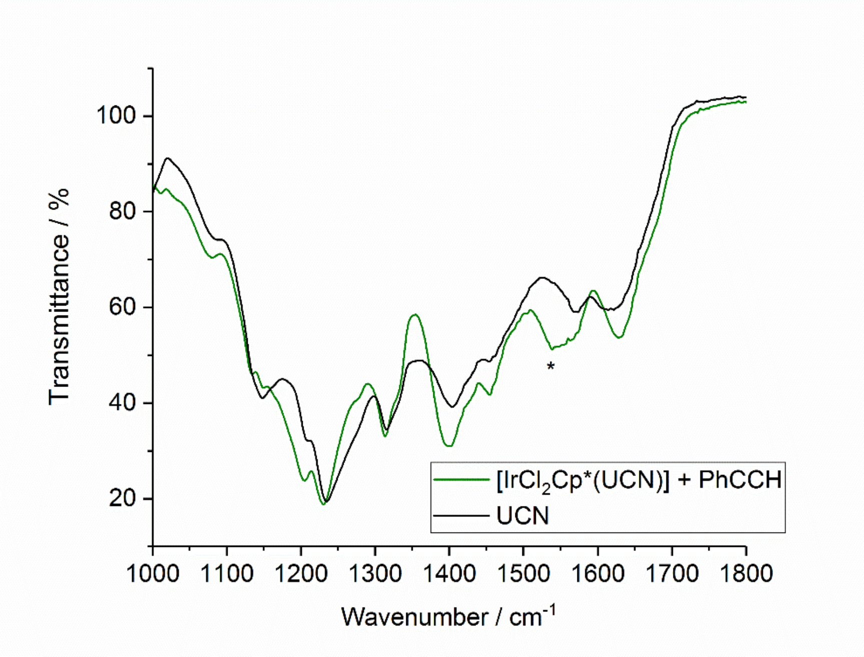

Figure 4.19: ATR-IR spectra of [IrCl$_2$Cp(UCN)] before and after treatment with phenylacetylene*

Infrared spectroscopy of [IrCl$_2$Cp*(UCN)] after it had been exposed to phenylacetylene was performed, and an additional signal observed at around 1550 cm^{-1} (marked with an asterisk in Figure 4.19) may correspond to an iridium vinylidene (v(C=C) = 1580-1650 cm^{-1}) being formed on the surface of the [IrCl$_2$Cp*(UCN)].[273] Further work could be done on this reaction to investigate whether this species can play a role in other catalytic reactions, however, due to the low loading of the iridium on the UCN, further investigating this species would be challenging.

4.6.4 Hydrogenation Reactions Performed by [IrCl$_2$Cp*(UCN)]

Following the measurements of initial turnover frequency listed in Table 4.12, reactions of those substrates which [IrCl$_2$Cp*(UCN)] was active towards were performed on a longer timescale. Selective hydrogenation of terminal C=C bonds is observed.

Table 4.13: Hydrogenation reactions performed using [IrCl$_2$Cp(UCN)] as a heteogeneous catalyst. To 25 mg of catalyst, 100 equivalents of substrate (compared to iridium) were added in 1 mL hexane. Yield and selectivity determined by GC analysis.*

Temp. / °C	Substrate	Reaction Time / h	Initial TOF / h^{-1}	Yield / %	Product	Selectivity / %
25	Styrene	3	50	94	Ethylbenzene	>99
25	1-octene	5	25	74	Octane	>99
25	α-methyl styrene	5	37	60	Cumene	>99
60	Limonene	17	-	99	1-menthene	>99

In addition to the substrates previously observed, [IrCl$_2$Cp*(UCN)] was used to hydrogenate a sample of limonene, which possesses both internal and terminal alkene environments (Scheme 4.8). An elevated reaction temperature and extended reaction time were required to drive the reaction to completion, but, interestingly, no further hydrogenation of the product, 1-menthene, was observed. This is unusual, as known heterogeneous catalysts are shown to further hydrogenate 1-menthene.[274] Therefore, [IrCl$_2$Cp*(UCN) is shown to be a highly selective (albeit slow) hydrogenation catalyst toward terminal alkene groups.

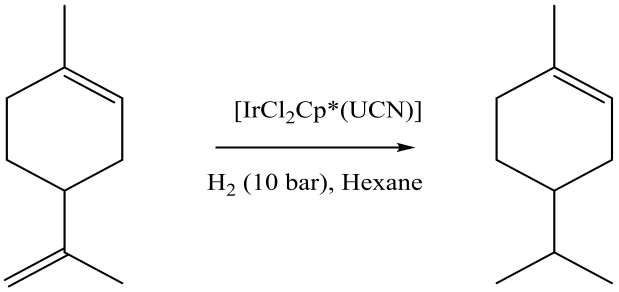

Scheme 4.8: The selective hydrogenation of Limonene to 1-menthene by [IrCl$_2$Cp(UCN)]*

4.6.5 Recycling of [IrCl$_2$Cp*(UCN)]

One of the aims of this chapter is to show that direct coordination of metal complex fragments to carbon nitride is a viable approach to design recyclable heterogeneous catalysts. To investigate the recyclability of [IrCl$_2$Cp*(UCN)], the same sample of catalyst was used for the hydrogenation of styrene and recycled four times, for a total of five runs. As with previous experiments, the initial TOF was measured using GC and is shown in Table 4.14. The TOF is also presented graphically in Figure 4.20. It is clearly seen that [IrCl$_2$Cp*(UCN)] maintains over 80% of activity after five runs. As the reactions are carried out for 1 hour, the turnover frequency (TOF) is interchangeable with the turnover number (TON).

Table 4.14: Activity of [IrCl$_2$Cp(UCN)] after multiple runs*

Run	TOF / h^{-1}
First	50
Second	49
Third	48
Fourth	43
Five	41

This is strong evidence of catalytic species existing on the surface of the [IrCl$_2$Cp*(UCN)] rather than in solution. The loss in activity likely occurs as small amounts of solid-state catalyst, dispersed in the solvent, are removed when the GC sample is taken, as well as due to a small amount of iridium leaching from solution. A more dedicated, larger scale experimental set-up may increase the recyclability of the catalyst.

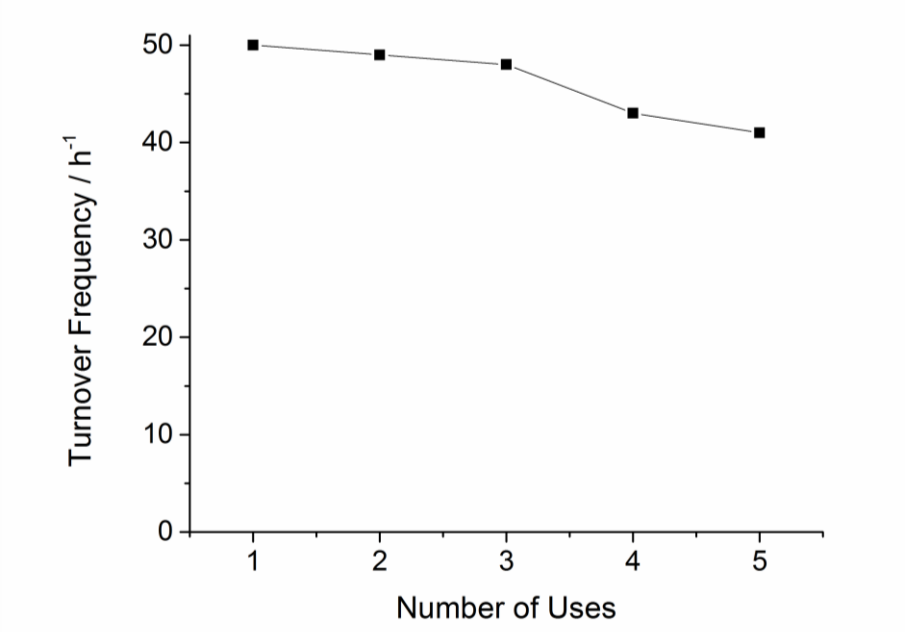

Figure 4.20: Activity of Ir-UCN after multiple runs

4.6.6 Comparison of the Activity of [$IrCl_2$Cp*(UCN)] to established catalysts

It has therefore been shown that [$IrCl_2$Cp*(UCN)], comprising a metal complex fragment coordinated to carbon nitride, can act as a recyclable, heterogeneous direct hydrogenation catalyst. There are only a small number of iridium-half sandwich complexes which are shown to perform direct hydrogenation, and of those, the majority utilise polar solvents, primarily methanol.[275-279] Isotopic labelling has shown methanol in these case to be the main source of hydrogen used for hydrogenations.[280] Therefore, as [$IrCl_2$Cp*(UCN)] is limited to relatively unfavourable conditions to prevent iridium loss into solution, it is difficult to fairly compare the activity of [$IrCl_2$Cp*(UCN)] as a hydrogenation catalyst to related half-sandwich systems.

However, there is an Crabtree-type iridium (I) complex (shown in Figure 4.21) which is reported to hydrogenate styrene (TOF = 400 h^{-1}) and cyclohexene (TOF = 260 h^{-1}) in hexanes at room temperature.[271]

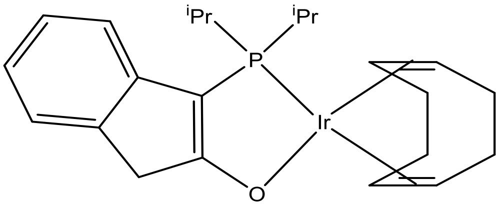

Figure 4.21: Structure of a Crabtree-type Iridium hydrogenation catalyst

In comparison to the compound shown in Figure 4.21, [$IrCl_2Cp^*$(UCN)] is a slower, but more selective, hydrogenation catalyst, as Crabtree catalysts will hydrogenate both terminal and non-terminal alkene groups.[236, 271] One advantage of [$IrCl_2Cp^*$(UCN)] is its good stability in hexane and that it therefore can be easily recycled for multiple uses as a result of the direct coordination of carbon nitride to an iridium half-sandwich complex fragment.

4.7 Investigation of Mechanism of Hydrogenation by [$IrCl_2Cp^*$(UCN)]

One of the primary advantages of homogeneous catalysts compared to heterogeneous catalysts is the greater ease by which the mechanism of a reaction can be investigated in homogeneous chemistry. Although [$IrCl_2Cp^*$(UCN)] is a heterogeneous catalyst, the supported metal fragment provides spectroscopic handles that may allow mechanism elucidation more easily in comparison to other heterogeneous catalysts.

4.7.1 Analysis of [$IrCl_2Cp^*$(UCN)] after hydrogenation

In order to determine whether the catalyst has changed after a hydrogenation experiment, a sample of [$IrCl_2Cp^*$(UCN)] was analysed by ^{13}C CP-MAS NMR both before and after the hydrogenation of styrene, with the spectra shown in Figure 4.22.

No significant differences are observed between the spectra, either in the Cp* peak position or intensity. As XPS does not suggest presence of any metallic iridium in the pre-catalyst and no loss of Cp* is seen during the reaction, this implies no oxidative degradation of Ir (III) occurs during hydrogenation.[256] In addition, this suggests that oxidative addition of dihydrogen to iridium does not occur during hydrogenation.[281, 282]Any proposed mechanism must therefore retain the Cp* ligand and should minimise changes in iridium oxidation state.

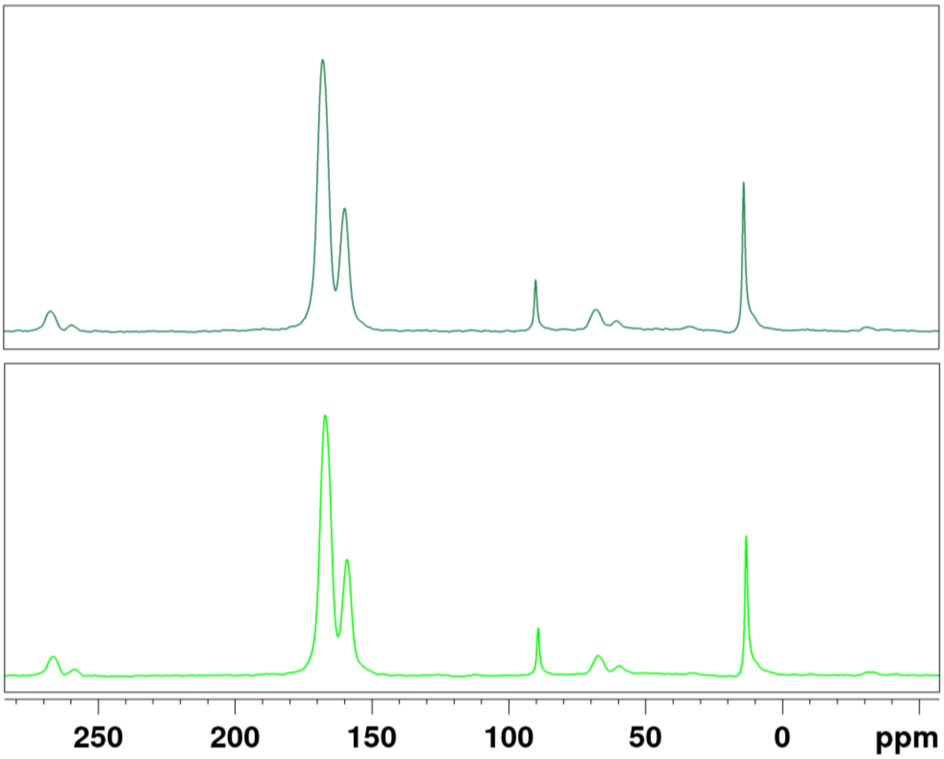

Figure 4.22: ^{13}C CP-MAS of [IrCl$_2$Cp(UCN)] before (bottom) and after (top) hydrogenation of styrene*

4.7.2 Isotopic labelling during styrene hydrogenation

Hydrogen can be added to unsaturated molecules either by transferring both hydrogen atoms in the same step (in concert) or by initially breaking the hydrogen-hydrogen bond to form a hydride species which can then attack the substrate (stepwise). By performing the hydrogenation of styrene under a 1:1 mixture of H_2:D_2 it can be determined whether hydrogen addition to styrene occurred stepwise or in concert by determining the relative sites of deuteration and hydrogenation.

Isotopically labelled hydrogenation was performed in hexane under 8 bar of 1: 1 D_2: H_2. The reaction mixture was analysed by GC-MS and extracted into d_6-DMSO and DMSO for analysis by ^{1}H and ^{2}H NMR spectroscopy.

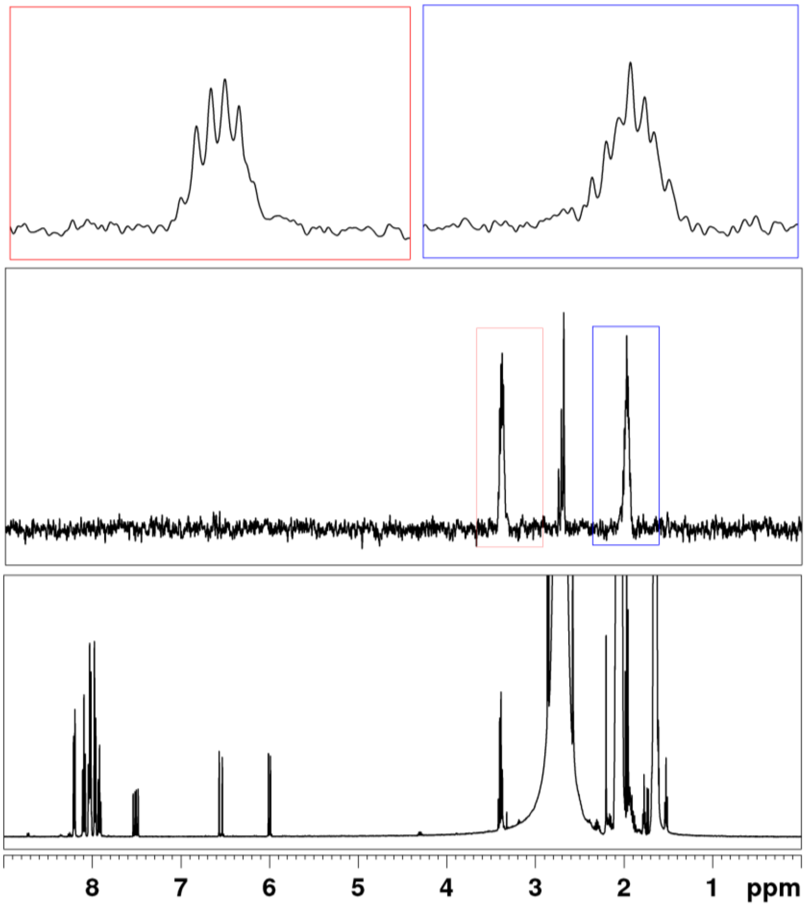

Figure 4.23: (top) expanded ^{2}H spectrum of styrene hydrogenation with 1:1 H_2:D_2 mix; (middle) full ^{2}H NMR spectrum; (bottom) ^{1}H NMR spectrum

NMR analysis of the reaction (Figure 4.23) clearly shows that deuterium incorporation is limited to the vinyl group, as shown in Figure 4.24. If hydrogen addition was concerted only products A and D would be observed. The complex splitting pattern in Figure 4.23 suggests that additional 'hydrogen-scrambled' products B and C are formed, implying that the hydrogen-hydrogen bond is stepwise.

GC-MS of the reaction was also performed, and the resulting mass spectrum of ethyl benzene (Figure 4.24) supports the NMR experiment finding of hydrogen scrambled products. Although MS cannot discriminate between B and C, the twofold increased intensity of the peak at m/z = 107.09 compared to m/z = 106.08, 108.09 is consistent with a statistical spread of products A, B, C and D.

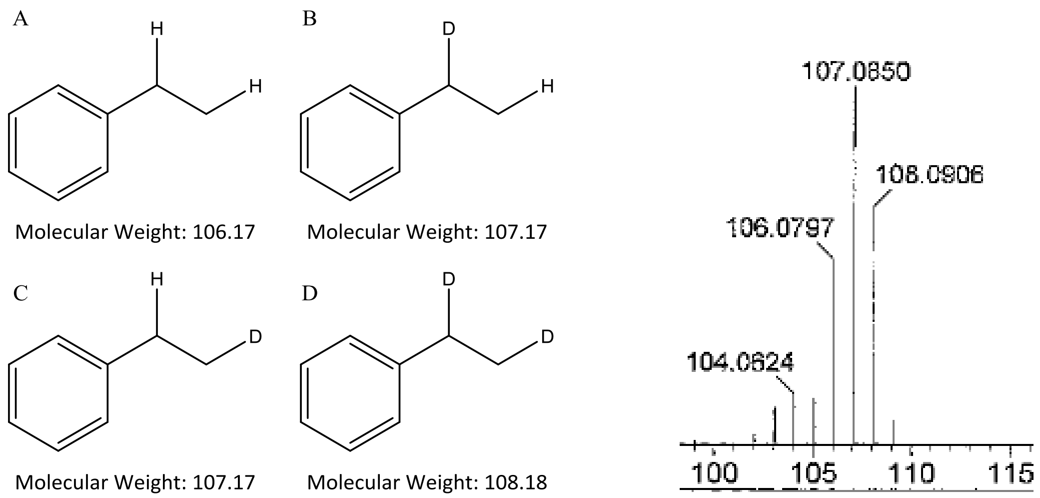

Figure 4.24: Extract from GC-MS data of product of styrene hydrogenation with 1:1 H_2:D_2 along with observed isotopically labelled ethylbenzenes

Isotopic labelling therefore indicates that the hydrogen-hydrogen bond is broken in a separate step to hydrogen addition across the unsaturated bond. This suggests that an iridium hydride species is formed in an early step of the mechanism.

4.7.3 Probing the reaction between hydrogen and [IrCl$_2$Cp*(UCN)] by DRIFTS

To attempt to directly observe formation of an iridium hydride species *in situ*, that is, to investigate whether the mechanism begins with hydrogen-hydrogen bond cleavage, a sample of [IrCl$_2$Cp*(UCN)] was placed inside a DRIFTS cell under hydrogen atmosphere (1 bar). It was proposed that iridium-hydride species would form, evidenced by vibrational signals around 2000 cm^{-1}.[283] The DRIFTS spectra of bare UCN and [IrCl$_2$Cp*(UCN)] collected both initially and after 1 hour of exposure to hydrogen are shown in Figure 4.25. As previously observed in ATR-IR (Figure 4.5), no significant difference in seen in the DRIFTS spectrum of the decorated and undecorated material. In addition, no new peaks are seen in the DRIFTS after hydrogen exposure.

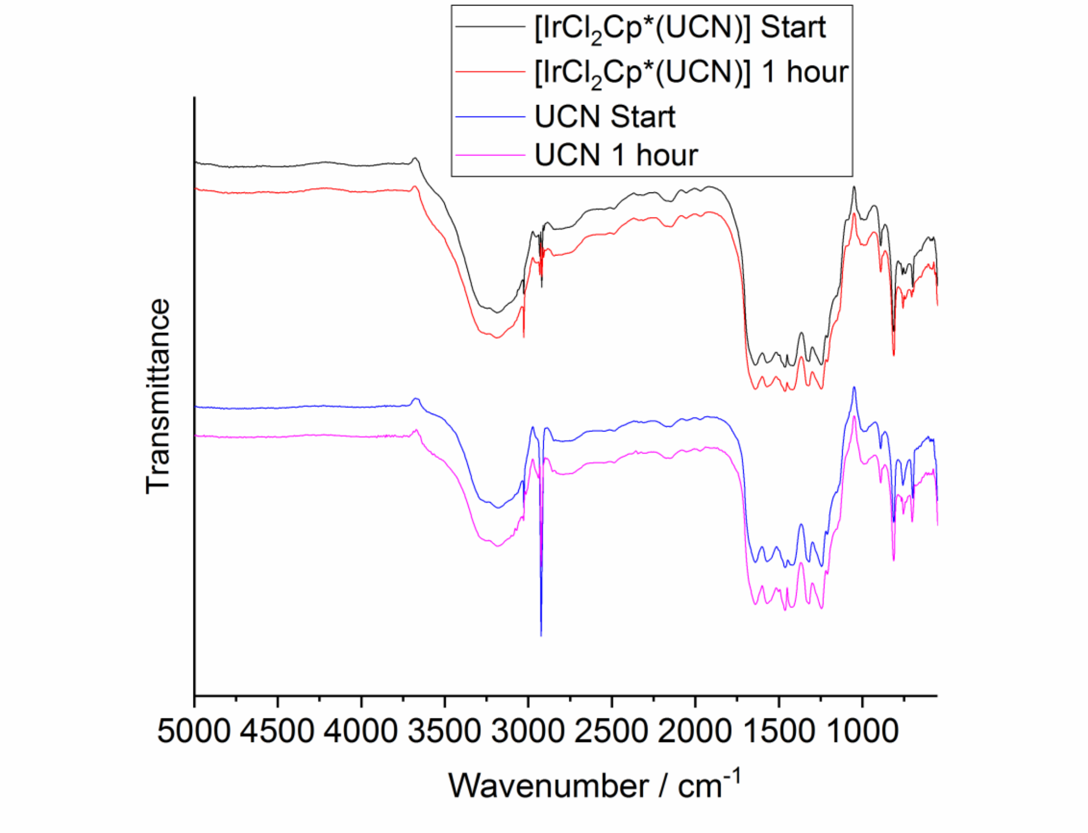

Figure 4.25: DRIFTS of [IrCl$_2$Cp(UCN)] and UCN under H_2*

Although this may be interpreted as iridium-hydride species not forming on the surface of [IrCl$_2$Cp*(UCN)], the conditions of this experiment differ significantly from the hydrogenation reaction conditions by necessity. A lack of iridium hydride signal in DRIFTS may also be due to the lower pressure of that the DRIFTS cell can safely contain hydrogen (1 bar in DRIFTS, compared to 10 bar used for hydrogenation reactions).

Hydrogen addition to metal centres is often reversible – bearing in mind the low pressure, and the already low concentration of iridium on the surface of the UCN, it is possible that any iridium-hydrogen equilibrium is too far shifted to free dihydrogen (i.e. away from an iridium hydride) under lower pressure DRIFTS conditions. Experimental set-ups capable of sustaining higher pressures of hydrogen should be investigated in future to determine the presence of surface iridium hydride species.

4.7.4 Proposed Mechanism

Scheme 4.9 outlines a tentatively suggested mechanism of direct hydrogenation by [IrCl$_2$Cp*(UCN)] based on the mechanism established for transfer hydrogenation seen in Scheme 4.1. It is proposed that addition of hydrogen to [$IrCl_2Cp$*(UCN)] causes formation of an iridium hydride species and protonation of a nearby amine.[238, 240, 247]

Following formation of an iridium hydride, the iridium hydride may then perform nucleophilic attack onto a molecule of styrene, before proton transfer from a nearby amine. Coordination of a carbanion to the iridium may stabilise the intermediate relative to hexane solution.

The formation of a monohydride iridium species is compatible with the observation of Cp* ligand retention and the retention of the iridium (III) oxidation state (Figure 4.22). Proton transfer from the proximal amine to the carbanion is likely key to allowing the hydrogen scrambling observed in section 4.7.2. As there are up to two primary amine groups (in an unknown protonation state) per heptazine moiety coordinated to iridium, the generic 'N' term has been used in Scheme 4.9 to present a basic nitrogen atom on the surface of the carbon nitride.

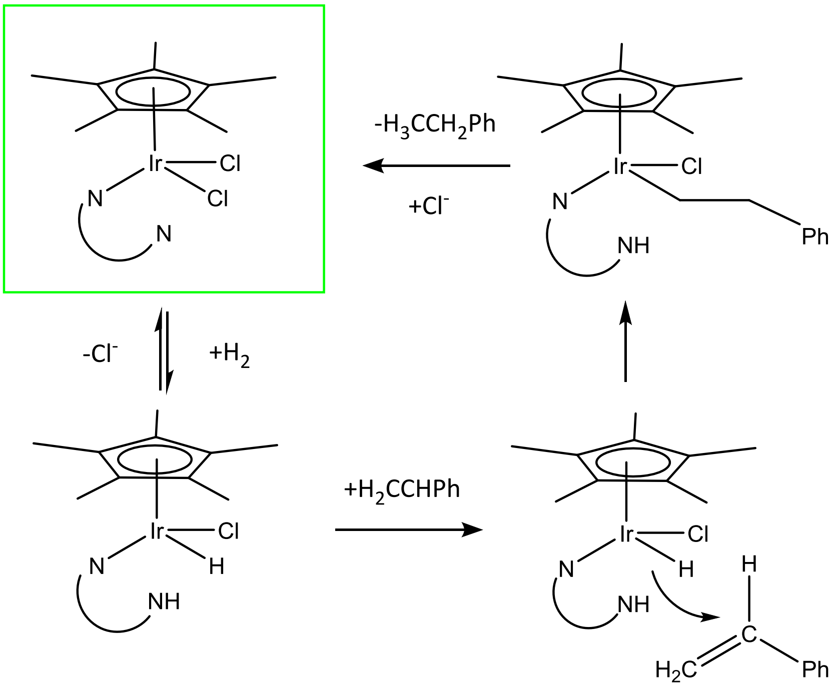

Scheme 4.9: Proposed mechanism of the hydrogenation of styrene by [$IrCl_2Cp$(UCN)]*

DRIFTS was unable to confirm the initial step of the reaction, which is speculated to be due to the lower iridium concentration on the surface as discussed in section 4.7.3. However, the mechanism in Scheme 4.9 is consistent with other observations. For instance, the oxidation state of the iridium does not appear to change during the reaction, nor does the Cp* ligand dissociate, as shown by the ^{13}C CP-MAS NMR (Figure 4.22) before and after hydrogenation. This is in contrast to Crabtree-like catalysts, where oxidative addition of H_2 to iridium causes oxidation state changes (Ir^{3+}/Ir^{5+}) and ancillary ligand loss during the course of a reaction.[281, 282] In addition, the alkene coordination after hydride transfer may explain the selectivity towards terminal alkenes, as steric factors on the surface of UCN make migratory insertion of the alkene into the M-H bond more challenging. The effect of steric factors on carbanion coordination is the cause of the high selectivity for terminal alkenes observed for Wilkinson's catalysts.[284]

It is reasonable to say that the investigation of hydrogenation performed by metal fragments on the surface of carbon nitride is challenging to investigate with established techniques. Specialist experimental set-up is required to investigate the formation of iridium-hydride species at higher hydrogen pressures to attempt to observe any organometallic iridium species *in situ.*

4.8 Conclusions

The primary goal of this chapter was to investigate whether coordination of an iridium half-sandwich complex fragment provided a path to development of novel heterogeneous catalysts. To this end, [$IrCl_2$Cp*(UCN)] and [IrClCp*(UCN)](PF_6) were both synthesised and fully characterised to determine whether the denticity of the carbon nitride to the iridium could be controlled.

Coordination of iridium half-sandwich fragments is suggested to occur in both materials based on ^{13}C CP-MAS spectroscopy. Comparing the slight differences observed via NMR of the two materials, and considering the spectroscopy of the two molecular analogues observed in the literature, [$IrCl_2$Cp*(napy)] and [IrClCp*(napy)](PF_6), it is tentatively suggested that different denticity of the heptazine unit to iridium is observed in each material in the solid state – however, the metal centres in these systems are difficult to probe.

[$IrCl_2$Cp*(UCN)] was then investigated as both an aqueous catalytic transfer and direct hydrogenation catalyst. Poor stability of the material in coordinating solvents limits the application of [$IrCl_2$Cp*(UCN)] to catalytic systems utilising hexane as a solvent, restricting the catalyst application. Comparison of the activity of this system is difficult, as there are very few examples of catalysts used under comparable conditions.

However, [$IrCl_2$Cp*(UCN)] is shown to act as a selective and recyclable catalyst under optimal conditions. [$IrCl_2$Cp*(UCN)] is therefore the first example of a catalyst designed using the heptazine units observed in carbon nitride as a ligand and is therefore a proof-of-principle of this novel catalyst design approach.

5 Conclusions and Further Work

In this work the surface of carbon nitride has been decorated with metal complex fragments coordinated to the material through inner-sphere coordination to the metal. Full characterisation of the decorated carbon nitrides supported the hypothesis of metal coordination. A molecular ligand, 5, 7-dimethyl-(1, 8)-naphthyridine-2-amine (DMNA), which presents comparable coordination environments to the carbon nitride, was used to synthesise molecular analogues to the metal-complex fragment decorated carbon nitrides and gain insight into the coordination of metal complex fragments to carbon nitride.

Coordination of both rhenium and manganese carbonyl fragments to carbon nitride were attempted. Coordination of a rhenium tricarbonyl chloride ([ReCl(CO)$_3$]) fragment to carbon nitride resulted in a material with a rhenium concentration of 0.39 mmol g^{-1}, whereas decoration with a manganese carbonyl species resulting a material 0.24 mmol Mn g^{-1}. Rhenium carbonyl-decorated carbon nitride, [ReCl(CO)$_3$(UCN)], showed strong absorptions in the carbonyl region of the infrared spectrum, however, no infrared vibrations were seen in the carbonyl region for manganese decorated carbon nitride. The lack of carbonyl signals in [Mn(UCN)] was therefore attributed to a decomposition of the manganese carbonyl fragment after a redox reaction between the manganese and the carbon nitride, showing that the redox behaviour of carbon nitride may interfere in future applications of carbon nitride as a ligand. DMNA complexes, [ReCl(CO)$_3$(DMNA-κ^2*N,N'*)] and [MnCl(CO)$_3$(DMNA-κ^2*N,N'*)], were synthesised and fully characterised. Crystal structures were obtained and the naphthyridine unit of the DMNA was observed to coordinate to the metal centre in a bidentate mode.

The strength of the coordination between carbon nitride and rhenium was qualitatively measured by stirring samples of [ReCl(CO)$_3$(UCN)] in different solvents and collecting the infrared spectrum of both the solvent and the isolated material. Rhenium leaching was observed in all investigated solvents after three hours, however significantly more rhenium loss was observed in coordinating solvents (acetonitrile, water) compared to non-coordinating solvents (toluene and hexane). The coordination between rhenium and carbon nitride in [ReCl(CO)$_3$(UCN)] is therefore relatively labile.

The photophysics of [ReCl(CO)$_3$(UCN)] was briefly investigated by UV-visible light reflectance and luminescence techniques. Increased absorbance at wavelengths above 400 nm was seen in [ReCl(CO)$_3$(UCN)] compared to undecorated

UCN, which was attributed to MLCT transitions occurring between d-orbitals in the surface rhenium atoms and the conduction band of the carbon nitride. Higher-energy transitions were also observed as XPS shake-up peaks, which were assigned as d-π* transitions. However, no luminescence was observed from these excited states, and it is assumed that a rapid, non-radiative quenching pathway exists for these states.

Having established that metal complex coordination to carbon nitride was achievable, two samples of carbon nitride, UCN and CCN were decorated with ruthenium (II) bis-2,2'-bipyridine fragments to give $[Ru(bpy)_2(UCN)](PF_6)_2$ and $[Ru(bpy)_2(CCN)](PF_6)_2$. Both $[Ru(bpy)_2(UCN)](PF_6)_2$ and $[Ru(bpy)_2(CCN)](PF_6)_2$ were suggested to be composite materials with direct coordination between a $[Ru(bpy)_2]^{2+}$ fragment and heptazine moieties within carbon nitride to result in materials with enhanced visible light absorption properties. Although the local environment in UCN and CCN was shown to be the same by CP-MAS NMR and ATR-IR spectroscopy, CCN was shown to have a more porous structure and a higher concentration of 'edge sites' with exposed naphthyridine-like coordination environments. This higher concentration of edge sites allowed the surface of CCN to host a larger quantity of ruthenium in the pores compared to UCN, with a ruthenium concentration of 0.076 mmol g^{-1} measured for $[Ru(bpy)_2(CCN)](PF_6)_2$ and 0.016 mmol g^{-1} measured for $[Ru(bpy)_2(UCN)](PF_6)_2$. The higher quantity of ruthenium in $[Ru(bpy)_2(CCN)](PF_6)_2$ corresponded with stronger spectroscopic signals for the ancillary ligands in ^{13}C CP-MAS NMR, ATR-IR, and XPS.

In order to probe the coordination environment on carbon nitride, a molecular analogue to the ruthenium-decorated materials, $[Ru(bpy)_2(DMNA\text{-}\kappa_2 N, N')](PF_6)_2$ was synthesised and fully characterised. It was proposed that the bidentate coordination observed in $[Ru(bpy)_2(DMNA\text{-}\kappa_2 N, N')](PF_6)_2$ was also active in both $[Ru(bpy)_2(UCN)](PF_6)_2$ and $[Ru(bpy)_2(CCN)](PF_6)_2$.

$[Ru(bpy)_2(UCN)](PF_6)_2$ and $[Ru(bpy)_2(CCN)](PF_6)_2$ along with the undecorated UCN and CCN were coated in platinum nanoparticles via photolytic deposition technique and tested for photocatalytic hydrogen evolution activity. Although UCN-Pt and CCN-Pt showed hydrogen evolution activity in water in the presence of sacrificial electron donor, neither $[Ru(bpy)_2(UCN)](PF_6)_2$-Pt nor $[Ru(bpy)_2(CCN)](PF_6)_2$-Pt showed hydrogen evolution activity.

The inactivity of $[Ru(bpy)_2(UCN)](PF_6)_2$-Pt and $[Ru(bpy)_2(CCN)](PF_6)_2$-Pt was intriguing and unexpected, as each ruthenium-decorated material showed enhanced visible light absorption properties compared to the corresponding undecorated material. It was observed that although both materials strongly absorb light with a wavelength of 500 nm, no luminescence is observed corresponding to this excitation. This in contrast to the strong luminescent properties of $[Ru(bpy)_2(DMNA\text{-}\kappa_2 N, N')](PF_6)_2$. It was proposed that the addition of the surface-bound ruthenium to carbon nitride allowed rapid quenching of excited states within the carbon nitride material. EPR analysis of $[Ru(bpy)_2(UCN)](PF_6)_2$ compared to UCN under dark and illuminated conditions confirmed that rapid quenching of the excited state was occurring. It is speculated that efficient FRET (Förster Resonance Energy Transfer) may be occurring between the MLCT state and the excited states within carbon nitride.

Transient absorption spectroscopy could be performed on $[Ru(bpy)_2(UCN)](PF_6)_2$ and $[Ru(bpy)_2(CCN)](PF_6)_2$ to provide further insight into the photochemical processes occurring in these composite materials by measuring the rates of formation of excited states. Altering the metal centre could also be investigated, e.g. comparing $[Os(bpy)_2(UCN)](PF_6)_2$ to $[Ru(bpy)_2(UCN)](PF_6)_2$. Comparison of the metal concentration, composite stability and photochemical processes would provide insight into the metal fragment-carbon nitride interactions.

It was proposed to use the inner-sphere coordination of a metal complex fragment to carbon nitride as the basis for a design of a novel heterogeneous catalyst. It was initially suggested to emulate high-profile aqueous catalytic transfer hydrogenation catalysts by reacting $[IrCl_2Cp^*]_2$ and UCN to synthesise $[IrCl_2Cp^*(UCN)]$. In order to determine whether to coordination mode of the iridium centre to carbon nitride could be altered, a second material was also synthesised. One equivalent of chloride per iridium was removed from $[IrCl_2Cp^*]_2$ by precipitation as AgCl and the resulting iridium solution reacted with UCN to result in $[IrClCp^*(UCN)](PF_6)$. Both $[IrCl_2Cp^*(UCN)]$ and $[IrClCp^*(UCN)](PF_6)$ were measured to have an iridium concentration of 0.07 mmol g^{-1}, suggesting that the same coordination sites are accessed in each material. Small differences in the ^{13}C CP-MAS NMR spectrum, zeta potential measurements and reactivity of the materials suggested a different coordination mode in $[IrCl_2Cp^*(UCN)]$ compared to $[IrClCp^*(UCN)](PF_6)$. Following previous work in the literature characterising $[IrCl_2Cp^*(napy\text{-}\kappa N)]$ and $[IrClCp^*(napy\text{-}\kappa_2 N, N')](PF_6)$, it was proposed that $[IrCl_2Cp^*(UCN)]$ displayed monodentate coordination between iridium and heptazine in contrast to the bidentate coordination likely for $[IrClCp^*(UCN)](PF_6)$. A molecular analogue of $[IrClCp^*(UCN)](PF_6)$, $[IrClCp^*(DMNA\text{-}\kappa_2 N, N')](PF_6)$ was successfully synthesised to gain insight into the coordination mode in this case.

$[IrCl_2Cp^*(UCN)]$ was briefly assessed as a catalyst for aqueous transfer hydrogenation reactions, but leaching of iridium into solution meant $[IrCl_2Cp^*(UCN)]$

was not a successfully recyclable catalyst. After assessing leaching of iridium into various solvents from [IrCl$_2$Cp*(UCN)], direct hydrogenations were carried out in hexane, which displayed minimum iridium leaching. [IrCl$_2$Cp*(UCN)] was shown to have higher activity towards the hydrogenation of styrene compared to [IrClCp*(UCN)](PF$_6$). Despite poor catalytic rate when compared to with similar homogeneous and heterogeneous hydrogenation catalysts in the literature, [IrCl$_2$Cp*(UCN)] displayed good selectivity toward terminal alkenes. Despite poor activity, [IrCl$_2$Cp*(UCN)] was shown to retain over 80% of its catalytic activity after 5 catalytic runs and is the first example of a recyclable hydrogenation catalyst designed using direct inner-sphere metal complex fragment coordination to carbon nitride.

Initial experiments to elucidate mechanism of hydrogenation by [IrCl$_2$Cp*(UCN)] were performed, including isotopic analysis and *in-situ* DRIFTS experiments, however the dilute nature of the iridium on carbon nitride made this investigation challenging. A hydrogenation mechanism was proposed which was consistent with the observations, however the results were not conclusive. Decorating carbon nitride with different metal fragments, such as ruthenium or rhodium half-sandwich complexes, may prove a valid pathway to novel catalysts.

Each metal fragment investigated coordinated to the carbon nitride to a different extent as measured by ICP-MS as shown by the different metal concentration in each case. The interaction between metal and carbon nitride was in all cases in this work seen to be relatively weak, with metal leaching occurring in coordinating solvents for all materials made. Although it is assumed that the coordination environments are identical across the surface of carbon nitride, the varying concentration suggests that there are several different coordination sites with different binding strengths, e.g. chain terminal edge-site heptazine units compared to edge-site heptazine units in the middle of a chain. The morphology of the carbon nitride was shown to effect on the quantity of metal that carbon nitride could support. Although very difficult to investigate directly, patterns in the metal loading may emerge if enough systems are synthesised.

In principle, the potential applications of carbon nitride as a ligand are very broad, both in novel heterogeneous catalyst design and in improving the intrinsic properties of carbon nitride. This work represents a first attempt to explore the use of the coordination chemistry accessible to carbon nitride.

6 Experimental

6.1 Measurements and Techniques

6.1.1 Acid Site analysis

Acid site analysis was carried out by Amin Osatiashtiani from the European Bioenergy Research institute at Aston University, UK. Acid site loadings and strength were determined via n-propylamine (Sigma Aldrich, ≥99 %) temperature programmed reaction using a Mettler Toledo TGA/DSC 2 STARe system connected to a Pfeiffer Vacuum ThermoStar GSD 301 T3 Benchtop Mass Spectrometer (MS). Propylamine adsorption was performed by dosing liquid n-propylamine onto pre-weighed samples (1 ml/20 mg) in the TGA crucible cell. Excess physisorbed propylamine was removed by drying in a vacuum oven at 40 °C prior to sample loading in the TGA. Samples were heated in the TGA furnace from 40 °C to 800 °C at a ramp rate of 10 °C.min-1 under flowing N_2 (40 ml min^{-1}), with evolved gases analysed by MS to monitor the appearance of reactively formed propene over the acid sites. Acid site loading then were calculated based on the mass loss in the range where propene was desorbed. To be accurate, mass loss due to reasons other than propene desorption were taken into account by subtracting the mass loss of the fresh sample (sample without propylamine).

6.1.2 BET Surface Area Analysis

BET (Brunauer-Emmett-Teller) surface area measurements for UCN, CCN and $[Ru(bpy)_2(UCN)](PF_6)_2$ were collected using a Micromeritics Tristar 3000 Porosimeter. A minimum of 50 mg of sample was heated to 120°C for 6 hours under nitrogen flow to degas and dry samples prior to weighing in triplicate. BET (N_2) surface area analysis was performed on a P/P_0 range between 0.05 and 0.2.

BET (Brunauer-Emmett-Teller) surface area measurements for $[Ru(bpy)_2(CCN)](PF_6)_2$ were collected using a Micromeritics ASAP 2020 Porosimeter. 30 mg of sample was heated to 150°C for 4 hours under nitrogen flow to degas and dry sample prior to weighing in triplicate. BET (N_2) surface area analysis was performed on a 5 point pressure range.

6.1.3 Cyclic Voltammetry

Electrochemical analysis was carried out using a BASi Epsilon-EC potentiostat and a single compartment cell. Cyclic voltammograms were collected from a solution of analyte (1 mmol dm^{-3}) in DMF with $(NEt_4)(PF_6)$ (100 mmol dm^{-3}) as electrolyte. Nitrogen was bubbled through solution for 20 minutes prior to analysis. A three-electrode set-up was used, with a Ag/AgCl electrode was used as reference, with carbon disk as working electrode and platinum wire as counter.

6.1.4 Diffuse Reflectance

DRS measured using Ocean Optics HR2000+ spectrometer with Mikropack DH-2000-BAL UV-VIS-NIR light source, with an integration time of 10 seconds, a boxcar width of 30, and averaged over 10 scans . Dark and light references were collected with a flat, white polystyrene reference sample. Powder DRS spectra collected by placing a small amount of sample onto a clean glass microscope slide and flattening sample with another slide.

6.1.5 Dynamic Light Scattering and Zeta Potential Measurements

DLS and Zeta potential measurements performed using 1 mg mL^{-1} dispersions of materials in Millipore water and using a Malvern Folded Capillary Zeta Cell and a Malvern Zetasizer Nano-ZS. Measurements were carried out at 25°C and in triplicate, with 10-15 runs used per single measurement.

6.1.6 Electron Paramagnetic Resonance (EPR)

EPR spectroscopy was carried out by Dr. Joyashish Debgupta. EPR spectra were recorded in a custom made Schlenck EPR tube, the bottom 100 mm of which was made up of commercially available medium wall Suprasil Quartz EPR tube (O.D. 4 mm) which has practically no background signal. Samples were introduced into the EPR tube and the whole EPR tube was evacuated in a Schlenck line for at least 30 min prior to record EPR spectrum of the sample (under vacuum).

EPR spectra were recorded at room temperature as well as at 77 K. For measurement at 77 K, a finger dewar was used with liquid nitrogen. A 100 W mercury lamp/300 W Xe lamp was used as the source of radiation for recording EPR under constant illumination.

JEOL JES RE1X EPR spectrometer was used to record all EPR spectra. A Cylindrical type resonator (TE_{011}) was used with a 30 mm hole to illuminate the sample. All spectra were recorded using the following parameters: Sweep Width = 40 mT, Sweep Time = 60 s, Number of Sweeps = 5/20, Points = 8192, Receiver Gain = 79, Modulation Frequency = 100 kHz, Modulation Width = 0.1, Time Constant = 0.1. A DPPH standard was used to calibrate the magnetic field and calculate the g-values and the accurate frequency was read using a digital frequency meter.

6.1.7 Elemental Analysis (CHN, Cl)

Carbon, Hydrogen and Nitrogen (CHN) analysis was performed by Dr Graeme McAllister using an Exeter Analytical Inc CE-440 analyser in conjunction with a Sartorius SE2 analytical balance.

For chlorine analysis, samples were combusted using the oxygen flask technique. The combustion products were analysed by ion chromatography on a Dionex Aquion Chromatography System fitted with an IonPac AS22 anion-exchange column.

6.1.8 Elemental Analysis (ICP-MS)

ICP-MS measurements of Ruthenium, Platinum and Iridium were obtained using an Agilent 7700x ICP-MS by Dr Emma Dux. Samples (ca. 10 mg) were digested in a microwave digestion system (Milestone Ethos UP) fitted with a SK 15 rotor. Calibration of the MS was performed using standards from 0-1000 ppb. ICP-MS measurement of Rhenium was carried out by Michael Thompson, Industrial Liason Officer from the University of Hull.

6.1.9 Gas Chromatography of Organic Molecules

For organic molecules, an Agilent/HP 6890 was used with 1 μL autoinjection into a Chrompack DB-5MS Non polar 30m x 0.250mm column (inlet temperature 250°C). Carrier gas was hydrogen with a flow rate of 1 mL/min. Column temperature was increased from 90-300°C at a rate of 20°C/min. Detection was performed using a flame ionisation detector at 250°C.

6.1.10 High Performance Liquid Chromatography (HPLC)

HPLC performed on Shimadzu Prominence RP-HPLC in reverse phase, using 'C18-Athena' column with 4:1 water:acetonitrile with 0.1% v/v formic acid and a flow rate of 1 mL/min. A low-pressure gradient was used to increase acetonitrile concentration in the mobile phase (20% - 50% over 20 minutes, then 50% - 90% over 5 minutes, then held at 90% acetonitrile for 13 minutes). Oven temperature was held at 35°C. Detection performed using a UV diode-array.

6.1.11 Infrared Spectroscopy (ATR-IR)

Infrared spectra were recorded on a PerkinElmer FT-IR Spectrum Two spectrometer in the region of 4000-500 cm^{-1} collected over 8 scans with a resolution of 1 cm^{-1}. ATR-IR spectra were collected by first cleaning the crystal with isopropanol and measuring a blank spectrum to use as reference. Solution spectra were collected in a quartz cell with the solvent used as the reference spectrum.

6.1.12 Infrared Spectroscopy (DRIFTS)

DRIFTS spectra were collected on a Bruker Equinox 55 spectrometer after dilution in KBr and grinding into a fine powder. Spectra were collected using 128 scans over the range 6000-500 cm^{-1}. Atmospheric correction for water and carbon dioxide performed using OPUS software.

6.1.13 Luminescence (Steady-State) Spectroscopy

Steady-state luminescence spectra were recorded on a Hitachi F-4500 spectrometer using both solid and solution cell holders. For solid samples, 50 mg was ground finely then placed in a quartz cell held at 45° to incident light and detector. Wavelength parameters and excitation/emission slot width were optimised for each sample to maximise signal.

6.1.14 Luminescence (Time-Resolved) Spectroscopy

Time-resolved fluorescence data collected using an Edinburgh Photonics FLS-980 with 380 nm and 470 nm picosecond pulsed diode laser sources over 2048 channels to a peak height of 20000. Solids were dispersed into 1 mg mL-1 suspensions and oxygen removed using a triple freeze-pump-thaw process. Data was processed using a tail fit analysis to fit to Equation 1 over the point ranges 300-2047 to optimise the fitting factor (χ^2).

$$\boldsymbol{R(t) = B_1 e^{\left(\frac{-t}{\tau 1}\right)} + B_2 e^{\left(\frac{-t}{\tau 2}\right)} + B_3 e^{\left(\frac{-t}{\tau 3}\right)}}$$

6.1.15 Mass Spectrometry

Electro-spray ionisation Mass Spectrometry collected on a Bruker microTOF Electrospray (ESI) mass spectrometer by Mr. K. Heaton as the departmental service. A minimum of 5mg was submitted and predissolved in DCM prior to analysis.

6.1.16 Melting Point

Melting points were measured using a Stuart Scientific Melting Point Apparatus SMP3. A small amount of sample was placed in a melting point tube and an initial heating rate of 5°C min^{-1} was used to determine melting range. When the melting range was approximately known, the heating rate was slowed to 1 °C min^{-1}.

6.1.17 NMR Spectroscopy

Solution ^{1}H and ^{13}C NMR spectra were recorded on a Bruker AV500B (^{1}H NMR 500 MHz) or JEOL ECX400 (^{1}H NMR 400 MHz) spectrometer. Samples were dissolved in deuterated solvent in air unless otherwise stated. Solid-state ^{13}C CP-MAS recorded on Bruker Ascend 400 WB NMR spectrometer by loading sample into 4mm zirconia rotor. Spin rate is stated where spectra are shown. All samples were referenced using an external standard sample of adamantane (29.5 ppm).

6.1.18 Powder X-Ray Diffraction (PXRD)

PXRD (Powder X-ray Diffraction) experiments were performed using a Bruker D8 X-ray Diffractometer fitted with a Lynxeye detector and acquired with Cu Kα radiation. The sample was placed on aluminium disk and spread out to achieve a flattened surface, with measurement taken between 5-90° 2θ with step size of 0.019775.

6.1.19 Scanning Electron Microscopy (SEM)

Approximately 10 mg of sample was dispersed in hexane before depositing on a silicon wafer. After solvent evaporation, silicon wafer was attached to an aluminium stub using carbon tape, then coated in Pt/Pd (5 nm) using a JEOL JFC 2300 HR High Resolution Fine Coater. SEM images then collected using a JSM 7800F Prime Field Emission Scanning Electron Microscope using the 5 kV LED (lower electron detector), a working distance of 10 mm and are shown at 50,000 times magnification.

6.1.20 Single Crystal X-ray Crystallography

Single crystals of molecular analogues were grown under conditions listed in experimental for each compound. Diffraction data were collected at 110 K, see item on an Oxford Diffraction SuperNova diffractometer with either Mo-K radiation (λ = 0.71073 Å) or Cu-K radiation (λ = 1.54184 Å) using a EOS CCD camera. The crystal was cooled with an Oxford Instruments Cryojet. Diffractometer control, data collection, initial unit cell determination, frame integration and unit-cell refinement was carried out with “Crysalis”. Face-indexed absorption corrections were applied using spherical harmonics, implemented in SCALE3 ABSPACK scaling algorithm. OLEX2 was used for overall structure solution, refinement and preparation of computer graphics and publication data. Within OLEX2, the algorithms used for structure solution were ShelXT dual-space. Refinement by full-matrix least-squares used the SHELXL-97 h algorithm within OLEX2. All non-hydrogen atoms were refined anisotropically. Hydrogen atoms were placed using a “riding model” and included in the refinement at calculated positions.

6.1.21 Transmission Electron Microscopy (TEM)

TEM images were obtained by Dr. Robert Mitchell at the JEOL Nanocentre using a JEOL JEM-2010 transmission electron microscope equipped with an EDAX Phoenix EDS X-ray spectrometer. Operation voltage was 200 kV. Samples were dispersed in hexane and sonicated to disperse samples. The dispersion was deposited onto a copper grid and the solvent allowed to evaporate prior to microscopy.

6.1.22 UV-visible Light Absorbance Spectroscopy

UV-visible spectra measured using Shimadzu UV-1800 in a quartz cell with 1 cm pathlength and a ‘medium’ scan speed in absorption mode with 0.5 nm resolution across 200-900 nm. A cuvette filled with pure solvent used to provide baseline immediately prior to data collection.

6.1.23 X-Ray Photoelectron Spectroscopy (XPS)

XPS measurements were performed by Dr Mark Isaacs at Aston University, UK. XPS measurements were taken using a Kratos Axis Supra using a monochromated Al -ray anode (1486.69 eV) and fitted with a charge neutraliser. All measurements were performed with a pressure of $<10^8$ Torr. Wide scans were performed using a pass energy of 160 and step size of 1 eV and high resolution scans with a pass energy of 20 and step size of 0.1 eV. Data was analysed using CASAXPS v2.3.15. C 1s, O 1s and N 1s peaks were fit using a GL(30) lineshape. Ru 3d peaks were fit using a DS(0.01,400)GL(30) lineshape and a doublet separation of 4.1 eV. Re 4f peaks were fit using a DS(0.01,400)GL(30) lineshape and a doublet separation of 2.43 eV. Ir 4 peaks were fit using a DS(0.01,400)GL(30) lineshape and a doublet separation of 3.2 eV. Mo 3d peaks were fit using a DS(0.01,400)GL(30) lineshape and a doublet separation of 3.15 eV. All spectra were charge corrected to adventitious carbon at 284.8 eV.

Materials and Reagents

[ReCl(CO)$_5$], [MnCl(CO)$_5$], [Ru(bpy)$_2$Cl$_2$] and [IrCp*Cl$_2$]$_2$ synthesised as previously described.[285-288] Urea (≥99.5%), cyanamide (99%), tetraethylorthosilicate (99%), 2,2'-bipyridine (≥99%), and triethanolamine(98%) was obtained from Sigma-Aldrich. 5,7-dimethyl-[1,8]-naphthyridine-2-amine (DMNA) was obtained from Santa Cruz Biotechnology. Rhenium carbonyl obtained from Fluorochem. Manganese carbonyl (98%) obtained from Strem Chemicals. Dimethylformamide, (+)-Limonene (96%), D(+)-Carvone (98%) and acetophenone (99%) obtained from Acros organics. Silver hexafluorophosphate, hexachloroplatinic acid (≥99.9%), phenylacetylene, oct-1-yne, trans-β-methyl styrene (99%), benzaldehyde (≥99%), 1-phenylethanol (98%), 1-octene (98%), allyl alcohol (98%), surfuryl chloride (97%) and ammonia in ethanol () obtained from Aldrich. N-Octane obtained from Fisons Scientific Apparatus. Ethyl benzene (≥99%) and ammonium bifluoride (98.5%) obtained from Fluka. Iridium (III) chloride trihydrate (99.8%), Cyclohexene (99%), α-methyl styrene (99%), pentamethylcyclopentadiene (94 %) obtained from Alfa Aesar.

Toluene, dichloromethane, 2-propanol and hexane d$_3$-MeCN obtained from VWR. Ethanol, Acetonitrile, Ethyl Acetate and d$_6$-DMSO were obtained from Sigma-Aldrich. Diethyl Ether obtained from Fisher Scientific. Toluene, DCM and hexane dried using an Innovative Technology PureSolv Solvent Purification System. Ethanol dried using activated molecular sieves (4Å). Water purified using a Millipore system. Unless otherwise stated compounds used as obtained without further purification.

6.2 Chapter 2 Experimental

6.2.1 Synthesis of CCN

A literature method for preparing highly porous carbon nitride was followed.[129] Cyanamide (CA) (8 g, 36 mmol) was dissolved in 0.01 M HCl (4 mL) and ethanol (4 mL) and adjusted to pH 2 using 1 M HCl. Tetraethylorthosilicate (TEOS) (1.25 g, 6 mmol) was then added. The mixture was stirred for 30 minutes and transferred to Petri dishes to evaporate in air overnight. After full evaporation, the composite was heated at 80°C for 24 hours to polymerise TEOS, and further heated to 550°C (for 4 hours under argon flow) to polymerise CA. Silica was then removed by addition of 4 M aqueous $NH_4(HF_2)$ and left to stand for 40 hours at room temperature. The precipitate was isolated by filtration and washed with water (4 x 10 mL) and then ethanol (2 x 10 mL).

The CCN was then transferred to a Schlenk tube and treated with ammonia in ethanol (2 M, 30 mL) under nitrogen to remove surface protons due to acidification in the prior step. The mixture was stirred for 3 hours before isolation by filtration. Base-treated CCN was then washed with ethanol (3 x 10 mL), water (3 x 10 mL), then ethanol (3 x 10 mL) and dried at 80°C overnight before use. Final product was a fine orange powder.

Yield:

1.52g (25%).

^{13}C CP-MAS NMR (10 kHz, 300K, Ref. Adamantane, 29.5 ppm):

δ = 164, 156

IR (ATR, cm^{-1}):

3164, 1621, 1557, 1416, 1321, 1240, 1151, 806, 557.

Elemental Analysis:

Calculated for C_3N_4: %C, 39.14, %H 0, %N 60.86;

Found %C 32.60, %H 2.35, %N 57.37.

Formula: $C_3H_{2.6}N_{4.53}$

6.2.2 Synthesis of UCN

Urea (31 g, 0.52 mol) placed in a ceramic crucible and covered with a lid was heated to 550°C in air (ramp rate of 5°C / min) for 180 minutes.

Raw UCN (500 mg) then placed in a Schlenk tube under nitrogen before addition of ammonia in ethanol (2 mol dm^{-3}, 20 mL). The mixture was stirred for 3 hours before isolation by filtration. Base treated UCN was then washed with ethanol (3 x 10 mL), water (3 x 10 mL), then ethanol (3 x 10 mL) and dried at 80°C overnight. Final product was a fine yellow powder.

Yield:

1.93g (12%).

^{13}**C CP-MAS NMR** (10 kHz, 300K, Ref. Adamantane, 29.5 ppm):

δ = 164, 156

IR (ATR, cm$_{-1}$):

3164, 1621, 1557, 1416, 1321, 1240, 1151, 806, 557.

Elemental Analysis (CHN):

Calculated for C_3N_4: C, 39.14, H, 0, N, 60.86

Found C, 33.74, H, 1.754, N, 59.57

Formula: $C_3N_{4.54}H_{1.86}$

6.2.3 Synthesis of Mn-UCN

Ammonia-treated UCN (200 mg, 1 mmol) was placed in a Schlenk tube under vacuum for 2 hours whilst heating at 110°C. [$Mn(CO)_5Cl$] (25 mg 0.084 mmol) was dissolved in dry toluene (20 mL) under nitrogen and the solution added to the UCN. The mixture was then refluxed under nitrogen for 21 hours before cooling and isolating the solid by filtration and washing with dry toluene (3 x 60 mL). The solid was dried at 80°C overnight under vacuum and handled under nitrogen. Final product was a fine yellow powder.

Yield:

160 mg obtained (80%).

Elemental Analysis (CHN):

Calculated for C_3N_4: C, 39.14, H, 0, N, 60.86

Found C, 28.17, H, 1.78 N, 41.46

Formula: $C_3N_{3.79}H_{2.28}$

Elemental Analysis (ICP-MS):

Percentage by mass (Mn): 1.33

6.2.4 Synthesis of [ReCl(CO)$_3$(UCN)]

Ammonia-treated UCN (700 mg, 3.53 mmol) was placed in Schlenk tube then placed under vacuum for 2 hours whilst heating at 110°C. [Re(CO)$_5$Cl] (150 mg, 0.42 mmol) was dissolved in dry toluene (20 mL) under nitrogen and the solution transferred to the UCN. The mixture was then refluxed under nitrogen for 21 hours before cooling. Solid was isolated by filtration and washed with dry toluene (3 x 60 mL). Solid dried at 80°C in air for at least 5 hours. Final product was a fine orange powder.

Yield:

550 mg (79%).

Elemental Analysis (CHN):

Calculated for C_3N_4: C, 39.14, H, 0, N, 60.86

Found C, 31.70, H, 1.87, N, 54.73

Formula: $C_3N_{4.44}H_{2.12}$

IR (ATR, cm-1):

3164, 2034, 1916 1621, 1557, 1416, 1321, 1240, 1151, 806, 557.

Elemental Analysis (ICP-MS):

Percentage by mass (Re): 7.35

6.2.5 Synthesis of [MnCl(CO)$_3$(DMNA)]

[Mn(CO)$_5$Cl (100 mg, 0.33 mmol) was placed into a Schlenk flask and dissolved in dry toluene (30 mL) under nitrogen. 5,7-dimethyl[1,8]naphthyridin-2-amine (60 mg, 0.34 mmol) was placed in a Schlenk flask under nitrogen and dissolved in DMF (6 mL) and heated to 90°C. [Mn(CO)$_5$Cl] solution in toluene was then transferred to the DMNA solution and stirred at 90°C for two hours. When solution infrared spectrum of the reaction mixture showed full conversion (approx., 2 hours), the solvent was reduced to ca. 2 mL *in vacuo*. Solution was then left to cool and diethyl ether (50 mL) added. The precipitate then isolated by filtration and washed with diethyl ether (4 x 5 mL). [MnCl(CO)$_3$(DMNA)] then dried *in vacuo* and stored in a glovebox under nitrogen. Product was a yellow microcrystalline solid.

Single crystals of were grown for crystallography by vapour diffusion of pentane into a saturated acetone solution of [MnCl(CO)$_3$(DMNA)].

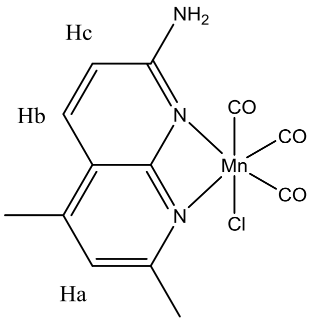

Figure 6.1: Structure of [MnCl(CO)$_3$(DMNA)]

Yield:

105 mg (0.29 mmol, 85%).

^{1}H NMR (500 MHz, CD_2Cl_2, N_2, 25 °C / ppm):

δ = 7.93 (s, 1H, Hb), 7.07 (s, 1H, Ha), 5.76, (s, 1H, Hc), 5.77 (br s, 2H, NH_2), 2.71 (s, 3H, CH_3), 2.56 (s, 3H, CH_3)

Mass Spectrometry (LIDFI-MS):

m/z calcd. [$C_{13}H_{11}ClN_3O_3Mn_1$]+ 346.99; found 347.01

Elemental Analysis (CHN):

Calculated for $C_{13}H_{11}ClN_3O_3Mn$ + 0.5 H_2O: C, 43.78, H, 3.22, N, 11.78

Found C, 43.39, H, 3.19, N, 11.88

IR (DCM / cm^{-1}):

3045, 3022, 2924, 2030, 1940, 1921, 1686, 1452

6.2.6 Synthesis of [Re(CO)$_3$Cl(DMNA)]

[Re(CO)$_5$Cl] (100 mg, 0.28 mmol) was placed into a Schlenk flask and dissolved in toluene (20 mL) under nitrogen. 5,7-dimethyl[1,8]naphthyridin-2-amine (48 mg, 0.28 mmol) was placed in a Schlenk flask under nitrogen and dissolved in DMF (3 mL). The [Re(CO)$_5$Cl] solution was transferred to the DMNA solution and stirred at 90°C for one hour. When the solution infrared spectrum of the reaction mixture showed full conversion, solvent reduced to ca. 2 mL *in vacuo*. Solution cooled and diethyl ether (35 mL) added. The resulting precipitate was then isolated by filtration and washed with diethyl ether (3 x 5 mL). [ReCl(CO)$_3$(DMNA)] was then dried *in vacuo* and stored in glovebox. Single crystals of [ReCl(CO)$_3$(DMNA)] were grown for crystallography by vapour diffusion of pentane into a saturated acetone solution of [ReCl(CO)$_3$(DMNA)]. The product was an ivory microcrystalline solid.

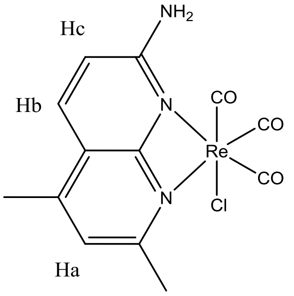

Figure 6.2: Structure of [ReCl(CO)$_3$(DMNA)]

Yield:

68 mg (0.14 mmol, 50%).

^{1}H NMR (400 MHz, CDCl$_3$, 25 °C / ppm):

δ = 8.08 (d, 9.2 Hz, 1H, Hb), 7.15 (d, 9.2 Hz, 1H, Ha), 7.08, (s, 1H, Hc), 5.77 (br s, 2H, NH$_2$), 2.97 (s, 3H, CH$_3$), 2.89 (s, 3H, CH$_3$)

Mass Spectrometry:

m/z calcd. [$C_{13}H_{11}ClN_3O_3Re_1$]+ 477.00; found 476.99

Elemental Analysis (CHN):

Calculated for $C_{13}H_{11}ClN_3O_3Re$: C, 32.60, H, 2.32, N, 8.77

Found C, 32.73, H, 2.35, N, 8.30

IR (DCM / cm^{-1}):

2964, 2933, 2870, 2025, 1916, 1899, 1723, 1291

UV-Visible Absorption Spectrum (DCM):

λ_{max} = 338 nm, ε = 13431 mol $^{-1}$ dm^{-3} cm^{-1}

Melting Point:

293-295 °C (decomp.)

6.2.7 Leaching of rhenium from Re-UCN into solution

Re-UCN (30 mg) was stirred in 2 mL solvent for three hours, after which 1 mL of solution was removed and filtered using a syringe filter before setting aside for solution IR spectroscopy. The remaining Re-UCN suspension was filtered and washed with solvent (3 x 2 mL) before drying for 2 hours at 60°C. ATR-IR spectroscopy was then performed on Re-UCN to monitor the presence of carbonyl region vibrations.

6.3 Chapter 3 Experimental

6.3.1 Synthesis of $[Ru(bpy)_2(CCN)](PF_6)_2$

$Ag(PF_6)$ (39 mg, 0.16 mmol) and $RuCl_2(bpy)_2$ (37 mg, 0.08 mmol) were combined in a Schlenk flask under argon. Ethanol (10 mL) was added and the reaction brought to reflux for one hour. The solution was transferred via filtration to an ampule containing base-treated CCN (200 mg, 1 mmol). The reaction was heated to 80°C under argon and then sealed. 100 µL aliquots of reaction mixture were periodically taken, filtered and diluted to 800 µL with ethanol before measuring the UV-visible absorption spectrum. After 145 hours, the reaction was allowed to cool to room temperature and thesolid isolated by filtration and washed with water (5 x 10 mL) and ethanol (3 x 10 mL) until filtrate ran colourless. Final product was a finely divided dark red powder.

Yield:

160 mg (70%)

^{13}C CP-MAS NMR (10 kHz, 300K, Ref. Adamantane, 29.5 ppm):

δ = 164, 156, 137, 125.

IR (ATR, cm^{-1}):

3156, 1614, 1556, 1403, 1231, 1144, 841 (PF_6), 804, 759, 727, 556.

Elemental Analysis:

Calculated for C_3N_4: %C, 39.14, %H 0, %N 60.86;

Found %C 30.46, %H 2.49, %N 47.18.

Formula: $C_3H_{2.94}N_{3.98}$

Elemental Analysis (ICP-MS):

Percentage by mass (Ru): 0.78

6.3.2 Synthesis of $[Ru(bpy)_2(UCN)](PF_6)_2$

$Ag(PF_6)$ (39 mg, 0.16 mmol) and $RuCl_2(bpy)_2$ (37 mg, 0.08 mmol) were combined in a Schlenk flask under argon. Ethanol (10 mL) was added and the reaction was brought to reflux for one hour. The ruthenium solution was transferred via filtration to ampule containing base-treated UCN (200 mg, 1 mmol). The reaction was heated to 80°C under argon and then sealed. 100 µL aliquots of reaction mixture were periodically taken, filtered and diluted to 800 µL with ethanol before measuring UV-visible spectrum. After 24 hours, the reaction was cooled to room temperature and the solid isolated by filtration and washed with water (5 x

10 mL) and ethanol (3 x 10 mL) until filtrate ran colourless. Final product was a finely divided pink powder.

Yield:

157 mg (68%)

^{13}**C CP-MAS NMR** (10 kHz, 300K, Ref. Adamantane, 29.5 ppm):

δ = 164, 156, 125 (weak).

IR (ATR, cm_{-1}):

3181, 1622, 1557, 1407, 1236, 1147, 1081, 841 (PF_6), 807, 768, 557.

Elemental Analysis:

Calculated for C_3N_4: %C, 39.14, %H 0, %N 60.86;

Found %C 31.15, %H 1.67, %N 52.96.

Formula: $C_3H_{1.93}N_{4.37}$

Elemental Analysis (ICP-MS):

Percentage by mass (Ru): 0.16

6.3.3 Synthesis of $[Ru(bpy)_2(DMNA)](PF_6)_2$

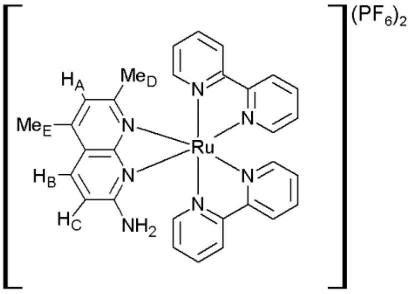

Figure 6.3 Structure of $[Ru(bpy)_2(DMNA)](PF_6)$

$Ru(bpy)_2Cl_2$ (170 mg, 0.351 mmol) and $Ag(PF_6)$ (194 mg, 760 mmol) were combined in a Schlenk flask under nitrogen. EtOH (10 mL) was added and the solution was heated to reflux for one hour with stirring. 5,7-dimethyl[1,8]naphthyridin-2-amine (58 mg, 0.335 mmol) was placed in a separate Schlenk flask under nitrogen and dissolved in MeOH (5 mL). After cooling, the ruthenium solution was transferred via cannula filtration into the DMNA solution leaving behind a residue of AgCl. The resulting red solution was then heated to reflux for one hour under nitrogen. After cooling, the solvent removed in vacuo. The crude solid was then dispersed in ethanol (5 mL) under nitrogen and precipitated by adding hexane

(40 mL). The product was isolated by filtration and washed with water (1 mL) and ethanol (1 mL). Product appearance was a red, microcrystalline solid.

Single crystals were obtained by vapour diffusion of diethyl ether into a saturated acetone solution of $[Ru(bpy)_2(DMNA)](PF_6)_2$.

Yield:

210 mg (68%).

^{1}H NMR (400 MHz, [d_4]-MeOH, 25 °C / ppm):

δ = 8.74 (d, J = 8.2 Hz, 2H), 8.69 (d, J = 5.5 Hz, 1H), 8.63 (dd, J = 8.2 Hz, J = 3.2 Hz, 2H), 8.33 (d, J = 5 Hz, 1H), 8.23, (d, J = 9.6 Hz, 1H, H_B), 8.22 (m, 2 H), 7.98 (td, J = 8.2 Hz, J = 1 Hz, 2H), 7.82 (dd, J = 13.3 Hz, J = 6 Hz, 2H), 7.66 (dt, J = 25 Hz, J = 6 Hz, 2H), 7.34 (td, J = 6 Hz, J = 1Hz, 2H), 7.07 (s, 1H, H_A), 6.88 (d, J = 9.6 Hz, 1H, H_C), 2.63 (s, 3H, Me_E), 1.71 (s, 3H, Me_D).

^{13}C NMR (100 MHz, [d_4]-MeOH,25 °C / ppm):

δ = 161.8, 157.3, 156.4, 151.2, 151.1, 150.3, 146.3, 136.1, 135.4, 132.4, 126.3, 126.2, 125.2, 122.4, 122.3, 122.2, 120.6, 112.7, 111.6, 18.4, 14.9.

MS-ESI (LIFDI-MS):

m/z calcd. $[C_{30}H_{27}N_7Ru]^+$ 586.14; found 586.1288; m/z calcd. $[C_{30}H_{27}F_6N_7PRu]^+$ 732.10; found 732.1023

Elemental Analysis:

Calculated for $C_{30}H_{27}F_{12}N_7P_2Ru$: C, 41.11, H, 3.10,N, 11.19;

Found C, 40.639, H, 3.105, N, 10.963.

Melting Point:

246-250 °C (decomp.)

IR (ATR / cm^{-1}):

3497, 3385, 1641, 1594, 1423, 837, 825, 764, 556

UV-visible light absorption-emission (Acetone, 10 µmol dm^{-3}):

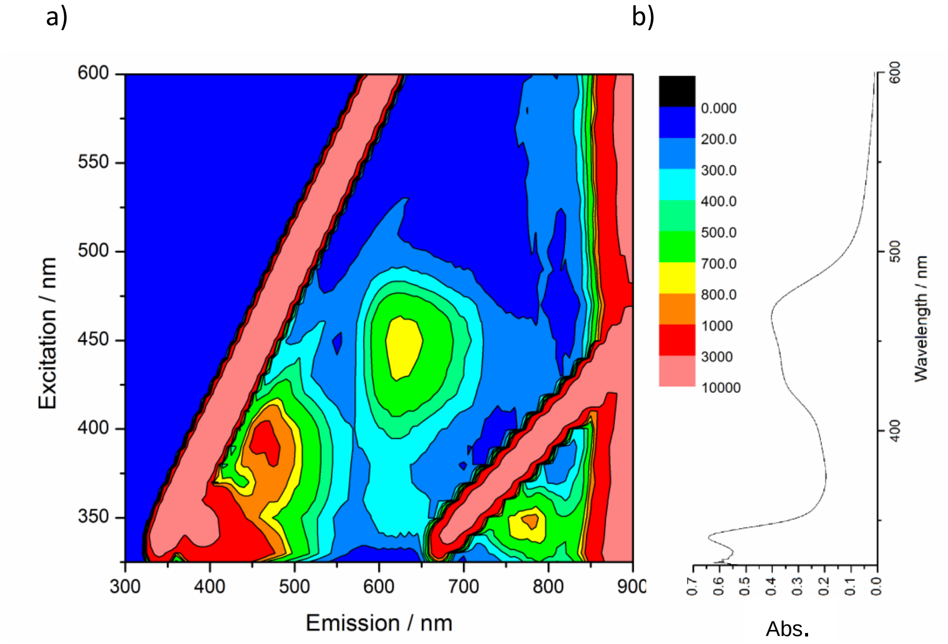

Figure 6.4 a) 3D Excitation-emission map of [Ru(bpy)$_2$(DMNA)](PF$_6$)$_2$ b) UV-visible light spectrum of [Ru(bpy)$_2$(DMNA)](PF$_6$)$_2$

6.3.4 Photocatalytic Testing

A closed loop, gastight setup was used to perform photocatalytic hydrogen generation and analysis of products. A schematic of the setup is shown in Figure 6.5.[289]

The design consists of a glass cell with a quartz window placed below a 300 W Xe lamp (Figure 6.6). The cell contains a 50 mL beaker for the catalyst and solution including the sacrificial reagent (20 mL). This beaker was placed inside a 100 mL beaker within the cell, with water jackets (10 mL in 100 mL beaker, 40 mL in main cell) and glass spacers used to ensure rigidity and good heat transfer from the external oil bath.

During photocatalytic runs, the glass cell was wrapped in foil to minimise light loss. The loop and cell were purged with Ar (0.5 bar overpressure) for 10 minutes or until chromatograms did not show peaks for air. Between runs, the loop was dried under vacuum (30 minutes) and argon (30 minutes) to prevent condensation build-up.

The loop comprises of 4.2 meters of metal tubing (0.5 mm ID), with Swagelok connections to the 4 mm ID Clearflex 60 PVC tubing between the metal tubing and pump. 4 mm ID metal tubing was used for the connections on the top of the cell, with a total length of approximately 0.8 meters. The total loop volume was ca. 11 mL. The empty cell volume was ca. 290 mL, 250 mL after addition of glass spacers and beakers. With 70 mL total liquid added to the cell, gas headspace is ca. 191 mL. The majority of the headspace is confined within the catalytic cell.

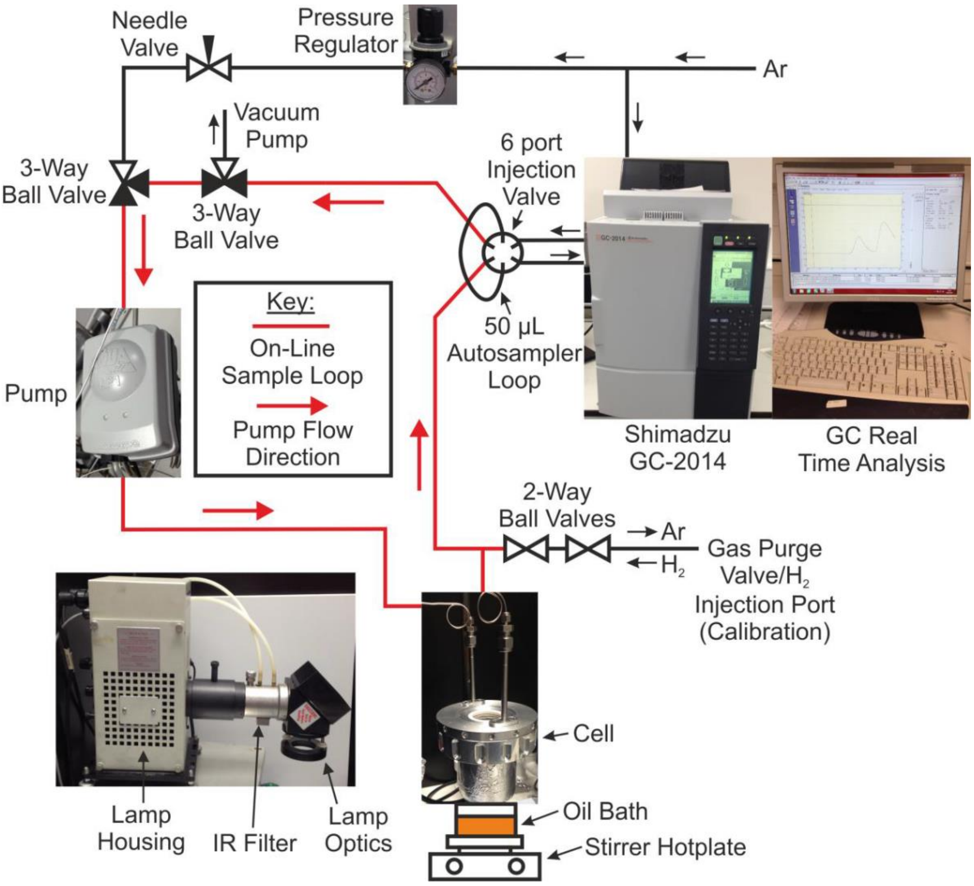

Figure 6.5:Photocatalytic testing closed system set-up, reproduced from thesis of R Mitchell[289]

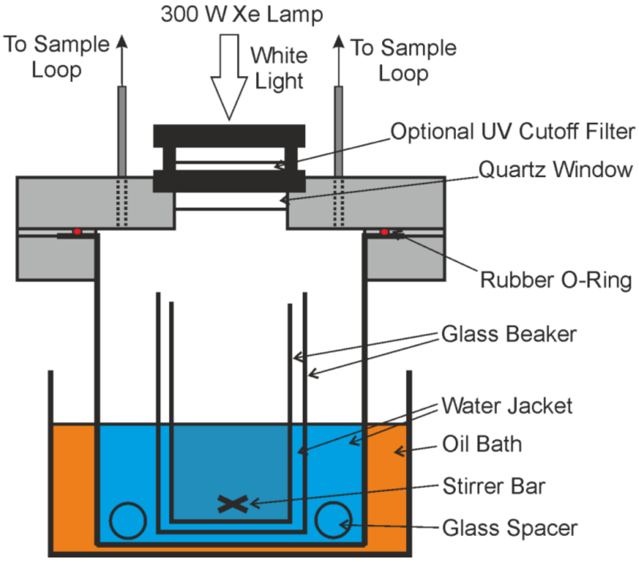

Figure 6.6: Photocatalytic testing cell, reproduced from thesis of R Mitchell[289]

Gas chromatography for hydrogen generation experiments was performed using a Shimadzu GC-2014 fitted with at 25 cm long 5Å molecular sieve packed column and TCD detector. 50 µL of gas was autosampled over the time course of the reaction and injected on to the column with a 20 mL / min flow rate, 90°C column temperature and 120°C detector temperature. Retention times of H_2, O_2 and N_2 under these conditions are 1.5 min, 2.3 min and 3 min respectively. A calibration curve was used to quantify hydrogen within the system (Figure 6.7).

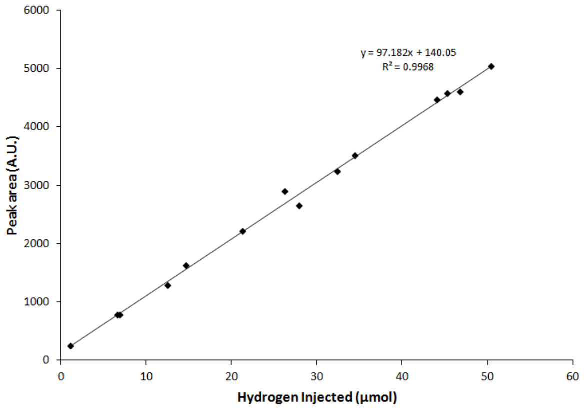

Figure 6.7: Calibration curve for hydrogen collected by R Mitchell[289]

6.3.5 Platinum Nanoparticle Deposition onto Carbon Nitrides

Carbon nitride (80 mg) was dispersed in 10% aqueous TEOA solution (80 mL) in a 50 mL beaker and H_2PtCl_6 (1.6 mg) was added. The beaker was transferred to the photolytic cell as for photocatalytic hydrogen evolution and subjected to UV irradiation from a 300 W Xe lamp. The reaction airspace was monitored by gas chromatography for five hours, during which time hydrogen evolution is observed. Unless otherwise stated, solid then isolated by filtration and washed with water (5 x 10 mL) and ethanol (3 x 10 mL). Solid was dried at 80°C for 12 hours prior to use. Samples took on a darker colour after treatment with platinum nanoparticles.

6.3.6 Photocatalytic Hydrogen Evolution

30 mg catalyst was sonicated into 20 mL sacrificial solution (10% aqueous solution of triethanolamine) in a 50 mL beaker. The 50 mL beaker was placed inside a glass photolysis cell with quartz window as described in section 6.3.4, with GC analysis was connected to the cell. Reaction mixture was purged with argon until GC trace showed no peaks for oxygen or nitrogen. Photolysis was the performed using 300 W Xe arc lamp fitted with water IR filter and variable visible light filters as light source.

6.4 Chapter 4 Experimental

6.4.1 Synthesis of [IrCl$_2$Cp*(UCN)]

[IrCp*Cl$_2$]$_2$ (10 mg, 0.126 mmol) was combined with UCN (pre-treated with ammonia in ethanol, 100 mg) and the solids were heated at 100°C under vacuum for 1 hour. Ethanol (10 mL) was then added and the mixture refluxed under nitrogen for 24 hours. The solid was isolated by filtration and washed with ethanol (3 x 10 mL). Product was a finely divided yellow powder.

Yield:

A total of 87 mg (87%) was obtained.

Elemental Analysis (CHN):

Calculated for C_3N_4: C, 39.14, H, 0, N, 60.86

Found C, 31.704, H, 1.867, N, 54.734

Formula: $C_3N_4H_{2.44}$

Elemental Analysis (ICP-MS):

Percentage by mass (Ir): 1.34

6.4.2 Synthesis of [IrCl$_2$Cp*(DMNA-H$_2$)]

[IrCp*Cl$_2$]$_2$ (114 mg, 0.14 mmol) and DMNA (50 mg, 0.29 mmol) were dissolved in EtOH (40 mL) and heated to reflux under nitrogen for 15 hours. The solvent was reduced *in vacuo* to ca. 2 mL. Et$_2$O (40 mL) was added to precipitate a microcrystalline yellow solid isolated by filtration.

Yield:

40 mg (0.07 mmol, 24%) obtained.

^{1}H NMR (400 MHz, $CDCl_3$, 25 °C / ppm):

δ = 9.27 (s, 1H), 6.97 (br s, 1H), 6.73, (s, 1H), 2.96 (t, J = 7.5 Hz, 2H), 2.81 (t, J = 7.5 Hz, 3H), 2.36 (s, 3H), 2.24 (s, 3H) 1.61 (s, 15H)

^{13}C CP-MAS NMR (100 MHz, Solid-state, 10 kHz)

δ = 167.6, 156.0, 150.1, 146.1, 121.3, 115.0, 86.1, 29.5, 24.1, 21.0, 17.7, 10.4

LIFDI-MS:

m/z calcd. 571.11 $[C_{20}H_{28}Cl_2IrN_3]^+$, found 571.05 $[C_{20}H_{28}Cl_2IrN_3]^+$

6.4.3 Synthesis of [IrClCp*(UCN)](PF_6)

UCN (200 mg, 1 mmol) was placed under vacuum for 1 hour at 100°C. [IrCp*Cl_2]$_2$ (58 mg, 0.07 mmol) and Ag(PF_6) (38 mg, 0.15 mmol) were dissolved in DCM (10 mL) under nitrogen and stirred for one hour. After cooling the UCN to 40°C, the solution of [IrClCp*](PF_6) was transferred via cannula filtration onto the UCN. The mixture was then refluxed under nitrogen for 24 hours. Product appear was a finely divided yellow powder.

Yield:

170 mg (85%).

Elemental Analysis (CHN):

Calculated for C_3N_4: C, 39.14, H, 0, N, 60.86

Found C, 33.41, H, 1.81, N, 57.21

Formula: $C_3N_{4.40}H_{1.95}$

Elemental Analysis (ICP-MS):

Percentage by mass (Ir): 1.33

6.4.4 Synthesis of [IrClCp*(DMNA)](PF_6) (Performed by Dr. Daniel Raines)

[IrCp*Cl_2]$_2$ (117 mg, 0.15 mmol) was dissolved in DCM under nitrogen (5 mL) before adding a solution of DMNA (51 mg, 0.30 mmol) in DMF (1.8 mL). After 15 minutes, Ag(PF_6) (74 mg, 0.30 mmol) was then added in MeOH (2 mL). After 1.5 hours, solution filtered to isolate a yellow solid which was recrystallised in acetonitrile/diether ether. Product was a yellow microcrystalline solid.

Yield:

109 mg (54%)

^{1}H NMR (400 MHz, $CDCl_3$, 25 °C / ppm):

δ = 8.29 (d, 9.6 Hz, 1H, CH), 7.25, (s, 1H, CH), 7.06 (d, 9.6 Hz, 1H, CH), 2.62 (s, 6H, CH_3), 1.85 (s, 15H, Cp*-CH_3)

^{13}C CP-MAS NMR (100 MHz, Solid-state, 10 kHz)

δ = 159.9, 157.0, 149.1, 134.8, 124.0, 114.9, 87.8 (Cp*-**C**CH_3), 24.8, 18.8, 9.9 (Cp*-C**C**H_3)

ESI-MS:

m/z calcd. 536.14 [$C_{20}H_{26}ClIrN_3$]$^+$, found 536.1447 [$C_{20}H_{26}ClIrN_3$]$^+$

Elemental Analysis (CHN):

Calculated for $C_{20}H_{26}ClF_6IrN_3P$: C, 35.27, H, 3.85, N, 6.17

Found C, 34.95, H, 3.71, N, 6.04

6.4.5 Catalytic Aqueous Transfer Hydrogenation of 1-methyl-6,7-dimethoxy-3,4-dihydroisoquinoline

A quantity of catalyst containing 0.72 μmol iridium was dispersed in 450 μL aqueous NH_4CO_2H solution (3 mol dm^{-3}), which was left to equilibrate to 15 minutes stirring at 500 rpm. An aliquot (50 μL) of a solution of 1-methyl-6,7-dimethoxy-3,4-dihydroisoquinoline (0.5 mol dm^{-3}) in NH_4CO_2H solution (3 mol dm^{-3}) was added.

Time points were taken by removing a 25 μL aliquot from the reaction mixture and adding it to a quenching vial filled with 925 μL H_2O and 50 μL aqueous glutathione solution (0.25 mol dm^{-3}). Samples were stored in the fridge if storing for longer than 24 hours. Analysis was by HPLC to quantify the amount of amine formed.

For recycling experiments, heterogeneous catalyst was removed by centrifugation (three times, with washing in 10 mL H_2O between each time) and dried at 80°C overnight.

6.4.6 Catalytic Aqueous Transfer Hydrogenation of other substrates and analysis by NMR

10 μL of substrate (benzaldehyde, acetophenone or allyl alcohol) was added to 10 mg $IrCl_2Cp^*$-UCN. 1 mL D_2O (containing NH_4CO_2H, 3 mol dm^{-3}) was added and reaction heated to 40°C for 15 hours with stirring. Analysis by ^1H NMR to determine reactant conversion and product formation *in situ*.

6.4.7 Leaching of [$IrCl_2Cp^*$(UCN)] and [$IrClCp^*$(UCN)](PF_6) in different solvents

10 mg of material was placed in a 2 mL vial and 1 mL of solvent added. Mixture was then stirred and aliquots removed and filtered for UV-vis absorption spectroscopy at 1 and 3 hour timepoints.

6.4.8 Direct Hydrogenation Assays

Catalyst (25 mg, 0.002 mmol Ir) was placed in a 2 mL vial. Substrate (0.2 mmol) was then added, followed by hexane (1 mL) and a stirrer bar. The vial containing reaction mixture was then placed within a steel autoclave and charged with 10 bar hydrogen. Reaction was stirred at 500 rpm for 1 hour at room temperature unless otherwise stated. After the reaction, a 0.2 mL aliquot was removed, diluted up to 1 mL and analysed by GC.

The recycling of [$IrCl_2Cp^*$(UCN)] was performed by removing remaining solvent and substrate *in vacuo*, and using the remaining catalyst as above.

6.4.9 Isotopically labelled Hydrogenation

For the isotopic labelling experiments, the vial of catalyst, solvent and substrate was placed in a steel autoclave and charged with 4 bar hydrogen. The pressure was then increased to 8 bar by addition of deuterium, and the reaction stirred for three hours. NMR samples were made up by extracting the substrate from the hexane using d_3-MeCN, and ^{1}H and ^{2}H NMR performed on each sample.

A1 Appendix 1 - Crystal Data

A1.1.1 Crystal Structure of [MnCl(CO)$_3$(DMNA-κ$_2$*N, N'*)]

Table A1. 1 Crystal Data Table for [MnCl(CO)$_3$(DMNA)]

Parameter	[MnCl(CO)$_3$(DMNA)]
Empirical Formula	$C_{13}H_{13}ClMnN_3O_4$
Formula Weight	365.65
Temperature / K	110.05(10)
Crystal System	Monoclinic
Space Group	$P_{2l/n}$
a / Å	13.05550(10)
b / Å	11.76100(10)
c / Å	19.8768(2)
α / °	90
β / °	96.9010(10)
γ / °	90
Volume / Å^3	3029.89(5)
Z	8
ρ_{calc} g/cm^3	1.603
μ / mm-1	1.068
F(000)	1488.0
Crystal Size / mm^3	0.407x0.171x0.124
Radiation	MoKα (λ = 0.71073)
2θ range for collection / °	6.602 – 64.166
Index Ranges	-19≥h≥15, -16≥k≥16, -29≥l≥28
Reflections Collected	36527
Independent Reflections	9873 [R_{int}=0.0260, R_{sigma}= 0.0259]
Data/Restraints/Parameters	9873/0/428
Goodness-of-fit on F^2	1.060
Final R indexes [I ≥ 2σ (I)]	R_1=0.0300 wR_2=0.0745
Final R indexes [all data]	R_1=0.0365 wR_2=0.0787
Largest diff. peak/hole /e Å^{-3}	0.42/-0.67

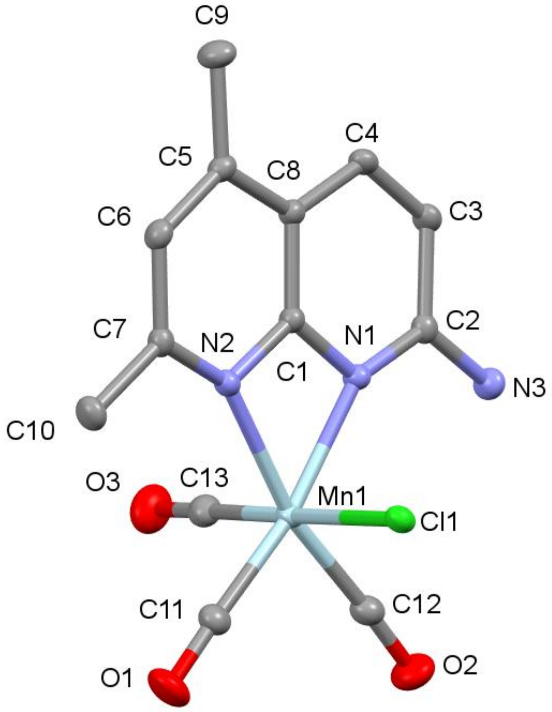

Figure A1. 1 X-Ray crystal structure of [MnCl(CO)$_3$(DMNA)]

with probability ellipsoids shown at the 50% level and hydrogens omitted for clarity

Table A1. 2 Fractional Atomic Coordinates (×10^4) and Equivalent Isotropic Displacement Parameters (Å^2×10^3) for [MnCl(CO)$_3$(DMNA)]. U_{eq} is defined as 1/3 of of the trace of the orthogonalised U_{IJ} tensor.

Atom	*x*	*y*	*z*	U(eq)
C2	-76.6(10)	5104.3(12)	3321.2(7)	14.1(2)
C3	-768.5(10)	6045.8(12)	3185.8(7)	15.7(2)
C4	-434.9(10)	7131.5(12)	3305.5(7)	15.4(2)
C8	608.8(10)	7336.6(12)	3579.4(6)	13.3(2)
C5	1109.7(10)	8393.4(12)	3720.0(7)	14.6(2)
C6	2133.3(10)	8370.2(12)	3998.2(7)	16.1(2)
C7	2665.7(10)	7345.6(12)	4153.8(7)	14.6(2)
C10	3765.8(10)	7317.0(14)	4467.2(7)	19.4(3)
C1	1205.8(10)	6365.1(11)	3724.0(6)	12.8(2)
C9	562.0(12)	9501.0(13)	3567.3(8)	21.5(3)

C13	1812.8(12)	4440.4(13)	4814.0(8)	20.5(3)
C11	3580.6(11)	4276.8(13)	4398.5(7)	19.1(3)
C12	2098.0(11)	3074.2(13)	3866.6(7)	19.1(3)
Cl1	2943.3(2)	4826.3(3)	2935.5(2)	15.73(7)
Mn1	2288.7(2)	4582.2(2)	4007.2(2)	12.96(5)
N2	2194.3(8)	6353.1(10)	4017.9(6)	13.8(2)
N1	889.7(8)	5275.4(10)	3591.8(6)	13.5(2)
N3	-408.4(10)	4034.2(11)	3187.7(7)	18.0(2)
O3	1514.9(11)	4336.1(12)	5327.2(6)	34.1(3)
O1	4384.8(9)	4040.5(12)	4648.1(6)	31.1(3)
O2	1990.6(10)	2115.0(10)	3803.8(7)	30.3(3)
C14	5350.0(10)	9705.7(11)	6722.2(6)	12.1(2)
C15	5853.4(10)	8636.9(12)	6890.7(7)	14.5(2)
C16	5335.8(10)	7640.2(12)	6783.5(7)	15.2(2)
C17	4279.8(10)	7650.0(11)	6495.1(7)	13.8(2)
C18	3610.5(11)	6711.8(12)	6362.6(7)	16.2(3)
C19	2616.4(11)	6926.9(12)	6069.1(7)	17.1(3)
C20	2265.5(10)	8030.4(12)	5898.5(7)	15.5(2)
C21	1178.4(11)	8251.1(14)	5597.1(8)	20.8(3)
C22	3869.2(9)	8720.1(11)	6325.0(6)	11.9(2)
C23	3964.7(13)	5525.9(13)	6537.9(9)	24.3(3)
C24	3522.0(11)	12123.9(12)	6013.1(7)	17.4(3)
C25	3616.7(10)	10584.4(12)	5165.7(7)	15.5(2)
C26	1886.4(11)	11126.1(13)	5538.7(7)	17.5(3)
Cl2	2492.2(2)	10791.0(3)	7053.4(2)	16.07(7)
Mn2	3111.9(2)	10658.7(2)	5965.8(2)	10.92(5)
N4	2898.9(8)	8916.4(10)	6022.6(6)	13.4(2)
N5	4373.8(8)	9730.6(9)	6433.7(5)	11.8(2)
N6	5874.1(9)	10673.7(11)	6848.9(6)	15.4(2)
O4	3758.5(10)	13058.2(10)	5997.7(7)	31.9(3)
O5	3942.0(9)	10582.1(11)	4658.7(6)	26.1(2)
O6	1120.5(9)	11433.4(11)	5256.2(6)	29.1(3)

O7	4505.1(11)	7039.2(11)	2693.1(7)	31.4(3)
O8	6503.2(11)	6691.6(13)	2377.6(8)	38.6(3)

*Table A1. 3 Anisotropic Displacement Parameters ($\text{Å}^2\times10^3$) for [MnCl$(CO)_3$(DMNA)]. The Anisotropic displacement factor exponent takes the form: -2π2[h2a*2U11+2hka*b*U12+…]*

Atom	U_{11}	U_{22}	U_{33}	U_{23}	U_{13}	U_{12}
C2	13.1(5)	16.4(6)	13.0(5)	-0.4(5)	2.8(4)	-1.5(5)
C3	10.7(5)	18.7(7)	17.6(6)	-1.6(5)	1.4(4)	0.5(5)
C4	12.5(5)	17.6(6)	16.2(6)	-0.3(5)	1.7(4)	3.6(5)
C8	12.9(5)	13.5(6)	13.6(5)	-0.9(5)	2.1(4)	0.8(4)
C5	16.3(6)	12.8(6)	15.2(6)	-0.8(5)	4.2(5)	0.4(5)
C6	16.5(6)	14.2(6)	17.8(6)	-2.7(5)	3.0(5)	-2.4(5)
C7	13.6(5)	16.7(6)	13.6(5)	-1.4(5)	1.9(4)	-1.5(5)
C10	13.6(6)	23.4(7)	20.5(6)	-1.1(6)	-1.3(5)	-2.4(5)
C1	12.2(5)	12.8(6)	13.2(5)	-0.8(5)	1.6(4)	-0.3(4)
C9	20.5(7)	14.1(7)	30.2(8)	0.7(6)	4.0(6)	1.7(5)
C13	23.0(7)	16.8(7)	21.5(7)	0.3(5)	2.0(5)	-0.6(5)
C11	19.7(6)	20.2(7)	17.0(6)	2.5(5)	1.2(5)	1.8(5)
C12	18.0(6)	18.8(7)	20.6(6)	3.1(5)	2.3(5)	1.5(5)
Cl1	12.96(13)	17.97(16)	16.12(14)	1.63(11)	1.18(10)	2.31(11)
Mn1	12.23(9)	12.41(10)	13.92(9)	1.54(7)	0.17(7)	1.01(7)
N2	11.8(5)	15.0(5)	14.2(5)	-0.5(4)	0.1(4)	0.3(4)
N1	12.3(5)	12.3(5)	16.0(5)	-0.3(4)	1.5(4)	0.0(4)
N3	14.6(5)	16.1(6)	23.1(6)	-2.1(5)	1.0(4)	-3.2(5)
O3	47.0(8)	34.4(7)	23.3(6)	1.3(5)	13.8(5)	-5.2(6)
O1	20.4(5)	42.0(8)	29.0(6)	6.5(5)	-4.8(4)	5.6(5)
O2	35.8(6)	16.2(6)	39.2(7)	-0.8(5)	5.7(5)	-1.3(5)
C14	11.9(5)	13.7(6)	10.9(5)	-0.4(4)	2.9(4)	0.8(4)
C15	13.0(5)	15.7(6)	14.6(5)	0.4(5)	1.0(4)	4.2(5)
C16	17.9(6)	12.8(6)	15.3(6)	0.9(5)	3.2(5)	5.7(5)
C17	15.9(6)	10.7(6)	15.2(6)	-0.4(5)	4.1(4)	2.1(4)

C18	22.1(6)	10.5(6)	17.2(6)	-0.9(5)	7.2(5)	0.4(5)
C19	19.6(6)	12.4(6)	20.2(6)	-3.3(5)	6.0(5)	-4.6(5)
C20	15.0(6)	16.2(6)	15.5(6)	-2.4(5)	2.8(4)	-2.7(5)
C21	15.2(6)	22.7(7)	24.0(7)	-2.0(6)	0.0(5)	-3.8(5)
C22	12.4(5)	11.0(6)	12.4(5)	-0.1(4)	2.5(4)	0.4(4)
C23	28.8(8)	10.4(6)	35.1(8)	0.5(6)	9.8(6)	0.5(5)
C24	18.2(6)	15.7(6)	18.1(6)	-0.7(5)	0.7(5)	3.3(5)
C25	15.0(6)	13.0(6)	17.8(6)	0.1(5)	-0.5(5)	0.5(5)
C26	16.7(6)	18.9(7)	17.0(6)	1.7(5)	2.3(5)	1.0(5)
Cl2	13.26(13)	20.38(16)	14.75(13)	1.29(11)	2.42(10)	3.96(11)
Mn2	10.58(9)	9.89(9)	12.09(9)	0.75(7)	0.57(6)	1.18(7)
N4	12.4(5)	12.6(5)	15.3(5)	-0.4(4)	1.7(4)	-0.6(4)
N5	11.0(4)	10.5(5)	13.7(5)	0.0(4)	1.1(4)	0.9(4)
N6	12.4(5)	15.1(6)	18.3(5)	-1.0(4)	0.2(4)	-0.7(4)
O4	39.1(7)	14.4(5)	42.0(7)	-3.3(5)	4.4(6)	-3.1(5)
O5	30.3(6)	31.2(6)	18.0(5)	0.1(4)	7.4(4)	1.7(5)
O6	19.2(5)	37.5(7)	29.0(6)	7.1(5)	-3.7(4)	6.3(5)
O7	26.4(6)	17.4(6)	49.9(8)	-5.1(5)	3.1(6)	-1.8(5)
O8	40.0(7)	30.6(7)	47.8(8)	-3.3(6)	16.1(6)	0.2(6)

Table A1. 4 Bond Lengths for $[MnCl(CO)_3(DMNA)]$.

Atom	Atom	Length/Å	Atom	Atom	Length/Å
C2	C3	1.4339(19)	C14	C15	1.4392(18)
C2	N1	1.3261(17)	C14	N5	1.3336(16)
C2	N3	1.3469(18)	C14	N6	1.3366(18)
C3	C4	1.361(2)	C15	C16	1.357(2)
C4	C8	1.4259(18)	C16	C17	1.4282(19)
C8	C5	1.4166(19)	C17	C18	1.4125(19)
C8	C1	1.3933(18)	C17	C22	1.3936(18)
C5	C6	1.3837(19)	C18	C19	1.381(2)
C5	C9	1.500(2)	C18	C23	1.497(2)

C6	C7	1.407(2)	C19	C20	1.404(2)
C7	C10	1.4957(19)	C20	C21	1.4954(19)
C7	N2	1.3320(18)	C20	N4	1.3346(17)
C1	Mn1	2.5538(13)	C22	Mn2	2.5526(13)
C1	N2	1.3513(16)	C22	N4	1.3551(16)
C1	N1	1.3623(17)	C22	N5	1.3633(17)
C13	Mn1	1.7958(15)	C24	Mn2	1.8035(15)
C13	O3	1.1412(19)	C24	O4	1.1428(19)
C11	Mn1	1.8065(15)	C25	Mn2	1.7953(14)
C11	O1	1.1404(18)	C25	O5	1.1396(17)
C12	Mn1	1.8080(16)	C26	Mn2	1.8046(14)
C12	O2	1.1417(19)	C26	O6	1.1449(18)
Cl1	Mn1	2.4058(4)	Cl2	Mn2	2.4025(4)
Mn1	N2	2.0867(12)	Mn2	N4	2.0729(12)
Mn1	N1	2.0784(11)	Mn2	N5	2.0982(11)

Table A1. 5 Bond Angles for [MnCl(CO)$_3$(DMNA)].

Atom	Atom	Atom	Angle/˚	Atom	Atom	Atom	Angle/˚
N1	C2	C3	120.41(13)	N5	C14	C15	120.35(12)
N1	C2	N3	119.30(13)	N5	C14	N6	120.23(12)
N3	C2	C3	120.27(12)	N6	C14	C15	119.41(12)
C4	C3	C2	120.70(12)	C16	C15	C14	120.87(12)
C3	C4	C8	119.77(12)	C15	C16	C17	119.64(12)
C5	C8	C4	128.40(13)	C18	C17	C16	127.90(13)
C1	C8	C4	115.17(12)	C22	C17	C16	115.43(12)
C1	C8	C5	116.44(12)	C22	C17	C18	116.68(12)
C8	C5	C9	121.65(12)	C17	C18	C23	121.16(13)
C6	C5	C8	117.54(12)	C19	C18	C17	117.69(13)
C6	C5	C9	120.81(13)	C19	C18	C23	121.15(13)
C5	C6	C7	122.18(13)	C18	C19	C20	122.28(13)
C6	C7	C10	122.36(13)	C19	C20	C21	121.56(13)
N2	C7	C6	120.13(12)	N4	C20	C19	120.01(13)

N2	C7	C10	117.51(13)	N4	C20	C21	118.40(13)
C8	C1	Mn1	179.09(10)	C17	C22	Mn2	177.82(10)
N2	C1	C8	125.40(12)	N4	C22	C17	124.98(12)
N2	C1	Mn1	54.65(7)	N4	C22	Mn2	54.11(7)
N2	C1	N1	108.96(12)	N4	C22	N5	109.27(11)
N1	C1	C8	125.64(12)	N5	C22	C17	125.75(12)
N1	C1	Mn1	54.33(7)	N5	C22	Mn2	55.20(6)
O3	C13	Mn1	179.11(15)	O4	C24	Mn2	175.39(14)
O1	C11	Mn1	177.30(15)	O5	C25	Mn2	177.32(13)
O2	C12	Mn1	177.34(14)	O6	C26	Mn2	178.41(14)
C13	Mn1	C1	91.79(6)	C24	Mn2	C22	137.41(5)
C13	Mn1	C11	90.14(7)	C24	Mn2	C26	88.53(7)
C13	Mn1	C12	89.48(7)	C24	Mn2	Cl2	91.21(5)
C13	Mn1	Cl1	178.35(5)	C24	Mn2	N4	169.30(6)
C13	Mn1	N2	93.23(6)	C24	Mn2	N5	105.17(5)
C13	Mn1	N1	90.54(6)	C25	Mn2	C22	91.90(5)
C11	Mn1	C1	136.19(6)	C25	Mn2	C24	87.39(6)
C11	Mn1	C12	88.60(7)	C25	Mn2	C26	89.83(6)
C11	Mn1	Cl1	89.56(5)	C25	Mn2	Cl2	177.96(5)
C11	Mn1	N2	104.32(6)	C25	Mn2	N4	93.78(5)
C11	Mn1	N1	168.36(6)	C25	Mn2	N5	90.86(5)
C12	Mn1	C1	135.16(6)	C26	Mn2	C22	134.06(6)
C12	Mn1	Cl1	92.13(5)	C26	Mn2	Cl2	91.61(4)
C12	Mn1	N2	166.78(6)	C26	Mn2	N4	102.10(6)
C12	Mn1	N1	103.02(6)	C26	Mn2	N5	166.30(6)
Cl1	Mn1	C1	87.31(3)	Cl2	Mn2	C22	88.12(3)
N2	Mn1	C1	31.88(4)	N4	Mn2	C22	31.98(4)
N2	Mn1	Cl1	85.28(3)	N4	Mn2	Cl2	87.31(3)
N1	Mn1	C1	32.17(4)	N4	Mn2	N5	64.21(4)
N1	Mn1	Cl1	89.43(3)	N5	Mn2	C22	32.25(4)
N1	Mn1	N2	64.05(4)	N5	Mn2	Cl2	88.07(3)
C7	N2	C1	118.20(12)	C20	N4	C22	118.32(12)

C7	N2	Mn1	148.25(10)	C20	N4	Mn2	147.77(10)
C1	N2	Mn1	93.47(8)	C22	N4	Mn2	93.91(8)
C2	N1	C1	118.19(12)	C14	N5	C22	117.88(11)
C2	N1	Mn1	148.15(10)	C14	N5	Mn2	149.42(10)
C1	N1	Mn1	93.50(8)	C22	N5	Mn2	92.55(8)

Table A1. 6 Hydrogen Bonds for [MnCl(CO)$_3$(DMNA)].

D	H	A	d(D-H)/Å	d(H-A)/Å	d(D-A)/Å	D-H-A/°
O7	H7B	O8	0.75(3)	2.08(3)	2.7854(19)	156(3)

Table A1. 7 Torsion Angles for [MnCl(CO)$_3$(DMNA)].

A	B	C	D	Angle/˚	A	B	C	D	Angle/˚
C2	C3	C4	C8	-1.1(2)	C14	C15	C16	C17	0.48(19)
C3	C2	N1	C1	-1.18(18)	C15	C14	N5	C22	1.92(17)
C3	C2	N1	Mn1	172.50(12)	C15	C14	N5	Mn2	-172.06(12)
C3	C4	C8	C5	177.93(13)	C15	C16	C17	C18	-178.24(13)
C3	C4	C8	C1	-1.93(18)	C15	C16	C17	C22	1.86(18)
C4	C8	C5	C6	178.96(13)	C16	C17	C18	C19	-179.03(13)
C4	C8	C5	C9	-1.8(2)	C16	C17	C18	C23	1.3(2)
C4	C8	C1	N2	-176.33(12)	C16	C17	C22	N4	177.34(12)
C4	C8	C1	N1	3.76(19)	C16	C17	C22	N5	-2.56(19)
C8	C5	C6	C7	-1.39(19)	C17	C18	C19	C20	0.5(2)
C8	C1	N2	C7	-3.53(19)	C17	C22	N4	C20	2.74(19)
C8	C1	N2	Mn1	178.88(12)	C17	C22	N4	Mn2	-177.56(11)
C8	C1	N1	C2	-2.22(19)	C17	C22	N5	C14	0.66(19)
C8	C1	N1	Mn1	-178.88(12)	C17	C22	N5	Mn2	177.59(12)
C5	C8	C1	N2	3.79(19)	C18	C17	C22	N4	-2.57(19)
C5	C8	C1	N1	-176.12(12)	C18	C17	C22	N5	177.53(12)
C5	C6	C7	C10	-178.75(13)	C18	C19	C20	C21	-178.43(13)
C5	C6	C7	N2	1.7(2)	C18	C19	C20	N4	-0.4(2)
C6	C7	N2	C1	0.64(18)	C19	C20	N4	C22	-1.17(19)
C6	C7	N2	Mn1	176.06(12)	C19	C20	N4	Mn2	179.39(12)

C10	C7	N2	C1	-178.88(12)	C21	C20	N4	C22	176.95(12)
C10	C7	N2	Mn1	-3.5(2)	C21	C20	N4	Mn2	-2.5(2)
C1	C8	C5	C6	-1.19(18)	C22	C17	C18	C19	0.87(18)
C1	C8	C5	C9	178.09(12)	C22	C17	C18	C23	-178.78(12)
C9	C5	C6	C7	179.33(13)	C23	C18	C19	C20	-179.86(13)
Mn1	C1	N2	C7	177.58(13)	Mn2	C22	N4	C20	-179.70(13)
Mn1	C1	N1	C2	176.66(13)	Mn2	C22	N5	C14	-176.94(13)
N2	C1	N1	C2	177.86(11)	N4	C22	N5	C14	-179.26(11)
N2	C1	N1	Mn1	1.20(11)	N4	C22	N5	Mn2	-2.32(10)
N1	C2	C3	C4	2.8(2)	N5	C14	C15	C16	-2.51(19)
N1	C1	N2	C7	176.39(11)	N5	C22	N4	C20	-177.35(11)
N1	C1	N2	Mn1	-1.20(10)	N5	C22	N4	Mn2	2.35(10)
N3	C2	C3	C4	-178.60(13)	N6	C14	C15	C16	178.41(12)
N3	C2	N1	C1	-179.79(12)	N6	C14	N5	C22	-179.01(11)
N3	C2	N1	Mn1	-6.1(3)	N6	C14	N5	Mn2	7.0(2)

Table A1. 8 Hydrogen Atom Coordinates (Å×10^4) and Isotropic Displacement Parameters (Å^2×10^3) for [MnCl(CO)$_3$(DMNA)].

Atom	*x*	*y*	*z*	U(eq)
H3	-1453	5913	3014	19
H4	-886	7738	3209	19
H6	2481	9055	4085	19
H10A	4176	6925	4171	29
H10B	3811	6928	4894	29
H10C	4017	8080	4538	29
H9A	-116	9462	3707	32
H9B	507	9647	3089	32
H9C	944	10103	3808	32
H3A	-963(16)	3954(17)	2942(10)	25(5)
H3B	30(16)	3527(18)	3145(10)	27(5)
H15	6543	8629	7075	17
H16	5667	6954	6897	18
H19	2163	6320	5981	21

H21A	1165	8880	5288	31
H21B	766	8428	5952	31
H21C	907	7587	5358	31
H23A	4288	5505	6998	36
H23B	4451	5291	6240	36
H23C	3382	5021	6489	36
H6A	6453(15)	10626(17)	7091(10)	22(5)
H6B	5562(15)	11309(18)	6859(10)	25(5)
H7A	4087(19)	6520(20)	2729(12)	42(7)
H7B	5040(20)	6790(20)	2680(13)	49(8)
H8A	6839	6157	2217	58
H8B	6957	7189	2506	58

A1.1.2 Crystal Data for [ReCl(CO)$_3$(DMNA)]

Table A1. 9 Crystal Data Table for [ReCl(CO)$_3$(DMNA)]

Parameter	[ReCl(CO)$_3$(DMNA)]
Empirical Formula	$C_{13}H_{12.18}ClN_3O_{3.59}Re$
Formula Weight	489.50
Temperature / K	110.05(10)
Crystal System	Monoclinic
Space Group	$C_{2/c}$
a / Å	12.6764(2)
b / Å	12.05740(10)
c / Å	20.0284(2)
α / °	90
β / °	95.0420(10)
γ / °	90
Volume / Å^3	3049.38(6)
Z	8
ρ_{calc} g/cm^3	2.132
µ / mm-1	8.162
F(000)	1855.0
Crystal Size / mm^3	0.153x0.101x0.017
Radiation	MoKα (λ=0.71073)
2θ range for collection / °	7.06-64.176
Index Ranges	-18≥h≥18, -17≥k≥17, -29≥l≥28
Reflections Collected	19729
Independent Reflections	4946 [R_{int}=0.0314, R_{sigma}= 0.0257]
Data/Restraints/Parameters	4946/0/226
Goodness-of-fit on F^2	1.102
Final R indexes [I ≥ 2σ (I)]	R_1=0.0254 wR_2=0.0511
Final R indexes [all data]	R_1=0.0291 wR_2=0.0525
Largest diff. peak/hole /e Å^{-3}	1.52/-2.00

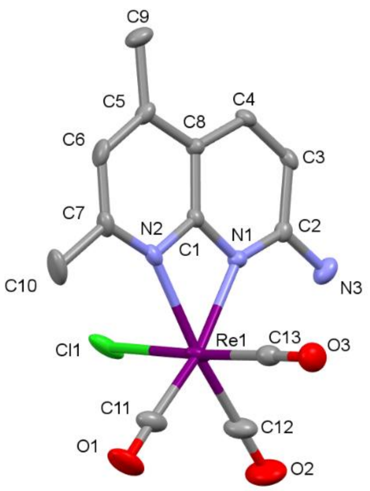

Figure A1. 2 X-Ray crystal structure of [ReCl(CO)$_3$(DMNA)] with probability ellipsoids shown at the 50% level and hydrogens omitted for clarity

Table A1. 10 Fractional Atomic Coordinates ($\times 10^4$) and Equivalent Isotropic Displacement Parameters (Å$^2\times 10^3$) for [ReCl(CO)$_3$(DMNA)]. Ueq is defined as 1/3 of of the trace of the orthogonalised UIJ tensor.

Atom	***x***	***y***	***z***	**U(eq)**
Re1	2920.8(2)	5407.5(2)	5984.0(2)	18.57(4)
Cl1	2166.8(7)	5136.7(8)	7081.1(4)	35.1(2)
N1	4310.4(19)	4477.7(18)	6433.4(11)	15.3(4)
O3	3942(2)	5671(2)	4670.4(12)	34.0(6)
N2	2887.2(19)	3568(2)	5989.3(11)	17.9(5)
O1	836(2)	6132(3)	5222.1(13)	40.3(7)
C12	3177(3)	6937(3)	6146.5(18)	32.4(8)
C13	3558(3)	5559(2)	5165.4(15)	22.4(6)
C11	1607(3)	5856(3)	5520.1(16)	28.5(7)
O2	3329(3)	7856(2)	6251.9(18)	55.0(9)
C1	3884(2)	3461(2)	6294.6(13)	14.2(5)
N3	5737(3)	5530(2)	6857.3(14)	25.2(6)
C2	5293(2)	4539(2)	6715.5(13)	15.4(5)
C3	5893(2)	3548(2)	6864.5(13)	17.0(5)
C7	2315(2)	2663(3)	5858.3(14)	20.2(6)
C8	4389(2)	2452(2)	6444.0(13)	14.0(5)
C6	2759(2)	1622(3)	6010.6(14)	21.9(6)
C4	5454(2)	2538(2)	6737.4(13)	16.1(5)

C5	3787(2)	1486(2)	6292.6(14)	18.7(5)
C10	1199(3)	2813(4)	5568.9(17)	33.7(8)
C9	4234(3)	352(2)	6432.2(17)	27.1(7)
O4	5338(8)	7770(5)	7301(6)	76(5)
O5	6439(19)	7860(20)	7325(9)	36(7)

Table A1. 11 Anisotropic Displacement Parameters ($Å^2×10^3$) for [ReCl(CO)$_3$(DMNA)]. The Anisotropic displacement factor exponent takes the form: -2π2[h2a*2U11+2hka*b*U12+…].

Atom	**U_{11}**	**U_{22}**	**U_{33}**	**U_{23}**	**U_{13}**	**U_{12}**
Re1	22.86(7)	19.18(6)	13.52(5)	1.29(4)	0.67(4)	10.88(4)
Cl1	33.3(4)	56.9(5)	15.6(3)	6.7(3)	5.0(3)	31.4(4)
N1	16.8(11)	13.6(10)	15.6(10)	0.6(8)	1.8(8)	1.1(8)
O3	38.7(15)	39.6(14)	24.9(12)	4.5(10)	9.4(10)	3.5(11)
N2	11.9(11)	25.7(12)	16.5(10)	1.5(9)	3.1(8)	2.8(9)
O1	34.4(15)	57.6(18)	27.6(12)	7.1(12)	-4.3(11)	24.9(13)
C12	41(2)	23.5(15)	32.5(17)	-4.2(13)	-1.0(15)	11.6(14)
C13	26.1(16)	21.0(14)	20.0(13)	0.5(10)	1.0(11)	4.2(11)
C11	35.5(19)	30.8(16)	19.3(14)	4.3(12)	4.1(13)	15.4(14)
O2	67(2)	24.1(13)	73(2)	-9.1(14)	1.6(18)	7.1(14)
C1	12.6(12)	17.1(12)	13.2(11)	-0.5(9)	2.7(9)	0.8(9)
N3	33.6(16)	20.3(13)	21.8(12)	-1.9(10)	2.4(12)	-9.0(12)
C2	17.6(13)	17.4(12)	11.7(11)	-1.4(9)	3.5(9)	-2.1(10)
C3	11.2(12)	23.6(13)	16.2(12)	-2.7(10)	1.1(9)	1.9(10)
C7	13.1(13)	30.4(15)	17.0(12)	2.4(11)	0.5(10)	-3.2(11)
C8	14.8(12)	13.4(11)	13.9(11)	0.7(9)	0.7(9)	0.7(9)
C6	20.8(15)	24.6(14)	20.2(13)	-0.9(11)	1.4(11)	-12.6(11)
C4	14.8(13)	18.2(12)	15.3(11)	0.2(9)	1.4(10)	5.7(10)
C5	24.4(15)	15.7(12)	16.0(12)	0.1(9)	2.4(10)	-4.9(10)
C10	13.1(14)	60(2)	27.7(16)	6.6(15)	-2.2(12)	-7.3(15)
C9	38.8(19)	13.6(13)	28.9(15)	3.1(11)	3.7(14)	0.5(12)
O4	90(10)	24(3)	103(10)	-8(4)	-57(7)	1(3)
O5	42(14)	49(14)	19(9)	-4(8)	9(8)	-15(10)

Table A1. 12 Bond Lengths for [ReCl(CO)$_3$(DMNA)].

Atom	Atom	Length/Å	Atom	Atom	Length/Å
Re1	Cl1	2.4935(8)	C12	O2	1.141(4)
Re1	N1	2.212(2)	C1	C8	1.395(4)
Re1	N2	2.218(3)	N3	C2	1.340(4)
Re1	C12	1.896(4)	C2	C3	1.433(4)
Re1	C13	1.899(3)	C3	C4	1.353(4)
Re1	C11	1.912(3)	C7	C6	1.398(4)
N1	C1	1.358(3)	C7	C10	1.492(4)
N1	C2	1.324(4)	C8	C4	1.428(4)
O3	C13	1.150(4)	C8	C5	1.411(4)
N2	C1	1.360(4)	C6	C5	1.384(4)
N2	C7	1.324(4)	C5	C9	1.497(4)
O1	C11	1.149(4)	O4	O4[1]	1.22(2)

[1]1-X,+Y,3/2-Z

Table A1. 13 Bond Angles for [ReCl(CO)$_3$(DMNA)].

Atom	Atom	Atom	Angle/°	Atom	Atom	Atom	Angle/°
N1	Re1	Cl1	85.89(6)	O2	C12	Re1	179.2(4)
N1	Re1	N2	60.41(9)	O3	C13	Re1	178.8(3)
N2	Re1	Cl1	81.71(6)	O1	C11	Re1	177.6(3)
C12	Re1	Cl1	92.82(12)	N1	C1	N2	110.1(2)
C12	Re1	N1	107.77(13)	N1	C1	C8	125.1(3)
C12	Re1	N2	167.14(13)	N2	C1	C8	124.7(3)
C12	Re1	C13	88.58(15)	N1	C2	N3	120.1(3)
C12	Re1	C11	86.37(16)	N1	C2	C3	120.3(2)
C13	Re1	Cl1	176.77(10)	N3	C2	C3	119.6(3)
C13	Re1	N1	90.91(11)	C4	C3	C2	120.6(3)
C13	Re1	N2	96.32(11)	N2	C7	C6	119.6(3)
C13	Re1	C11	88.39(14)	N2	C7	C10	117.5(3)
C11	Re1	Cl1	94.61(10)	C6	C7	C10	122.9(3)
C11	Re1	N1	165.82(13)	C1	C8	C4	115.1(2)

C11	Re1	N2	105.59(13)	C1	C8	C5	116.4(3)
C1	N1	Re1	94.89(17)	C5	C8	C4	128.5(3)
C2	N1	Re1	146.24(19)	C5	C6	C7	122.7(3)
C2	N1	C1	118.7(2)	C3	C4	C8	120.1(2)
C1	N2	Re1	94.55(17)	C8	C5	C9	121.7(3)
C7	N2	Re1	146.5(2)	C6	C5	C8	117.6(3)
C7	N2	C1	118.8(3)	C6	C5	C9	120.7(3)

Table A1. 14 Hydrogen Bonds for [ReCl(CO)$_3$(DMNA)].

D	**H**	**A**	**d(D-H)/Å**	**d(H-A)/Å**	**d(D-A)/Å**	**D-H-A/°**
N3	H3A	O4	0.76(4)	2.31(4)	2.902(8)	136(4)

Table A1. 15 Torsion Angles for [ReCl(CO)$_3$(DMNA)].

A	**B**	**C**	**D**	**Angle/˚**	**A**	**B**	**C**	**D**	**Angle/˚**
Re1	N1	C1	N2	-1.4(2)	C1	N2	C7	C10	175.6(3)
Re1	N1	C1	C8	178.7(2)	C1	C8	C4	C3	1.4(4)
Re1	N1	C2	N3	5.8(5)	C1	C8	C5	C6	0.1(4)
Re1	N1	C2	C3	-173.6(2)	C1	C8	C5	C9	-179.6(3)
Re1	N2	C1	N1	1.4(2)	N3	C2	C3	C4	178.7(3)
Re1	N2	C1	C8	-178.7(2)	C2	N1	C1	N2	-178.1(2)
Re1	N2	C7	C6	-176.5(2)	C2	N1	C1	C8	2.0(4)
Re1	N2	C7	C10	1.6(5)	C2	C3	C4	C8	0.8(4)
N1	C1	C8	C4	-3.0(4)	C7	N2	C1	N1	-175.3(2)
N1	C1	C8	C5	176.5(2)	C7	N2	C1	C8	4.6(4)
N1	C2	C3	C4	-1.9(4)	C7	C6	C5	C8	1.7(4)
N2	C1	C8	C4	177.2(2)	C7	C6	C5	C9	-178.6(3)
N2	C1	C8	C5	-3.3(4)	C4	C8	C5	C6	179.6(3)
N2	C7	C6	C5	-0.5(4)	C4	C8	C5	C9	-0.2(4)
C1	N1	C2	N3	179.9(2)	C5	C8	C4	C3	-178.0(3)
C1	N1	C2	C3	0.5(4)	C10	C7	C6	C5	-178.5(3)
C1	N2	C7	C6	-2.5(4)					

Table A1. 16 Hydrogen Atom Coordinates (Å×10^4) and Isotropic Displacement Parameters (Å^2×10^3) for [ReCl(CO)$_3$(DMNA)]

Atom	***x***	***y***	***z***	**U(eq)**
H3	6605	3600	7054	20
H6	2336	980	5917	26
H4	5854	1886	6843	19
H10A	765	3072	5919	51
H10B	921	2103	5391	51
H10C	1177	3361	5207	51
H9A	4664	134	6071	41
H9B	3653	-179	6458	41
H9C	4676	359	6859	41
H4A	4787	8174	7257	114
H4B	5850	8225	7307	114
H5A	6907	7727	7644	55
H5B	5897	8069	7513	55
H3A	5390(30)	6040(40)	6810(20)	26(11)
H3B	6330(50)	5530(40)	7110(30)	58(16)

A1.1.3 Crystal Structure of [Ru(bpy)$_2$(DMNA)](PF$_6$)$_2$

Table A1. 17 Crystal Collection Data for [Ru(bpy)$_2$(DMNA)](PF$_6$)$_2$

Parameter	[Ru(bpy)$_2$(DMNA)](PF$_6$)$_2$
Empirical Formula	$C_{39}H_{45}F_{12}N_7O_3P_2Ru$
Formula Weight	1050.83
Temperature / K	110.05(10)
Crystal System	Triclinic
Space Group	P-1
a / Å	9.2125(3)
b / Å	15.0204(10)
c / Å	17.4143(2)
α / °	112.178(4)
β / °	91.895(3)
γ / °	90.945
Volume / Å^3	2229.13(17)
Z	2
ρ_{calc} g/cm^3	1.566
μ / mm^{-1}	4.387
F(000)	1068.0
Crystal Size / mm^3	0.1269x0.0926x0.0755
Radiation	CuKα (λ = 1.54184)
2θ range for collection / °	9.61 to 142.232
Index Ranges	-11≥h≥11, -18≥k≥16, -21≥l≥17
Reflections Collected	15462
Independent Reflections	8437 [R_{int}=0.0457, R_{sigma}= 0.0697]
Data/Restraints/Parameters	8437/0/622
Goodness-of-fit on F^2	1.007
Final R indexes [I ≥ 2σ (I)]	R_1=0.0415 wR_2=0.0998
Final R indexes [all data]	R_1=0.0543 wR_2=0.1042
Largest diff. peak/hole /e Å^{-3}	0.85/-0.65

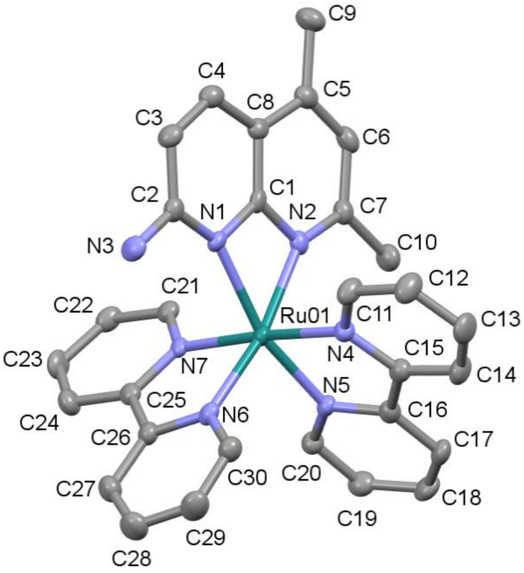

Figure A1. 3 X-Ray crystal structure of [Ru(bpy)$_2$(DMNA)](PF$_6$)$_2$ with probability ellipsoids shown at the 50% level and hydrogens omitted for clarity

Table A1. 18 Fractional Atomic Coordinates (×10^4) and Equivalent Isotropic Displacement Parameters (Å^2×10^3) for [Ru(bpy)$_2$(DMNA)](PF$_6$)$_2$. Ueq is defined as 1/3 of of the trace of the orthogonalised UIJ tensor.

Atom	*x*	*y*	*z*	U(eq)
Ru01	5049.2(3)	7385.1(2)	2499.0(2)	16.58(8)
P2	265.0(9)	2736.6(6)	174.2(6)	27.05(19)
P1	9228.9(10)	7727.3(6)	5190.5(6)	31.3(2)
F1	9684(3)	8805.5(16)	5303.9(17)	43.5(6)
F3	8849(3)	8098.7(19)	6148.2(16)	47.8(6)
F2	7595(3)	7928.6(18)	4976.4(18)	44.9(6)
N1	4177(3)	6335.0(17)	1360.7(16)	17.4(5)
N7	6872(3)	6586.1(17)	2381.6(16)	17.2(5)
N6	4763(3)	6820.7(18)	3384.5(17)	20.1(5)
N2	5290(3)	7682.1(18)	1418.1(17)	19.6(5)
N5	5848(3)	8632.4(17)	3386.0(16)	18.9(5)
N4	3247(3)	8208.6(18)	2705.9(17)	20.1(5)
F6	9597(4)	7377(2)	4242.2(18)	60.9(8)
F5	8757(4)	6657.1(18)	5066(2)	63.1(8)
N3	3024(3)	4986.9(19)	1408.1(18)	26.2(6)
F4	10847(3)	7559(3)	5438(2)	70.4(9)

C21	7942(3)	6518(2)	1850.1(19)	20.6(6)
O3	-4088(4)	-648(3)	-1223(2)	54.5(8)
F12A	1646(12)	3026(5)	780(8)	49(3)
O1	12915(4)	6388(2)	6484(2)	48.4(7)
C1	4571(3)	6859(2)	904(2)	18.2(6)
F9B	469(4)	1660(2)	28(3)	84.4(13)
C16	4936(4)	9377(2)	3620(2)	22.0(6)
C3	3081(4)	5188(2)	102(2)	23.8(6)
C26	5807(3)	6213(2)	3453(2)	21.3(6)
O2	2436(4)	4901(3)	2937(2)	61.0(10)
F7B	99(4)	3848(2)	345(3)	90.2(14)
C30	3693(4)	7031(2)	3927(2)	25.7(7)
C25	6958(3)	6051(2)	2860(2)	20.8(6)
C2	3434(3)	5508(2)	969(2)	20.8(6)
C19	7747(4)	9685(2)	4236(2)	27.5(7)
C22	9098(3)	5910(2)	1764(2)	24.3(7)
C15	3454(4)	9140(2)	3252(2)	23.0(6)
C11	1915(4)	7933(2)	2336(2)	26.6(7)
C8	4276(3)	6603(2)	59(2)	20.2(6)
C20	7232(4)	8791(2)	3706(2)	22.2(6)
C24	8077(4)	5420(2)	2785(2)	28.3(7)
C14	2347(4)	9784(2)	3424(2)	28.2(7)
C6	5469(4)	8095(2)	233(2)	24.8(7)
C23	9150(4)	5345(2)	2229(2)	28.8(7)
C18	6828(4)	10450(2)	4458(2)	28.6(7)
C12	782(4)	8546(3)	2472(3)	33.0(8)
C4	3479(3)	5717(2)	-342(2)	23.8(6)
C17	5399(4)	10290(2)	4155(2)	26.2(7)
C7	5741(3)	8292(2)	1079(2)	21.8(6)
C10	6551(4)	9195(2)	1638(2)	29.4(7)
C5	4754(4)	7266(2)	-291(2)	24.5(7)
C13	994(4)	9488(3)	3028(2)	32.3(8)

C29	3651(4)	6691(3)	4558(2)	33.7(8)
C27	5783(4)	5834(2)	4062(2)	29.3(7)
F8B	1660(20)	2857(15)	-314(17)	97(7)
C9	4493(4)	7059(3)	-1197(2)	31.8(8)
F10A	-720(15)	2879(11)	893(6)	96(5)
C28	4703(5)	6087(3)	4630(2)	35.1(8)
C32	12717(5)	7227(3)	6897(3)	41.4(9)
C34	1109(5)	4793(3)	4028(3)	47.7(10)
C38	-2875(5)	-342(3)	-947(3)	42.9(10)
C35	2177(5)	4453(4)	3363(3)	44.1(10)
C31	13712(7)	8001(3)	6881(3)	56.2(13)
C37	-2599(5)	289(3)	-53(3)	46.0(10)
C33	11447(7)	7512(5)	7442(3)	65.3(16)
C36	2914(7)	3531(5)	3234(4)	70.7(17)
C39	-1562(7)	-595(5)	-1470(4)	71.2(17)
F11A	-810(30)	2561(16)	-561(12)	113(7)
F8A	1232(12)	2520(13)	-592(7)	85(4)
F12B	1400(20)	2992(13)	938(13)	106(7)
F11B	-1159(10)	2431(9)	-432(9)	43(3)
F10B	-1070(20)	2790(12)	736(14)	102(6)

*Table A1. 19 Anisotropic Displacement Parameters (Å^2×10^3) for [Ru(bpy)$_2$(DMNA)](PF$_6$)$_2$. The Anisotropic displacement factor exponent takes the form: -2π2[h2a*2U11+2hka*b*U12+…].*

Atom	U_{11}	U_{22}	U_{33}	U_{23}	U_{13}	U_{12}
Ru01	17.00(12)	12.63(11)	18.03(12)	3.43(8)	0.33(8)	1.36(7)
P2	23.1(4)	28.4(4)	29.9(5)	11.1(4)	4.4(3)	0.8(3)
P1	32.1(5)	22.3(4)	34.4(5)	5.1(4)	-3.5(4)	7.7(3)
F1	35.5(12)	30.5(11)	57.0(16)	8.1(10)	4.5(11)	-4.9(9)
F3	58.9(16)	46.6(14)	38.2(14)	15.6(11)	3.5(11)	17.0(12)
F2	33.9(12)	42.2(13)	64.9(17)	28.9(12)	-14.1(11)	-4.8(10)
N1	17.5(12)	14.0(11)	16.6(12)	1.0(9)	0.6(9)	2.3(9)
N7	19.7(12)	11.2(11)	17.4(12)	2.2(9)	-3.5(10)	-0.2(9)

N6	23.2(13)	13.7(11)	20.2(13)	2.6(10)	2.2(10)	-1.4(9)
N2	18.1(12)	17.2(12)	24.7(14)	9.2(10)	1.4(10)	3.2(9)
N5	23.1(13)	13.0(11)	18.4(13)	3.4(10)	0.5(10)	0.1(9)
N4	21.0(13)	17.4(12)	20.5(13)	5.9(10)	-2.1(10)	0.0(10)
F6	87(2)	48.7(15)	38.6(15)	4.7(12)	16.5(14)	19.6(15)
F5	97(2)	25.6(12)	68(2)	19.3(12)	-6.2(17)	5.1(13)
N3	32.1(15)	18.6(12)	25.7(15)	6.3(11)	0.3(12)	-8.2(11)
F4	46.4(16)	78(2)	77(2)	17.7(17)	-1.7(15)	35.8(15)
C21	21.9(15)	16.6(13)	19.4(15)	2.8(11)	-1.9(12)	-1.8(11)
O3	45.9(19)	54.5(19)	65(2)	26.6(17)	-9.8(16)	-6.4(15)
F12A	35(3)	25(3)	74(6)	5(3)	-20(3)	-8(2)
O1	60(2)	33.4(15)	56(2)	19.8(14)	7.5(15)	8.6(13)
C1	15.2(13)	13.4(13)	24.0(16)	4.3(11)	2.2(11)	4.5(10)
F9B	70(2)	34.5(15)	147(4)	35.1(19)	-35(2)	-7.6(14)
C16	24.3(16)	20.9(15)	21.8(15)	8.8(12)	3.8(12)	3.4(12)
C3	21.6(15)	22.9(15)	22.4(16)	3.7(13)	-1.1(12)	-2.4(12)
C26	23.7(15)	16.1(13)	21.9(16)	4.8(12)	-0.2(12)	1.2(11)
O2	65(2)	87(3)	40.9(18)	36.6(18)	-5.2(16)	-20.1(19)
F7B	53.8(19)	41.9(16)	175(4)	41(2)	-2(2)	7.3(14)
C30	26.2(16)	23.5(15)	25.8(17)	7.1(13)	4.0(13)	3.7(12)
C25	23.5(15)	16.0(13)	20.9(15)	5.0(12)	-2.9(12)	-2.0(11)
C2	18.5(14)	18.8(14)	24.3(16)	6.7(12)	3.7(12)	4.1(11)
C19	27.1(17)	25.8(16)	27.1(17)	7.8(14)	-2.7(13)	-5.2(13)
C22	16.4(14)	25.5(15)	25.4(17)	2.9(13)	2.9(12)	0.9(12)
C15	26.5(16)	18.6(14)	23.2(16)	7.4(12)	1.0(12)	-0.8(12)
C11	18.6(15)	24.8(16)	28.8(18)	1.5(13)	0.3(13)	2.6(12)
C8	18.0(14)	21.4(14)	19.8(15)	6.1(12)	-0.2(11)	4.9(11)
C20	22.1(15)	19.8(15)	22.7(16)	6.0(12)	-2.4(12)	0.3(12)
C24	30.3(17)	26.6(16)	30.3(18)	13.3(14)	-1.8(14)	7.7(13)
C14	27.2(17)	20.8(15)	31.2(18)	3.2(13)	4.9(14)	7.8(13)
C6	22.5(15)	27.2(16)	31.5(18)	18.5(14)	2.1(13)	3.3(12)
C23	21.7(16)	27.2(16)	35.3(19)	8.8(14)	1.3(14)	12.8(13)

C18	34.8(18)	19.0(15)	24.7(17)	0.5(13)	-0.7(14)	-5.2(13)
C12	21.4(16)	30.6(18)	38(2)	2.8(15)	0.4(14)	3.7(13)
C4	20.1(15)	27.8(16)	21.5(16)	6.9(13)	0.4(12)	3.0(12)
C17	35.1(18)	14.5(14)	26.0(17)	3.9(12)	3.3(14)	2.8(12)
C7	20.5(15)	19.1(14)	27.0(17)	9.9(13)	1.7(12)	3.1(12)
C10	36.1(19)	22.3(16)	31.8(18)	12.7(14)	-0.7(15)	-2.7(14)
C5	23.3(16)	28.2(16)	23.7(17)	11.4(13)	2.3(12)	7.3(13)
C13	27.3(17)	27.8(17)	37(2)	6.4(15)	8.4(15)	14.5(14)
C29	39(2)	32.3(18)	31.6(19)	12.3(15)	15.2(16)	2.8(15)
C27	36.7(19)	23.9(16)	29.9(18)	13.1(14)	0.1(15)	3.1(14)
F8B	63(9)	123(11)	172(16)	125(11)	81(9)	63(8)
C9	36.0(19)	37.2(19)	26.2(18)	16.9(15)	-1.7(14)	-0.7(15)
F10A	44(6)	196(12)	29(5)	20(5)	26(3)	4(5)
C28	45(2)	33.5(19)	32(2)	18.9(16)	7.2(16)	1.0(16)
C32	59(3)	38(2)	29(2)	15.5(17)	-1.8(18)	14.6(19)
C34	47(2)	49(2)	55(3)	29(2)	7(2)	2(2)
C38	39(2)	45(2)	58(3)	35(2)	-1.4(19)	-1.8(18)
C35	37(2)	61(3)	38(2)	25(2)	-4.9(17)	-7.6(19)
C31	86(4)	36(2)	45(3)	16(2)	-16(2)	-1(2)
C37	40(2)	40(2)	62(3)	24(2)	0(2)	-5.4(18)
C33	70(4)	83(4)	45(3)	25(3)	7(2)	40(3)
C36	55(3)	82(4)	85(4)	40(4)	30(3)	16(3)
C39	56(3)	111(5)	60(3)	46(4)	10(3)	6(3)
F11A	126(14)	142(13)	44(6)	5(7)	-29(9)	54(10)
F8A	34(4)	192(13)	52(5)	69(6)	20(3)	22(5)
F12B	91(12)	161(15)	82(8)	71(9)	-56(8)	-37(8)
F11B	18(3)	54(5)	44(6)	4(3)	-7(3)	12(2)
F10B	37(6)	133(10)	190(17)	118(11)	48(7)	19(5)

Table A1. 20 Bond Lengths for [Ru(bpy)$_2$(DMNA)](PF$_6$)$_2$.

Atom	Atom	Length/Å	Atom	Atom	Length/Å

Ru01	N1	2.134(3)	O3	C38	1.213(6)
Ru01	N7	2.051(3)	O1	C32	1.213(5)
Ru01	N6	2.043(3)	C1	C8	1.389(5)
Ru01	N2	2.109(3)	C16	C15	1.468(5)
Ru01	N5	2.033(2)	C16	C17	1.386(5)
Ru01	N4	2.046(3)	C3	C2	1.426(5)
P2	F12A	1.571(10)	C3	C4	1.355(5)
P2	F9B	1.554(3)	C26	C25	1.464(5)
P2	F7B	1.593(3)	C26	C27	1.380(5)
P2	F8B	1.606(12)	O2	C35	1.202(6)
P2	F10A	1.521(8)	C30	C29	1.376(5)
P2	F11A	1.530(17)	C25	C24	1.389(5)
P2	F8A	1.561(11)	C19	C20	1.377(5)
P2	F12B	1.590(16)	C19	C18	1.380(5)
P2	F11B	1.603(12)	C22	C23	1.377(5)
P2	F10B	1.579(13)	C15	C14	1.379(5)
P1	F1	1.603(2)	C11	C12	1.370(5)
P1	F3	1.599(3)	C8	C4	1.425(5)
P1	F2	1.600(2)	C8	C5	1.421(5)
P1	F6	1.583(3)	C24	C23	1.383(5)
P1	F5	1.590(3)	C14	C13	1.385(5)
P1	F4	1.589(3)	C6	C7	1.401(5)
N1	C1	1.367(4)	C6	C5	1.376(5)
N1	C2	1.334(4)	C18	C17	1.385(5)
N7	C21	1.353(4)	C12	C13	1.386(5)
N7	C25	1.359(4)	C7	C10	1.505(5)
N6	C26	1.370(4)	C5	C9	1.498(5)
N6	C30	1.345(4)	C29	C28	1.373(6)
N2	C1	1.366(4)	C27	C28	1.382(5)
N2	C7	1.332(4)	C32	C31	1.478(7)
N5	C16	1.354(4)	C32	C33	1.496(7)
N5	C20	1.355(4)	C34	C35	1.488(6)

N4	C15	1.368(4)	C38	C37	1.497(7)
N4	C11	1.350(4)	C38	C39	1.505(7)
N3	C2	1.341(4)	C35	C36	1.496(7)
C21	C22	1.389(5)			

Table A1. 21 Bond Angles for [Ru(bpy)$_2$(DMNA)](PF$_6$)$_2$.

Atom	Atom	Atom	Angle/˚	Atom	Atom	Atom	Angle/˚
N7	Ru01	N1	89.19(10)	C30	N6	Ru01	126.0(2)
N7	Ru01	N2	96.61(10)	C30	N6	C26	117.8(3)
N6	Ru01	N1	106.22(10)	C1	N2	Ru01	94.68(19)
N6	Ru01	N7	78.67(11)	C7	N2	Ru01	148.2(2)
N6	Ru01	N2	168.61(10)	C7	N2	C1	117.0(3)
N6	Ru01	N4	98.11(11)	C16	N5	Ru01	116.1(2)
N2	Ru01	N1	63.07(10)	C16	N5	C20	118.4(3)
N5	Ru01	N1	163.20(10)	C20	N5	Ru01	125.3(2)
N5	Ru01	N7	98.32(10)	C15	N4	Ru01	115.5(2)
N5	Ru01	N6	90.03(10)	C11	N4	Ru01	126.5(2)
N5	Ru01	N2	100.96(10)	C11	N4	C15	117.9(3)
N5	Ru01	N4	79.06(11)	N7	C21	C22	122.5(3)
N4	Ru01	N1	94.16(10)	N1	C1	C8	125.7(3)
N4	Ru01	N7	175.91(11)	N2	C1	N1	108.6(3)
N4	Ru01	N2	87.01(10)	N2	C1	C8	125.7(3)
F12A	P2	F7B	87.9(3)	N5	C16	C15	114.8(3)
F9B	P2	F12A	90.2(3)	N5	C16	C17	121.6(3)
F9B	P2	F7B	178.1(2)	C17	C16	C15	123.6(3)
F9B	P2	F8B	96.6(6)	C4	C3	C2	121.1(3)
F9B	P2	F8A	84.6(7)	N6	C26	C25	114.2(3)
F9B	P2	F12B	87.3(7)	N6	C26	C27	121.6(3)
F9B	P2	F11B	89.1(5)	C27	C26	C25	124.1(3)
F9B	P2	F10B	91.3(5)	N6	C30	C29	122.5(3)
F7B	P2	F8B	82.9(6)	N7	C25	C26	114.7(3)
F7B	P2	F11B	92.7(5)	N7	C25	C24	121.3(3)

F10A	P2	F12A	91.2(7)	C24	C25	C26	124.0(3)
F10A	P2	F9B	92.2(6)	N1	C2	N3	118.7(3)
F10A	P2	F7B	87.8(6)	N1	C2	C3	120.4(3)
F10A	P2	F11A	103.2(13)	N3	C2	C3	120.9(3)
F10A	P2	F8A	176.1(8)	C20	C19	C18	119.4(3)
F11A	P2	F12A	163.9(15)	C23	C22	C21	118.8(3)
F11A	P2	F9B	96.4(8)	N4	C15	C16	114.2(3)
F11A	P2	F7B	85.4(8)	N4	C15	C14	121.6(3)
F11A	P2	F8A	75.1(12)	C14	C15	C16	124.2(3)
F8A	P2	F12A	91.0(6)	N4	C11	C12	123.0(3)
F8A	P2	F7B	95.6(7)	C1	C8	C4	115.3(3)
F12B	P2	F7B	90.8(7)	C1	C8	C5	116.5(3)
F12B	P2	F8B	83.7(10)	C5	C8	C4	128.1(3)
F12B	P2	F11B	165.2(11)	N5	C20	C19	122.2(3)
F11B	P2	F8B	111.0(13)	C23	C24	C25	119.7(3)
F10B	P2	F7B	89.1(6)	C15	C14	C13	119.4(3)
F10B	P2	F8B	171.1(9)	C5	C6	C7	122.5(3)
F10B	P2	F12B	92.5(10)	C22	C23	C24	119.2(3)
F10B	P2	F11B	73.1(11)	C19	C18	C17	118.8(3)
F3	P1	F1	89.79(14)	C11	C12	C13	118.9(3)
F3	P1	F2	88.74(15)	C3	C4	C8	119.8(3)
F2	P1	F1	89.03(13)	C18	C17	C16	119.5(3)
F6	P1	F1	89.38(16)	N2	C7	C6	120.9(3)
F6	P1	F3	179.02(16)	N2	C7	C10	117.4(3)
F6	P1	F2	90.74(17)	C6	C7	C10	121.7(3)
F6	P1	F5	90.11(17)	C8	C5	C9	120.9(3)
F6	P1	F4	91.25(19)	C6	C5	C8	117.3(3)
F5	P1	F1	179.03(17)	C6	C5	C9	121.8(3)
F5	P1	F3	90.72(17)	C14	C13	C12	119.1(3)
F5	P1	F2	90.15(16)	C28	C29	C30	119.7(3)
F4	P1	F1	89.93(18)	C26	C27	C28	119.6(3)
F4	P1	F3	89.26(17)	C29	C28	C27	118.7(3)

F4	P1	F2	177.75(18)	O1	C32	C31	121.6(5)
F4	P1	F5	90.90(19)	O1	C32	C33	120.7(5)
C1	N1	Ru01	93.57(18)	C31	C32	C33	117.7(5)
C2	N1	Ru01	148.5(2)	O3	C38	C37	121.4(4)
C2	N1	C1	117.8(3)	O3	C38	C39	122.4(5)
C21	N7	Ru01	125.7(2)	C37	C38	C39	116.2(4)
C21	N7	C25	118.3(3)	O2	C35	C34	121.2(5)
C25	N7	Ru01	115.9(2)	O2	C35	C36	120.7(5)
C26	N6	Ru01	116.2(2)	C34	C35	C36	118.2(4)

Table A1. 22 Hydrogen Bonds for [Ru(bpy)$_2$(DMNA)](PF$_6$)$_2$.

D	H	A	d(D-H)/Å	d(H-A)/Å	d(D-A)/Å	D-H-A/°
N3	H3A	O2	0.86	2.11	2.784(4)	135.0

Table A1. 23 Torsion Angles for [Ru(bpy)$_2$(DMNA)](PF$_6$)$_2$.

A	B	C	D	Angle/˚	A	B	C	D	Angle/˚
Ru01	N1	C1	N2	1.8(2)	C1	C8	C5	C6	0.4(4)
Ru01	N1	C1	C8	-177.5(3)	C1	C8	C5	C9	179.9(3)
Ru01	N1	C2	N3	-5.1(6)	C16	N5	C20	C19	-2.2(5)
Ru01	N1	C2	C3	174.6(3)	C16	C15	C14	C13	178.7(3)
Ru01	N7	C21	C22	-175.4(2)	C26	N6	C30	C29	2.7(5)
Ru01	N7	C25	C26	-6.5(3)	C26	C25	C24	C23	-177.3(3)
Ru01	N7	C25	C24	174.6(2)	C26	C27	C28	C29	2.0(6)
Ru01	N6	C26	C25	-1.2(3)	C30	N6	C26	C25	-177.9(3)
Ru01	N6	C26	C27	175.9(3)	C30	N6	C26	C27	-0.7(5)
Ru01	N6	C30	C29	-173.6(3)	C30	C29	C28	C27	-0.1(6)
Ru01	N2	C1	N1	-1.8(2)	C25	N7	C21	C22	1.5(4)
Ru01	N2	C1	C8	177.5(3)	C25	C26	C27	C28	175.3(3)
Ru01	N2	C7	C6	-174.1(3)	C25	C24	C23	C22	0.7(5)
Ru01	N2	C7	C10	6.1(6)	C2	N1	C1	N2	178.8(3)
Ru01	N5	C16	C15	5.6(4)	C2	N1	C1	C8	-0.5(4)
Ru01	N5	C16	C17	-173.2(2)	C2	C3	C4	C8	0.6(5)

Ru01	N5	C20	C19	172.4(3)	C19	C18	C17	C16	-1.7(5)
Ru01	N4	C15	C16	-2.1(4)	C15	N4	C11	C12	1.3(5)
Ru01	N4	C15	C14	177.4(3)	C15	C16	C17	C18	-178.7(3)
Ru01	N4	C11	C12	-176.0(3)	C15	C14	C13	C12	0.5(6)
N1	C1	C8	C4	0.7(4)	C11	N4	C15	C16	-179.6(3)
N1	C1	C8	C5	178.4(3)	C11	N4	C15	C14	-0.1(5)
N7	C21	C22	C23	0.8(5)	C11	C12	C13	C14	0.6(6)
N7	C25	C24	C23	1.6(5)	C20	N5	C16	C15	-179.3(3)
N6	C26	C25	N7	5.0(4)	C20	N5	C16	C17	1.9(5)
N6	C26	C25	C24	-176.1(3)	C20	C19	C18	C17	1.4(5)
N6	C26	C27	C28	-1.6(5)	C18	C19	C20	N5	0.5(5)
N6	C30	C29	C28	-2.3(6)	C4	C3	C2	N1	-0.4(5)
N2	C1	C8	C4	-178.6(3)	C4	C3	C2	N3	179.3(3)
N2	C1	C8	C5	-0.8(5)	C4	C8	C5	C6	177.8(3)
N5	C16	C15	N4	-2.3(4)	C4	C8	C5	C9	-2.7(5)
N5	C16	C15	C14	178.2(3)	C17	C16	C15	N4	176.5(3)
N5	C16	C17	C18	0.1(5)	C17	C16	C15	C14	-3.0(5)
N4	C15	C14	C13	-0.7(5)	C7	N2	C1	N1	-179.0(3)
N4	C11	C12	C13	-1.5(6)	C7	N2	C1	C8	0.3(4)
C21	N7	C25	C26	176.3(3)	C7	C6	C5	C8	0.5(5)
C21	N7	C25	C24	-2.6(4)	C7	C6	C5	C9	-179.0(3)
C21	C22	C23	C24	-1.9(5)	C5	C8	C4	C3	-178.1(3)
C1	N1	C2	N3	-179.3(3)	C5	C6	C7	N2	-1.1(5)
C1	N1	C2	C3	0.4(4)	C5	C6	C7	C10	178.8(3)
C1	N2	C7	C6	0.7(4)	C27	C26	C25	N7	-172.0(3)
C1	N2	C7	C10	-179.2(3)	C27	C26	C25	C24	6.9(5)
C1	C8	C4	C3	-0.7(4)					

Table A1. 24 Hydrogen Atom Coordinates (Å×104) and Isotropic Displacement Parameters (Å^2×10^3) for [Ru(bpy)$_2$(DMNA)](PF$_6$)$_2$

Atom	*x*	*y*	*z*	U(eq)
H3A	3240	5188	1931	31
H3B	2544	4452	1166	31

H21	7902	6893	1530	25
H3	2568	4607	-164	29
H30	2954	7420	3873	31
H19	8705	9773	4442	33
H22	9824	5885	1398	29
H11	1759	7298	1972	32
H20	7855	8278	3562	27
H24	8105	5048	3108	34
H14	2506	10412	3802	34
H6	5785	8542	18	30
H23	9898	4919	2170	35
H18	7163	11062	4806	34
H12	-115	8334	2196	40
H4	3234	5502	-907	29
H17	4755	10792	4309	31
H10A	5947	9738	1732	44
H10B	7420	9279	1381	44
H10C	6803	9143	2159	44
H13	238	9915	3134	39
H29	2912	6870	4933	40
H27	6490	5411	4089	35
H9A	4979	6485	-1517	48
H9B	4865	7589	-1321	48
H9C	3469	6971	-1333	48
H28	4689	5853	5054	42
H34A	1582	4891	4554	72
H34B	334	4320	3915	72
H34C	720	5389	4043	72
H31A	14252	8276	7402	84
H31B	13159	8491	6789	84
H31C	14372	7740	6441	84
H37A	-2268	916	-11	69

H37B -1870	13	188	69
H37C -3481	343	238	69
H33A 10703	7751	7177	98
H33B 11750	8006	7964	98
H33C 11070	6963	7535	98
H36A 2602	3055	2704	106
H36B 2666	3310	3665	106
H36C 3948	3634	3249	106
H39A -959	-1004	-1295	107
H39B -1022	-17	-1407	107
H39C -1867	-925	-2042	107

A1.1.4 Crystal Structure of [IrClCp*(DMNA)](PF_6)

Table A1. 25 Crystal data for [IrClCp(DMNA)](PF_6)*

Parameter	[IrClCp*(DMNA)](PF_6)
Empirical Formula	$C_{20}H_{26}ClF_6IrN_3P$
Formula Weight	681.06
Temperature / K	110.05(10)
Crystal System	Triclinic
Space Group	P-1
a / Å	8.0067(3)
b / Å	11.5597(5)
c / Å	12.5470(5)
α / °	83.813(4)
β / °	83.461(4)
γ / °	82.117(4)
Volume / $Å^3$	1137.81(8)
Z	2
ρ_{calc} g/cm^3	1.988
μ / mm^{-1}	6.117
F(000)	724.0
Crystal Size / mm^3	0.135x0.074x0.025
Radiation	MoKα (λ = 0.71073)
2θ range for collection / °	6.642 to 60.156
Index Ranges	-10≥h≥11, -16≥k≥16, -17≥l≥17
Reflections Collected	11204
Independent Reflections	6640 [R_{int}=0.0457, R_{sigma}= 0.0697]
Data/Restraints/Parameters	6640/38/379
Goodness-of-fit on F^2	1.047
Final R indexes [I ≥ 2σ (I)]	R_1=0.0293 wR_2=0.0536
Final R indexes [all data]	R_1=0.0345 wR_2=0.0560
Largest diff. peak/hole /e Å^{-3}	1.34/-0.87

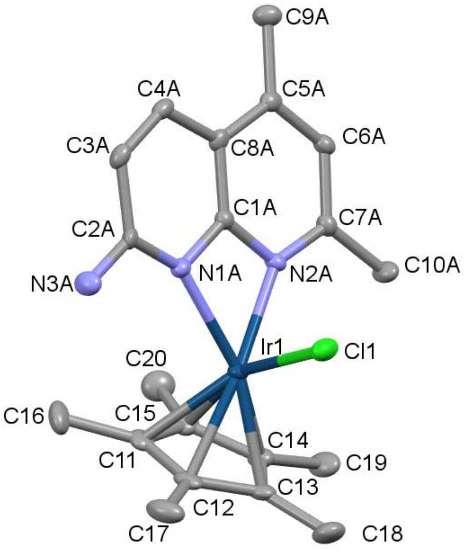

Figure A1. 4 Crystal Structure of [IrClCp(DMNA)](PF$_6$) with hydrogen and counterions omitted for clarity. Probability ellipsoids at 50%.*

Table A1. 26 Fractional Atomic Coordinates (×10^4) and Equivalent Isotropic Displacement Parameters (Å^2×10^3) for [IrClCp(DMNA)](PF$_6$). Ueq is defined as 1/3 of of the trace of the orthogonalised UIJ tensor.*

Atom	*x*	*y*	*z*	U(eq)
C11	5915(5)	8396(3)	9004(3)	21.3(7)
C12	4611(4)	9318(3)	8695(3)	20.5(7)
C13	5357(4)	10059(3)	7823(3)	20.0(7)
C14	7099(4)	9583(3)	7590(3)	19.4(7)
C15	7434(4)	8538(3)	8310(3)	20.4(7)
C16	5762(5)	7441(3)	9898(3)	32.6(9)
C17	2831(5)	9555(4)	9213(3)	32.0(9)
C18	4503(5)	11136(3)	7263(3)	31.2(9)
C19	8356(5)	10162(3)	6808(3)	28.4(9)
C20	9113(4)	7786(3)	8385(3)	29.6(8)
Cl1	3255.1(11)	8753.8(7)	6202.3(7)	22.12(17)
Ir1	5466.3(2)	8303.2(2)	7366.9(2)	13.93(4)
C2A	3903(5)	5725(3)	7932(3)	15.2(8)
C3A	4071(5)	4585(3)	7538(3)	17.4(8)
C4A	5203(5)	4306(3)	6686(3)	16.7(8)
C8A	6215(5)	5150(3)	6153(3)	14.6(8)
C1A	5963(5)	6221(3)	6586(3)	13.8(8)

C5A	7402(5)	5052(3)	5231(3)	15.7(8)
C6A	8146(5)	6033(4)	4818(3)	15.8(8)
C7A	7802(5)	7099(3)	5295(3)	15.3(8)
C9A	7805(5)	3911(3)	4735(3)	21.0(8)
C10A	8582(6)	8171(4)	4832(4)	21.7(9)
N3A	2771(5)	5985(4)	8765(3)	21.7(8)
N1A	4885(5)	6505(3)	7458(3)	14.8(7)
N2A	6722(5)	7175(3)	6194(3)	13.8(7)
C2B	7890(30)	7644(15)	5009(15)	15.3(8)
C3B	8400(30)	6631(15)	4421(17)	15.8(8)
C4B	7850(30)	5580(19)	4767(17)	15.7(8)
C8B	6770(30)	5430(15)	5733(15)	14.6(8)
C1B	6340(30)	6420(17)	6289(19)	13.8(8)
C5B	5960(30)	4462(14)	6218(16)	16.7(8)
C6B	4870(30)	4525(18)	7147(17)	17.4(8)
C7B	4560(30)	5593(17)	7620(18)	15.2(8)
C9B	6400(30)	3323(16)	5722(18)	21.0(8)
C10B	3350(40)	5710(30)	8620(20)	21.7(8)
N3B	8360(30)	8702(16)	4690(20)	21.7(9)
N1B	6990(40)	7430(20)	5946(18)	13.8(7)
N2B	5290(40)	6540(20)	7210(20)	14.8(7)
F1	10256(6)	4144(3)	9269(4)	32.6(8)
F2A	7602(3)	4422(3)	8747(2)	33.1(7)
F3A	9859(4)	4636(3)	7526(3)	34.6(8)
F4A	11034(4)	2789(3)	8064(3)	32.3(8)
F5A	8766(4)	2601(3)	9294(2)	36.6(7)
F6	8395(4)	3085(4)	7526(4)	38.4(8)
P1A	9302(3)	3617.7(15)	8402(2)	18.3(4)
F1A	10020(40)	3850(30)	9380(30)	32.6(8)
F2B	9240(40)	4560(30)	7690(30)	82(7)
F3B	11350(40)	3240(30)	7910(30)	76(6)
F4B	9620(40)	2140(20)	8960(20)	82(7)

F5B	7570(30)	3640(30)	8880(20)	76(6)
F6A	8920(30)	2890(30)	7430(30)	38.4(8)
P1B	9470(20)	3359(13)	8388(16)	18.3(4)

Table A1. 27 Anisotropic Displacement Parameters (Å^2×10^3) for [IrClCp(DMNA)](PF$_6$). The Anisotropic displacement factor exponent takes the form: -2π2[h2a*2U11+2hka*b*U12+…].*

Atom	U_{11}	U_{22}	U_{33}	U_{23}	U_{13}	U_{12}
C11	29.2(19)	21.5(18)	17.2(15)	-6.0(13)	-8.3(14)	-9.4(15)
C12	22.4(17)	21.9(18)	21.0(16)	-12.3(14)	0.0(14)	-10.2(14)
C13	24.8(18)	15.9(16)	21.6(16)	-9.9(13)	-0.6(14)	-5.6(14)
C14	21.5(17)	16.0(16)	22.4(16)	-5.6(13)	-1.1(14)	-6.7(13)
C15	25.0(18)	17.7(17)	21.8(16)	-3.7(14)	-9.2(14)	-7.3(14)
C16	48(3)	36(2)	17.3(17)	5.9(16)	-12.3(17)	-17.4(19)
C17	28(2)	35(2)	36(2)	-19.8(18)	7.1(17)	-12.3(17)
C18	40(2)	15.7(18)	37(2)	-7.9(16)	-3.0(18)	1.8(16)
C19	30(2)	23.7(19)	33(2)	-6.9(16)	6.5(17)	-15.2(16)
C20	20.0(18)	32(2)	39(2)	-5.2(18)	-9.9(16)	-2.7(16)
Cl1	25.0(4)	15.7(4)	27.3(4)	-2.9(3)	-12.5(3)	0.5(3)
Ir1	16.16(6)	11.84(6)	14.85(6)	-3.87(4)	-3.08(5)	-2.24(4)
C2A	21(2)	13.0(17)	12(2)	3.1(14)	-4.8(15)	-3.2(16)
C3A	15.3(19)	14.3(18)	22(2)	4.1(16)	-4.3(16)	-3.4(15)
C4A	19(2)	11.2(18)	21(2)	0.6(16)	-9.3(17)	-2.7(15)
C8A	13.1(18)	13.3(19)	17.1(19)	1.6(15)	-5.6(15)	-0.1(14)
C1A	14(2)	13.7(19)	13(2)	-1.0(16)	-3.3(16)	-1.2(14)
C5A	16.6(18)	15.3(19)	16.3(18)	-2.5(15)	-7.4(15)	0.0(15)
C6A	16.3(18)	18(2)	13.6(18)	-4.3(15)	-1.9(15)	-1.2(16)
C7A	14.2(17)	18(2)	13.5(18)	-1.7(15)	-1.0(14)	-1.3(16)
C9A	17.8(19)	19(2)	27(2)	-7.1(16)	-4.0(16)	0.4(15)
C10A	27(2)	16(2)	23(2)	-4(2)	4.5(17)	-10(2)
N3A	22(2)	21(2)	23.4(19)	-3.9(16)	4.1(16)	-8.7(17)
N1A	18(2)	12.5(14)	15(2)	-1.0(14)	-3.7(14)	-3.5(14)
N2A	13.9(18)	15(2)	13(2)	-4.7(15)	-1.1(14)	-2.2(13)

C2B	14.2(17)	18(2)	13.5(18)	-1.7(15)	-1.0(14)	-1.3(16)
C3B	16.3(18)	18(2)	13.6(18)	-4.3(15)	-1.9(15)	-1.2(16)
C4B	16.6(18)	15.3(19)	16.3(18)	-2.5(15)	-7.4(15)	0.0(15)
C8B	13.1(18)	13.3(19)	17.1(19)	1.6(15)	-5.6(15)	-0.1(14)
C1B	14(2)	13.7(19)	13(2)	-1.0(16)	-3.3(16)	-1.2(14)
C5B	19(2)	11.2(18)	21(2)	0.6(16)	-9.3(17)	-2.7(15)
C6B	15.3(19)	14.3(18)	22(2)	4.1(16)	-4.3(16)	-3.4(15)
C7B	21(2)	13.0(17)	12(2)	3.1(14)	-4.8(15)	-3.2(16)
C9B	17.8(19)	19(2)	27(2)	-7.1(16)	-4.0(16)	0.4(15)
C10B	22(2)	21(2)	23.4(19)	-3.9(16)	4.1(16)	-8.7(17)
N3B	27(2)	16(2)	23(2)	-4(2)	4.5(17)	-10(2)
N1B	13.9(18)	15(2)	13(2)	-4.7(15)	-1.1(14)	-2.2(13)
N2B	18(2)	12.5(14)	15(2)	-1.0(14)	-3.7(14)	-3.5(14)
F1	36(2)	34(3)	32.4(17)	-5.3(18)	-8.8(15)	-16.2(14)
F2A	21.7(13)	38.7(17)	35.1(15)	-9.5(14)	3.1(12)	8.7(13)
F3A	51(2)	26.3(16)	23.1(14)	3.6(12)	8.5(15)	-7.5(15)
F4A	20.4(15)	27.5(16)	46.2(19)	-8.9(15)	1.2(14)	7.7(12)
F5A	36.1(17)	32.2(17)	38.8(16)	9.5(13)	4.7(14)	-11.7(13)
F6	35(2)	38(2)	46.8(17)	-19.6(15)	-21(2)	4.9(17)
P1A	16.3(8)	18.4(11)	19.3(4)	-2.8(8)	0.6(5)	-0.2(7)
F1A	36(2)	34(3)	32.4(17)	-5.3(18)	-8.8(15)	-16.2(14)
F2B	98(12)	57(10)	90(12)	32(8)	-27(10)	-27(9)
F3B	49(9)	112(13)	59(9)	-5(10)	18(8)	-7(9)
F4B	98(12)	57(10)	90(12)	32(8)	-27(10)	-27(9)
F5B	49(9)	112(13)	59(9)	-5(10)	18(8)	-7(9)
F6A	35(2)	38(2)	46.8(17)	-19.6(15)	-21(2)	4.9(17)
P1B	16.3(8)	18.4(11)	19.3(4)	-2.8(8)	0.6(5)	-0.2(7)

Table A1. 28 Bond Lengths for [IrClCp(DMNA)](PF$_6$).*

Atom	Atom	Length/Å	Atom	Atom	Length/Å
C11	C12	1.440(5)	C5A	C9A	1.498(5)
C11	C15	1.431(5)	C6A	C7A	1.407(5)

C11	C16	1.494(5)	C7A	C10A	1.496(5)
C11	Ir1	2.141(3)	C7A	N2A	1.345(5)
C12	C13	1.441(5)	C2B	C3B	1.439(7)
C12	C17	1.500(5)	C2B	N3B	1.335(7)
C12	Ir1	2.136(3)	C2B	N1B	1.325(7)
C13	C14	1.437(5)	C3B	C4B	1.358(7)
C13	C18	1.483(5)	C4B	C8B	1.418(7)
C13	Ir1	2.155(3)	C8B	C1B	1.387(7)
C14	C15	1.442(5)	C8B	C5B	1.416(7)
C14	C19	1.497(5)	C1B	N1B	1.352(7)
C14	Ir1	2.163(3)	C1B	N2B	1.352(7)
C15	C20	1.504(5)	C5B	C6B	1.379(7)
C15	Ir1	2.137(3)	C5B	C9B	1.498(7)
Cl1	Ir1	2.3902(8)	C6B	C7B	1.406(7)
Ir1	N1A	2.180(4)	C7B	C10B	1.496(7)
Ir1	N2A	2.143(4)	C7B	N2B	1.343(7)
Ir1	N1B	2.29(2)	F1	P1A	1.611(6)
Ir1	N2B	2.09(2)	F2A	P1A	1.584(3)
C2A	C3A	1.440(5)	F3A	P1A	1.596(4)
C2A	N3A	1.334(5)	F4A	P1A	1.615(4)
C2A	N1A	1.325(5)	F5A	P1A	1.601(4)
C3A	C4A	1.357(5)	F6	P1A	1.602(5)
C4A	C8A	1.418(5)	F1A	P1B	1.55(4)
C8A	C1A	1.386(5)	F2B	P1B	1.56(4)
C8A	C5A	1.415(5)	F3B	P1B	1.54(3)
C1A	N1A	1.354(5)	F4B	P1B	1.51(3)
C1A	N2A	1.351(5)	F5B	P1B	1.58(3)
C5A	C6A	1.378(6)	F6A	P1B	1.51(4)

Table A1. 29 Bond Angles for [IrClCp(DMNA)](PF$_6$).*

Atom	Atom	Atom	Angle/˚	Atom	Atom	Atom	Angle/˚
C12	C11	C16	127.1(3)	C3A	C4A	C8A	120.0(4)

C12	C11	Ir1	70.13(19)	C1A	C8A	C4A	114.8(3)
C15	C11	C12	108.7(3)	C1A	C8A	C5A	116.4(3)
C15	C11	C16	124.2(3)	C5A	C8A	C4A	128.7(4)
C15	C11	Ir1	70.30(18)	N1A	C1A	C8A	126.1(3)
C16	C11	Ir1	125.8(2)	N2A	C1A	C8A	125.8(3)
C11	C12	C13	107.4(3)	N2A	C1A	N1A	108.1(3)
C11	C12	C17	128.0(3)	C8A	C5A	C9A	120.0(3)
C11	C12	Ir1	70.52(18)	C6A	C5A	C8A	117.6(4)
C13	C12	C17	124.5(3)	C6A	C5A	C9A	122.3(4)
C13	C12	Ir1	71.08(17)	C5A	C6A	C7A	122.6(3)
C17	C12	Ir1	127.2(2)	C6A	C7A	C10A	122.5(3)
C12	C13	C18	126.6(3)	N2A	C7A	C6A	119.6(4)
C12	C13	Ir1	69.67(18)	N2A	C7A	C10A	117.9(3)
C14	C13	C12	108.2(3)	C2A	N1A	Ir1	146.3(3)
C14	C13	C18	125.2(3)	C2A	N1A	C1A	118.8(3)
C14	C13	Ir1	70.87(18)	C1A	N1A	Ir1	94.7(2)
C18	C13	Ir1	125.7(3)	C1A	N2A	Ir1	96.4(2)
C13	C14	C15	108.1(3)	C7A	N2A	Ir1	145.6(3)
C13	C14	C19	124.6(3)	C7A	N2A	C1A	117.9(3)
C13	C14	Ir1	70.27(19)	N3B	C2B	C3B	124.1(19)
C15	C14	C19	127.0(3)	N1B	C2B	C3B	114.2(19)
C15	C14	Ir1	69.45(18)	N1B	C2B	N3B	121.5(19)
C19	C14	Ir1	130.6(2)	C4B	C3B	C2B	121.7(19)
C11	C15	C14	107.7(3)	C3B	C4B	C8B	121(2)
C11	C15	C20	125.8(3)	C1B	C8B	C4B	115.2(17)
C11	C15	Ir1	70.61(19)	C1B	C8B	C5B	113.0(15)
C14	C15	C20	126.4(3)	C5B	C8B	C4B	131.7(18)
C14	C15	Ir1	71.37(19)	N1B	C1B	C8B	121(2)
C20	C15	Ir1	127.2(2)	N1B	C1B	N2B	110.6(15)
C11	Ir1	C13	65.42(13)	N2B	C1B	C8B	128(2)
C11	Ir1	C14	65.21(13)	C8B	C5B	C9B	117.8(17)
C11	Ir1	Cl1	140.63(10)	C6B	C5B	C8B	122.2(16)

C11	Ir1	N1A	100.23(14)
C11	Ir1	N2A	130.51(15)
C11	Ir1	N1B	133.8(8)
C12	Ir1	C11	39.34(13)
C12	Ir1	C13	39.25(12)
C12	Ir1	C14	65.65(12)
C12	Ir1	C15	66.18(13)
C12	Ir1	Cl1	104.27(10)
C12	Ir1	N1A	119.11(13)
C12	Ir1	N2A	169.44(15)
C12	Ir1	N1B	165.5(7)
C13	Ir1	C14	38.87(12)
C13	Ir1	Cl1	95.70(10)
C13	Ir1	N1A	157.88(12)
C13	Ir1	N1B	130.1(5)
C14	Ir1	Cl1	121.60(10)
C14	Ir1	N1A	151.96(16)
C14	Ir1	N1B	100.1(6)
C15	Ir1	C11	39.09(13)
C15	Ir1	C13	65.74(13)
C15	Ir1	C14	39.18(12)
C15	Ir1	Cl1	160.24(9)
C15	Ir1	N1A	114.53(16)
C15	Ir1	N2A	103.80(15)
C15	Ir1	N1B	101.4(8)
N1A	Ir1	Cl1	85.21(13)
N2A	Ir1	C13	141.27(12)
N2A	Ir1	C14	109.11(13)
N2A	Ir1	Cl1	86.29(12)
N2A	Ir1	N1A	60.84(11)
N1B	Ir1	Cl1	85.1(8)
N2B	Ir1	C11	106.6(8)

C6B	C5B	C9B	119.9(16)
C5B	C6B	C7B	118.1(18)
C6B	C7B	C10B	120(2)
N2B	C7B	C6B	123(2)
N2B	C7B	C10B	117(2)
C2B	N1B	Ir1	143.4(17)
C2B	N1B	C1B	126(2)
C1B	N1B	Ir1	89.9(12)
C1B	N2B	Ir1	98.7(13)
C7B	N2B	Ir1	145.4(17)
C7B	N2B	C1B	116(2)
F1	P1A	F4A	89.5(3)
F2A	P1A	F1	90.3(2)
F2A	P1A	F3A	90.31(18)
F2A	P1A	F4A	179.3(3)
F2A	P1A	F5A	89.9(2)
F2A	P1A	F6	90.9(2)
F3A	P1A	F1	88.9(2)
F3A	P1A	F4A	90.3(2)
F3A	P1A	F5A	179.0(3)
F3A	P1A	F6	90.6(3)
F5A	P1A	F1	90.1(2)
F5A	P1A	F4A	89.46(18)
F5A	P1A	F6	90.4(3)
F6	P1A	F1	178.7(3)
F6	P1A	F4A	89.32(19)
F1A	P1B	F2B	96(2)
F1A	P1B	F5B	88.1(19)
F2B	P1B	F5B	87.3(17)
F3B	P1B	F1A	88(2)
F3B	P1B	F2B	87.1(19)
F3B	P1B	F5B	173.0(19)

N2B	Ir1	C12	129.8(6)	F4B	P1B	F1A	90.6(18)
N2B	Ir1	C13	169.0(5)	F4B	P1B	F2B	173(2)
N2B	Ir1	C14	146.5(9)	F4B	P1B	F3B	93.9(18)
N2B	Ir1	C15	113.4(10)	F4B	P1B	F5B	92.2(18)
N2B	Ir1	Cl1	86.1(10)	F6A	P1B	F1A	179(2)
N2B	Ir1	N1B	60.8(6)	F6A	P1B	F2B	84(2)
N3A	C2A	C3A	120.0(4)	F6A	P1B	F3B	92.4(19)
N1A	C2A	C3A	119.2(4)	F6A	P1B	F4B	89.3(19)
N1A	C2A	N3A	120.8(4)	F6A	P1B	F5B	91.1(17)
C4A	C3A	C2A	121.0(4)				

Table A1. 30 Hydrogen Bonds for [IrClCp(DMNA)](PF$_6$).*

D	H	A	d(D-H)/Å	d(H-A)/Å	d(D-A)/Å	D-H-A/°
N3A	H3AA	F1[1]	0.86(4)	2.26(5)	3.095(5)	165(4)
N3A	H3AB	F5A[2]	0.88(5)	2.58(5)	3.121(5)	121(4)
C3B	H3B	F3B[3]	0.95	2.18	2.90(4)	131.1

[1]-1+X,+Y,+Z; [2]1-X,1-Y,2-Z; [3]2-X,1-Y,1-Z

Table A1. 31 Torsion Angles for [IrClCp(DMNA)](PF$_6$).*

A	B	C	D	Angle/˚	A	B	C	D	Angle/˚
C11	C12	C13	C14	0.8(4)	C8A	C5A	C6A	C7A	1.8(6)
C11	C12	C13	C18	-178.5(3)	C1A	C8A	C5A	C6A	-2.7(5)
C11	C12	C13	Ir1	61.5(2)	C1A	C8A	C5A	C9A	177.6(4)
C12	C11	C15	C14	2.3(4)	C5A	C8A	C1A	N1A	179.6(4)
C12	C11	C15	C20	177.6(3)	C5A	C8A	C1A	N2A	1.4(6)
C12	C11	C15	Ir1	-59.9(2)	C5A	C6A	C7A	C10A	-178.6(4)
C12	C13	C14	C15	0.6(4)	C5A	C6A	C7A	N2A	0.7(6)
C12	C13	C14	C19	-173.8(3)	C6A	C7A	N2A	Ir1	-177.7(4)
C12	C13	C14	Ir1	59.9(2)	C6A	C7A	N2A	C1A	-2.1(6)
C13	C14	C15	C11	-1.7(4)	C9A	C5A	C6A	C7A	-178.5(4)
C13	C14	C15	C20	-177.1(3)	C10A	C7A	N2A	Ir1	1.7(8)
C13	C14	C15	Ir1	59.9(2)	C10A	C7A	N2A	C1A	177.3(4)
C15	C11	C12	C13	-1.9(4)	N3A	C2A	C3A	C4A	179.4(4)

C15	C11	C12	C17	−177.5(3)	N3A	C2A	N1A	Ir1	−5.7(9)
C15	C11	C12	Ir1	60.0(2)	N3A	C2A	N1A	C1A	−177.2(4)
C16	C11	C12	C13	177.7(3)	N1A	C2A	C3A	C4A	−0.7(6)
C16	C11	C12	C17	2.1(6)	N1A	C1A	N2A	Ir1	0.1(4)
C16	C11	C12	Ir1	−120.4(3)	N1A	C1A	N2A	C7A	−177.4(4)
C16	C11	C15	C14	−177.3(3)	N2A	C1A	N1A	Ir1	−0.1(4)
C16	C11	C15	C20	−2.0(5)	N2A	C1A	N1A	C2A	175.2(4)
C16	C11	C15	Ir1	120.5(3)	C2B	C3B	C4B	C8B	−1(4)
C17	C12	C13	C14	176.6(3)	C3B	C2B	N1B	Ir1	−173(3)
C17	C12	C13	C18	−2.7(5)	C3B	C2B	N1B	C1B	−10(4)
C17	C12	C13	Ir1	−122.7(3)	C3B	C4B	C8B	C1B	−1(4)
C18	C13	C14	C15	179.9(3)	C3B	C4B	C8B	C5B	176(2)
C18	C13	C14	C19	5.5(5)	C4B	C8B	C1B	N1B	−3(4)
C18	C13	C14	Ir1	−120.8(3)	C4B	C8B	C1B	N2B	178(3)
C19	C14	C15	C11	172.4(3)	C4B	C8B	C5B	C6B	−176(3)
C19	C14	C15	C20	−2.9(6)	C4B	C8B	C5B	C9B	7(4)
C19	C14	C15	Ir1	−126.0(3)	C8B	C1B	N1B	Ir1	180(3)
Ir1	C11	C12	C13	−61.9(2)	C8B	C1B	N1B	C2B	9(5)
Ir1	C11	C12	C17	122.5(3)	C8B	C1B	N2B	Ir1	−179(3)
Ir1	C11	C15	C14	62.1(2)	C8B	C1B	N2B	C7B	−1(5)
Ir1	C11	C15	C20	−122.5(3)	C8B	C5B	C6B	C7B	0(4)
Ir1	C12	C13	C14	−60.7(2)	C1B	C8B	C5B	C6B	0(4)
Ir1	C12	C13	C18	120.0(4)	C1B	C8B	C5B	C9B	−177(2)
Ir1	C13	C14	C15	−59.4(2)	C5B	C8B	C1B	N1B	180(3)
Ir1	C13	C14	C19	126.3(3)	C5B	C8B	C1B	N2B	1(5)
Ir1	C14	C15	C11	−61.6(2)	C5B	C6B	C7B	C10B	179(3)
Ir1	C14	C15	C20	123.0(3)	C5B	C6B	C7B	N2B	0(4)
C2A	C3A	C4A	C8A	−1.5(6)	C6B	C7B	N2B	Ir1	178(3)
C3A	C2A	N1A	Ir1	174.5(5)	C6B	C7B	N2B	C1B	1(5)
C3A	C2A	N1A	C1A	3.0(7)	C9B	C5B	C6B	C7B	176(2)
C3A	C4A	C8A	C1A	1.3(6)	C10B	C7B	N2B	Ir1	−1(6)
C3A	C4A	C8A	C5A	−177.0(4)	C10B	C7B	N2B	C1B	−178(3)

C4A	C8A	C1A	N1A	1.1(6)	N3B	C2B	C3B	C4B	-179(3)
C4A	C8A	C1A	N2A	-177.1(4)	N3B	C2B	N1B	Ir1	11(5)
C4A	C8A	C5A	C6A	175.6(4)	N3B	C2B	N1B	C1B	174(3)
C4A	C8A	C5A	C9A	-4.2(6)	N1B	C2B	C3B	C4B	6(4)
C8A	C1A	N1A	Ir1	-178.6(4)	N1B	C1B	N2B	Ir1	1(3)
C8A	C1A	N1A	C2A	-3.3(7)	N1B	C1B	N2B	C7B	180(3)
C8A	C1A	N2A	Ir1	178.6(4)	N2B	C1B	N1B	Ir1	-1(3)
C8A	C1A	N2A	C7A	1.1(7)	N2B	C1B	N1B	C2B	-171(3)

Table A1. 32 Hydrogen Atom Coordinates (Å×10^4) and Isotropic Displacement Parameters (Å^2×10^3) for [IrClCp(DMNA)](PF$_6$).*

Atom	*x*	*y*	*z*	U(eq)
H16A	4564	7413	10152	49
H16B	6369	7596	10493	49
H16C	6254	6687	9635	49
H17A	2065	9823	8656	48
H17B	2770	10164	9708	48
H17C	2495	8835	9615	48
H18A	4970	11210	6505	47
H18B	4692	11823	7607	47
H18C	3284	11089	7305	47
H19A	9369	9600	6663	43
H19B	8669	10837	7115	43
H19C	7852	10428	6134	43
H20A	8929	6962	8543	44
H20B	9684	8023	8962	44
H20C	9820	7883	7698	44
H3A	3379	4021	7881	21
H4A	5318	3544	6448	20
H6A	8921	5989	4188	19
H9AA	8331	3312	5251	31
H9AB	8590	4008	4083	31
H9AC	6759	3667	4549	31

H10A	9024	8087	4080	33
H10B	9510	8269	5247	33
H10C	7723	8861	4866	33
H3AA	2090(60)	5500(40)	9030(30)	22(12)
H3AB	2790(60)	6700(50)	8930(40)	36(15)
H3B	9135	6699	3774	19
H4B	8207	4932	4354	19
H6B	4333	3866	7459	21
H9BA	7425	2893	6006	31
H9BB	6609	3478	4938	31
H9BC	5462	2852	5899	31
H10D	2546	5136	8656	33
H10E	2737	6503	8593	33
H10F	3986	5562	9251	33
H3BA	8076	9276	5114	26
H3BB	8958	8825	4069	26

A2 Appendix 2 – GC Calibration Curves

Table A2. 1 GC response factors of relevant substrates

Analyte	Response Factor / V µmol^{-1} s^{-1}	Standard Deviation
Styrene	38.5	1.1
Ethyl Benzene	41.4	1.3
Benzaldehyde	21.7	1.3

α-methyl styrene	51.6	0.3
Cumene	44.6	0.9
β-methyl styrene	45.1	0.4
n-Propyl Benzene	43.6	0.6
1-Octene	39.2	0.6
2-Octene	42.0	0.4
Octane	36.9	0.5
Mesitylene	46.4	0.4
1-menthene	48.8	0.6
Limonene	52.8	0.7

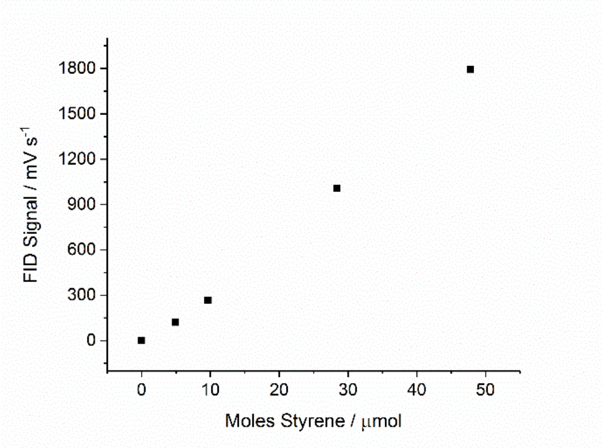

Figure A2. 1 Calibration curve for Styrene

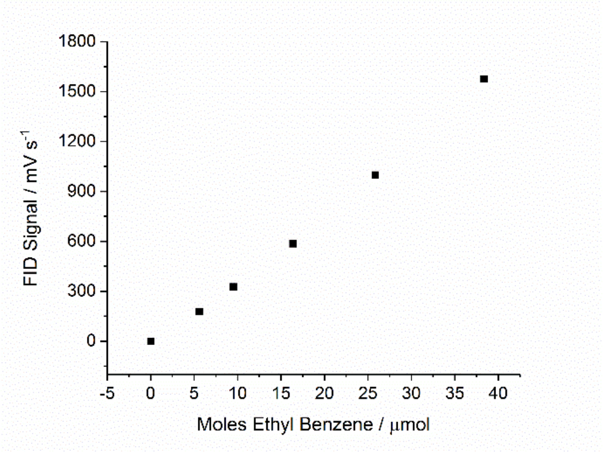

Figure A2. 2 Calibration curve for Ethyl Benzene

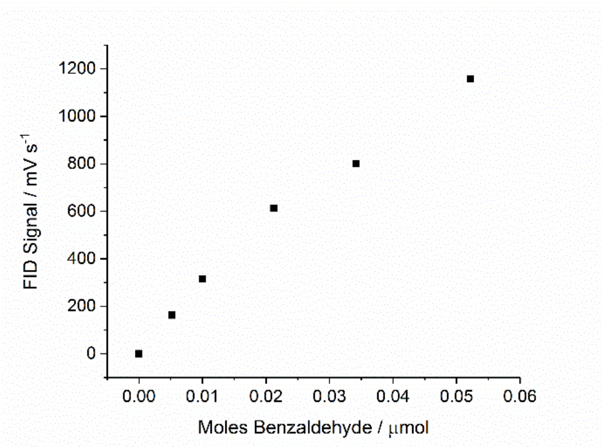

Figure A2. 3 Calibration curve for Benzaldehyde

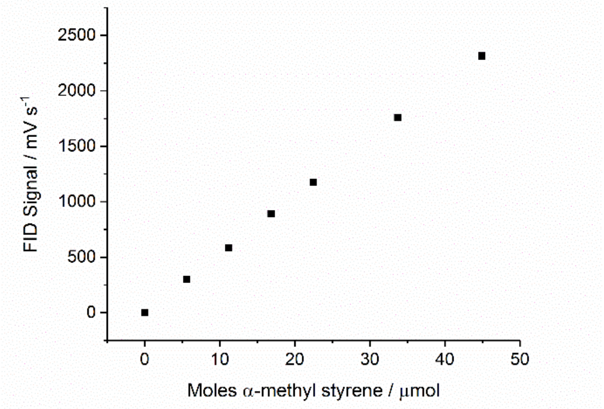

Figure A2. 4 Calibration curve for α-methyl styrene

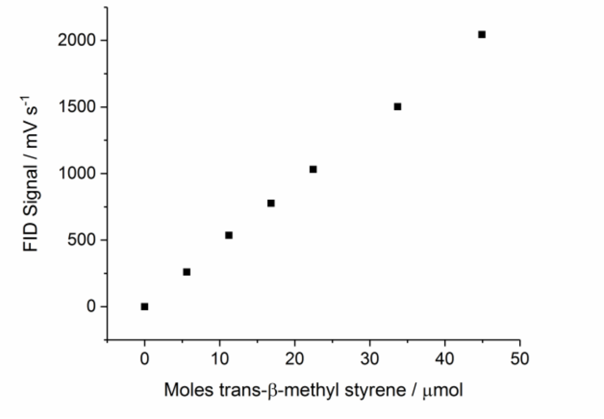

Figure A2. 5 Calibration curve for trans-β-methyl styrene

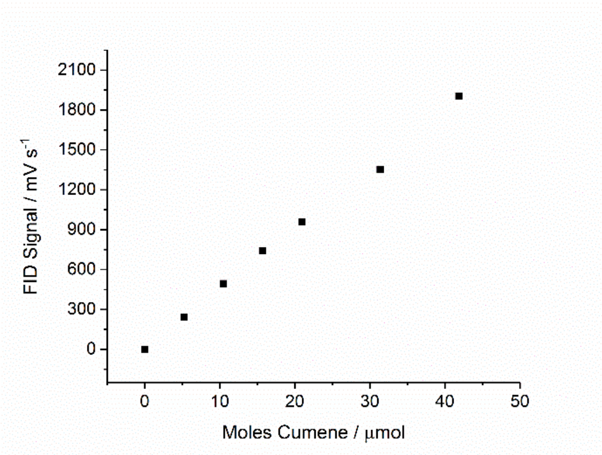

Figure A2. 6 Calibration curve for cumene

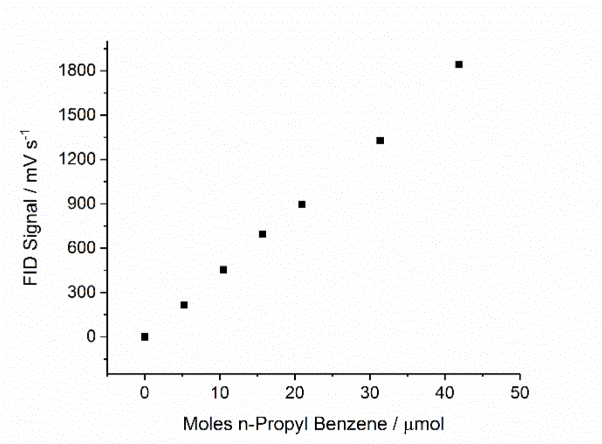

Figure A2. 7 Calibration curve for n-propyl benzene

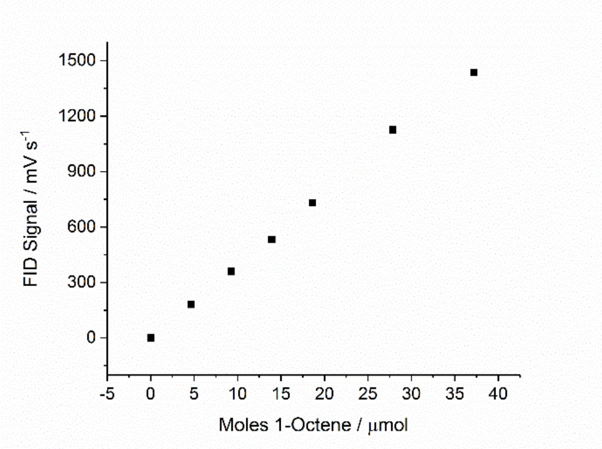

Figure A2. 8 Calibration curve for 1-octene

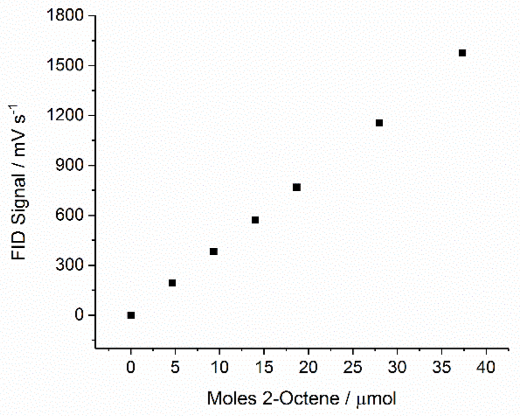

Figure A2. 9 Calibration curve for 2-octene

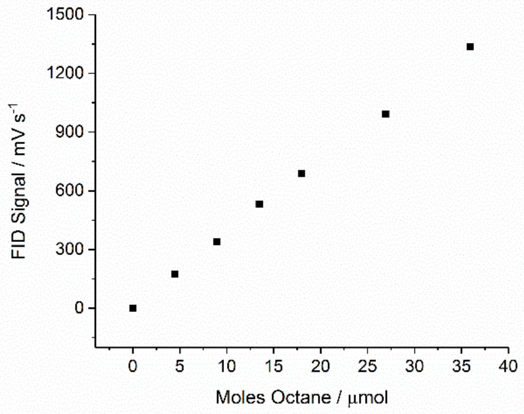

Figure A2. 10 Calibration curve for Octane

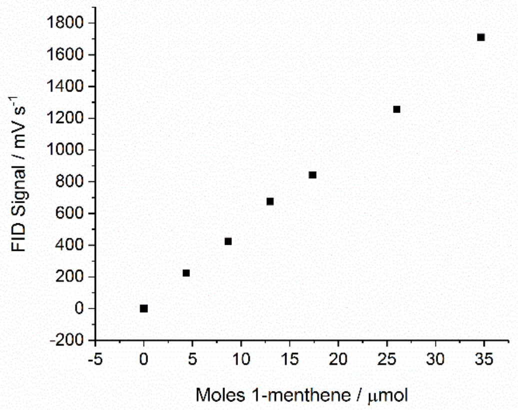

Figure A2. 11 Calibration curve for 1-menthene

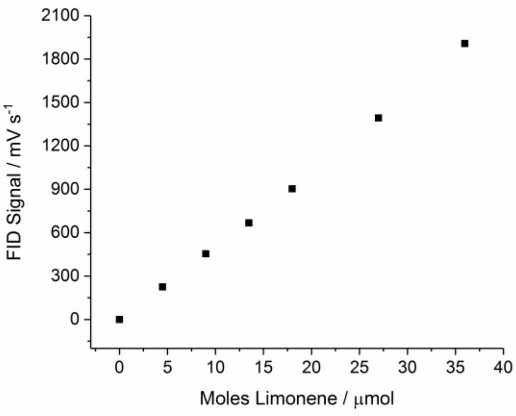

Figure A2. 12 Calibration curve for limonene

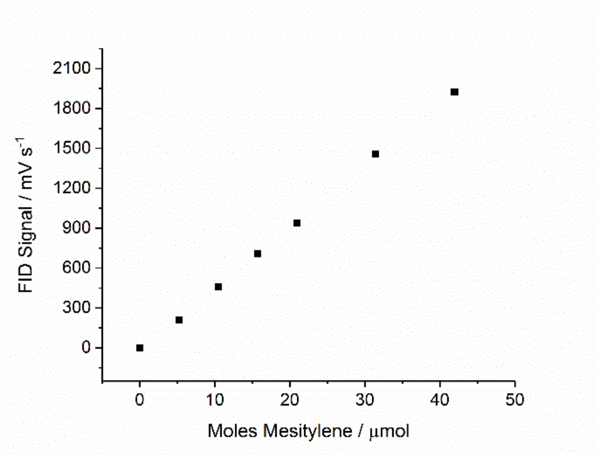

Figure A2. 13 Calibration curve for Mesitylene

Abbreviations

AC-STEM – Aberration-corrected scanning electron microscopy
ATR-IR - Attenuated total reflectance infra-red
BET – Brunauer-Emmett-Teller
bpy – 2, 2’-bipyridine
CCN – Cyanamide-derived carbon nitride
CP-MAS – cross polarisation-magic angle spinning
CV – cyclic voltammetry
DCM - dichloromethane
DFT – density functional theory
DLS – dynamic light scattering
DMF – dimethyl formamide
DMNA – 5, 7-dimethyl-[1, 8]-naphthyridine-2-amine
DRIFTS – diffuse reflectance infrared fourier transform spectroscopy
DRS – Diffuse reflectance spectroscopy
EDTA – ethylene diamine tetraacetic acid
EPR – electron paramagnetic resonance
EXAFS – Extended X-rat absorption fine structure
FRET – Förster resonance energy transfer
FWHM – Full width half maximum
HER – Hydrogen evolution reaction
HOMO – highest occupied molecular orbital
HPLC – High performance liquid chromatorgraphy
ICP-MS – inductively coupled plasma mass spectrometry
IPA – isopropyl alcohol (2-propanol)
IR – Infra-red
LIDFI-MS – Liquid injection field desorption/ionisation mass spectrometry
LUMO – Lowest occupied molecular orbital
MLCT – metal-to-ligand charge transfer
MO – molecular orbital
NMR – Nuclear Magnetic Resonance
PXRD – Powder X-ray diffractometry
RHE – reversible hydrogen electrode
SAC- single-atom catalyst
SEM – scanning electron microscopy

SHE – standard hydrogen electrode
TEM – transmission electron microscopy
TOF – Turnover frequency
tpy - terpyridine
TRPL – time resolved photoluminescence
UCN – Urea-derived carbon nitride
XANES – X-ray absorption near edge structure
XPS – X-ray photoelectron spectroscopy

References

1. A. W. A. D. McNaught, *Compendium of Chemical Terminology*, IUPAC, 2nd edn., 1997.
2. F. Haber and G. van Oordt, *Z. Anorg. Chem.*, 1905, **44**, 341-378.
3. V. Smil, *Nature*, 1999, **400**, 415.
4. J. W. Erisman, M. A. Sutton, J. Galloway, Z. Klimont and W. Winiwarter, *Nat. Geosci.*, 2008, **1**, 636.
5. W. N. Delgass, G. L. Haller, R. Kellerman and J. H. Lunsford, in *Spectroscopy in Heterogeneous Catalysis*, eds. W. N. Delgass, G. L. Haller, R. Kellerman and J. H. Lunsford, Academic Press, 1979, pp. 1-18.
6. F. Goettmann, A. Fischer, M. Antonietti and A. Thomas, *Angew. Chem. Int. Ed.*, 2006, **45**, 4467-4471.
7. B. V. Lotsch, M. Döblinger, J. Sehnert, L. Seyfarth, J. Senker, O. Oeckler and W. Schnick, *Chem. Eur. J.*, 2007, **13**, 4969-4980.
8. A. Thomas, A. Fischer, F. Goettmann, M. Antonietti, J.-O. Muller, R. Schlogl and J. M. Carlsson, *J. Mater. Chem.*, 2008, **18**, 4893-4908.
9. K. Maeda, X. Wang, Y. Nishihara, D. Lu, M. Antonietti and K. Domen, *J. Phys. Chem. C*, 2009, **113**, 4940-4947.
10. F. Su, C. Mathew Smitha, L. Möhlmann, M. Antonietti, X. Wang and S. Blechert, *Angew. Chem. Int. Ed.*, 2010, **50**, 657-660.
11. Y. Zhang, J. Liu, G. Wu and W. Chen, *Nanoscale*, 2012, **4**, 5300-5303.
12. C. Merschjann, T. Tyborski, S. Orthmann, F. Yang, K. Schwarzburg, M. Lublow, M. C. Lux-Steiner and T. Schedel-Niedrig, *Phys. Rev. B*, 2013, **87**, 205204.
13. J. Liu, Y. Liu, N. Liu, Y. Han, X. Zhang, H. Huang, Y. Lifshitz, S.-T. Lee, J. Zhong and Z. Kang, *Science*, 2015, **347**, 970-974.
14. W.-J. Ong, L.-L. Tan, Y. H. Ng, S.-T. Yong and S.-P. Chai, *Chem. Rev.*, 2016, **116**, 7159-7329.
15. J. Liebig, *Annalen*, 1834, **10**.
16. E. C. Franklin, *J. Am. Chem. Soc.*, 1922, **44**, 486-509.
17. E. Kroke, M. Schwarz, E. Horath-Bordon, P. Kroll, B. Noll and A. D. Norman, *New J. Chem.*, 2002, **26**, 508-512.
18. A. Y. Liu and R. M. Wentzcovitch, *Phys. Rev. B*, 1994, **50**, 10362-10365.
19. C. Niu, Y. Z. Lu and C. M. Lieber, *Science*, 1993, **261**, 334.
20. A. Y. Liu and M. L. Cohen, *Science*, 1989, **245**, 841.
21. J. R. Holst and E. G. Gillan, *J. Am. Chem. Soc.*, 2008, **130**, 7373-7379.
22. J. Sehnert, K. Baerwinkel and J. Senker, *J Phys. Chem. B*, 2007, **111**, 10671-10680.
23. A. Thomas, A. Fischer, F. Goettmann, M. Antonietti, J.-O. Müller, R. Schlögl and J. M. Carlsson, *J. Mater. Chem.*, 2008, **18**, 4893-4908.
24. R. Godin, Y. Wang, M. A. Zwijnenburg, J. Tang and J. R. Durrant, *J. Am. Chem. Soc.*, 2017, **139**, 5216-5224.
25. B. V. Lotsch and W. Schnick, *Chem. Mater.*, 2005, **17**, 3976-3982.
26. B. V. Lotsch and W. Schnick, *Chem. Mater.*, 2006, **18**, 1891-1900.
27. J. Bojdys Michael , J. O. Müller, M. Antonietti and A. Thomas, *Chem. Eur. J.*, 2008, **14**, 8177-8182.
28. B. Jürgens, E. Irran, J. Schneider and W. Schnick, *Inorg. Chem.*, 2000, **39**, 665-670.
29. B. Jürgens, E. Irran, J. Senker, P. Kroll, H. Müller and W. Schnick, *J. Am. Chem. Soc.*, 2003, **125**, 10288-10300.

30. E. Wirnhier, B. Mesch Maria, J. Senker and W. Schnick, *Chem. Eur. J.*, 2012, **19**, 2041-2049.
31. G. Zhang, J. Zhang, M. Zhang and X. Wang, *J. Mater. Chem.*, 2012, **22**, 8083-8091.
32. H. Zhang and A. Yu, *J. Phys. Chem. C*, 2014, **118**, 11628-11635.
33. T. Tyborski, C. Merschjann, S. Orthmann, F. Yang, M. C. Lux-Steiner and S.-N. Th, *J. Phys.: Condens. Matter*, 2013, **25**, 395402.
34. Y. Cui, J. Zhang, G. Zhang, J. Huang, P. Liu, M. Antonietti and X. Wang, *J. Mater. Chem.*, 2011, **21**, 13032-13039.
35. F. Dong, L. Wu, Y. Sun, M. Fu, Z. Wu and S. C. Lee, *J. Mater. Chem.*, 2011, **21**, 15171-15174.
36. S. C. Yan, Z. S. Li and Z. G. Zou, *Langmuir*, 2009, **25**, 10397-10401.
37. F. Dong, Z. Wang, Y. Sun, W.-K. Ho and H. Zhang, *J. Colloid Interface Sci.*, 2013, **401**, 70-79.
38. B. Long, J. Lin and X. Wang, *J. Mater. Chem. A*, 2014, **2**, 2942-2951.
39. J. Liu, T. Zhang, Z. Wang, G. Dawson and W. Chen, *J. Mater. Chem.*, 2011, **21**, 14398-14401.
40. X. Zhang, X. Xie, H. Wang, J. Zhang, B. Pan and Y. Xie, *J. Am. Chem. Soc.*, 2013, **135**, 18-21.
41. J. Zhang, M. Zhang, L. Lin and X. Wang, *Angew. Chem. Int. Ed.*, 2015, **54**, 6297-6301.
42. T. Y. Ma, Y. Tang, S. Dai and S. Z. Qiao, *Small*, 2014, **10**, 2382-2389.
43. P. Niu, L. Zhang, G. Liu and H.-M. Cheng, *Adv. Funct. Mater.*, 2012, **22**, 4763-4770.
44. W. Bian, H. Zhang, Q. Yu, M. Shi, S. Shuang, Z. Cai and M. M. F. Choi, *Spectrochim. Acta. A-M.*, 2016, **169**, 122-127.
45. R. Kuriki, M. Yamamoto, K. Higuchi, Y. Yamamoto, M. Akatsuka, D. Lu, S. Yagi, T. Yoshida, O. Ishitani and K. Maeda, *Angew. Chem. Int. Ed.*, 2017, **56**, 4867-4871.
46. X. Wang, X. Chen, A. Thomas, X. Fu and M. Antonietti, *Adv. Mater.*, 2009, **21**, 1609-1612.
47. S. Le, T. Jiang, Q. Zhao, X. Liu, Y. Li, B. Fang and M. Gong, *RSC Adv.*, 2016, **6**, 38811-38819.
48. X. Zou, R. Silva, A. Goswami and T. Asefa, *Appl. Surf. Sci.*, 2015, **357**, 221-228.
49. Y. Wang, Y. Wang, Y. Li, H. Shi, Y. Xu, H. Qin, X. Li, Y. Zuo, S. Kang and L. Cui, *Catal. Commun.*, 2015, **72**, 24-28.
50. X. a. Dong, J. Li, Q. Xing, Y. Zhou, H. Huang and F. Dong, *Appl. Catal B-Environ*, 2018, **232**, 69-76.
51. J. Jiang, S. Cao, C. Hu and C. Chen, *Chinese J. Catal.*, 2017, **38**, 1981-1989.
52. S. Hu, F. Li, Z. Fan, F. Wang, Y. Zhao and Z. Lv, *Dalton T.*, 2015, **44**, 1084-1092.
53. M. Wu, J.-M. Yan, X.-n. Tang, M. Zhao and Q. Jiang, *ChemSusChem*, 2014, **7**, 2654-2658.
54. M. Zhang, X. Bai, D. Liu, J. Wang and Y. Zhu, *Appl. Catal B-Environ*, 2015, **164**, 77-81.
55. Y. Wang, X. Zhao, D. Cao, Y. Wang and Y. Zhu, *Appl. Catal B-Environ*, 2017, **211**, 79-88.
56. Z. Ding, X. Chen, M. Antonietti and X. Wang, *ChemSusChem*, 2010, **4**, 274-281.
57. X. Li, P. Cui, W. Zhong, J. Li, X. Wang, Z. Wang and J. Jiang, *Chem. Commun.*, 2016, **52**, 13233-13236.
58. Y. Zheng, Y. Jiao, Y. Zhu, Q. Cai, A. Vasileff, L. H. Li, Y. Han, Y. Chen and S.-Z. Qiao, *J. Am. Chem. Soc.*, 2017, **139**, 3336-3339.
59. Q. Liu and J. Zhang, *Langmuir*, 2013, **29**, 3821-3828.

60. W. Zhang, J. Albero, L. Xi, K. M. Lange, H. Garcia, X. Wang and M. Shalom, *ACS Appl. Mater. Interfaces*, 2017, **9**, 32667-32677.
61. H. Dou, L. Chen, S. Zheng, Y. Zhang and G. Q. Xu, *Mater. Chem. Phys.*, 2018, **214**, 482-488.
62. J. Jin, X. Fu, Q. Liu and J. Zhang, *J. Mater. Chem. A*, 2013, **1**, 10538-10545.
63. Y. Cao, S. Chen, Q. Luo, H. Yan, Y. Lin, W. Liu, L. Cao, J. Lu, J. Yang, T. Yao and S. Wei, *Angew. Chem. Int. Ed.*, 2017, **56**, 12191-12196.
64. C. R. Groom, I. J. Bruno, M. P. Lightfoot and S. C. Ward, *Acta Crystallogr. B.*, 2016, **72**, 171-179.
65. T. Tong, B. Zhu, C. Jiang, B. Cheng and J. Yu, *Appl. Surf. Sci.*, 2018, **433**, 1175-1183.
66. T. L. O. P. W. Aktins, J. P. Rourke, M. T. Weller, F. A. Armstrong, *Shriver and Atkins' Inorganic Chemistry*, Oxford University Press, 5th Edition edn., 2010.
67. X. Rong, F. Qiu, J. Rong, J. Yan, H. Zhao, X. Zhu and D. Yang, *J. Solid State Chem.*, 2015, **230**, 126-134.
68. X. Li, W. Bi, L. Zhang, S. Tao, W. Chu, Q. Zhang, Y. Luo, C. Wu and Y. Xie, *Adv. Mater.*, 2016, **28**, 2427-2431.
69. G. Marzun, C. Streich, S. Jendrzej, S. Barcikowski and P. Wagener, *Langmuir*, 2014, **30**, 11928-11936.
70. G. Kyriakou, M. B. Boucher, A. D. Jewell, E. A. Lewis, T. J. Lawton, A. E. Baber, H. L. Tierney, M. Flytzani-Stephanopoulos and E. C. H. Sykes, *Science*, 2012, **335**, 1209.
71. C. Zhu, S. Fu, Q. Shi, D. Du and Y. Lin, *Angew. Chem. Int. Ed.*, 2017, **56**, 13944-13960.
72. H. Zhang, G. Liu, L. Shi and J. Ye, *Adv. Energy Mater.*, 2017, **8**, 1701343.
73. J. Liu, *ACS Catal.*, 2017, **7**, 34-59.
74. X. Wang, K. Maeda, A. Thomas, K. Takanabe, G. Xin, J. M. Carlsson, K. Domen and M. Antonietti, *Nat Mater*, 2009, **8**, 76-80.
75. F. Su, S. C. Mathew, G. Lipner, X. Fu, M. Antonietti, S. Blechert and X. Wang, *J. Am. Chem. Soc.*, 2010, **132**, 16299-16301.
76. Z. Chen, S. Mitchell, E. Vorobyeva, R. K. Leary, R. Hauert, T. Furnival, Q. M. Ramasse, J. M. Thomas, P. A. Midgley, D. Dontsova, M. Antonietti, S. Pogodin, N. López and J. Pérez-Ramírez, *Adv. Funct. Mater.*, 2017, **27**, 1605785-n/a.
77. Z. Chen, E. Vorobyeva, S. Mitchell, E. Fako, M. A. Ortuño, N. López, S. M. Collins, P. A. Midgley, S. Richard, G. Vilé and J. Pérez-Ramírez, *Nat. Nanotechnol.*, 2018, **13**, 702-707.
78. B. O'Regan and M. Gratzel, *Nature*, 1991, **353**, 737-740.
79. M. Grätzel, *J. Photochem. Photobiol., C*, 2003, **4**, 145-153.
80. G. Liu, A. Klein, A. Thissen and W. Jaegermann, *Surf. Sci.*, 2003, **539**, 37-48.
81. C. Y. Chen, M. K. Wang, J. Y. Li, N. Pootrakulchote, L. Alibabaei, C. H. Ngoc-le, J. D. Decoppet, J. H. Tsai, C. Gratzel, C. G. Wu, S. M. Zakeeruddin and M. Gratzel, *ACS Nano*, 2009, **3**, 3103-3109.
82. K. Maeda, R. Kuriki and O. Ishitani, *Chem. Lett.*, 2016, **45**, 182-184.
83. M. A. Gross, A. Reynal, J. R. Durrant and E. Reisner, *J. Am. Chem. Soc.*, 2014, **136**, 356-366.
84. C. A. Caputo, M. A. Gross, V. W. Lau, C. Cavazza, B. V. Lotsch and E. Reisner, *Angew. Chem. Int. Ed.*, 2014, **53**, 11538-11542.
85. H. Kasap, C. A. Caputo, B. C. M. Martindale, R. Godin, V. W. H. Lau, B. V. Lotsch, J. R. Durrant and E. Reisner, *J. Am. Chem. Soc.*, 2016, **138**, 9183-9192.
86. H. Kasap, D. S. Achilleos, A. Huang and E. Reisner, *J. Am. Chem. Soc.*, 2018, DOI: 10.1021/jacs.8b07853.
87. K. Maeda, K. Sekizawa and O. Ishitani, *Chem. Commun.*, 2013, **49**, 10127-10129.

88. R. Kuriki, O. Ishitani and K. Maeda, *ACS Appl. Mater. Interfaces*, 2016, **8**, 6011-6018.
89. K. Maeda, D. An, C. S. Kumara Ranasinghe, T. Uchiyama, R. Kuriki, T. Kanazawa, D. Lu, S. Nozawa, A. Yamakata, Y. Uchimoto and O. Ishitani, *J. Mater. Chem. A*, 2018, **6**, 9708-9715.
90. R. Kuriki, H. Matsunaga, T. Nakashima, K. Wada, A. Yamakata, O. Ishitani and K. Maeda, *J. Am. Chem. Soc.*, 2016, **138**, 5159-5170.
91. E. H. Yonemoto, G. B. Saupe, R. H. Schmehl, S. M. Hubig, R. L. Riley, B. L. Iverson and T. E. Mallouk, *J. Am. Chem. Soc.*, 1994, **116**, 4786-4795.
92. R. Kuriki and K. Maeda, *Phys. Chem. Chem. Phys.*, 2017, **19**, 4938-4950.
93. K. Wada, M. Eguchi, O. Ishitani and K. Maeda, *ChemSusChem*, 2016, **10**, 287-295.
94. K. Mori, T. Itoh, H. Kakudo, T. Iwamoto, Y. Masui, M. Onaka and H. Yamashita, *Phys. Chem. Chem. Phys.*, 2015, **17**, 24086-24091.
95. J. C. Fontecilla-Camps, A. Volbeda, C. Cavazza and Y. Nicolet, *Chem. Rev.*, 2007, **107**, 4273-4303.
96. A. Kumar, P. Kumar, R. Borkar, A. Bansiwal, N. Labhsetwar and S. L. Jain, *Carbon*, 2017, **123**, 371-379.
97. J. Hawecker, J. M. Lehn and R. Ziessel, *J. Chem. Soc., Chem. Commun.*, 1984, 328.
98. P. Kurz, B. Probst, B. Spingler and R. Alberto, *Eur. J. Inorg. Chem.*, 2006, **2006**, 2966-2974.
99. T. Morimoto, T. Nakajima, S. Sawa, R. Nakanishi, D. Imori and O. Ishitani, *J. Am. Chem. Soc.*, 2013, **135**, 16825-16828.
100. C. Riplinger, M. D. Sampson, A. M. Ritzmann, C. P. Kubiak and E. A. Carter, *J. Am. Chem. Soc.*, 2014, **136**, 16285-16298.
101. M. W. George, F. P. A. Johnson, J. R. Westwell, P. M. Hodges and J. J. Turner, *J. Chem. Soc., Dalton Trans.*, 1993, 2977-2979.
102. R. W. Balk, D. J. Stufkens and A. Oskam, *J. Chem. Soc., Dalton Trans.*, 1981, 1124-1133.
103. W. K. Smothers and M. S. Wrighton, *J. Am. Chem. Soc.*, 1983, **105**, 1067-1069.
104. C. Kutal, A. J. Corbin and G. Ferraudi, *Organometallics*, 1987, **6**, 553-557.
105. K. Kalyanasundaram, *J. Chem. Soc. Farad. T. 2*, 1986, **82**, 2401-2415.
106. M. Wrighton and D. L. Morse, *J. Am. Chem. Soc.*, 1974, **96**, 998-1003.
107. C. Kutal, M. A. Weber, G. Ferraudi and D. Geiger, *Organometallics*, 1985, **4**, 2161-2166.
108. J. Hawecker, J.-M. Lehn and R. Ziessel, *J. Chem. Soc., Chem. Commun.*, 1984, 328-330.
109. J. M. Smieja and C. P. Kubiak, *Inorg. Chem.*, 2010, **49**, 9283-9289.
110. J. M. Smieja, E. E. Benson, B. Kumar, K. A. Grice, C. S. Seu, A. J. M. Miller, J. M. Mayer and C. P. Kubiak, *P Natl Acad Sci*, 2012, **109**, 15646.
111. E. E. Benson, C. P. Kubiak, A. J. Sathrum and J. M. Smieja, *Chem. Soc. Rev.*, 2009, **38**, 89-99.
112. F. P. a. Johnson, M. W. George, F. Hartl and J. J. Turner, *Organometallics*, 1996, **15**, 3374.
113. J. M. Smieja, M. D. Sampson, K. A. Grice, E. E. Benson, J. D. Froehlich and C. P. Kubiak, *Inorg. Chem.*, 2013, **52**, 2484-2491.
114. M. Bourrez, F. Molton, S. Chardon-Noblat and A. Deronzier, *Angew. Chem. Int. Ed.*, 2011, **50**, 9903-9906.
115. W. M. Haynes, *CRC Handbook of Chemistry and Physics*, CRC Press: Boca Raton, FL, 92 edn., 2011.
116. A. M. Bond, R. Colton and M. E. McDonald, *Inorg. Chem.*, 1978, **17**, 2842-2847.

117. K. Wu, D. Mukherjee, A. Ellern, A. D. Sadow and W. E. Geiger, *New J. Chem.*, 2011, **35**, 2169-2178.
118. R. Kuriki, K. Sekizawa, O. Ishitani and K. Maeda, *Angew. Chem. Int. Ed.*, 2015, **54**, 2406-2409.
119. P. S. Kirlin, F. A. DeThomas, J. W. Bailey, H. S. Gold, C. Dybowski and B. C. Gates, *J. Phys. Chem-US*, 1986, **90**, 4882-4887.
120. G. D'Alfonso, D. Roberto, R. Ugo, C. L. Bianchi and A. Sironi, *Organometallics*, 2000, **19**, 2564-2572.
121. M. Komiyama, K. Yamamoto and Y. Ogino, *J. Mol. Catal.*, 1989, **56**, 78-85.
122. S. Oh, J. R. Gallagher, J. T. Miller and Y. Surendranath, *J. Am. Chem. Soc.*, 2016, **138**, 1820-1823.
123. S. Khabuanchalad, J. Wittayakun, R. J. Lobo-Lapidus, S. Stoll, R. D. Britt and B. C. Gates, *Langmuir*, 2013, **29**, 6279-6286.
124. M. A. Wright and J. A. Wright, *Dalton T.*, 2016, **45**, 6801-6811.
125. S. Diring, A. Carné-Sánchez, J. Zhang, S. Ikemura, C. Kim, H. Inaba, S. Kitagawa and S. Furukawa, *Chem. Sci.*, 2017, **8**, 2381-2386.
126. A. Schwarzer, T. Saplinova and E. Kroke, *Coord. Chem. Rev.*, 2013, **257**, 2032-2062.
127. J.-L. Zuo, W.-F. Fu, C.-M. Che and K.-K. Cheung, *Eur. J. Inorg. Chem.*, 2003, **2003**, 255-262.
128. M. Andrews, R. Laye and S. A. Pope, *Transition Met Chem*, 2009, **34**, 493-497.
129. K. Kailasam, J. D. Epping, A. Thomas, S. Losse and H. Junge, *Energy Environ Sci*, 2011, **4**, 4668-4674.
130. M. Groenewolt and M. Antonietti, *Adv. Mater.*, 2005, **17**, 1789-1792.
131. X. Li, J. Zhang, L. Shen, Y. Ma, W. Lei, Q. Cui and G. Zou, *Appl. Phys. A*, 2009, **94**, 387-392.
132. M. Kim, S. Hwang and J.-S. Yu, *J. Mater. Chem.*, 2007, **17**, 1656-1659.
133. F. Fina, S. K. Callear, G. M. Carins and J. T. S. Irvine, *Chem. Mater.*, 2015, **27**, 2612-2618.
134. X. Wang, K. Maeda, A. Thomas, K. Takanabe, G. Xin, J. M. Carlsson, K. Domen and M. Antonietti, *Nature Materials*, 2008, **8**, 76.
135. Y. Wang, X. Wang and M. Antonietti, *Angew. Chem. Int. Ed.*, 2012, **51**, 68-89.
136. M. Kawaguchi and K. Nozaki, *Chem. Mater.*, 1995, **7**, 257-264.
137. T. Komatsu, *Macromol. Chem. Phys.*, 2001, **202**, 19-25.
138. M. Thommes, K. Kaneko, V. Neimark Alexander, P. Olivier James, F. Rodriguez-Reinoso, J. Rouquerol and S. W. Sing Kenneth, *Journal*, 2015, **87**, 1051.
139. M. F. De Lange, T. J. H. Vlugt, J. Gascon and F. Kapteijn, *Microporous Mesoporous Mater.*, 2014, **200**, 199-215.
140. C. Shen, C. Chen, T. Wen, Z. Zhao, X. Wang and A. Xu, *J. Colloid Interface Sci.*, 2015, **456**, 7-14.
141. L. Maxwell, S. Gomez-Coca, T. Weyhermuller, D. Panyella and E. Ruiz, *Dalton T.*, 2015, **44**, 15761-15763.
142. O. Kresnawahjuesa, R. Gorte, D. de Oliveira and L. Lau, *A Simple, Inexpensive, and Reliable Method for Measuring Brønsted-Acid Site Densities in Solid Acids*, 2002.
143. Z. W. Deng and R. Souda, *Thin Solid Films*, 2002, **406**, 46-53.
144. J. Hong, X. Xia, Y. Wang and R. Xu, *J. Mater. Chem.*, 2012, **22**, 15006-15012.
145. M. Baar and S. Blechert, *Chem. Eur. J.*, 2015, **21**, 526-530.
146. H. Zhang, Y. Huang, X. Lin, F. Lu, Z. Zhang and Z. Hu, *Sensors and Actuators B: Chemical*, 2018, **255**, 2218-2222.
147. X. Guo, Y. Wang, F. Wu, Y. Ni and S. Kokot, *Microchim. Acta*, 2016, **183**, 773-780.

148. Y. Zhu, H. Li, B. Shi, W. Qu, Y. Zhang, Q. Lin, H. Yao and T. Wei, *RSC Adv.*, 2014, **4**, 61320-61323.
149. F. Hartl, D. Rossenaar Brenda, J. Stor Gerard and J. Stufkens Derk, *Recl. Trav. Chim. Pays-Bas*, 1995, **114**, 565-570.
150. L. A. Worl, R. Duesing, P. Chen, L. D. Ciana and T. J. Meyer, *J. Chem. Soc., Dalton Trans.*, 1991, 849-858.
151. A. Vlček, in *Photophysics of Organometallics*, ed. A. J. Lees, Springer Berlin Heidelberg, Berlin, Heidelberg, 2010, pp. 115-158.
152. A. M. Bond, R. Colton and P. Panagiotidou, *Organometallics*, 1988, **7**, 1767-1773.
153. J. V. Caspar and T. J. Meyer, *J. Am. Chem. Soc.*, 1983, **105**, 5583-5590.
154. E. M. Kober and T. J. Meyer, *Inorg. Chem.*, 1982, **21**, 3967-3977.
155. N.-H. Kim, I.-C. Hwang and K. Ha, *Acta Crystallogr. E.*, 2009, **65**, m180.
156. A. Savini, P. Belanzoni, G. Bellachioma, C. Zuccaccia, D. Zuccaccia and A. Macchioni, *Green Chem.*, 2011, **13**, 3360-3374.
157. R. Kawahara, K.-i. Fujita and R. Yamaguchi, *J. Am. Chem. Soc.*, 2012, **134**, 3643-3646.
158. W. Xiang, F. Huang, Y.-B. Cheng, U. Bach and L. Spiccia, *Energy Environ Sci*, 2013, **6**, 121-127.
159. Z. Xu, P. Yan, H. Li, K. Liu, X. Liu, S. Jia and Z. C. Zhang, *ACS Catal.*, 2016, **6**, 3784-3788.
160. D. Wang, S. L. Marquard, L. Troian-Gautier, M. V. Sheridan, B. D. Sherman, Y. Wang, M. S. Eberhart, B. H. Farnum, C. J. Dares and T. J. Meyer, *J. Am. Chem. Soc.*, 2018, **140**, 719-726.
161. V. N. Khabashesku, J. L. Zimmerman and J. L. Margrave, *Chem. Mater.*, 2000, **12**, 3264-3270.
162. Y. Hu, Y. Shim, J. Oh, S. Park, S. Park and Y. Ishii, *Chem. Mater.*, 2017, **29**, 5080-5089.
163. K. G. Orrell, A. G. Osborne, V. Šik and M. W. da Silva, *Polyhedron*, 1995, **14**, 2797-2802.
164. T. H. Walter, L. Reven and E. Oldfield, *J. Phys. Chem-US*, 1989, **93**, 1320-1326.
165. J. Martin David, K. Qiu, A. Shevlin Stephen, D. Handoko Albertus, X. Chen, Z. Guo and J. Tang, *Angew. Chem. Int. Ed.*, 2014, **53**, 9240-9245.
166. P. Sundberg, C. Andersson, B. Folkesson and R. Larsson, *J. Electron. Spectrosc. Relat. Phenom.*, 1988, **46**, 85-92.
167. J. Yi, T. Miller Jeffrey, Y. Zemlyanov Dmitry, R. Zhang, J. Dietrich Paul, H. Ribeiro Fabio, S. Suslov and M. Abu-Omar Mahdi, *Angew. Chem. Int. Ed.*, 2013, **53**, 833-836.
168. Y. Yuan and Y. Iwasawa, *J Phys. Chem. B*, 2002, **106**, 4441-4449.
169. M. Komiyama, Y. Ogino, Y. Akai and M. Goto, *J. Chem. Soc. Farad. T. 2*, 1983, **79**, 1719-1728.
170. J. P. Lomont, S. C. Nguyen and C. B. Harris, *J Phys Chem A*, 2013, **117**, 3777-3785.
171. H. Yang, P. T. Snee, K. T. Kotz, C. K. Payne, H. Frei and C. B. Harris, *J. Am. Chem. Soc.*, 1999, **121**, 9227-9228.
172. T. S. Chong, P. Li, W. K. Leong and W. Y. Fan, *J. Organomet. Chem.*, 2005, **690**, 4132-4138.
173. R. Carballo, E. García-Martínez, G. Pereiras-Gabián and M. Vázquez-López Ezequiel, *Journal*, 2003, **58**, 1021.
174. L. A. P. Kane-Maguire and D. A. Sweigart, *Reactivity of tricarbonyl(arene)manganese(I) and -rhenium(I) cations. Nucleophilic addition of tributylphosphine to the arene and arene displacement with acetonitrile*, 1979.

175. D. Donghi, D. Maggioni, G. D’Alfonso, F. Amigoni, E. Ranucci, P. Ferruti, A. Manfredi, F. Fenili, A. Bisazza and R. Cavalli, *Biomacromolecules*, 2009, **10**, 3273-3282.
176. B. Choudhury, K. K. Paul, D. Sanyal, A. Hazarika and P. K. Giri, *J. Phys. Chem. C*, 2018, **122**, 9209-9219.
177. Y. Zhang, Q. Pan, G. Chai, M. Liang, G. Dong, Q. Zhang and J. Qiu, *Scientific Reports*, 2013, **3**, 1943.
178. J. Bian, J. Li, S. Kalytchuk, Y. Wang, Q. Li, T. C. Lau, T. A. Niehaus, A. L. Rogach and R.-Q. Zhang, *ChemPhysChem*, 2015, **16**, 954-959.
179. J. Li, H. Wang, Z. Guo, Y. Wang, H. Ma, X. Ren, B. Du and Q. Wei, *Talanta*, 2017, **162**, 46-51.
180. L. Chen, Z. Song, X. Liu, L. Guo, M.-j. Li and F. Fu, *Analyst*, 2018, **143**, 1609-1614.
181. J. Bhuvaneswari, A. K. Fathima and S. Rajagopal, *J. Photochem. Photobiol. A-Chem.*, 2012, **227**, 38-44.
182. H. Dang, G. Tan, W. Yang, F. Su, H. Fan, X. Dong and L. Ye, *J Taiwan Inst. Chem. E.*, 2017, **78**, 185-194.
183. S. Min and G. Lu, *J. Phys. Chem. C*, 2011, **115**, 13938-13945.
184. K. Kalyanasundaram, *Coord. Chem. Rev.*, 1982, **46**, 159-244.
185. G. J. Wilson and G. D. Will, *Inorg. Chim. Acta*, 2010, **363**, 1627-1638.
186. R. F. Dallinger and W. H. Woodruff, *J. Am. Chem. Soc.*, 1979, **101**, 4391-4393.
187. C.-J. Wallentin, J. D. Nguyen, P. Finkbeiner and C. R. J. Stephenson, *J. Am. Chem. Soc.*, 2012, **134**, 8875-8884.
188. F. G. Gao and A. J. Bard, *J. Am. Chem. Soc.*, 2000, **122**, 7426-7427.
189. C. K. Prier, D. A. Rankic and D. W. C. MacMillan, *Chem. Rev.*, 2013, **113**, 5322-5363.
190. J. Xie, H. Jin, P. Xu and C. Zhu, *Tetrahedron Lett.*, 2014, **55**, 36-48.
191. Y. Xi, H. Yi and A. Lei, *Org. Biomol. Chem.*, 2013, **11**, 2387-2403.
192. A. B. Ducrot, B. A. Coulson, R. N. Perutz and A.-K. Duhme-Klair, *Inorg. Chem.*, 2016, **55**, 12583-12594.
193. C. Agnes, J.-C. Arnault, F. Omnes, B. Jousselme, M. Billon, G. Bidan and P. Mailley, *Phys. Chem. Chem. Phys.*, 2009, **11**, 11647-11654.
194. M. K. Nazeeruddin, E. Baranoff and M. Grätzel, *Sol. Energy*, 2011, **85**, 1172-1178.
195. N. Marinakis, C. Wobill, E. C. Constable and C. E. Housecroft, *Polyhedron*, 2018, **140**, 122-128.
196. S. Chu, Y. Wang, Y. Guo, J. Feng, C. Wang, W. Luo, X. Fan and Z. Zou, *ACS Catal.*, 2013, **3**, 912-919.
197. A. Juris, V. Balzani, P. Belser and A. von Zelewsky, *Helv. Chim. Acta*, 1981, **64**, 2175-2182.
198. P. Xia, B. Zhu, J. Yu, S. Cao and M. Jaroniec, *J. Mater. Chem. A*, 2017, **5**, 3230-3238.
199. P. Sharma and Y. Sasson, *Green Chem.*, 2016, **19**, 844-852.
200. E. R. Talaty, S. Raja, V. J. Storhaug, A. Dölle and W. R. Carper, *J Phys. Chem. B*, 2004, **108**, 13177-13184.
201. P. K. Mallick, G. D. Danzer, D. P. Strommen and J. R. Kincaid, *J. Phys. Chem-US*, 1988, **92**, 5628-5634.
202. D. Hollmann, M. Karnahl, S. Tschierlei, K. Kailasam, M. Schneider, J. Radnik, K. Grabow, U. Bentrup, H. Junge, M. Beller, S. Lochbrunner, A. Thomas and A. Brückner, *Chem. Mater.*, 2014, **26**, 1727-1733.
203. L. Pazderski, T. Pawlak, J. Sitkowski, L. Kozerski and E. Szłyk, *Magn. Reson. Chem.*, 2010, **48**, 450-457.
204. J. Morgan David, *Surf. Interface Anal.*, 2015, **47**, 1072-1079.

205. S. Mallakpour, M. Dinari, H. Hadadzadeh, M. Daryanavard and F. Roudi, *J. Fluoresc.*, 2014, **24**, 1841-1848.
206. W. Dong, S. I. Shu-Feng, D.-Z. Liao, Z.-H. Jiang and S.-P. Yan, *J. Coord. Chem.*, 2003, **56**, 531-538.
207. B. Kraeutler and A. J. Bard, *J. Am. Chem. Soc.*, 1978, **100**, 4317-4318.
208. K. Hashimoto, M. Hiramoto, A. B. P. Lever and T. Sakata, *J. Phys. Chem-US*, 1988, **92**, 1016-1018.
209. M. J. Lundqvist, E. Galoppini, G. J. Meyer and P. Persson, *J Phys Chem A*, 2007, **111**, 1487-1497.
210. L. De Cola and F. Barigelletti, *Inorg. Chim. Acta*, 1989, **159**, 169-172.
211. K. M. Omberg, J. R. Schoonover, J. A. Treadway, R. M. Leasure, R. B. Dyer and T. J. Meyer, *J. Am. Chem. Soc.*, 1997, **119**, 7013-7018.
212. P. Dongare, B. D. B. Myron, L. Wang, D. W. Thompson and T. J. Meyer, *Coord. Chem. Rev.*, 2017, **345**, 86-107.
213. A. Soupart, I. M. Dixon, F. Alary and J.-L. Heully, *Theor. Chem. Acc.*, 2018, **137**, 37.
214. C. Daul, E. J. Baerends and P. Vernooijs, *Inorg. Chem.*, 1994, **33**, 3538-3543.
215. Y. Tachibana, J. E. Moser, M. Grätzel, D. R. Klug and J. R. Durrant, *J. Phys. Chem-US*, 1996, **100**, 20056-20062.
216. C. F. Chiu, N. Dementev and E. Borguet, *J Phys Chem A*, 2011, **115**, 9579-9584.
217. M. Rong, L. Lin, X. Song, Y. Wang, Y. Zhong, J. Yan, Y. Feng, X. Zeng and X. Chen, *Biosens. Bioelectron.*, 2015, **68**, 210-217.
218. Y. S. Jun, Z. Lee Eun, X. Wang, H. Hong Won, D. Stucky Galen and A. Thomas, *Adv. Funct. Mater.*, 2013, **23**, 3661-3667.
219. T. Christidis, M. Tabbal, S. Isber and S. Rizk, *Diamond Relat. Mater.*, 2004, **13**, 1561-1564.
220. D. Rovnyak, M. Baldus, B. A. Itin, M. Bennati, A. Stevens and R. G. Griffin, *J Phys. Chem. B*, 2000, **104**, 9817-9822.
221. M. Tabbal, T. Christidis, S. Isber, P. Mérel, M. A. El Khakani, M. Chaker, A. Amassian and L. Martinu, *J. Appl. Phys.*, 2005, **98**, 044310.
222. L. Le Quang, *TiO2/[Ru(bpy)3]2+ based hybrid nanomaterials associated with [Cr(ttpy)2]3+, [Mn(ttpy)(CO)3Br] or a pyrrole moiety: Synthesis, spectroscopic studies and applications in solar energy conversion*, HAL, Universite Grenoble Alpes, 2017.
223. S. Barman and M. Sadhukhan, *J. Mater. Chem.*, 2012, **22**, 21832-21837.
224. YunYang, W. Lei, Y. Xu, T. Zhou, M. Xia and Q. Hao, *Microchim. Acta*, 2017, **185**, 39.
225. Q. Zhuang, L. Sun and Y. Ni, *Talanta*, 2017, **164**, 458-462.
226. G. Shiravand, A. Badiei and G. Mohammadi Ziarani, *Sensor Actuat. B- Chem*, 2017, **242**, 244-252.
227. X. Yue, L. Liu, Z. Li, Q. Yang, W. Zhu, W. Zhang and J. Wang, *Food Chem.*, 2018, **256**, 45-52.
228. T. Förster, *Annalen der Physik*, 1948, **437**, 55-75.
229. F. Fennel and S. Lochbrunner, *Phys. Rev. B*, 2012, **85**, 094203.
230. J. G. d. V. a. C. J. Elsevier, *Handbook of Homogeneous Hydrogenation*, Wiley-VCH Verlag GmbH & Co. KGaA, Weinheim, 2008.
231. S. Nishimura, *Handbook of Heterogeneous Catalytic Hydrogenation for Organic Synthesis*, John Wiley & Sons, Inc., 2001.
232. D. Sanfilippo and P. N. Rylander, *Hydrogenation and Dehydrogenation*, Wiley-VCH, 2009.
233. J. A. Osborn, F. H. Jardine, J. F. Young and G. Wilkinson, *J. Chem. Soc. A.*, 1966, 1711-1732.
234. P. Meakin, J. P. Jesson and C. A. Tolman, *J. Am. Chem. Soc.*, 1972, **94**, 3240-3242.

235. R. Crabtree, *Acc. Chem. Res.*, 1979, **12**, 331-337.
236. R. H. Crabtree and M. W. Davis, *J. Org. Chem.*, 1986, **51**, 2655-2661.
237. X. Wu, J. Liu, X. Li, A. Zanotti-Gerosa, F. Hancock, D. Vinci, J. Ruan and J. Xiao, *Angew. Chem. Int. Ed.*, 2006, **45**, 6718-6722.
238. X. Wu, X. Li, A. Zanotti-Gerosa, A. Pettman, J. Liu, A. J. Mills and J. Xiao, *Chem. Eur. J.*, 2008, **14**, 2209-2222.
239. S. Ogo, N. Makihara and Y. Watanabe, *Organometallics*, 1999, **18**, 5470-5474.
240. X. Wu, D. Vinci, T. Ikariya and J. Xiao, *Chem. Commun.*, 2005, 4447-4449.
241. D. Wang and D. Astruc, *Chem. Rev.*, 2015, **115**, 6621-6686.
242. A. Bartoszewicz, N. Ahlsten and B. Martín-Matute, *Chem. Eur. J.*, 2013, **19**, 7274-7302.
243. C. Li, C. Wang, B. Villa-Marcos and J. Xiao, *J. Am. Chem. Soc.*, 2008, **130**, 14450-14451.
244. Y. Suna, M. Z. Ertem, W.-H. Wang, H. Kambayashi, Y. Manaka, J. T. Muckerman, E. Fujita and Y. Himeda, *Organometallics*, 2014, **33**, 6519-6530.
245. T. Thorpe, J. Blacker, S. M. Brown, C. Bubert, J. Crosby, S. Fitzjohn, J. P. Muxworthy and J. M. J. Williams, *Tetrahedron Lett.*, 2001, **42**, 4041-4043.
246. Y. Ma, H. Liu, L. Chen, X. Cui, J. Zhu and J. Deng, *Org. Lett.*, 2003, **5**, 2103-2106.
247. M. Zhu, *Catal Lett*, 2016, **146**, 575-579.
248. X. Wu, C. Wang and J. Xiao, *Platinum Met. Rev.*, 2010, **54**, 3-19.
249. M. Blanco, P. Álvarez, C. Blanco, M. V. Jiménez, J. Fernández-Tornos, J. J. Pérez-Torrente, J. Blasco, G. Subías, V. Cuartero, L. A. Oro and R. Menéndez, *Carbon*, 2016, **96**, 66-74.
250. M. Blanco, P. Álvarez, C. Blanco, M. V. Jiménez, J. Fernández-Tornos, J. J. Pérez-Torrente, L. A. Oro and R. Menéndez, *ACS Catal.*, 2013, **3**, 1307-1317.
251. A. M. Rasero-Almansa, A. Corma, M. Iglesias and F. Sanchez, *Green Chem.*, 2014, **16**, 3522-3527.
252. X. Xu, R. Wang, J. Wan, X. Ma and J. Peng, *RSC Adv.*, 2013, **3**, 6747-6751.
253. P. Barbaro, L. Gonsalvi, A. Guerriero and F. Liguori, *Green Chem.*, 2012, **14**, 3211-3219.
254. G. Liu, H. Gu, Y. Sun, J. Long, Y. Xu and H. Li, *Adv. Synth. Catal.*, 2011, **353**, 1317-1324.
255. H. Zhang, R. Jin, H. Yao, S. Tang, J. Zhuang, G. Liu and H. Li, *Chem. Commun.*, 2012, **48**, 7874-7876.
256. J. F. Hull, D. Balcells, J. D. Blakemore, C. D. Incarvito, O. Eisenstein, G. W. Brudvig and R. H. Crabtree, *J. Am. Chem. Soc.*, 2009, **131**, 8730-8731.
257. C. Zuccaccia, G. Bellachioma, S. Bolaño, L. Rocchigiani, A. Savini and A. Macchioni, *Eur. J. Inorg. Chem.*, 2011, **2012**, 1462-1468.
258. X. Liu, Y. Maegawa, Y. Goto, K. Hara and S. Inagaki, *Angew. Chem. Int. Ed.*, 2016, **55**, 7943-7947.
259. M. Waki, Y. Maegawa, K. Hara, Y. Goto, S. Shirai, Y. Yamada, N. Mizoshita, T. Tani, W.-J. Chun, S. Muratsugu, M. Tada, A. Fukuoka and S. Inagaki, *J. Am. Chem. Soc.*, 2014, **136**, 4003-4011.
260. G. Gunniya Hariyanandam, D. Hyun, P. Natarajan, K.-D. Jung and S. Yoon, *Catal. Today*, 2016, **265**, 52-55.
261. H. Nakajima, H. Nagao and K. Tanaka, *J. Chem. Soc.-Dalton T.*, 1996, 1405-1409.
262. T. Suzuki, *Inorg. Chim. Acta*, 2006, **359**, 2431-2438.
263. U. Hintermair, S. W. Sheehan, A. R. Parent, D. H. Ess, D. T. Richens, P. H. Vaccaro, G. W. Brudvig and R. H. Crabtree, *J. Am. Chem. Soc.*, 2013, **135**, 10837-10851.
264. S. J. Freakley, J. Ruiz-Esquius and D. J. Morgan, *Surf. Interface Anal.*, 2017, **49**, 794-799.

265. V. Thangaraj, J. Bussiere, J. M. Janot, M. Bechelany, M. Jaber, S. Subramanian, P. Miele and S. Balme, *Eur. J. Inorg. Chem.*, 2016, **2016**, 2125-2130.
266. S. Adhikari, N. R. Palepu, D. Sutradhar, S. L. Shepherd, R. M. Phillips, W. Kaminsky, A. K. Chandra and M. R. Kollipara, *J. Organomet. Chem.*, 2016, **820**, 70-81.
267. P. Sudakar, G. H. Gunasekar, I. H. Baek and S. Yoon, *Green Chem.*, 2016, **18**, 6456-6461.
268. M. Zhu, *Tetrahedron Lett.*, 2016, **57**, 509-511.
269. I. McManus, H. Daly, J. M. Thompson, E. Connor, C. Hardacre, S. K. Wilkinson, N. Sedaie Bonab, J. ten Dam, M. J. H. Simmons, E. H. Stitt, C. D'Agostino, J. McGregor, L. F. Gladden and J. J. Delgado, *J. Catal.*, 2015, **330**, 344-353.
270. P. J. Dyson and P. G. Jessop, *Catal. Sci. Technol.*, 2016, **6**, 3302-3316.
271. J. Cipot, R. McDonald and M. Stradiotto, *Organometallics*, 2006, **25**, 29-31.
272. M.-Y. Ngai, A. Barchuk and M. J. Krische, *J. Am. Chem. Soc.*, 2007, **129**, 280-281.
273. M. D. Fryzuk, L. Huang, N. T. McManus, P. Paglia, S. J. Rettig and G. S. White, *Organometallics*, 1992, **11**, 2979-2990.
274. G. Rubulotta, K. L. Luska, C. A. Urbina-Blanco, T. Eifert, R. Palkovits, E. A. Quadrelli, C. Thieuleux and W. Leitner, *ACS Sustain. Chem. Eng.*, 2017, **5**, 3762-3767.
275. T. Ohkuma, N. Utsumi, M. Watanabe, K. Tsutsumi, N. Arai and K. Murata, *Org. Lett.*, 2007, **9**, 2565-2567.
276. T. P. Brewster, N. M. Rezayee, Z. Culakova, M. S. Sanford and K. I. Goldberg, *ACS Catal.*, 2016, **6**, 3113-3117.
277. T. P. Brewster, A. J. M. Miller, D. M. Heinekey and K. I. Goldberg, *J. Am. Chem. Soc.*, 2013, **135**, 16022-16025.
278. Y. Sato, Y. Kayaki and T. Ikariya, *Organometallics*, 2016, **35**, 1257-1264.
279. Z. Xu, P. Yan, W. Xu, X. Liu, Z. Xia, B. Chung, S. Jia and Z. C. Zhang, *ACS Catal.*, 2015, **5**, 788-792.
280. J. Moritani, Y. Kayaki and T. Ikariya, *RSC Adv.*, 2014, **4**, 61001-61004.
281. K. H. Hopmann and A. Bayer, *Organometallics*, 2011, **30**, 2483-2497.
282. P. Brandt, C. Hedberg and G. Andersson Pher, *Chem. Eur. J.*, 2002, **9**, 339-347.
283. T. M. Gilbert and R. Bergman, *Synthesis of trimethylphosphine-substituted (pentamethylcyclopentadienyl)iridium hydride complexes; protonation and deprotonation of (pentamethylcyclopentadienyl)(trimethylphosphine)iridium dihydride*, 1985.
284. C. O'Connor and G. Wilkinson, *J. Chem. Soc. A.*, 1968, 2665-2671.
285. A. Y. C. White, P. M. Maitlis, D. M. Heinekey, in *Inorganic Syntheses*, ed. R. N. Grimes, 2007, vol. 29, p. 230.
286. S. P. Schmidt, W. C. Trogler, F. Basolo, M. A. Urbancic and J. R. Shapley, in *Inorganic Syntheses*, ed. R. J. Angelici, 2007, vol. 28, p. 161.
287. P. A. Lay, A. M. Sargeson, H. Taube, M. H. Chou and C. Creutz, in *Inorganic Syntheses*, ed. J. M. Shreeve, 2007, vol. 24, p. 292.
288. K. J. Reimer, A. Shaver and M. H. Quick, in *Inorganic Syntheses*, ed. R. J. Angelici, 2007, vol. 28, ch. 155.
289. R. Mitchell, PhD, University of York, 2014.